Manufacturing Construction Materials on Mars

A feasibility study on the use of Spark Plasma Sintering (SPS) for bulk manufacturing of a viable ISRU Mars construction material using regolith simulant.

MSc. Thesis

Theo-Jan Min

TU Delft

Manufacturing Construction Materials on Mars

A feasibility study on the use of Spark Plasma Sintering (SPS) for bulk manufacturing of a viable ISRU Mars construction material using regolith simulant.

by

Theo-Jan Min

A thesis
submitted to the faculty of Civil Engineering
at the Delft University of Technology
in partial fulfilment of the requirements
for the degree of Master of Science
in Civil Engineering.

To be defended publicly on September 9th, 2022 from 16:00-18:00 CET.

Student number:	4592166
1st examiner (Chair):	Dr. O. Çopuroğlu
2nd examiner:	Dr. ir. F.A. Veer
3rd examiner (Daily supervisor):	Ir. F. Mendonça Filho
Institution:	Delft University of Technology
Place:	Faculty of Civil Engineering and Geosciences, Delft
Project timeline:	15 November, 2021 – 9 September, 2022

Cover: Perseverance Captures Image of Kodiak (Jezero Crater) [1]

TU Delft Delft University of Technology

Acknowledgements

To start, I would like to express my heartfelt appreciation to Oğuzhan Çopuroğlu for taking on my thesis. Without him, this thesis would not have existed. He took time from his busy schedule to be my committee chair. He helped me with difficult questions, supported me in decision making and guided me through the process of graduation. He also went out of his way to ensure feasibility of this thesis. With support from his personal research budget, the expensive materials and processing techniques were made available. He also dubbed it the ”most expensive thesis” he ever had. His continued enthusiasm, kindness, vision and patience have helped to bring the thesis to the next level.

Next, I would like to thank Fernando F. de Mendonca Filho for being my daily supervisor. I could always come to him with my questions. His constructive criticism helped me improve my work and think about what I was doing. I also really appreciate the time he took to read through and check all of my submitted material.

I would also like to thank Fred Veer for taking the time to have discussions and check my work. His knowledge on the topic brought great input. His kindness and openness helped me start this project and reflect on it.

My immense gratitude goes to Hans Brouwer. Firstly, he welcomed me to his lab at 3ME and put great effort into learning me the process of SPS. He also put great time and effort into helping me perform sintering. He was continually there for me whenever I needed him and went out of his way to help me. He was so kind to even arrange alternative compression tests for me when it was impossible at my own faculty. Besides the technical discussions, Hans has also shown to be a great and likeable person in normal conversation. He lightened my spirit whenever I felt down and broadened my view on life. He even allowed me to go over my budget constraints and covered the extra cost himself. My appreciation for him is only increased by the fact that he did all of this, without having any official obligation to.

Special thanks to Maiko van Leeuwen. He always excitedly helped me find my way in the lab and was my go-to person for any questions about lab-equipment or contacting other staff members. He knows the lab like the back of his hand. He also arranged basic materials, learned me how to use most of the equipment and performed strength tests with me. He found the patience to work with the talkative person that I am and enjoyed it. This also shows his sociability, which is further expressed by his efforts to make the department a fun place where people go for drinks and other fun activities.

Many thanks to Arjan Thijssen for taking the time to perform SEM, CT and MIP with me. With his expertise we were able to make beautiful and detailed images. Together we could use our time most efficiently, while having good conversation. His encouraging words helped me with my motivation.

Also many thanks for the help and knowledge from the other Microlab technicians, Ton Blom and John van den Berg. With an added thanks for allowing me to use their material in the 3ME lab to Sean Scott, Ton Riemslag and Kevork Perez Bustos.

Some extra honourable mentions are in order; to Willem Hoekman for helping me learn about the SPS process and guiding me through his thesis; to Agata Mintus for helping me decide on the simulant material and for her thesis serving as a starting point; to Patrick Holthuizen for helping me with microscopy and IT problems; to my frequently contacted office colleagues Shan He, Yu Zheng and Anna van Ekenstein. I greatly appreciate the help and conversation from all other students, staff, PhD researchers, the secretariat and everybody else related to the lab.

Last but certainly not least, I thank my family and everyone near me for supporting me and raising me to who I have become today. Without them I could have never have achieved this.

Thank you.

Theo-Jan Min
Delft, September 2022

Abstract

For economic, scientific and survival reasons, colonisation of other planets is proposed [2–11]. Mars is the most suitable place to start [2, 4, 6, 8, 12–14]. To start an early Martian colony, viable In-Situ Resource Utilisation (ISRU) methods of low energy consumption are required to manufacture strong bulk construction materials [4, 15–22]. Most other studies have used infeasible materials or processes to investigate the possibility of manufacturing construction materials on Mars [23–26]. This study investigated answers to this problem and assessed the feasibility thereof under strict requirements.

A literature study has specified Martian regolith as the optimal raw resource. The use of water was not feasible [21, 27, 28]. Simulants MGS-1 [29] and JEZ-1 [30] were used as materials analogous to Martian regolith [22, 31]. Spark Plasma Sintering (SPS) has been chosen as the optimal production method considering Martian regolith and the environment.

An experimental study has verified the feasibility of the proposed material combined with the proposed method. Standard compressive tests, CT, SEM, SEM-EDS, DSC-TGA, Taguchi Design, MSEL and SPS, accompanied by standard measurements, yielded the following information: uniaxial compressive strength, density (distribution), macro porosity, microstructure, elemental composition, compaction, and energy requirement. Both simulant types were subject to three modifications: particle size, particle size reduction method and drying. Four SPS parameters have been analysed: temperature, duration, applied coating and applied pressure.

The minimum required compressive strength of 1.9 MPa was readily achieved. A maximum compressive strength of 137 MPa was found with an average of 48.50 MPa. Combined with the possible shape geometries of SPS, the manufactured material is expected to be structurally applicable. The measured theoretical energy requirement was 17.07 GJ/m^3. The applied energy use was 2.72 TJ/m^3. A reference dome [26] requires a feasible theoretical 89.5 kW or infeasible applied 14.3 MW for one year. The latter value was elevated due to experimental factors. The actual energy requirement of a Martian mission is expected to be closer to the theoretical energy requirement due to efficiency improvements. Water vapour was produced during sintering. This is a vital benefit to a Martian colony [21, 27]. To conclude, *ISRU bulk construction material manufacturing on Mars, for early colony development, is possible with regolith simulant and SPS.*

Contents

List of Tables

List of Figures

List of Abbreviations

BN	Boron Nitrite.
BSE	Back Scatter Electron.
CT	Computed Tomography.
DMSI	Dry-Mix/Steam Injection.
DSC	Differential Scanning Geometry.
EDS	Energy Dispersive X-ray Spectroscopy.
ESA	European Space Agency.
ISRU	In-Situ Resource Utilisation.
JEZ-1	Jezero Crater Simulant.
LEO	Low Earth Orbit.
LLO	Low Lunar Orbit.
MGS-1	Mars Global Simulant.
MIP	Mercury Intrusion Porosimetry.
MSEL	Modified Size Effect Law.
mt	metric ton.
NASA	National Aeronautics and Space Administration.
SPS	Spark Plasma Sintering.
TGA	Thermogravimetric Analysis.
VNIR	Visible/Near-Infrared.

1 Introduction

Increasing efforts are made toward Martian colonisation. Both NASA and ESA have their eyes set on the Red Planet. In their *National Space Policy* (2020) [6], the U.S.A. focuses directly on setting up human settlements on the Moon and Mars. NASA is putting this policy to use in its *Journey to Mars* (2015) strategy [8]. With ESA's *Terrae Novae 2030+* (2021) strategic roadmap [12], they make a bold claim of putting Europeans on Mars by 2040. Next to these public organisations, SpaceX, a private company, also aims for Martian colonisation [13]. Other space agencies, e.g. Roscosmos [32], CNSA [33] and ISRO [34], have a continued vision on Martian exploration. However, they have yet to announce official plans for a Martian colony.

Why is there such an interest in Martian exploration and even colonisation? The answers depend on who is asked. Governmental space agencies have a political motive. They aim to bring the benefits of space exploration to society [6, 12]. It can also be argued that it is a matter of being the first, similar to the space race between the USA and the USSR from 1957 to 1975.

Proponents of Martian colonisation argue that it is a possible way to diversify for specific planetary risks of extinction events [14]. Man-made disasters, such as climate change, can have devastating effects on humanity [11]. Naturally occurring extinction events also pose a real threat to humanity [3]. It could therefore be cost effective to prevent or circumnavigate them [3]. Having a human civilisation on an entirely different planet is one such method.

Private companies have a profit driven motive. They expect economic profits from exploitation of Mars. For similar reasons people emigrated from Europe to North America during the colonial era, people might want to emigrate from Earth to Mars [2]. Mars can prove to be a useful base for further asteroid mining operations and as an interplanetary hub for hydrogen fuel generation [4].

1.1. Problem Statement and Boundary Conditions

For humans to be able to survive on Mars, a functioning colony is necessary. Buildings are necessary to house all systems a functioning space colony requires, such as greenhouses, living quarters, oxygen facilities, laboratories and more. Additionally, Martian buildings should protect their inhabitants and equipment from substantial threats [26, 35].

Solar and cosmic radiation, low temperatures, meteorite impacts, dust storms and an unbreathable atmosphere are all hazardous to life. These conditions are further elaborated on in Chapter 2.2 and 2.3. Thus, tough structures should be built. There are several problems when trying to manufacture a suitable construction material for use on Mars. They will be commented on in this section and are separately explained in detail in Chapter 2 and 3.

It takes a lot of time, energy and cost to transport mass to Mars. This makes In-Situ Resource Utilisation (ISRU) a necessity. ISRU means local extraction and use of material. Thus, no raw resources should be send from Earth to Mars and the manufacturing method should be possible on Mars. In Chapter 2.1.1, this is elaborated on further. For this study, it means that a local bulk resource must be identified. This material must be usable in the manufacturing of a construction material. It also means that a manufacturing process must be chosen that is viable and applicable locally on Mars. It should not be too energy intensive, as energy is a very limited and valuable resource. It should also not require pre-existing processes, as it should be applicable on the first missions to Mars. The exact specifications will depend heavily on future, not-yet designed, Mars missions.

In this thesis, the chosen local resource was Martian regolith. Martian regolith is not directly available on Earth, as no mission has brought any material back from Mars yet. This problem has been tackled by using simulants. Simulants are analogous materials that simulate real Martian regolith as closely as possible [31]. It was concluded that water is not available for use in construction materials.

Differences between the Martian and Earth atmosphere can result in unrepresentative tests. The main reason is oxidation, which has little effect in the oxygen poor atmosphere of Mars but a large influence on

Earth. On Earth, moisture is also prevalent, which can have numerous effects. In Chapter 3.3 this is further explained and methods to tackle it are presented. The choice of production process, Spark Plasma Sintering (SPS), was also tailored to minimise this effect, see Chapter 2.6.10.

Before the SPS manufacturing method is tested. It should first be defined what a viable construction material for use on Mars requires. The proposed minimum strength of a suitable construction material for Mars is 1.9 MPa. This is explained in Chapter 3.5. Other properties, such as the density and porosity, are also important, but no quantitative goals have been set. The manufactured material must also be applicable in a structural sense. This is discussed in Chapter 6.14.

Other studies have used either infeasible materials or processes to investigate the possibility of manufacturing construction materials on Mars [23–26]. The strict requirements of this study result in direct applicability of the investigated method on Mars.

Lastly, the challenge of sustainability is discussed in Chapter 2.6.12. Due to small scale of an initial Martian colony, sustainability is not considered an issue. In the long term however, it can become a real problem which should be solved as quickly as possible. Therefore, sustainability is touched upon in this study, but not quantified.

1.2. Aim of the Study

The aim of the thesis is to study and explore suitable possibilities for manufacturing in-situ bulk construction materials on Mars for use during the founding stages of a Martian colony. This results in the general question: **What is a viable bulk construction material for use on Mars during early stages of colony development, manufactured using ISRU processes?**

In this thesis, it is hypothesised that a sufficiently strong and dense construction material can be manufactured with SPS, using MGS-1 and JEZ-1 simulants as a substitute for real Martian regolith. Due to the properties and scalability of SPS [36, 37], it is also suitable for manufacturing bulk construction material on the surface of Mars. The studied properties of the resulting construction material are hypothesised to show strength performance suitable for construction materials.

1.2.1. Sub-questions

Answers to the following sub-questions were explored in this thesis:

1. Which raw resources are available on Mars?
   (a) Where are they located?
   (b) In what quantities are they present?
   (c) How can they be extracted and how difficult is this process?
   (d) What is their chemical composition?
   (e) What is their mineral composition?
   (f) What is their grain size distribution?
2. What production processes are available to convert these raw materials into construction materials?
   (a) What is the energy requirement?
   (b) Is the process suitable for manufacturing bulk construction materials?
   (c) What is the proposed strength of the material?
   (d) Can the proposed material be utilised as a structural element?
3. Which of these processes should be subject to further study and tested in experimental research?
   (a) Are the answers given to 1.(a-f) sufficient for this specific production process?
   (b) Are the answers given to 2.(a-d) sufficient for the proposed structural requirements? (See 1.2.1 for the definitions of sufficient.)
   (c) Is the production process suitable for lab-scale testing?
   (d) How could Martian conditions influence the production process?
4. What are the properties of the production process?
   (a) What influences the physical properties of the manufactured material and how?

(b) Does the process yield enough material?
(c) What is the energy consumption of the process and is this feasible?

5. What are the physical properties of the manufactured construction material?

(a) What is the strength of the material and is it sufficient?
(b) What is the microstructure of the manufactured material?
(c) What is the density of the material?
(d) What is the density distribution inside the material?
(e) What is the macro porosity of the material?
(f) Is the manufactured material applicable as a structural element and how should it be applied?

Sufficiency

Sufficiency for sub-questions 2.(a-c) is limited by the proposed early stage of a Martian colony. Common sense and estimations enforce these limits. Even though these are not strict requirements, a ranking is possible to be made. From this ranking, a manufacturing method is chosen. This circumnavigates the impossible task of predicting exact figures, such as energy requirement, launch mass, reliability, and more. The ranking still allows for a qualitative choice and is presented in 2.6.10.

Sufficient for question sub-2.(b) is defined as being able to build at least enough domes for the first stage of colonisation with resources available within transportable reach. Transportable reach is defined by NASA's HLS2 workshop as a radius of 100 km [27]. In this study, the early stages of colony development are defined by a human population of about 16. This is equivalent to an "established research station or small settlement" [38]. For a population size of 16, this is equivalent to about 3 reference domes from the thesis of Mintus [26]. For this study, calculations are made for a single dome. The specifications of the dome are: a halve circle elongated dome of 20 meters length, with an inner diameter of 8 meters. A wall thickness of 0.5 metres is assumed.

Sufficient for sub-question 2.(c) is defined as having a minimum strength of conventional brick (5 MPa) times the gravitational factor for mars (0.38), see Chapter 3.5. Thus a minimum strength that is aimed for is 1.9 MPa. The same minimum is set for the results of sub-question 5.(d).

1.3. Methodology

To answer the research questions and test the hypothesis, a two part study was designed. The first part is a literature study. Here, the available resources on Mars and their characteristics are presented and discussed, answering research question 1.(a-f). This results in a choice of raw resource. Next, different proposed production methods were studied for viability as ISRU processes on Mars, presenting an answer to research question 2.(a-d). This results in a choice of manufacturing method.

The literature study shows the process of selecting a manufacturing technique and resource material. Using theoretical constraints, like available energy or technology, both are narrowed down to suitable methods and materials. The practical constraints limit these down to tangible manufacturing machines and materials within the resources of the lab and this thesis. This results in choice of methods and materials that should provide an answer to the main research questions. These choices are an answer to research questions 3.(a-c). The results, implications and conclusions for the mentioned research questions are discussed within the literature study itself.

The chosen methods are applied with the precautions explained in Section 1.1. Due to time and budget constraints, an unusual design method is chosen, the Taguchi method [39]. Practical handling and operation details are also described and reasoned.

Performing the steps outlined in the methods, results in answers to the research questions 4 and 5. Results about individual process variables will provide an answer to research question 4.(a). Results about mass loss provide an answer to question 4.(b). A calculation using of the energy requirement using data from the process will answer question 4.(c).

Uniaxial compressive strength measurements will answer research question 5.(a). Density measurements and Computed Tomography (CT) will answer questions 5.(b-d). Question 5.e will be answered using a combination of data available from both the results as well as the literature study.

Due to a lack of knowledge about the future design of an actual Martian colonisation mission, many conclusions cannot be drawn quantitatively. For example, energy production on Mars cannot accurately be predicted, as well as the energy consumption of a device that will actually be used on Mars. This limits this study to a

feasibility study. Processes and results are quantitatively reported. The real application of these figures can only be verified for use on Mars in future studies.

1.4. Thesis Layout

The main layout of this thesis has four parts. A literature review, the methods used, the characterisation and verification of the materials and the test results of the manufactured Martian construction material. Next to these four main parts, a discussion of the results, a conclusion and recommendations for further study are given. An overview is presented in Figure 1.1.

A literature study is presented in Chapter 2. A technical background is presented that serves as a fallback for information. In this part, the requirements for a Martian construction material become clear. Then, the available resources on Mars are presented. In the next section, different proposed methods in literature, for manufacturing construction materials on Mars and the Moon, are presented. Of these methods, SPS sintering is chosen and further elaborated on in Chapter 3.4. The choice and technical details of the Martian simulants are presented in Chapters 2.5 and 4.

In Chapter 3, the experimental setup and methodology of this thesis are described and substantiated. Here, the experimental setup and tests to be performed are presented. Storage, handling and pre-processing of material are also explained.

Chapter 4 presents details and verifications of the chosen Martian simulants. Both MGS-1 and JEZ-1 are described and limitations are presented. In-lab verification of the received material is presented. Mineralogy per particle size is extensively described to add to limitations in the producers technical data.

The results of the tests are presented in Chapter 5. Strength results are presented and discussed in Chapter 5.1. These results are most important to determine the practical application of the manufactured materials structural performance and viability. This allows for a conclusion on the viability of the manufactured material as a construction material on Mars. Density results are presented in Chapter 5.2. Next to density measurements, the density distribution throughout the sample is also shown. Porosity results are presented in Chapter 5.3. Then, compaction results of data from the SPS process are presented in 5.4. After this, mass loss is given in Chapter 5.5. Some notable examples from microstructure imaging are presented in Chapter 5.6. Afterwards, the energy consumption is calculated in Chapter 5.7. The feasibility of this method on Mars is calculated in Chapter 5.8.

The results are discussed in Chapter 6. In this Chapter, the influence of individual variables is discussed. Implications of the results are presented and substantiated. The limitations and influences of the test methods are then discussed.

Conclusions are presented in Chapter 7. Here, an answer to the main research question is presented. Furthermore, individual sub-questions are answered in a concise manner.

Afterwards, in Chapter 8, recommendations for further study are presented based on newly arisen questions, gaps in knowledge and interesting findings.

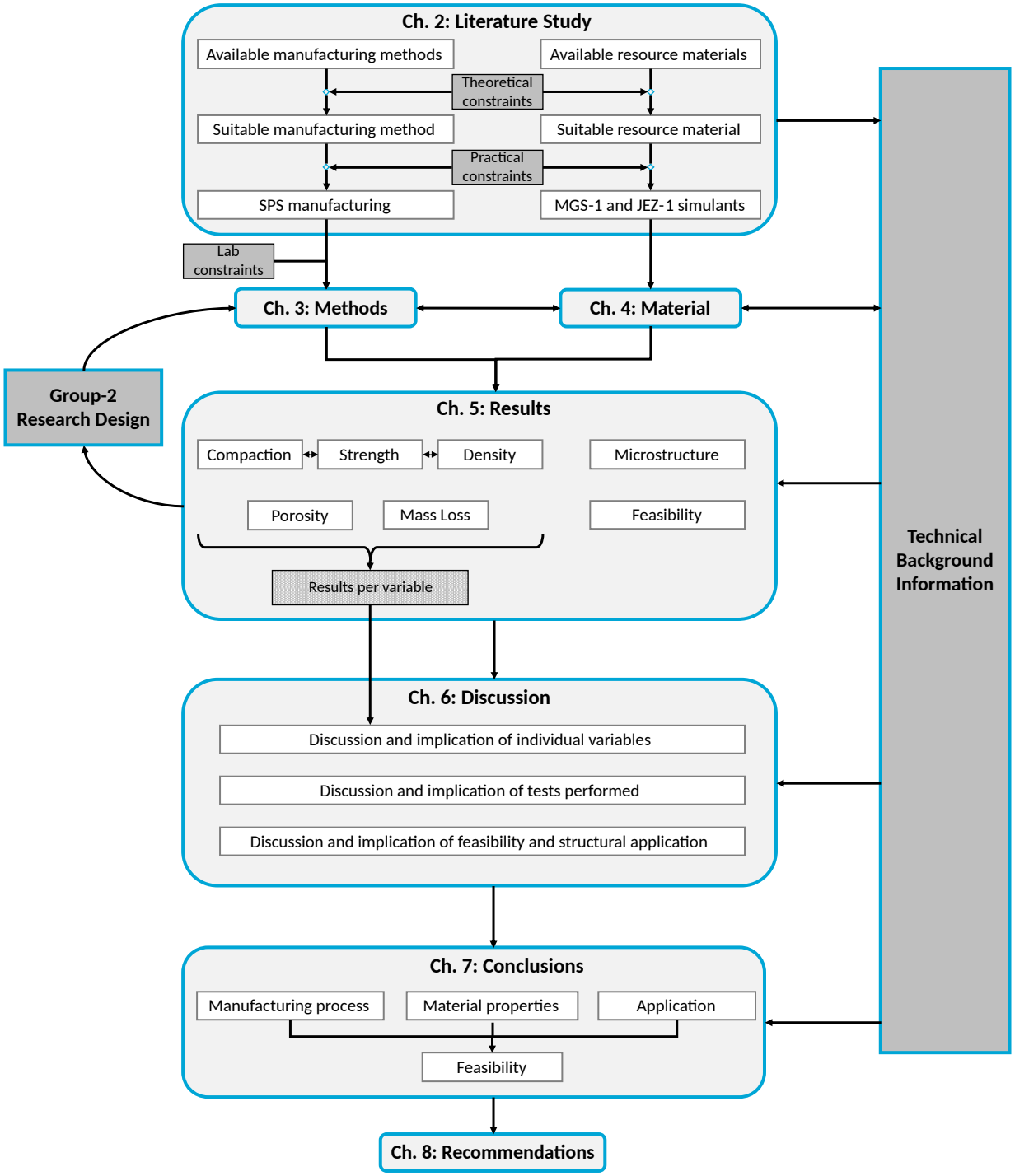

Figure 1.1: Overview of the thesis. Chapters are presented as rounded boxes. The literature study sets the base for the thesis. The findings are referred to throughout the thesis, as presented by the ”Technical Background Information” block. Next to this information, the literature study shows the process of selecting a manufacturing technique and resource material using theoretical and practical constraints. The methods are influenced by lab constraints. Together with the material, the methods yield results. These results are then discussed. A conclusion then presented where the research questions are answered. Afterwards recommendations for further study are given.

2
Literature Study and Discussion

First, a technical background about general Martian conditions and characteristics is presented. The orbital statistics about Mars and the Moon, the need for ISRU and its imposed limitations are explained. Furthermore, the effect of Martian gravity on the results of this study is stated. Then, the influence of planetary conditions is elaborated on while also presenting a comparison between Mars and the Earth in terms of planetary data. With information about the Martian environment, the requirements of construction materials and buildings on Mars are discussed. Furthermore, the local resources are described and Martian regolith is provided and discussed as the most suitable resource for manufacturing of construction materials. The challenges of testing Martian regolith on Earth are explained and a Martian simulant, a chemically and mineralogically analogous material, is chosen. Then different manufacturing methods are presented and discussed. From these, SPS is chosen. Lastly, the limitations of an early Martian colony are discussed in terms of energy use and sustainability.

2.1. Transportation to Mars

The distance between Mars and Earth varies widely between 54.6×10^6 km and 401.4×10^6 km, but has little correlation with the difficulty to transport material to Mars. For spacecraft, travel "distance" is measured in change in velocity required, called delta-v, ΔV, measured in km/s. This spacecraft-independent variable can be converted with the Tsiolkovsky rocket equation to obtain actual propellant, mass and propulsion figures depending on the type of spacecraft [40].

There are different routes a spacecraft can take to its destination, but a minimum is always sought for. For Mars this minimum can mean either a minimal time or minimal energy requirement. Both of these requirements lead to a certain launch window, a time frame in which a spaceship can be launched from Earth to fulfil certain transfer time and energy requirements. In Table 2.1, the ΔV requirements for Mars compared to the Moon are shown.

Table 2.1: ΔV requirements for Mars compared to the Moon [41, 42].

From - To	Δ**V** (km/s)
Earth - LEO[1]	9.3 - 10
LEO - Mars orbit	4.51
Mars orbit - Mars surface	0.0[3]- 5.5
Earth - Mars surface	14.51[3]
LEO - LLO[2]	4.4
LLO - Moon surface	1.87
Earth - Moon surface	15.93

[1] Low Earth Orbit (LEO)
[2] Low Lunar Orbit (LLO)
[3] Aerobraking is possible due to the Martian atmosphere. This can reduce ΔV to zero.

An interesting observation is that it requires less energy to send mass to Mars than to the Moon. This is the result of aerobraking. Aerobraking implies the loss of kinetic energy due to atmospheric drag. Basically, if a spacecraft comes into contact with an atmosphere, it will slow down. If this manoeuvre is performed right, a spacecraft does not need to spend energy to lower its orbit and land on a body which has an atmosphere. As the Moon does not have an atmosphere, but Mars has, energy requirements for a soft surface landing on the Moon are higher than on Mars. It should be noted, however, that it does require far longer to reach Mars, 7 months, compared to the Moon, 3 days [41].

2.1.1. In-Situ Resource Utilisation (ISRU)

Current research about Martian construction materials often utilises resource materials that are unavailable on Mars, elaborated in Chapter 2.6. To sustain a permanent presence on Mars, resources must be used locally. It is infeasible to send all required resources to Mars [4, 16–21]. This is mainly due to the difficulty of transporting mass to Mars from Earth, as described above. For oxygen and return fuel production, ISRU is expected to lower the transfer mass from 31.6 metric ton (mt), to as low as 1.6 mt [21]. Measured in terms of lifetime usable mass emplaced on Mars, at the same cost, ISRU can have more than twice the benefit [19]. Overall costs have been estimated to be reduced by 10 to 50 times when using ISRU [18]. Therefore, it is necessary to only consider ISRU manufacturing techniques.

Other research about Martian construction materials, consider precursor materials that are theoretically possible to produce on Mars, but not practically [23–26]. Sulphur concrete is such an example, as explained in Chapter 2.6.6. Using elemental sulphur as a precursor enables the manufacturing of suitable Martian construction materials [23, 24, 26]. The only issue is, elemental sulphur is not present on Mars [25, 26]. To obtain it, vast amount of energy and industrial processes are required [25, 26]. This directly counteracts most of the benefits of sulphur concrete.

For these reasons, in the context of ISRU, this study assumes no import of bulk resources from Earth. It is assumed that only equipment can be sent to Mars. Also no pre-existing processes are assumed. Thus, only raw resources are considered and not, for example, pre-made hydrogen or elemental sulphur. No limits are set to the size and scale of equipment. They should be refined before real application. However, common sense is used. This means that it is assumed impossible for large scale infrastructure to exist. For example, transportation of ice from the Martian poles to more equatorial regions is assumed impossible.

These ISRU limitations vastly broaden the applicability of this study. The main advantage is direct applicability. The very first robots or humans on Mars, tasked with creating the first buildings, can directly apply the techniques presented in this thesis, as no existing infrastructure is required. Furthermore, the assurance of applicability is of importance. It is unwise to send a very costly mission to Mars, when application is not significantly reliable.

2.2. General Martian Characteristics

Mars has different planetary characteristics from Earth. Although Mars has an aqueous geological history [43], currently it differs a lot from Earth. In Table 2.2 and overview is given for Martian planetary parameters compared to Earth.

Table 2.2: Martian characteristics summary.

Characteristic	**Mars**	**Earth**	**Ratio** (Mars/Earth)
Mass (10^{24} kg)	0.64	5.97	0.107
Volume (10^{10} km^3)	16.32	108.32	0.151
Mean density (kg/m^3)	3934	5513	0.714
Surface gravity (m/s^2)	3.71	9.8	0.379
Solar irradiance (W/m^2)	586.2	1361	0.431
Black-body temperature (K)	209.8	254	0.826
Number of natural satellites	2	1	
Average atmospheric pressure (mbar)	6.1	1013	0.006
Solar day	24h 37m	24h	1.026

It can be observed from Table 2.2 that a lower gravitational constant is present at the Martian surface compared to Earth. This is beneficial for construction as it results in lower self-weight. At about 0.38 times Earths gravity, construction on Mars requires different characteristics. To take this effect into account, load and strength values measured during this thesis, will be presented both normally and as Mars equivalents.

2.3. Martian Atmosphere and Environment

Although the Martian environment is not the most hazardous of our solar system [44], it is also not the kindest. On Earth, our buildings and us are protected from meteors and solar radiation by our atmosphere and magnetic field [45, 46]. Mars does not have an active magnetic field [46] and is home to only a very thin atmosphere. The atmospheric composition of Mars is presented in Table 2.3.

Table 2.3: Composition of the Martian atmosphere according to revised models by Franz et al. [47] compared to the Earth atmosphere [48].

Compound	**Mars** (vol.%)	**Earth** (vol.%)
CO_2	94.90	3.14×10^{-4}
N_2	2.79	78.08
Ar	2.08	9.34×10^{-3}
O_2	1.74×10^{-3}	20.95
CO	7.47×10^{-4}	-

Mars has few reactive chemicals in its atmosphere. The most abundant compound is CO_2. Under most conditions, including Martian conditions, CO_2 is regarded as non-reactive and even inert [49]. The second most abundant compound, N_2 is also considered an inert gas. It can thus be concluded that spontaneous reaction with the Martian atmosphere is highly unlikely.

2.3.1. Atmospheric Density

Mars has a very thin atmosphere. At the surface, it only has a density of 0.020 kg/m^3 [50], compared to Earths 1.217 kg/m^3. The atmosphere on Mars at surface level is on average 6.1 mbar [50, 51], only a fraction of Earth's 1013 mbar. Due to Martian seasons, the surface pressure can vary between 4.0 and 8.7 mbar [50]. This thin atmosphere has trouble retaining heat, even though it mainly consists of the greenhouse gas CO_2. Its low density provides little drag to moving objects, but it is enough to lift dust and create dust clouds and storms.

This results in bombardments of (micro)meteorites. Martian geological features are distinct due to weathering and bombardment from these meteorites [52]. While on Earth, meteorites usually burn up before they reach the surface, on Mars they frequently impact. Thus, structures should be able to resists them. This is a structural and material problem. Material properties are described, but structural design is outside the scope of this thesis.

The thin Martian atmosphere can also have an influence on construction materials. The low density can influence manufacturing methods that rely on heat, as convection is altered compared to Earth. It does enable easier vacuum manufacturing methods [53]. Secondly, the manufactured material is at risk of out-gassing. Fluids can more easily evaporate and some solids might sublimate due to low pressures [15]. Thirdly, depending on the actual structure that will be built, a difference in pressure between the habitable inside and the atmosphere could lead to tensile forces in light weight structures. For higher weight structures, this provides an added benefit of reducing the dead-load. This difference must also be accounted for by creating a sealed environment.

Low atmospheric pressures on Mars could result in sublimation of certain structural materials, such as sulphur concrete and magnesium alloys [15]. For regolith based materials, sublimation is not expected. Due to the extensive time periods that regolith has been subject to on Mars, any element or mineral that could sublime would have already done so. However, due to processing, new minerals can be created, or previously encapsulated elements and materials could be freed and exposed to the Martian atmosphere. Within this thesis, sublimation is not considered. Often sublimation rates are low compared to the thickness of proposed Martian structures [15].

2.3.2. Temperature

Mars' distance to the Sun, leads to lower solar irradiance, see Table 2.2. Combining this with the thin atmosphere results in low temperatures and high temperature fluctuations. The average atmospheric surface temperature on Mars is -63 °C [50, 54, 55]. Comparing different sources, the maximum and minimum reported surface temperatures are 35 °C [56] and -140 °C [54, 55]. Data provided by the Viking 1 [50] mission shows that typical diurnal temperatures are in the range of -89 °C to -31 °C at the location of the Viking 1 lander site. It must also be noted that, depending on a materials' albedo, the maximum surface temperature may be higher than the maximum atmospheric temperature.

Low temperatures can lead to altered material properties. Steel, for example, has the tendency to become more brittle in colder environments. Preferably, every test is performed in Martian conditions with respect to temperature. Taking the average of -63 °C would be a representative choice, but it would be better to test the material at temperature extremes. The albedo of the material and the specific heat capacity also influence

the actual temperature of the material. For this thesis, cryogenic testing is not considered.

Thermal expansion is an important parameter. Temperature variations within the Martian environment can lead to thermal stresses, and ultimately cracking. Expansion of structural materials is also known to lead to structural failures. These properties can be accounted for in design. Allowing for expansion within a structure is one such example. Therefore this is not investigated in this study.

2.3.3. Radiation

On Earth, the magnetic field protects us from most harmful radiation [46]. In combination with our thick atmosphere, this results in a safe location from cosmic and solar radiation, but also from meteorites [45, 46]. Mars does not have a strong magnetic field. In combination with Mars' thin atmosphere, solar winds and cosmic radiation can reach the surface in high doses. Discoveries by NASA have determined that an astronaut will be exposed to 0.66 Sv over a six-month period [57]. With maximum total career doses set for 1 Sv [35], a one year expedition is impossible. Therefore, the structures should provide this protection [35]. Different methods are proposed, but most of them rely on thickening the structure. Again, this is a structural problem. This thesis will provide density figures, which can only give an indication of radiation protection. Further study is necessary to investigate the radiation protective properties. One example is a thesis by Johnson [58].

2.4. Martian Resources

One consequence of the ISRU requirement form Section 2.1.1, is the use of local material as a resource. In this chapter, different (surface) resources are described. Martian regolith is extensively elaborated on as it is the choice of resource for this study.

Three factors strongly influence the usability of resources. Firstly, their location, both geographically as well as local distribution. Secondly, the amount present on Mars, both within reach of a colony as well as total amounts on Mars. Thirdly, their ease of extraction. A material that can only be found kilometres deep is too difficult to extract for early Martian colonies. If any condition is not sufficient, a resource is infeasible to consider. Other limitations for usable resources come from the manufacturing processes. Depending on the process, grain size distribution and chemical and mineral composition determine a resources' feasibility. The feasibility of each resource is discussed by noting how well it performs in the three mentioned factors. In Section 2.4.7, this is summarised and concluded upon.

2.4.1. Martian Regolith

Most of the surface of Mars is covered with regolith [59]. In Figure 2.1 the dust coverage of the surface of Mars can be seen. From an orbital perspective, dust coverage is similar to regolith coverage. Regolith consist of the unconsolidated layer of soil. The soil layer can extend from about 2 m up to 17 m in depth [60, 61]. The composition of regolith differs per location. In Table 2.4, the average oxide compositions of Martian soil in a few locations is presented. Martian dust is the dust that is present in the Martian air and forms thin layers of dust on most surface areas [62]. The Panda Subclass soil is the soil type that is generally considered as representative for average Martian regolith [62]. The MoessBerry Subclass is a soil subclass that contains high amounts of spherules [62, 63], which are discussed in Section 2.4.4. In Table 2.6 the mineral composition is presented.

Due to its availability and abundance, regolith is generally considered as the most feasible material to manufacture (bulk) materials from [15, 22–24, 26, 53, 64–67]. Regolith contains 1-7% by weight of ferromagnetic material [68, 69]. Magnetic components of Martian soil consist mainly of magnetite [69–72], see also Table 2.5. Not all particles of regolith are magnetic. It is also possible to extract magnetic particles from dust in the atmosphere [72]. They contain about 2% ferromagnetic minerals by weight.

Particle size distributions of regolith differ per location. Depending on location, a unimodal or multimodal grain-size distribution is present. For more fine-grained soils, particle sizes range between 50-650 µm, while courser multimodal soils range between 50-2150 µm. Figure 2.2 shows the differences in median and mean grain size across Spirits traverse. Figure 2.3 shows grain size distributions for different soils analysed by both Spirit and Curiosity rovers.

2.4.2. The Atmosphere

As the atmosphere is available everywhere on the surface, it could be a source of material. Due to its abundance in the atmosphere and our knowledge about carbon chemistry, CO_2 is a likely constituent that could be used to manufacture materials. Both nitrogen and argon are infeasible to utilise as a construction material

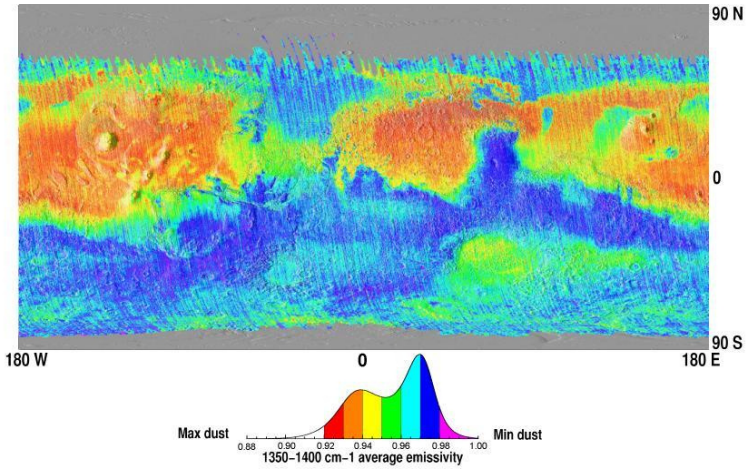

Figure 2.1: Map of the global DCI (Dust Cover Index) as developed by Ruff and Christensen in [59]. The average emissivity value in the 1350 –1400 cm^{-1} range is shown, binned at eight pixels per degree with gaps filled by interpolation. The index is sensitive to the occurrence of silicate spectral particle size effects and thus serves as an indicator for the presence of silicate dust on the surface. Orange, red, and white colours indicate areas that likely are dust covered while blue and magenta areas likely are dust-free. The colour scale bar is a histogram of the index values.

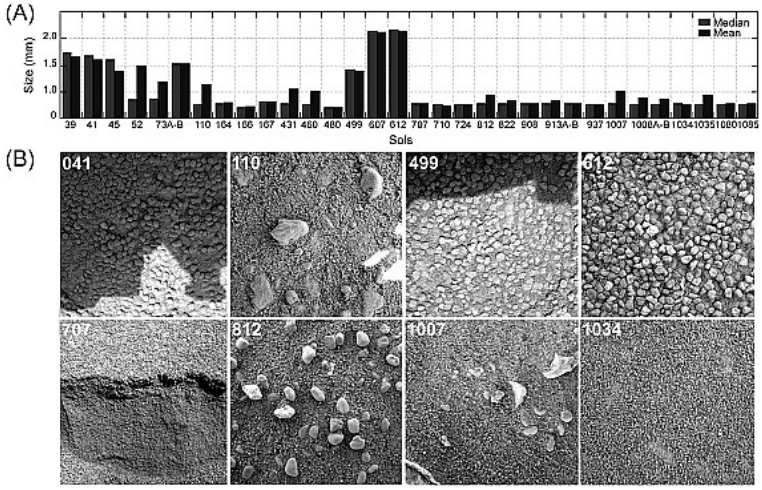

Figure 2.2: (A) Median and mean grain sizes across the traverse of the Spirit rover [74]. The ”A” and ”B” suffix indicate multiple measurements on the same sol. (B) Microscopic Imager images respective soil types. Each frame is 3.2 cm across

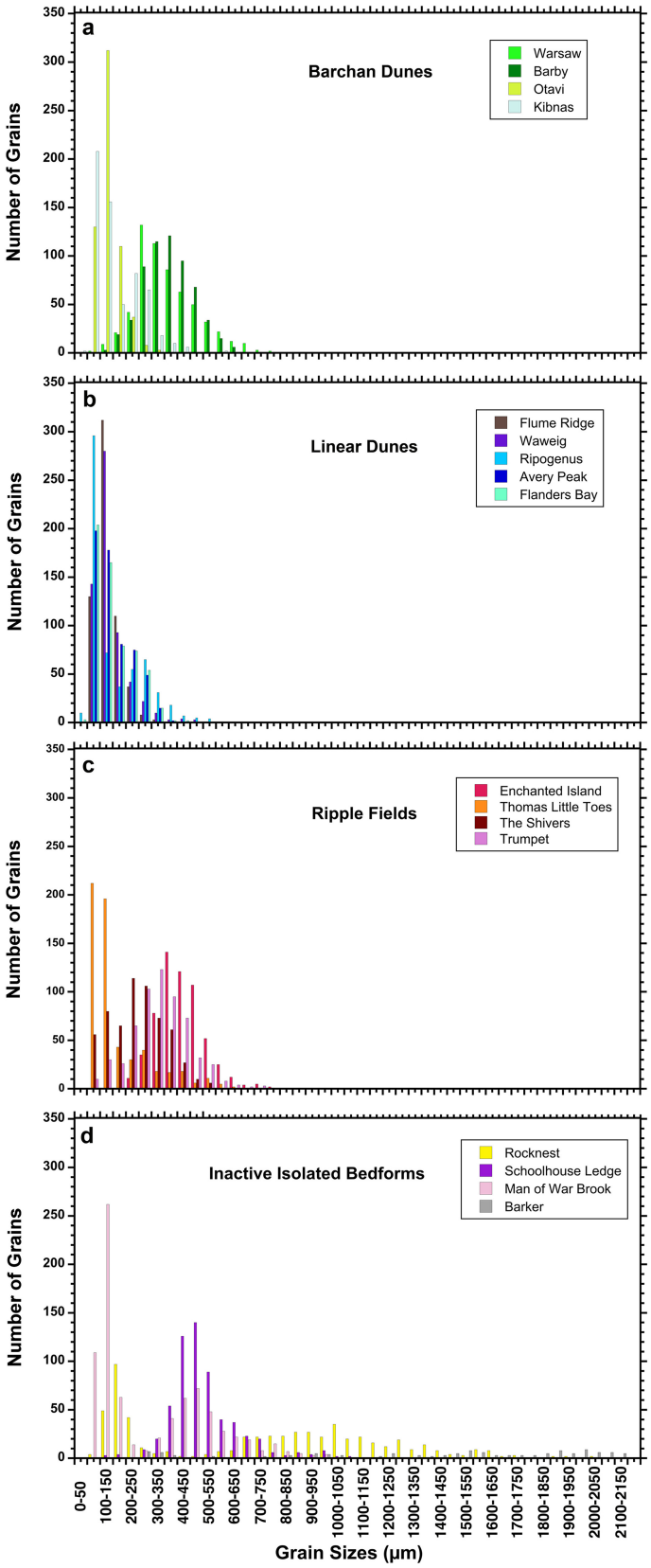

Figure 2.3: Grain distribution histograms for different soils at Gale crater [75]. Different dunes were analysed across the Curiosity rover's traverse. Every dune had multiple measurements, each indicated with its own name. For more information about the exact locations, naming, analyses and interpretation, it is recommended to read the original publication by Weitz et al. [75].

Table 2.4: Average oxide composition on Mars [63] for dust, Panda Subclass soil and MoesBerry Subclass soil. Differences exist for different sample locations, sample locations Gusec Crater (GC) and Meridiani Planum (MP) are presented. Panda subclass is generally accepted as a good average for Martian soil [62]. Values are presented in weight percentage (wt. %). Uncertainties are reported as $\pm 1\sigma$.

	Martian Dust			**Panda Subclass Soil**		**MoessBerry Subclass**
Oxide	GC (wt. %)	MP (wt. %)	Average (wt. %)	GC (wt. %)	MP (wt. %)	Observed (wt. %)
SiO_2	44.71 ± 0.52	44.97 ± 0.29	44.84 ± 0.52	46.52 ± 0.57	46.78 ± 1.22	38.54 ± 1.10
TiO_2	0.89 ± 0.08	1.01 ± 0.07	0.95 ± 0.08	0.87 ± 0.15	1.02 ± 0.18	0.73 ± 0.05
Al_2O_3	9.49 ± 0.16	9.14 ± 0.09	9.32 ± 0.18	10.46 ± 0.71	9.67 ± 0.49	7.63 ± 0.23
Cr_2O_3	0.31 ± 0.04	0.32 ± 0.03	0.32 ± 0.04	0.36 ± 0.08	0.41 ± 0.08	0.28 ± 0.03
Fe_2O_3	6.58 ± 0.07	7.97 ± 0.03	7.28 ± 0.70	4.20 ± 0.54	4.36 ± 0.74	20.24 ± 4.37
FeO	10.52 ± 0.11	10.31 ± 0.04	10.42 ± 0.11	12.18 ± 0.57	13.75 ± 1.00	11.17 ± 3.55
MnO	0.31 ± 0.02	0.34 ± 0.01	0.33 ± 0.02	0.33 ± 0.02	0.38 ± 0.02	0.28 ± 0.02
MgO	8.20 ± 0.15	7.57 ± 0.08	7.89 ± 0.32	8.93 ± 0.45	7.31 ± 0.30	6.55 ± 0.25
CaO	6.13 ± 0.07	6.54 ± 0.04	6.34 ± 0.20	6.27 ± 0.23	7.12 ± 0.28	5.23 ± 0.37
Na_2O	2.89 ± 0.29	2.22 ± 0.19	2.56 ± 0.33	3.02 ± 0.37	2.23 ± 0.23	2.16 ± 0.11
K_2O	0.48 ± 0.07	0.48 ± 0.06	0.48 ± 0.07	0.41 ± 0.03	0.49 ± 0.07	0.38 ± 0.03
P_2O_5	0.90 ± 0.09	0.93 ± 0.07	0.92 ± 0.09	0.83 ± 0.23	0.82 ± 0.05	0.81 ± 0.04
SO_3	7.56 ± 0.13	7.28 ± 0.07	7.42 ± 0.13	4.90 ± 0.74	4.97 ± 0.58	5.17 ± 0.42
Cl	0.88 ± 0.03	0.78 ± 0.01	0.83 ± 0.05	0.61 ± 0.08	0.57 ± 0.06	0.69 ± 0.03
Br ($x10^4$)	29 ± 22	26 ± 14	28 ± 22	49 ± 12	39 ± 27	56 ± 22
Ni ($x10^4$)	636 ± 73	467 ± 42	552 ± 85	544 ± 159	399 ± 100	854 ± 182
Zn ($x10^4$)	406 ± 32	401 ± 14	404 ± 32	204 ± 71	238 ± 63	329 ± 25
Total	99.85	99.87	99.86	99.89	99.89	99.84
Fe_3^+/FeT	0.36 ± 0.03	0.41 ± 0.03	0.39 ± 0.03	0.24 ± 0.02	0.22 ± 0.03	0.66 ± 0.06

Table 2.5: Magnetic dust particle mineralogy [72]

Spectral Component	**Dust on MER-A Capture Magnet** (wt. %)	**Dust on MER-B Capture Magnet** (wt.%)
Olivine, Fe^{2+}	4	16
Pyroxene, Fe^{2+}	7	14
Ferric doublet, Fe^{3+}	21	23
Magnetite (tetrahedral), Fe^{3+}	24	32
Magnetite (octahedral), $Fe^{2.5+}$	44	14
Hematite, Fe^{3+}	0	0
Total	100	100

Table 2.6: Mineralogy on Mars. Crystalline mineralogy is presented as analysed at Rocknest, Gale crater [73]. Uncertainties are reported as $\pm 1\sigma$.

Sample	**Sample** (wt.%)	**Sample** (wt.%)	**Sample**
Plagioclase	40.7 ± 5	26.3 ± 7	$(Ca_{0.50(4)}Na_{0.50})(Al_{1.50}Si_{2.50})O_8$
Olivine	20.5 ± 4	13.3 ± 4	$(Mg_{1.15(5)}Fe_{0.85})SiO_4$
Augite	18.1 ± 13	11.7 ± 9	$(Mg_{1.01(15)}Ca_{0.80(11)}Fe_{0.19(19)})Si_2O_6$
Pigeonite	12.3 ± 12	8.0 ± 8	$(Mg_{1.02(16)}Fe_{0.88(18)}Ca_{0.10(9)})Si_2O_6$
Magnetite	2.8 ± 5	1.8 ± 3	Fe_3O_4
Anhydrite	1.4 ± 3	0.9 ± 2	$CaSO_4$
Hematite	1.6 ± 1	1.0 ± 1	Fe_2O_3
Quartz	1.3 ± 3	0.8 ± 2	SiO_2
Ilmenite	1.3 ± 5	0.9 ± 3	$FeTiO_3$
Amorphous		35 ± 15	
Total	100	99.7	

due to their inert properties. The concentrations of other constituents are too low to be feasibly used.

The atmosphere is available at every location. Due to seasonal changes, pressures fluctuate, but generally the same amount is available at all times. However, the total mass that is available is lacking. With a density of only 0.020 kg/m^3 [50], not a lot of material can be extracted per cubic metre of air. The main compound of interest is CO_2. Converting volume percentages to mass percentages results in a CO_2 content of 96.1%. Combining this with the atmospheric density results in a total 0.0192 kg/m^3. Although there is enough total atmosphere available to obtain a substantial mass of CO_2, the extraction will be difficult. About 52 m^3 is necessary to obtain 1 kg of CO_2. As for most processes, only the carbon part is of interest, one would need about 191 m^3 of atmosphere to obtain 1 kg of carbon. This all assumes perfect conversion, something which is most likely not true. Therefore, the atmosphere and consequently CO_2 is considered infeasible.

2.4.3. Water and Ice

Water has been present on Mars throughout its history [43]. It is still present on Mars in different forms. The largest reservoir of water on Mars is ice. This ice is present on the north- and south poles. The upper layer of the ice consists of CO_2 ice. Its thickness and abundance fluctuates with seasons [51]. Beneath this layer, a permanent layer of water-ice is present [76]. The total ice layer on the Northern icecap has a thicknesses of around 2500 m [76]. Ice can be used to create buildings, comparable to how igloos are constructed [77]. Ice can also be melted to utilise it as water. However, the Human Landing Site design workshop [27] pointed out the unfavourable location and difficulties of a colony near one of the poles. Instead, potential landing sites are proposed to be near the equator. Due to the distance to the poles from the equator, it is not considered feasible to use ice as a resource.

Using data from ESA's *Mars Express*, the presence of subsurface lakes was postulated [78]. Although the interpretation of the data is debated, liquid water could prove useful for a colony on Mars. If there are subsurface lakes, they are thought to be extremely saline, as they would otherwise turn to solid ice. Considering the difficulty of drilling for water compared to alternatives [21], subsurface lakes are not considered feasible.

Ice within the shallow subsurface of Mars was postulated. This ice might be extractable at locations where this ice is present near the surface. Unfortunately, recent discoveries have proved that there likely is no ice or liquid water present within the upper 300 m of the Martian crust [28].

Furthermore, NASA's in house study about the availability and extraction of water, "Report of the Mars Water In-Situ Resource Utilization (ISRU) Planning (M-WIP) Study" [21], notes the difficulty of extracting water on Mars. Due to waters vital role in human life, this thesis will focus on water-less manufacturing of materials.

2.4.4. Spherules

The Opportunity rover has discovered hematite, Fe_2O_3, rich spherules scattered across the surface [79], also known as "blueberries". The origin of the spherules is debated. They could come from geological processes, where rocks weather and the stronger spherules are left [79], or as a more recent study suggest, they can be the result of meteorites [80]. Their size is rather uniform with a mean diameter of 4.2 mm and a standard deviation of 0.8 mm [81]. Their chemical composition and mineralogy cannot be measured by current rovers due to their small size [81]. They do have a different chemistry from the rock or meteor they were embedded in. Soil containing these spherules are classified as MoessBerry Subclass soils. In Table 2.4, the composition of MoessBerry Subclass soil including spherules is presented. It is estimated that the spherules consist of 71% to 100% of Fe_2O_3 noted as oxide content [82]. This high ratio of ferrous material makes spherules a major source of iron. Unfortunately, their abundance and presence are not well-known. Thus, spherules are not considered a stable and thus viable material.

2.4.5. Rocks and Volcanic Rocks

At locations where regolith is not present, rocky formations protrude the surface. Similarly to regolith, their composition varies widely [63]. In aggregate, rocky formations have a similar composition to regolith. Throughout Mars' history, volcanic activity has been present [83]. Until recently (on geological scales), volcanoes have been active [84]. This results in substantial amounts of volcanic rock being deposited on the surface. Volcanic rocks could have a higher basalt content than regular rocks [85]. Mining rocks can prove difficult. Their hardness requires tools, such as chisels or drills, which wear and tear, or explosives to extract. This adds unnecessary complexity and extra launch mass to any Martian mission. Therefore, rocky formations are not considered a viable resource.

2.4.6. Meteorites

Most meteors do not burn up in the Martian atmosphere [86]. Many can be found lying at the surface. Some of them have been analysed and show high concentrations of metals [52]. Unfortunately, Meteorites are not a reliable source of material. Once they are used up, it is unsure when new material arrives and how much [87, 88]. The amount available is limited. As their origin varies widely, so does their composition, which makes it difficult to design a manufacturing process for. Their scattered locations add extra transportation complexity. In further stages of colony development, meteorites could supply easy access to rare metals and minerals, but they are not suited for reliable construction material manufacturing.

2.4.7. Suitability Resources

As discussed, there are three main factors which determine a resources feasibility for this study. From the above results and discussion, it is clear that only regolith and rocks are feasible for this study, but that regolith has favourable extraction compared to rocks, while resulting in a similar material. Below, in Table 2.7, an overview can be found of the feasibility of all discussed resources.

Regolith can be used in several forms. The first one being unaltered regolith aggregates. In this case, unaltered regolith particles are used as a main material or constituent of a larger material mix. The second method is preparation of regolith. The regolith can be sieved, or ball milled to reduce its grain size. Magnetic particles can also be extracted from the regolith. Those particles can either be used separately, discarded, or used to achieve a higher ferromagnetic particle content.

The simplest method is sieving. Sieving enables the use of only the smaller (or larger) fractions of grain sizes. Although the method is simple, it has some drawbacks. With sieving, any fraction not used needs to be discarded. Depending on sieve sizes, this can result in only a few percentage of the regolith being used. Another problem is grain sizes of constituents. Regolith is very heterogeneous. Thus it can be the case that only larger particles consist of certain elements or minerals. Sieving might then result in a composition difference between fractions. This can be beneficial, but it can also result in lesser performance. Ball milling excludes both these drawbacks. Ball milling is a bit more complex and prone to failure. Ball milling can only result in smaller grain sizes. Ball milling can also result in certain minerals being ball milled more than others, depending on hardness.

Another way to use regolith is to extract useful elements. Certain elements can be extracted and used as a precursor. On such example is the extraction of iron to form pure iron or steel, if combined with carbon. From Table 2.4, it is easy to notice the abundance metals such as iron (Fe), aluminium (Al), magnesium (Mg) and titanium (Ti). Combining specific extracted elements can then make a possible construction material.

Extra emphasis is placed on the unavailability of water on Mars [21, 27, 28]. This results in water not being a feasible resource for this study. The infeasibility of water extraction results in a limited number of viable manufacturing methods. This is surprising considering the amount of studies that do use water to study Martian or Lunar construction materials.

Table 2.7: Table of proposed sources of available raw materials for use in construction materials at an early Mars colonisation stage. For every source, the extracable materials are presented and feasibility commented on.

Source	Extractable Materials	Feasibility
Atmosphere	CO_2 or C	Low
Regolith	Regolith	Yes
	Sieved regolith	Yes
	Milled regolith	Yes
	Magnetic particles	Somewhat
	Individual elements	No
	Water	No
Ice	CO_2 ice	No
	Water ice	No
Subsurface lakes	Saline water	No
Spherules	Iron	Somewhat
Meteors	Iron	Somewhat
	Other metals	Somewhat

2.5. Martian Simulants

No mission has yet returned from the Martian surface. Future missions such as the Mars Sample Return mission by ESA have been planned. This means that no real Martian regolith samples are available for testing on Earth. Martian regolith and rocks have been sampled in-situ by different missions [62, 63, 68–72, 74, 75, 79, 80]. Although analysing samples on Earth yields greater accuracy, Martian soil composition is known to usable significance. To perform tests on and with Martian soil, it needs to be recreated (simulated) on Earth. These are Martian simulants. They aim to provide a similar composition, grain size and other properties to Martian soil, at a commercially viable price.

Different types of simulants are available, see Table 2.8. They have been developed over the years to

overcome some shortcomings. One such shortcoming is hydroscopic tendencies, the tendency for a material to attract water. Other shortcomings are particle size distributions and mineralogy. One shortcoming that cannot be overcome easily, is oxidation by the Earths atmosphere. As these simulants are used on Earth, they can oxidise (or have other reactions) with the atmosphere. The Martian atmosphere is highly inert, thus some compounds can exist there, while they are impossible to implement on Earth.

Among multiple small-scale simulants, MMS, JSC and MGS have been widely used. JSC Mars-1 was designed as a spectral simulant by NASA. Its goal was to provide a matching spectral component, mainly in the Visible/Near-Infrared (VNIR) wavelengths [89]. The simulant is composed of the <1 mm fraction of weathered volcanic ash from Puú Nene, Hawaii. They observed a much wetter condition than Martian regolith. JSC Mars-1 was estimated to consist of about 21.1 wt.% water. XRD results show Ca-feldspar and minor magnetite. Its chemical composition is presented in Table 2.8 and differs significantly from real Martian soil. Magnetic properties of JSC Mars-1 are also heightened. Around 25 wt.% of the sample could be lifted with a magnet, compared to the 1-7% of Martian regolith. Neither its mineralogy nor chemical composition is representative of Martian regolith. It consists of mainly amorphous material, while real Martian regolith contains only about 35% amorphous material. Besides its poor properties, JSC Mars-1 has been widely used because it was one of the first Martian simulants available.

MMS was designed as a geotechnical simulant by NASA [90]. Although closer in mineralogy, it is still lacking in both mineral and chemical composition. It has since been discontinued and re-continued by The Martian Garden. Although similar in name, their simulants use a different source. They offer both MMS-1 and MMS-2, an enhanced version. Due to the limited information publicly available about these simulants, they are hard to compare with real Martian soil. It is known that they are almost completely crystalline, something which is not representative of Martian soil [31].

MGS-1 is designed as a mineralogically accurate simulant, by ExolithLab [31]. By designing from the mineral perspective, the properties of the simulant should highly match the real Martian soil. Their reference has been Rocknest soil. In Table 2.9, a comparison of minerals between MGS-1 and Rocknest soil is presented. The amorphous content of Martian soil is not clearly defined yet. By combining several phases that are postulated to be a constituent, they could simulate the chemical composition of the amorphous content. Currently, MSG-1 is regarded as the best Martian simulant available [22, 31]. It is an open standard and most closely relates to real Martian soil. MSG-1 has an extensive publicly available data which includes trace elements, detailed particle size data, mineralogy and more [29, 31]. It can therefore accurately be compared to data from Martian missions. Furthermore, it is also readily available for order. The detailed published spec-sheets provide clear information about the simulant. Its chemical composition is shown in Table 2.8 and mineralogy in Table 2.9.

Table 2.8: Most popular Martian simulant types and their oxide composition [29, 31, 89, 90], compared to average Martian soil [62]

Oxide/Element	**Average Martian Soil** (wt.%)	**JSC Mars-1(a)** (wt.%)	**MMS-2** (wt.%)	**MGS-1** (wt.%)	**JEZ-1** (wt.%)
SiO_2	46.52	43.5	43.8	42.9	36.4
FeO	12.18	As Fe_2O_3	As Fe_2O_3	11.2	11.9
Fe_2O_3	4.2	15.6	18.37	As FeO	As FeO
Al_2O_3	10.46	23.3	13.07	12.8	8
MgO	8.93	3.4	6.66	14.6	25.6
CaO	6.27	6.2	7.98	7.4	4.6
SO_3	4.9	n.a.	6.11	1.27	0.7
Na_2O	3.02	2.4	2.51	1.5	0.9
TiO_2	0.87	3.8	0.83	0.6	0.4
P_2O_5	0.83	0.9	0.13	0.1	0.1
Cr_2O_3	0.36	0.03	0.04	0.14	0.21
Cl	0.61	n.a.	-	0.005	0.002
K_2O	0.41	0.6	0.37	0.6	0.3
MnO	0.33	0.3	0.13	0.1	0.1
Ni	5.44×10^{-2}	n.a.	n.a.	5.40×10^{-2}	1.06×10^{-1}
Zn	2.04×10^{-2}	n.a.	n.a.	5.1×10^{-3}	5.6×10^{-3}
Br	4.90×10^{-3}	n.a.	n.a.	2×10^{-4}	1×10^{-4}

As the simulant is the main ingredient for this study, its characteristics strongly influence any results. A careful consideration has been made about simulant choices. It is concluded that MGS-1 and JEZ-1 are most desirable. This sound choice impacts the reliability and applicability of the results of this thesis. Still, not everything is known about the simulant. Also, until a mission returns actual Martian soil, it cannot be verified that the simulant behaves similarly to real Martian soil. For this thesis, the simulants MGS-1 and JEZ-1 are

Table 2.9: Mineralogy on Mars compared to used simulants [29, 30]. Crystalline mineralogy is presented as analysed at Rocknest, Gale crater [73]. Uncertainties are reported as $\pm 1\sigma$.

Mineral	**Crystaline** (wt.%)	**Total** (wt.%)	**MGS-1** (wt.%)	**JEZ-1** (wt.%)	**Chemical formula**
Plagioclase	40.7 ± 5	26.3 ± 7	27.1	16	$(Ca_{0.50(4)}Na_{0.50})(Al_{1.50}Si_{2.50})O_8$
Olivine	20.5 ± 4	13.3 ± 4	13.7	32	$(Mg_{1.15(5)}Fe_{0.85})SiO_4$
Augite	18.1 ± 13	11.7 ± 9	20.3	12	$(Mg_{1.01(15)}Ca_{0.80(11)}Fe_{0.19(19)})Si_2O_6$
Pigeonite	12.3 ± 12	8.0 ± 8	As Augite	As Augite	$(Mg_{1.02(16)}Fe_{0.88(18)}Ca_{0.10(9)})Si_2O_6$
Magnetite	2.8 ± 5	1.8 ± 3	1.9	1.1	Fe_3O_4
Anhydrite	1.4 ± 3	0.9 ± 2	1.7	1	$CaSO_4$
Hematite	1.6 ± 1	1.0 ± 1	0.5	0.3	Fe_2O_3
Quartz	1.3 ± 3	0.8 ± 2	As Plagioclase	As Plagioclase	SiO_2
Ilmenite	1.3 ± 5	0.9 ± 3	As Plagioclase	As Plagioclase	$FeTiO_3$
Smecite	n.a.	n.a.	n.a.	6	Multiple
Mg-carbonate	n.a.	n.a.	n.a.	11	$MgCO_3$
Amorphous		35 ± 15	34.8	20.6	
Total	100	99.7	100	100	
Amorphous					
Basaltic glass			22.9	13.5	SiO_2
Hydrated silica			3	1.8	$SiO_2 \cdot nH_2O$
Mg-Sulfate			4	2.4	$MgSO_4$
Ferrihydrite			3.5	2.1	$Fe_2O_3 \cdot 0.5\,H_2O$
Fe-carbonate			1.4	0.8	$FeCO_3$
Total			34.8	20.6	

assumed to be accurate enough for reliable results.

Due to the heterogeneity of the simulant and Martian regolith itself, (chemical) interactions are difficult to quantify. During heating, crystalline phases may recombine, chemical reactions are sped up or reach their activation energy, and melting enables diffusion and transportation of elements. For such a heterogeneous material, it is infeasible to quantify all these interactions. In this thesis, interactions that can be quantified and significantly influence the material characteristics are analysed. Furthermore, these interactions can be chaotic and case-specific. This is expected to lead to variation within data. To combat this, handling and processing of materials is performed similarly throughout testing.

2.6. Manufacturing Methods

One consequence of the ISRU requirement from Section 2.1.1, is that materials must be manufactured locally. Several manufacturing methods are described in this chapter. The selection of processes are suggested in literature to be suitable to manufacture construction materials either on Mars or the Moon. Methods that have only been studied for Lunar application, are thought to also be applicable to Mars. This is due to the similarities in particle size distribution and chemical makeup. From this list, it is clear that production of a construction material by ISRU is possible. In Table 2.14 an overview of the discussed manufacturing methods is presented.

Four factors strongly influence the viability of production methods for application on Mars. Firstly, the energy requirement of a process must not be too high. It is difficult to generate energy on Mars, as is discussed in Chapter 2.6.11. Energy use is qualitatively discussed, but backed by calculated estimations. This is because the energy requirements of production methods depends highly on the actual application and the amount of energy available on Mars is speculative at best. The second factor is the scalability of the method. Is the method suitable to produce bulk construction materials? The third factor is the resulting strength of the manufactured material. This should be sufficient to use them as structural elements. The last factor is the structural application of the manufactured elements. If a manufactured material cannot be used to create buildings, it is not feasible. In Section 2.6.10, this is summarised and concluded upon.

2.6.1. Cold Pressing

Cold pressing is the act of pressing regolith particles together with high pressures, commonly above 200 MPa. Adhesive forces of the regolith will bind them together, specifically the adhesive forces between smectite-like clay mineral and water [15, 66].

Three notable studies have been performed on this subject [65–67]. The studies used different clay types, such as bentonite and nontronite, as Martian simulant. Ishikawa [65, 66] only used clay, water and sand, in differing ratios. Boyd, Thompson, and Clark [67] used clay magnesium sulfate, ferric oxide and sodium

chloride. At the time of these studies, the composition of Martian soil was not fully charted. They assumed it consisted of basaltic type materials and Smectite type clay minerals. This led to them assuming bentonite as a good simulant. This can be debated, as the regolith has a far more complex composition. No recent study for cold pressing of Martian regolith has been found. One newer study [64] did use a better Martian simulant. A study on shock compression of Lunar fines indirectly suggest cold pressing is also viable for more complex materials [15]. Although the Martian regolith differs from Lunar regolith, it shows promising results for cold-pressing of more complex fines.

No numbers on energy requirement were specified, but it is expected to be low. No heating is applied, only pressure. This does not require significant energy. This material can be produced in bulk with relative ease. The proposed strength of the material are given in Table 2.10. They are sufficient for building a brick structure. Heating/firing of the cold pressed bricks has been proposed. For the purpose of overview, this method will be considered as sintering.

Table 2.10: Achieved cold-pressing method results, showing only the best mixtures [64–67]

Test	Pressure (MPa)	Composition	Conditions	Strength (MPa)
Ishikawa [65, 66]	30	70% bentonite (20% water), 30% sand	Dry Non-Dry	7.39 2.00
Boyd, Thompson, and Clark [67]	-	85% clay 12% magnesium sulfate, 2% ferric oxide		
		Additive: 45% sulphur	Baked and compressed	2.19
		Additive: 2% glass wool	Compressed and air dried	3.97
Chow et al. [64]	800	JSC Mars-1a simulant [89]	Quasi static compaction free boundary	27 (flexural)
	>800		Dynamic compaction free boundary	40 (flexural)
	400		Dynamic compaction flexible boundary	50 (flexural)

2.6.2. Regolith Melting

In the process of melting regolith, the regolith is heated until a phase transition occurs. The (semi-)liquid is then poured into a mould, obtaining a solid in the desired shape. It is not necessary that all phases in the regolith melt. If enough phases fully melt, a heterogeneous brick is formed where the melted glass-phase acts as a strong binder. Depending on the degree of crystallisation, a glass, glass-ceramic or cast will be formed [91]. This process is energy intensive due to the high temperatures involved in melting the minerals.

Only studies with regolith melting for Lunar application have been found. Their application shows that this production process is possible for complex regolith compositions. It shows a great variance between initial simulant and resulting material. Although this can be seen as a problem, it also shows an opportunity for fine-tuning of the resulting material. An overview has been given in Table 2.11. Only one study noted the resulting compressive strength [65]. Two other studies manufactured glass fibres, which can be used as reinforcement [91, 92].

Glass manufacturing on Earth is a very developed technology. Using analogies from Earth manufacturing, predictions might be made on the material behaviour due to the range of elements present in Martian regolith. Melting temperature and strength are important parameters that can be adjusted for. As the goal of this study is to create a simple method, chemical refining of precursors is limited. Simple actions such as sieving or removing magnetic particles are possible. Altering the regolith to form a glass precursor is deemed impossible.

Farries et al. [91] have shown regolith melting to be a good option for use on other planets, but note that it might require too complex fabrication to produce refined clear glass. For construction purposes, the glass has no need to be transparent or translucent. This could provide a good stepping stone towards more advanced colonies. If glass production already exists, it can later be modified to produce refined clear glass.

Table 2.11: Achieved Lunar regolith melting method results [65, 92–95]

Test	**Melting temperature** (°C)	**Annealing temperature** (°C)	**Strength** (MPa)
Mackenzie and Claridge [93]	1350-1500	-	-
Magoffin and Garvey [94]	1200	-	500 (tensile)
Ishikawa, Sasaki, and Higasayama [65]	1200-1500	-	120
Tucker, Ethridge, and Toutanji [92]	1400-1600	600	-
Schleppi et al. [95]	1400	560	-

2.6.3. Sintering

Sintering is a more efficient way of creating a solid with heat than through melting [15, 91]. Sintering binds particles into a solid due to mass transport at the atomic scale [96]. Sintering is achieved by first consolidating a mass of particles into a *green body*. This *green body* is then heated to approximately 50 to 80% of the melting temperature [15, 96]. Different mechanisms contribute to the agglomeration of particles, as presented in Figure 2.4.

There are three distinct types of sintering [96]. Solid-state sintering is achieved by performing the aforementioned steps for particles without additives. Liquid-phase sintering is the use of an additive which forms a small amount of liquid between the particles. This liquid phase provides a high-diffusivity path for transportation that allows matter to flow into pores for further densification and lower sintering temperatures. The third method is pressure-assisted sintering or pressure sintering. Here, a pressure is applied during the sintering process, which leads to more densification and lower sintering temperatures.

Viscous sintering is referred to the sintering process of amorphous materials, such as glasses, where the sintering process creates a viscous flow [96]. Vitrification is referred to as the sintering of clay-based ceramics [96]. This results in a large portion of liquid phases that fill up the pores and create a glassy appearance.

Different methods of achieving sintering temperatures exist in literature [91]. Radiant sintering is the process of applying heat from the outside. Microwave sintering applies heat from the inside using electromagnetic waves within the microwave spectrum. Hybrid sintering is the process of combining radiant sintering and microwave sintering to uniformly heat the material. According to Farries et al. [91], radiant sintering is the most viable version of sintering on another planet. Microwave sintering would have troubles keeping the high-power microwaves cool in a low-pressure environment.

Another process is direct sintering. Direct sintering is the process of sintering regolith without first shaping it into a *green body*. This can be used for roads, where the regolith would be direct-sintered to manufacture pavement. Direct sintering cannot provide high-strength materials [91].

Most extraterrestrial sintering studies have focused on Lunar application. A very informative review paper by Farries et al. [91] shows application of different sintering methods for Lunar use. They identified 53 experimental studies on sintered and melted regolith. Notable results from these studies are shown in Table 2.12. It was noted that higher densities are strongly correlated with higher strength. Only one study showed pressure-assisted sintering. For Lunar simulants, the study showed a lower sintering temperature (600 °C compared to >1100 °C) while achieving similar densities of 2.8 g/cm^3, among the highest of all studies. For application on Mars, a lower sintering temperature might be beneficial due to the decrease in energy requirement.

One study investigated Martian application [53], using industry standard Martian simulants, different manufacturing techniques and testing production within a simulated Martian environment. However, they combined the simulant with smectite clay and water, with the assumption of availability of these materials. In this thesis, water extraction is assumed to be infeasible.

Tests by Simonds [97] have been performed with pressure sintering conditions. Results show a significant decrease in required temperature for a given density. Using a temperature of 600 °C, their samples needed a week to sinter and reached densities of 2.8 g/cm^3. Using higher temperatures resulted in faster sintering times, at 850 °C almost complete sintering was performed in less than 2 hours.

A clear relationship between grain size, sintering temperatures and sintering time exist for glasses [97]. This relationship is plotted in Figure 2.5. The exact values differ for different compositions of the glass. These result show that for application on Mars, grain size can be an important factor. Lowering the maximum or average grain size permit the use of lower temperatures for energy savings, or shorter production times.

Table 2.12: Achieved sintering method results, only high resulting strength studies are noted. All methods use radiant sintering exept for Simonds. [53, 91, 97–100]

Test	Sintering temperature (°C)	Green body pressure (MPa)	Strength (MPa)	Density (g/cm^3)
Gualtieri and Bandyopadhyay [98]	1200	145	103-232	2.7-2.9
Indyk and Benaroya [99]	1120	4	84-219	2.2-2.6
Meurisse et al. [100]	1100-1125	255	55-210	2.3-2.5
Karl et al. [53]	1130-1160	70 (at 1000°C)	53.53 (flexural)	2.49
Simonds [97]	>600	50 (during sintering)	-	2.8

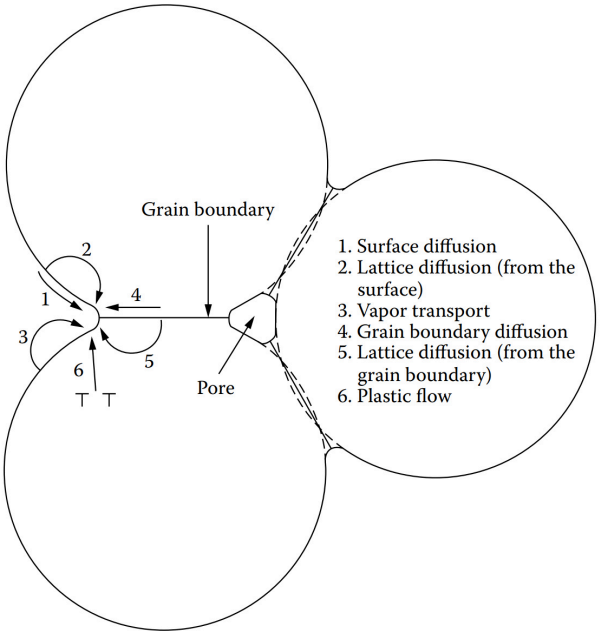

Figure 2.4: Mechanicsms of sintering. Only mechanisms 4-6 lead to densification. [96]

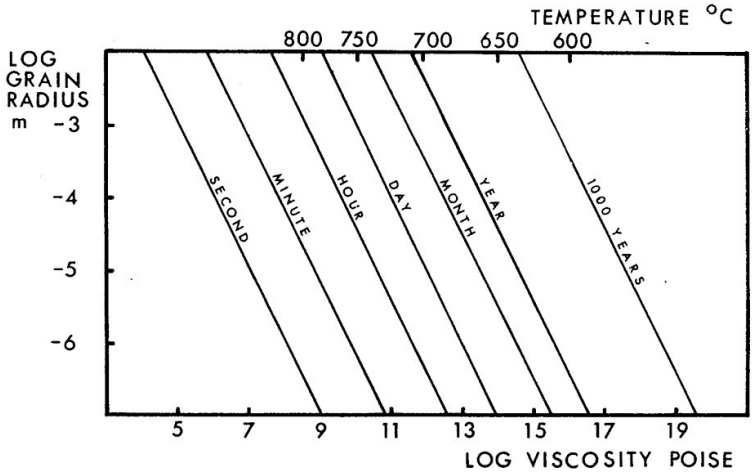

Figure 2.5: Graph showing the theoretical time necessary for sintering of two spheres by viscous flow. Grain radius and temperature are important parametes for sintering time. Values presented are for synthetic Fra Mauro composition glass. Neck radius is 0.2 times the grain radius, surface tension is 0.3 N/m. [97]

Sintering on Mars will be different than sintering on Earth. On Mars, low pressures and mostly inert gasses are present. On Earth, oxygen and high pressures can induce oxidation and increase the sintering temperature required for the same strength, compared to lower pressure and/or inert atmospheres [91]. This is due to void coalescence and migration the the surface being more rapid in a vacuum resulting in greater densification [91]. Simulating a Martian environment in the production process will yield more accurate results. It can be expected that results on Mars are improved over non-simulated environment sintering [26, 53].

2.6.4. Combustion Synthesis

Combustion synthesis, also called self-propagating high-temperature synthesis (SHS), is the process of exploiting high-exothermic reactions that are self sustaining [101]. These exothermic reactions create high combustion temperatures, which can melt the regolith. This exothermic reaction is the result of an oxidation-reduction reaction. Such a reaction can be achieved by combining powdered minerals such as aluminium, magnesium or nickel with regolith. [15, 101]

The elements that could create the exothermic are not considered feasible according to Chapter 2.4.7. They fall within the category of metals and require complex pre-existing processes. They would also require vast amounts of energy to manufacture.

2.6.5. Dry-Mix/Steam Injection (DMSI)

Dry-Mix/Steam Injection (DMSI) is a method to produce concrete-like materials within a low-gravity vacuum environment. The vacuum would lead to outgassing losses, while lower gravity can lead to mixing problems [15]. In this method, steam of around 100°C to 200°C is injected to a cement-aggregate mixture. Efficiency of hydration is improved and thus less water is needed. [15, 102]

While it has been suggested Mars could contain sources of limestone ($CaCO_3$), they are rare and probably impure [25]. Creating $CaCO_3$ is a complex and energy intensive method. The necessity for water, albeit less than normal concrete, is also troublesome. Therefore, DSMI is not considered a viable manufacturing method for this study.

2.6.6. Sulphur Concrete

Sulphur concrete on Mars can be made by combining elemental sulphur with aggregate particles from regolith or rock [23, 25]. A relatively high sulphur (S) content is present on Mars. Sulphur melts at low temperatures, making the energy requirement for sulphur concrete less than most other methods. A recent paper shows that in combination with present magnetite, sulphur concrete can be made with relatively low energy requirements [23]. The sulphur is used to manufacture concrete-like materials by combining aggregates with the liquid sulphur. Strengths of op to 50 MPa were acquired using this method, see Table 2.13.

Although this process has high prospects for Mars due to its low energy requirement and high strengths, one problem persists. Elemental sulphur is not known to exist on Mars. Instead, common sulphate minerals on the surface should be converted into elemental sulphur. This process requires H_2 and CO_2. Whereas CO_2 is easily extracted from the Martian atmosphere, H_2 needs to be extracted from water. Thus, indirectly, water is a necessary resource for sulphur concrete. High energy demands and high waste involved in this process limit applicability on Mars [25]. Other ways of extracting elemental sulphur, for example by heating troilite found in meteorites, also have high energy requirements [23].

Table 2.13: Achieved sulfur concrete strengths. Only the strongest mixture for a given study is reported. [23]

Test	Mixture (wt.%)	Strength (MPa)
Li et al. [23]	40% sulfur, 30% Magnetite, 30% sand	17.41
Wan, Wendner, and Cusatis [24]	50 % sulfur 50 % regolith (JSC Mars-1A) [89]	50, 1.65 flexural, 3.9 tensile

2.6.7. Geopolymer Concrete

A geopolymer concrete can have a high resistance to temperature cycling, good mechanical properties and can be vacuum stable [15, 103]. With the help of special recycling techniques, geopolymers might be producible using virtually no water [103]. Geopolymer concretes are alkali activated. Therefore a source of alkali's must be found on Mars, synthesis may prove challenging [25]. Using these with the existing regolith

could yield a well-performing geopolymer. Volcanic ash might be used as alkali activated material [15, 104]. The absence of alkali's as a resource combined with the limited knowledge about volcanic ash on Mars results in geopolymer concrete not being considered feasible for this study.

2.6.8. Metal Alloys

Metals are abundant on Mars. As properties of metals are well studied on Earth, they can directly be applied on Mars. Iron or steel is one such example, although it suffers from ductility loss at cold temperatures. Therefore aluminium is proposed, as it does not lose ductility in low temperatures [15]. Aluminium also do not sublime (lose mass) in a vacuum environment [15]. Other candidates are magnesium and titanium [15]. It is also possible to create a plethora of alloys using a combination of these metals and other less available metals [15]. It is thus expected that a metal alloy exists with favourable properties for use on Mars. A drawback of metals is their high production energy requirement. Iron atoms are abundantly available on Mars. Because steel is a very popular and well-studied material on Earth, using iron on Mars to make steel is proposed by some papers described below.

The first paper is from G. Landis [105]. In this paper, meteoric steel is considered as a source for iron making on Mars. The source of iron is dubious. Using meteors is not a reliable source [87, 88]. They are not located everywhere, plus there are not a lot of them. Other proposed sources of iron are also not abundant on mars. They require extra processes, such as electrolysis of water and conversion of CO_2 into CO, without providing energy requirements and feasibility for these specific processes. These kind of processes might be useful for later stage Mars, but not for the early settlers. As was discussed in Chapter 2.4, water is not available as a resource. Therefore this method of iron making is not considered.

Another paper that discusses steel making on Mars is "Steelmaking on Mars" by S. Moss [106]. This paper dives a deep into different production methods. It describes common steelmaking methods in Earth and proposes a few alternatives for use on Mars. The authors address issues qualitatively, so the use of actual numbers for e.g. energy use is omitted. This makes it difficult to verify. No method in this paper is directly suitable without some other process already being large scale use on Mars, such as hydrogen or methane production. Thus, this paper is more applicable to a theoretical advanced Martian civilisation than the current state of research. Therefore the methods described in this paper are not considered suitable.

A third paper is about the microbial extraction of iron [107]. The authors propose the use of microbes to extract iron from plain regolith. The feasibility of this method is quantitatively discussed. The paper is highly theoretical, but application is shown with experimental results. These experimental results only prove survivability of the microbes but do not prove their theoretical point of iron extraction. The method is very early stage and probably not feasible for large scale production. Unfortunately, the authors used an old simulant (JSC Mars-1) [89] that is generally not regarded as representative of real Martian regolith [31, 53]. Its composition is far from the real Martian composition [63, 73, 89].

These papers show the difficulties of producing iron on Mars. Only for more advanced colonies could iron-making be feasible. As this thesis aims to find a process that generates construction materials for early Martian settlements, iron cannot be used. The added drawback of availability of reliable iron sources is something that must fist be overcome.

2.6.9. CO_2 into Carbon NanoTubes (C2CNT)

C2CNT is the process of converting CO2 into Carbon NanoTubes and is almost exclusively done by molten carbonate electrolysis [108] [109]. First CO_2 is dissolved from the atmosphere or flu gasses (for this study: the Martian atmosphere, possibly pressurised) into a Li_2O solution, creating Li_2CO_3. Then this solution is put between an anode and cathode, electrolysis. The anode and cathode can be made from steel and nickel, two cheap resources. Then nucleation starts and carbon nanotubes start to form.

$$\textbf{Dissolution:} \quad CO_2(\text{gas}) + Li_2O(\text{dissolved}) \rightleftharpoons Li_2CO_3(\text{molten}) \tag{2.1}$$

$$\textbf{Electrolysis:} \quad Li_2CO_3(\text{molten}) \longrightarrow C(\text{CNT}) + Li_2O(\text{dissolved}) + O_2 \tag{2.2}$$

No waste is created in the process, as O_2 is a highly valued molecule for life on Mars. The Li_2O is used to lower the energy requirement for capturing CO_2 and nucleating carbon nanotubes. This method also allows for other carbon based products to be formed [108]. Namely carbon nano-onions (CNO), carbon nano-platelets (CNP), graphene and carbon nano-scaffolds (CNS). As this process gets refined, it is expected that almost any desired possible carbon structure can be made.

C2CNT has not been well studied yet and is therefore not ready for practical application. It is unknown if the material can be used as large structural elements. Therefore it is not considered feasible for this study.

2.6.10. Suitable Manufacturing Methods

As discussed, there are four main factors which determine a resources feasibility for this study. From the above results and discussion, it is apparent that only cold-pressing, sintering and melting are feasible for this study. These options are further discussed in this section. Below, in Table 2.14, an overview can be found of the feasibility of all discussed manufacturing methods.

Table 2.14: Overview of feasibility of manufacturing methods as discussed in the previous chapter.

Rank	Production method	Raw resource	Viability resource	Viability method	Viability material	Comment
1	Sintering	Regolith; sieved regolith; other	Feasible	Feasible	Feasible	High energy requirement, but low compared to alternatives
2	Regolith melting	Regolith	Feasible	Somewhat feasible	Feasible	Even higher energy requirement than sintering, while not resulting in significantly better material
3	Cold pressing	Regolith; sieved regolith	Feasible	Feasible	Somewhat feasible	Does not yield best strength parameters
4	Geopolymer concrete	Alkali source, alkali activated material (ash), aggregates (regolith or rocks)	Somewhat feasible	Feasible	Feasible	Resource is unavailable
5	DMSI	Carbonates/ cement, water and aggregates (regolith or rocks)	Low feasibility	Feasible	Feasible	Water is not available. Cement requires high energy to create while precursors are dubious
6	Sulphur concrete	Regolith and sulphur	Not feasible	Feasible	Feasible	Sulphur must be synthesised. Yields high strength material that can be cast or 3D printed.
7	Metal alloys	Spherules; regolith; ores; meteors	Feasible	Not Feasible	Feasible	Spherules and meteors can be found and are metal-rich. Production process is cumbersome and difficult. Could be used in later colony stages.
8	Combustion synthesis	Regolith and powdered minerals	Not feasible	Somewhat feasible	Feasible	Powdered minerals are hard to get, low energy requirement, heat resistant moulds needed.
9	C2CNT	CO_2 from the atmosphere	Feasible	Not feasible	Not feasible	Has never been proven to provide bulk construction material

Strengths obtained through cold-pressing are just above the minimum requirement for this study. A study for cold-pressing Martian regolith [26] concluded that without additives, Martian regolith was not suitable as a cold-pressed material. Cohesion was low and cold-pressing had proven difficult. The use of additives is not considered in this thesis due to the ISRU requirement. Therefore, although cold-pressing shows promising results in literature, it is not considered for this study.

Melting of regolith has been proven to yield structural material with good physical properties. The fact that material can be cast in any shape is a great benefit. Unfortunately, the energy requirements are extremely high. Similar physical properties can be achieved by sintering, while using far less energy. Materials cannot be cast by sintering, but can have most 3D shapes. As long as a green body can be made, it can be sintered in that shape. Therefore, the only drawback would be transportation of structural elements from the manufacturing site to the building site. These reasons result in sintering being chosen as the manufacturing method for this thesis.

Often, additives are used to enhance the manufactured materials properties. Additives are not considered in this thesis. This would increase launch mass and complexity of the study. The results of this study are therefore immediately applicable on Mars.

Spark Plasma Sintering

As is presented in research question 3.c, the process must be possible in a lab. Due to oxidation at higher temperatures [26], described in Chapter 3.3, not every sintering method is suitable. The environment for sintering must be similar to the environment on Mars to be considered representative. This limits the devices used for sintering to environmentally controlled ovens. It has also been noted that applying pressure during sintering, so called ”hot-pressing” can significantly increase physical properties at minimal added energy expenditure [91, 96]. For these reasons SPS has been chosen as sintering process.

SPS is a method for sintering where material is put inside a die and pressure is applied through two punches. An overview is presented in Figure]3.6 in Chapter 3.4. This punch and die combination is heated by applying electricity. Induction heating heats the punch and the die, which can, in turn, heat the material. It is also possible for the electricity to flow through the material. If the material is electrically conductive, this results in heating from inside the material [110–112]. This enables smaller temperature gradients and an even temperature distribution.

The addition of applying pressure during sintering changes the proportional effect of the 6 sintering mechanisms as indicated in Chapter 2.6.3, Figure 2.4. The same mechanisms apply, but non-densifying mechanisms can be neglected [96]. This is because they are not enhanced by the applied pressure, while for SPS the densifying mechanisms have a significantly larger influence and are thus dominant.

In addition to mechanism 4-6 (grain boundary diffusion, lattice diffusion and plastic flow), three other effects are present [96]. These are, viscous flow, grain boundary sliding and particle rearrangement. Viscous flow is the transport of matter of amorphous materials. This happens due to the lowered material viscosity from the high sintering temperatures. Grain boundary sliding is illustrated in Figure 2.6. Particle rearrangement is the effect where particles obtain better packing due to the applied pressure overcoming some inter-particle forces. Particles can then move to an open, more favourable position, resulting in better packing. Most of the particle rearrangement happens during the initial stages of sintering [96].

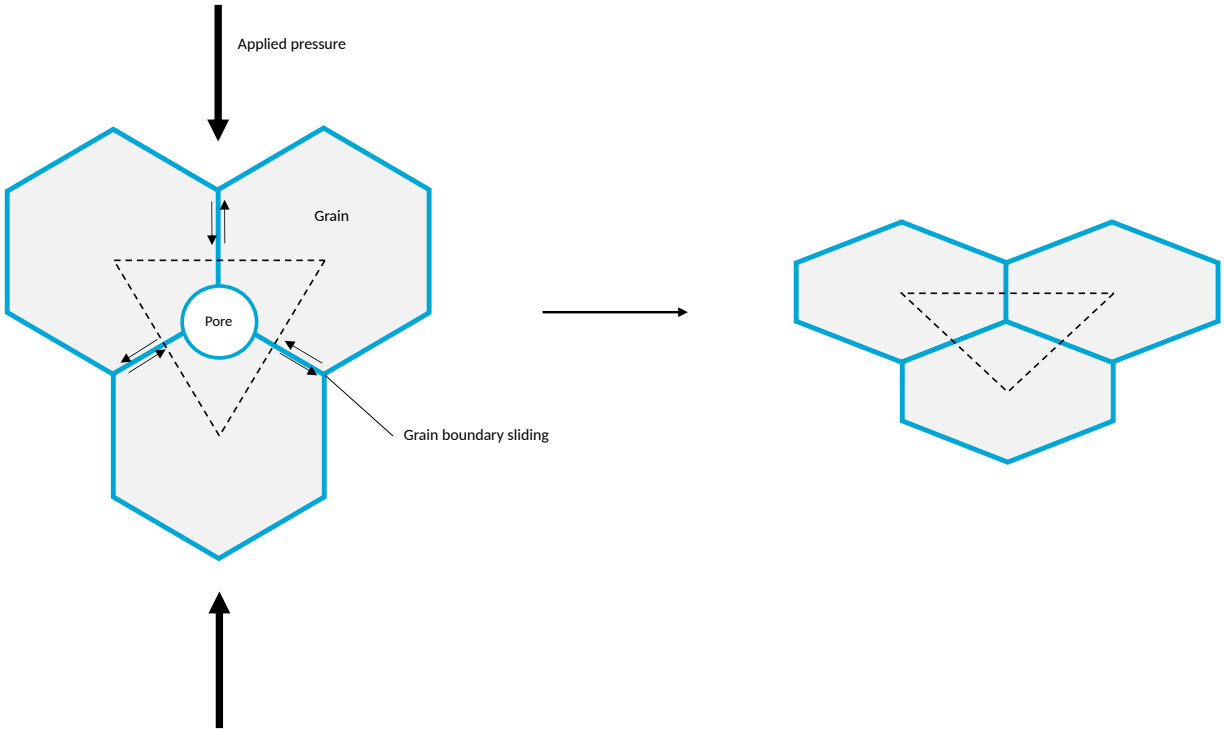

Figure 2.6: The effect of applied pressure during sintering. The grains are flattened and the pores are eliminated by grain boundary sliding. This grain boundary sliding is necessary to account for the change in grain shape due to diffusional transportation of molecules. Adapted from Rahaman [96].

With SPS, a tightly controlled sintering environment is possible. A vacuum environment has been chosen for this study. This can easily be created on Mars, due to the already low atmospheric pressures. It eliminates interference with atmospheric compounds and increases energy efficiency as convection is not possible. A pressure can be applied, which can significantly increase material performance at almost no extra energy requirement. The only drawback of SPS is the shape of elements possible. Instead of any 3D shape, sintering only allows for stretched 2D shapes. This is a non-issue for structural elements. Most structural elements are prisms, such as bricks and beams.

2.6.11. Energy Requirement

Certain ISRU manufacturing methods from literature, could be eliminated based on energy consumption, as presented in Chapter 2.6. A problem for ISRU on Mars is energy constraints [4, 7, 26, 113]. Fossil fuels

have not been discovered on Mars, thus renewable energy sources should be used or non-renewable energy sources should be imported from Earth. The only feasible non-renewable energy source to import is nuclear energy due to its high energy density [7, 26]. Proposed renewable energies on Mars consist of: solar power, wind power, or geothermal power [4].

An overview of the advantages and disadvantages between solar and nuclear power are presented in Table 2.15. Nuclear power is the most viable option [7, 114]. The main reasons are a continuous power supply and an almost 3 fold reduction in launch mass compared to solar. Two notable drawbacks are radiation and nuclear waste. It is proposed to leave one side of the nuclear reactor unshielded to lower the mass [7]. This side is turned away from the colony. This results in an area with higher radiation doses. These zones cannot be entered for extended periods of time. The generated nuclear waste is only a small problem. The relatively small amount of waste created can easily be stored somewhere. Due to the lack of floods and strong earthquakes, the risk of rupture is negligible. Even when storage is compromised, there is no water to transport the radioactive material.

According to reference designs for human Mars missions, multiple 30 kWe nuclear plants are feasible to be brought to Mars [7]. This results in a limit being set for this study to 100 kWe nuclear power for use in ISRU construction material manufacturing. There is interchangeability between time and power, for the same amount of manufactured construction material, taking longer requires less power per unit of time. Thus the presented 100 kWe figure serves as a guideline for which certain processes can be excluded, based on either time or minimum power draw constraints.

Most methods for sintering on Earth are not optimised for energy in a way that sintering on Mars will be. Thus, measuring energy consumption is not representative. It is expected that Martian sintering energy-consumption will be between the theoretical optimum and Earth-processes. This is because on Earth, energy savings due to increased material cost has a lower optimum than for Mars. Energy consumption can mainly be communicated in terms of temperature, hold time and heating method. This will keep results independent of specific lab-equipment. Further studies can show and improve on inefficient energy use.

Table 2.15: Advantages and disadvantages of Solar vs Nuclear power from NASA [7].

	Solar Power	**Fission Power**
Total landed mass (mt)	22.5	7.8
Autonomous Deployment complexity	High	Moderate
Power level stability	Variable with dust settling and atmospheric obscuration	Continuous
Sensitivity to dust storms	High	Low
Reliability	High	High
Ability to repair	Moderate	Low
Increase in crew radiation exposure	None	Small (5 rem/year)
Latitude flexibility	Mass increase with latitude	No restrictions
Scalability	Linear with power	Relatively moderate increase with power in ranges of interest
Development Complexity	Moderate	High
Similarity to Lunar system	Moderate	High
Surface access exlusion zone	None	Small areas of forbidden access moderate areas of limited access
Cost Through First mission	Disadvantage	Advantage
Cost Through Third mission	Disadvantage	Advantage

2.6.12. Sustainability

If sustainability problems on Earth are a reason for Martian colonisation [3, 11], it would be contradictory to be unsustainable on Mars. On the larger scales of Martian colonisation, sustainability must be implemented early on to prevent future problems. This study will focus on the early stages, or founding stages, of Martian colonisation. A small population has a very low, almost zero, impact on a large system. This is also true for Mars. Even if waste is produced or toxic waste is expelled, this will be a benign fraction of the total planet Mars. As the priorities for this colonisation phase are more about survival and setting up an initial base, it is senseless to put too much focus on sustainability [114]. That said, it is unclear at what stage exactly sustainability becomes important.

It is expected that the manufactured material, is somewhat sustainable. In primitive civilisations, when buildings are made from locally available resources and only simple manufacturing is possible, the resulting construction materials are a reflection of the environment itself. This analogy is expected to hold for Mars too.

As only regolith is processed, the manufactured material is closely related to the original regolith. Crushing the manufactured material should result in a similar soil to the original regolith, with only minor mineralogical differences. A good other example is pressed Martian regolith brick [26].

Another issue for sustainability is presented by the proposed power source. It has been discovered that nuclear energy is the most, if not the only, viable power source for use on Mars, see Chapter 2.6.11. Bringing a nuclear power source does result in nuclear waste being generated. This waste must be disposed of. No truly sustainable disposal methods for nuclear waste currently exists. However, containing the radioactive waste material is the best option.

The leftover nuclear waste should not be an immediate hazard on Mars. Typical power sources are self-contained [7]. A spend reactor on Mars is also not subjected to the same possible failures as on Earth. Here, flooding and earthquakes pose a real threat to nuclear waste storage. This is less of a problem on Mars. No dangerous earthquakes or flooding is present there. Water cannot transport the radioactive material to unwanted locations. The high initial radiation on Mars already requires protection for humans. Combining this with the relatively small amount of nuclear material present results in nuclear waste not being a problem for future generations. However, as a Martian colony develops, other more sustainable sources of power must be used.

3
Experimental Setup and Methodology

3.1. Taguchi Design

Due to practical limits, such as funding and time, only 20 samples were possible to be manufactured. The process of SPS has a large variety of input settings. There are also plenty of manipulations of the simulants possible. There are too many variables for too few samples. For the first group, four variables were of importance, the basics of sintering: particle size, temperature, sintering time and pressure. With three levels for each variable, a full factorial design would result in $3^4 = 81$ runs. Multiplying that with a repetition size of 3, for statistical significance, yields 243 runs, an impossible amount.

First of all, the repetition amount would be limited to one. No sufficient design could be made if every run would be triplicated. This limits statistical significance. Therefore, data should not be interpreted as absolute. As this is a feasibility study, general trends are of interest. Further studies can use this information to make informed decisions. Even with a group size of one, the maximum sample amount would be exceeded if four variables of three levels were chosen.

Therefore a better design has been chosen, the Taguchi design [39]. Next to allowing for more variables with fewer samples, the Taguchi design enhances statistical robustness when using no duplicates [39, 115]. The Taguchi design of experiments has been applied numerous times to SPS [115–118]. The ability to simultaneously test the large amounts of variables of SPS with only a few runs is ideal.

3.1.1. Taguchi Comparison

A classical full factorial design measures every possible combination of variable and variable levels. The Taguchi design only measures the outer solution spaces, the orthogonal array, presented in Figure 3.1. This enables for fewer tests to be performed. Instead of 81 runs, only 9 have to be performed for our example, while still measuring all variables. The deconvoluted solution space itself was calculated using Python, see Appendix K.

The solution space of an L4(2^3), three factor, two level, problem is presented in 3.1(i). Next to it is a similar design in the classical full factorial method. The full factorial results in 8 runs to be performed, while the Taguchi design only needs 4 runs to achieve a similar solution, a 2 fold reduction of tests. This effect greatly and non-linearly increases with every increase of variables or level. The solution space of a reduced L9(3^3), three factor, three level, problem is presented in 3.1(ii). It is reduced because normally, four factors can be chosen. As a 4D cube is impossible to properly present in a figure, a reduction of one factor is shown. A full factorial design would require 27 runs, while the Taguchi design only requires 9, a three fold reduction. Be mind-full of the reduction of the Taguchi design for presentational reasons. It is more fair to compare a full L9(3^4) design to a similar factorial design. For a full factorial design, 81 runs are needed, while the Taguchi design still only requires 9. This is a 4 fold reduction.

The downside is that the design cannot be modified and no extra test can be added [39]. This would result in an unbalanced matrix and therefore unreliable results. One test array results in one solution space. If more variable levels are tested, they cannot add to the solutions. This is because the array needs to be orthogonal. They can only be shown within the solution space, or be used to create a new solution space. More tests can be used as duplicates, to eliminate variance in the results.

Another possible disadvantage is that the results are relative to each other. Thus they cannot accurately be compared individually. As can be seen in Table 3.1 and 3.2, one run contains variations of each variable instead of one. Each variable's influence is be separated by analysing the results. It cannot be said for certain if the variables have influenced each other. As all variables are controlled, this is not suspected. As mentioned, a group size of one limits the statistical significance of absolute values tested. Therefore already only the convoluted results are relevant for comparison.

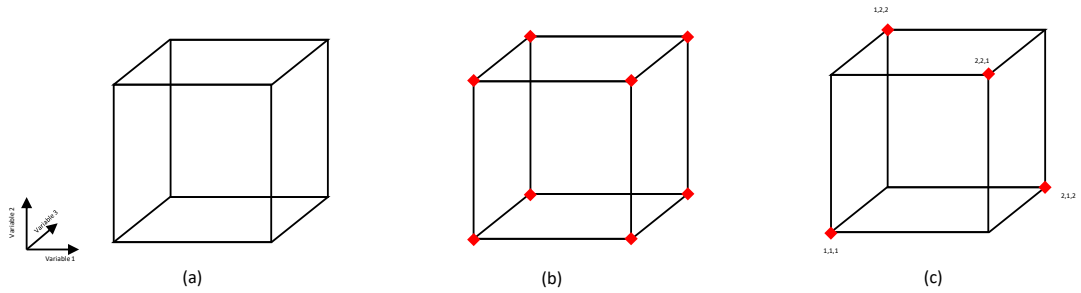

(i) Solution space (a) of problem with three variable each with two levels. (b) shows a full factorial design. (c) shows an L4(2^3) Taguchi design.

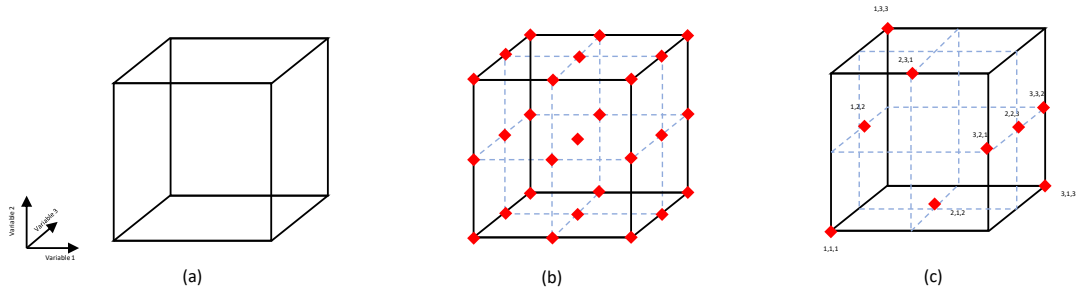

(ii) Solution space (a) of problem with three variable each with three levels. (b) shows a full factorial design. (c) shows an L9(3^3) Taguchi design.

Figure 3.1: Comparison of two Taguchi designs to full factorial designs. The solution space is represented by a cube. Each red diamond is a combination of variables that needs testing. The three numbers reference the three variables. The numbers themselves represent the variable level.

3.2. Material Characterisation

Most material properties are readily provided by ExolithLab [29–31]. These properties are used throughout the study. The effect of heating the material was not provided. Therefore, Differential Scanning Geometry (DSC) and Thermogravimetric Analysis (TGA) test were performed. From these tests, the behaviour of MGS-1 and JEZ-1 under both argon and air environment were characterised for temperatures up to 1450 °C. The difference between air and argon presents the importance of sintering in inert conditions. Another characteristic that was deemed important was the mineralogy per particle size. This test has been performed for MGS-1.

3.2.1. DSC-TGA

DSC-TGA tests have been performed to obtain the theoretical energy input necessary to heat the material to a certain temperature. Another reason was to later verify certain mineral changes with peaks in the DCS graph. The latter has been impossible due to the heterogeneity of the material. It was aimed to also perform mass spectrometry, to study the gasses that evaporate when heating. This could give an indication of what percentage of mass loss was water.

For the test, the particle size needed to be reduced to <45 µm. This was performed with a mortar and pestle. Five grams of material was milled in the mortar and pestle. It was sieved multiple times during milling. Only the material that remained on the sieve was put back into the mortar and pestle. All material passed after about 45 minutes of milling. This was performed for both MGS-1 and JEZ-1 simulants.

Measurements were made up to a temperature of 1450 °C. Up to 400 °C, a heating rate of 20 °C/min was used. After this a heating rate of 10 °C/min was applied. It was the intention of using a mass spectrometer. Due to technical problems, the mass spectrometer was not operational and yielded no results for all tests. Proper calibration files were chosen for both argon and air environments. A calibration run was performed with a blank crucible. These values were used for all subsequent runs. Material was put into a crucible. 29.2 mg was used for MGS-1 in air. 30.1 mg was used MGS-1 in argon. 27.8 mg was used for JEZ-1 in air. 26.8 mg was used JEZ-1 in argon.

The specific heat capacity of the material was calculated for all four tests. The capacity was calculated by multiplying the energy usage, the DSC curve, in milliWatts per milligram (mW/mg), by the time delta of each steps, in seconds (s). This resulted in energy used per milligram (mJ/mg per time-step). The mass at

each specific time-step was calculated by multiplying the mass loss, the TGA curve, in percentages, by the input mass in milligrams. This resulted in the absolute mass at each time-step in milligrams (mg). The energy used per milligram was multiplied by the mass at its respective time-step. This resulted in energy used (J per time-step). The cumulative sum was calculated up to the specified temperature of interest. This yielded the total energy used to heat the material to that specific temperature. Dividing this by the initial mass resulted in the specific heat capacity per input mass. Dividing this by the mass at the specified temperature resulted in the specific heat capacity for the resulting output mass. Dividing both results by the difference in start and end temperature results in the specific heat capacity as J/mgK.

3.2.2. Mineralogy per Particle Size

The method to analyse MGS-1 particle data consist of 5 steps, as presented in Figure 3.2. First, the simulant is prepared for SEM analysis. In step 2, both Back Scatter Electron (BSE) and Energy Dispersive X-ray Spectroscopy (EDS)-mapping images are obtained. In step 3, EDS data is processed according to characteristic formulas, obtaining mineralogy maps. In the next step, these results are used to train a classifier model, which then classifies all other particles within a magnification. In the last step, image analysis of BSE images is used to obtain discrete particle data. These particles are then ascribed a mineral according to the classifier models. Application of this method is shown in Chapter 4.

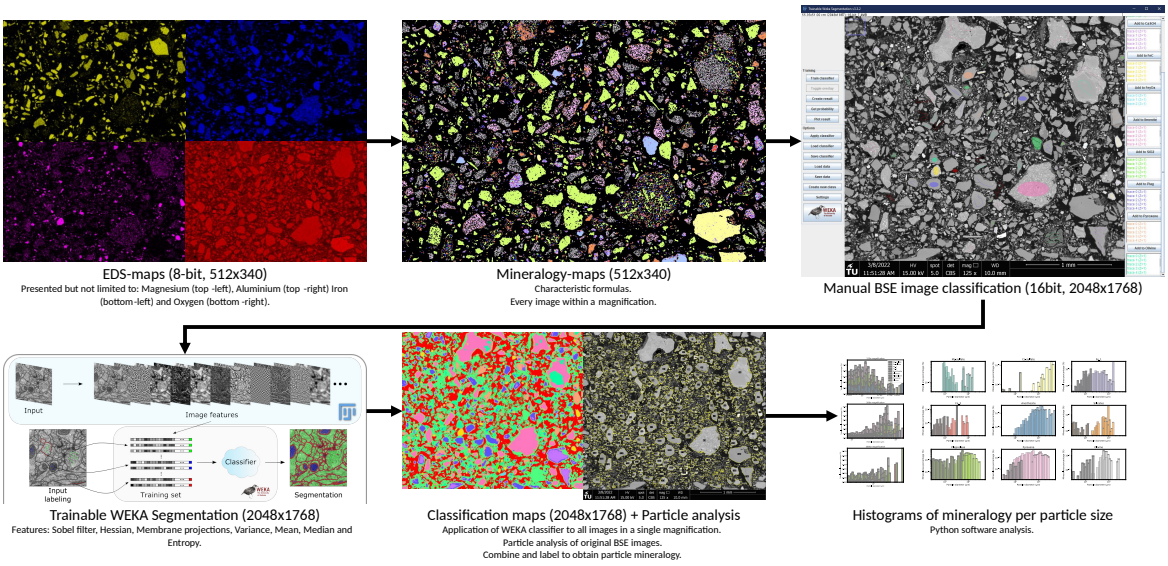

Figure 3.2: Software workflow for identifying mineralogy per particle size. After obtaining EDS-maps (step 2), processing using characteristic formulas (step 3) results in mineralogy maps. These are input in the TWS and used to train a classifier model (step 4). This classifier then classifies all images. Original BSE images are used to analyse particles. Particle data is combined with classified images to obtain particle mineralogy (step 5). Resulting data is processed using custom software, resulting in mineralogy per particle size.

Step 1, Preparation

MGS-1 is cast in epoxy, sanded and polished for use in SEM. Ethanol is used during sanding and polishing to prevent interaction with water. For polishing, diamond paste is used. Between steps, an ultrasonic bath is applied to rid all loose particles. A carbon coating for electrical conductivity is applied. A carbon wire is attached from the surface to the bottom to aid the discharge of the surface, as to circumvent the thick insulating epoxy. The sample is stored in a desiccator to prevent influences of moisture.

Step 2, Imaging

Both BSE and EDS-mapping images are acquired at different magnifications. A 15 kV beam and a spot size of 5 are used to detect iron, Fe, atoms in EDS. Fe is the highest expected atomic number to be significantly detectable. 2048x1768 pixel, 16-bit greyscale BSE images are obtained. EDS-mapping is obtained as a 512x340 pixel, 8-bit greyscale elemental EDS image.

Originally, a grid of 5 images per magnification was aimed for. Due to the uneven distribution of particle sizes across the specimen, selective pictures have been made for every magnification except the largest. This

results in the following BSE and EDS data: 5 pictures of 125x magnification, 4 pictures of 500x magnifications and 3 pictures of 2000 magnification. More pictures were made, but not analysed due to in-applicability. The total analysed area for each magnification was 55 mm^2, 2.75 mm^2 and 0.139 mm^2, respectively.

Step 3, EDS Processing

EDS-map values reported are atomic percentage values within the range of 0-255. EDS-map data is combined, calculated and analysed to obtain estimated mineralogy maps. The individual elemental EDS maps were combined using several formula, explained next. These formula are based on the characteristics of expected minerals. Thresholds were applied based on individual image characteristics.

Magnesium-sulfate and calcium-sulfate were detected by using the formulas $MgSO_4 = Mg \times S$ and $CaSO_4 = Ca \times S$ respectively. The notable presence of sulphur, S, resulted in a clear distinction between all other minerals. The difference between either magnesium, Mg, or calcium, Ca, resulted in the identification of the correct mineral.

Group Fe_1 had a significant presence of carbon (C) and iron (Fe). Detection was made possible by using the following formula: Fe_1 $= (36 < C < 100) \cup (25 < Fe)$ combined with contrast enhancement.

Group Fe_2 consisted almost solely of iron, Fe, and oxygen, O, atoms. The oxygen to iron ratio proved a good marker, as it should be between below 2. This is the range for magnetite (1.33), hematite (1.5) and ferrihydrite (1.75), with an added error of 0.25. Thus, the following formula made detection possible: Fe_2 $= (\frac{O}{(25<Fe)\times Fe} < 2) \cup (25 < Fe)$.

The anorthosite group could be detectable visually, but also showed high ilmenite presence. Thus the following formula was used to verify ilmenite presence: ilmenite = $Ti \times Fe$.

To detect silicates, the absence of other characteristic elements was verified, namely aluminium and magnesium. These elements are characteristic for the other minerals sharing a silicon-oxide part bond, Si_yO_x. Verifying a silicon oxide presence and excluding other minerals proved the best method to verify silicates. The following formula was used: silicates $= (Si > 20 \cap O > 100) \setminus (Mg > 20 \cup Al > 10)$.

Due to its characteristic aluminium content, plagioclase could easily be detected using $10 < Al < 100$.

Due to similarities of pyroxene with olivine, more complex measures are necessary to detect them. For pyroxene $(2.6 < \frac{O}{Si} < 3.7) \cup (Plagioclase > 5) \cup (Si > 30)$ was used. Here, an oxygen to silicon ratio is determined. For pyroxene, this ratio should be 3. For olivine, this ratio can be determined as 4. Due to an overlap with plagioclase, its corresponding map was subtracted from the results. Olivine also has characteristic Fe and Mg presence. Thus olivine uses the formula: Olivine = $(3 < \frac{O}{Si} < 6) \cup (Fe > 17 \cap Mg > 20) \setminus (Si > 30)$.

Step 4, Classifier Model

The resulting maps are then manually analysed and input in a Trainable Weka Segmentation (TWS) [119]. The TWS learns from selected features in the original BSE grayscale image. Training on one image of a sequence is performed according to the following training features: Sobel filter, Hessian, Membrane projections, Variance, Mean, Median and Entropy. These features are chosen to ensure a good analysis of areas, surface features, edges and particle textures. After training the classifier model, it classifies all images. These steps are performed for each magnification individually.

Step 5, Particle Analysis

The original BSE images are also analysed using a particle analyser package. This results in discrete particles with their accompanying data. The resulting particles are then overlapped with the classification data from the TWS. Each particle is ascribed a best-fit mineral label. The particle size is estimated as if particles are perfect circles: $D = 2 \times \sqrt{\frac{A_{particle}}{\pi}}$, where D is the particle diameter and $A_{particle}$ is the area of each individual particle. These results can then be used to estimate necessary sieve sizes. The area percentage per particle size bin is calculated as the cumulative sum of the areas of each particle within a bin, divided by the total image area. When combining magnification data, ratios have been linearly extrapolated to indicate a similar total observed area.

3.3. Material Storage, Handling and Preparation

Handling simulants on Earth has its problems. The foremost problem is oxidation. Constituents can oxidise in our oxygen rich atmosphere, unlike in the oxygen poor atmosphere of Mars. This oxidation can happen during storage, handling, processing and testing. It is assumed that oxidation at room temperature occurs slowly

enough that no noticeable difference can be measured during the course of this thesis. Similarly, room conditions during transportation and storage at the manufacturer cannot be prevented. During heating, oxidation occurs more rapidly. A noticeable effect has been reported by different studies [26, 53]. Thus it is preferable that any processing of the material is performed in a vacuum, inert or simulated Martian environment. This should present a representative result of Martian application. Another problem is moisture. On the Martian surface, liquid water is not present due to the local temperature. On Earth, moisture from the atmosphere can moisten the simulant. This can lead to interaction with the chemicals present.

3.3.1. Storage and Handling

To mitigate these problems, care has been taken with the storage and handling of the material. The raw MGS-1 and JEZ-1 material was stored as received. This was in plastic resealable bags. Bags were carefully resealed after use. The contents of the bag was mixed with a large spoon before extracting any material. This is to prevent segregation of particles due to density or size. Therefore a representative sample was used every time.

All material and all samples were stored at room temperature during the entire thesis, unless specifically stated otherwise. Some material was dried in an oven at 105 °C before use, manufactured by Jouan, type EU115 class O. This drying was to prevent influences from moisture ingress during storage or shipping. This material was dried in the oven for at least seven days inside an open aluminium container.

Any material that was transported or stored outside an oven or the original resealable bag, is stored inside sealed plastic containers. At the bottom, orange coloured indicator silica gel was present to keep the environment inside the container dry. The material itself was stored inside an open aluminium container. For reference, see Figure 3.3.

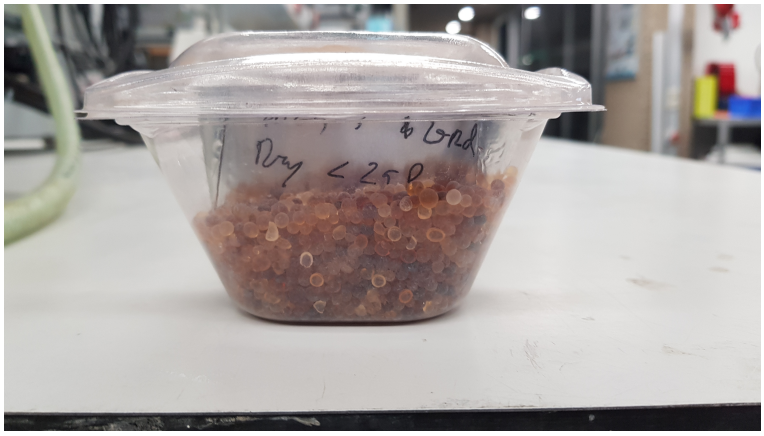

Figure 3.3: Example of a storage container for material. The plastic container keeps moisture out. The bottom layer of silica gel lowers the moisture content of the whole container. As long as the silica gel is coloured bright, the moisture content has not been too high. The material itself is contained in an aluminium container.

Samples were stored in airtight plastic vials. They are designed as personal desiccators. A layer of orange coloured indicator silica gel was separated by an aluminium sheet from the sample on top. The vials and their caps were clearly labelled and only one could be open at a time. This was to eliminate sample mix-ups. Top and bottom of the samples were always in the correct orientation. A reference figure is presented in Figure 3.4.

3.3.2. Material Preparation

Material preparation is an important factor. Regolith can be sieved, ball milled or magnetically separated. The exact influence of these actions is unknown. Sieving can result in a difference in mineralogy and bulk chemistry between sieved fractions. This is due to a potential discrepancy between particle size and mineralogy. This can either be beneficial to or counteractive for the sintering process. With sieving, all unused particle sizes are discarded. They result in waste and increased regolith extraction requirements.

Ball milling does retain mineralogy and bulk chemistry. It also utilises 100% of the regolith and does not create waste. The process is a little more complex and therefore less preferred than sieving. Ball milling can still provide a difference in grain sizes between minerals, a harder mineral is less prone to break.

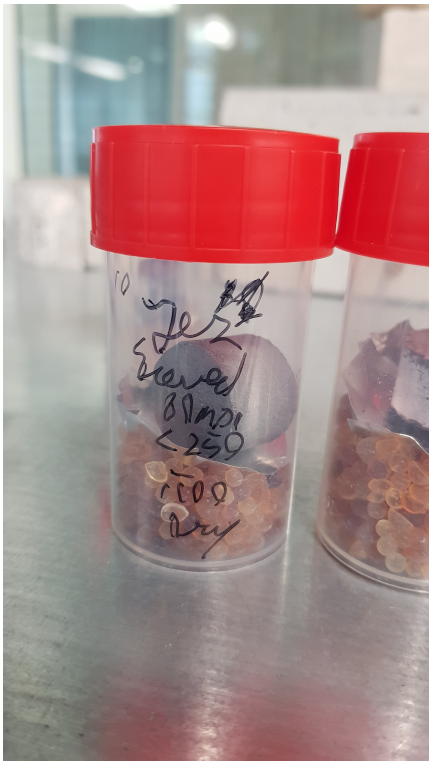

Figure 3.4: Example of a storage container for samples. The plastic container keeps moisture out. The bottom layer of silica gel lowers the moisture content of the whole container. As long as the silica gel is coloured bright, the moisture content has not been too high. The sample is separated from the silica gel by an aluminium sheet.

Magnetic separation is an easy and reliable way of treating regolith. Electromagnets can be turned on and collect ferromagnetic particles, move them and turn off to collect them separately. A problem is the collection of other, non-ferromagnetic particles, that are embedded or stick to the ferromagnetic particles. If the intend is to use the magnetic part of the separated regolith, large quantities of regolith need to be magnetically combed to obtain enough material, as only 1-7% of regolith is ferromagnetic [69]. Magnets can also continually collect magnetic particles from dust blowing past. The collection rate is variable with respect to time, but does not require the combing of regolith. Within this thesis, only sieving and ball milling are considered, as magnetic separation is impractical. The effects of sieving on Mineralogy is presented in Chapter 4.2.

Sieving of materials was performed with an Haver & Boecker 200 Pure 3D sieve shaker. The ”Fine” setting was used. For sieving to <250µm, 10 minutes of sieving was used. For sieving to <53 µm, three times 10 minutes, for a total of 30 minutes, was used. In between time intervals, material was redistributed per sieve, as particle aggregation prevented passing of smaller particles. In Figure 3.5 this effect is presented. Not more than 20 grams of material was sieved at a time, also to prevent the aggregation effect.

The mesh sieved used are from ABM and are build according to ISO 565 DIN, ISO 3310-1 and NEN 2560. They are 200 by 50 mm. For sieving to <250 µm, a 500 µm and 250 µm sieve were used. For sieving to <53 µm, a 500 µm, 250 µm, 125 µm and 53 µm sieves were used. The sieves were carefully cleaned before use, after switching material and after use with a clean cloth and pressurised air.

Ball milling was performed in a Retsch MM301 mill. 50 grams of material was used as a starting amount. First, the material was sieved according to the aforementioned method. The material that passed the requirement was put aside. The other material was put inside the mill, at a maximum of 5 grams at a time. The material was ball milled for 2 minutes at a frequency of 30 hertz. Then the material was sieved again. Any leftover material was ball milled using the same method. This was repeated until all original 50 grams of material was ball milled according to the specified particle size. The obtained material was weighted and losses were noted. These losses consist of particles stuck in the sieves and dust that blows away during handling. The ball milled material was properly mixed again before use. This was done in a clean sealed vial that was shaken vigorously. The ball milling capsules were cleaned before use, after use and between every change of material.

Figure 3.5: Example of material aggregation on a large sieve size. The humps of lighter material are of a smaller particle size than the sieve, but do not pass through easily. Aggravation was necessary to redistribute the cohesive material over the sieve and to sieve again.

3.4. Spark Plasma Sintering

Sintering proposes an easy method of obtaining structural material from regolith. Sintering is only representative if performed in a vacuum, inert gas, or Martian atmosphere. This poses a problem to many sintering methods. An oven or other heating device that can operate under such conditions is a must. Therefore, SPS is chosen. In Chapter 2.6.10, the choice for SPS is elaborated on further.

Sintering was be performed on small specimen sizes, due to lab conditions. These results should still be applicable for larger scale sintering [36, 37]. Sintering for application on Mars should also be analysed further, to enable the most energy-efficient and reliable way of manufacturing desired structural shapes. The adaptation from lab-scale to applicable scale is outside the scope of this thesis, but is assumed feasible for large cooperations or institutions, such as ESA or NASA. Large-scale devices already exist on the market [120]. The current largest offering is a diameter of 750 mm for hot-pressed sintering. Custom devices can be ordered, increasing the maximum size further.

3.4.1. SPS Layout

Sintering was performed in an SPS device made by FCT Systeme GmbH, of type HP D 25. In Figure 3.6 it is presented. A schematic of this specific SPS system is provided in Figure 3.6. Here a punch and die combination can be seen. This is where the material was loaded into. The punches can be pressed by a mechanical force-guided press. The die is able to move freely, but stays in place due to friction and tight fitting with the punches. This combination is encompassed within a chamber, in which different environments can be accurately simulated. The whole punch and die combination was electrified by a DC pulse. The press itself is liquid cooled. A pyrometer at the top measures the temperature in the top punch, at a distance of around 5 mm above the material.

3.4.2. Punch and Die Combination

The punch and die are made from ISO68 graphite, manufactured by Toyo Tanso France. The punch is 20 mm in diameter and 50 mm high. It has a hollow core of 10 mm diameter up until 5 mm from one end. The die has a hole of 22 mm diameter, which is protected by a 2 mm thick graphite paper sheet. This results in a material cylinder of 20 mm diameter. The die thickness is 20 mm, resulting in a total diameter of 64 mm. Two graphite

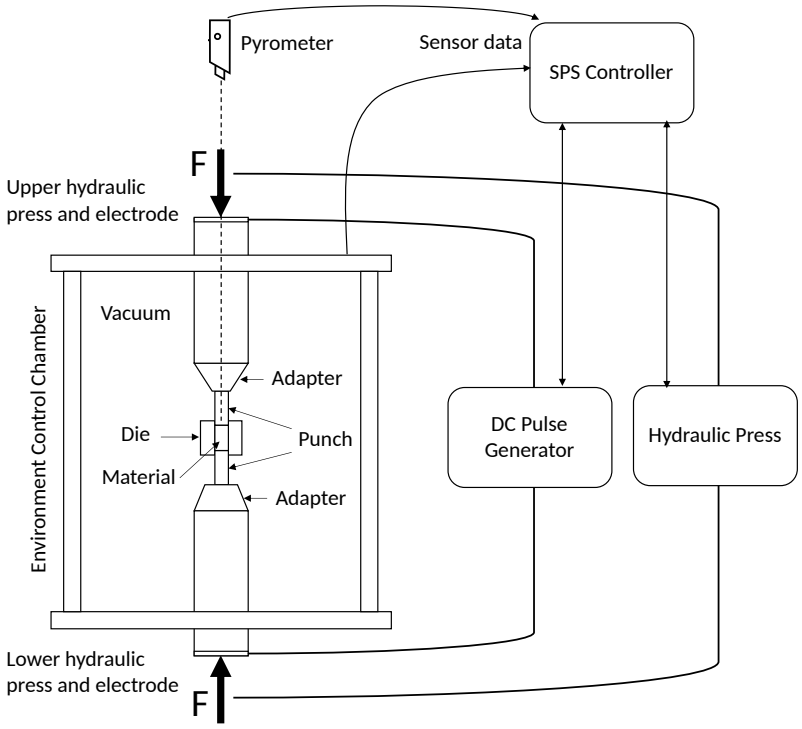

Figure 3.6: Schematic of the SPS device used. The schematic is described from the sintered material outwards. The material is contained in a die, which is lined with a graphite sheet. Two punches close the cylindrical hole in the die. Both punches are separated from the material by two graphite sheets. The punch and die combination is placed between adapters. These adapters make sure electrical conduction is smooth between the punches and the electrode. This all is placed inside an environmental control chamber, which, for the purposed of this study, has a maintained vacuum. The hydraulic press, which also functions as the electrode, pushed on the punch with a force F. This force F is therefore also present between the punch and the material. A small part of this force is present within the die due to friction. A pyrometer measures the temperature of the top punch. This punch has a hollow core, which allows the pyrometer to measure the temperature just above the material, at 5 mm separation. Sensor data from the chamber, hydraulic press, electrode and pyrometer are fed to the SPS controller. The controller determines the required pulse and pressure to ensure the specified profile is applied.

paper circles of 20 mm diameter were added between the punch and the material. The graphite paper was made from Permafoil PF-20HP, by Toyo Tanso France.The system has a maximum sample diameter of 80 mm and maximum sample input height of 40 mm. The 80 mm, 70 mm, 50 mm and 10 mm dies were not suited for the tested material of this thesis, resulting in explosive failure or melt-outs. Therefore, a 20 mm die has been used throughout the sample preparation.

Due to the ISO68 graphite's compressive strength of 172 MPa and the hollow shape of the punch, a maximum safe compressive force of 16 kN could be applied. Heat affects the graphite's strength performance. Therefore a safe compressive force of 25 kN could be applied when the graphite was up to temperature. The system has a minimum applied pressure of 5 kN. This pressure is necessary to ensure good contact between all elements. Not doing so could prevent electricity to homogeneously heat the punch, die and sample. This pressure is applied from the loading of the material into the device until the end.

After the graphite paper, of dimensions 125x48x2 mm, was inserted into the die, one punch was added and two graphite circular sheets are added. Then, the material for the specified run was inserted. It was inserted in two to three parts. Each part was weighed with a Mettler PM480 Delta Range until the specified mass had all been inserted into the die. For some material with a lower packing and/or lower density, the material was tamped in between parts. This had to be done to ensure all material would fit. The tamping was done at a maximum of 2.5 kN to ensure it had an insignificant effect compared to later applied pressure. The filled material was about 35 mm high. This meant that there was only 7.5 mm left at the top and bottom for the punches. Once filled, another two circular graphite sheets were added on top and the second punch was inserted. The whole punch and die combination was compressed with a manual press up to 5 kN to ensure it did not fall apart. The whole punch, die and material assembly was about 135 mm high.

For tests where a Boron Nitrite (BN) coating was applied, the graphite paper was first put into the die. Then, the BN spray was applied liberally. The die was then put onto a rotatory for 30 minutes. This ensured an evenly distributed coating. The circular graphite sheets were covered in BN on one side and left to dry for 30 minutes. Of the two sheets applied on each side, only one had this coating. The side of the coating was in contact with the material.

The punch, die and material combination was inserted into the chamber and pistons. Two cut-cones were added to the top and bottom. These serve as an adaptor between the 80 mm pistons and the 20 mm punches. The bottom adaptor was a 80 mm to 40 mm adaptor, where a 10 mm solid punch was inserted to ensure a hold between the 20 mm punch and 40 mm adaptor surface. This adapted was chosen due its reduced height. Otherwise, the whole punch, die, material and adaptor assembly did not fit inside the device. This is shown in Figure 3.7a.

3.4.3. Chamber and Chamber environment

The environment chamber is a closed chamber with a small circular window. For sample loading, it can be lowered. One outlet and one inlet is attached. The outlet splits into three and is only used as a vacuum pump outlet in this study. The inlet splits into three as well. One split is for one-way inlet of process gasses, e.g. atmosphere, argon or nitrogen. The other two splits are for flushing the outlet pipes by the same process gasses.

The startup phase of every run was identical and consisted of slowly creating a vacuum over the course of 2 minutes, resulting in a vacuum of around 1 hPa. Then, the system was filled with argon for 3 minutes up to atmospheric pressures (1̃000 hPa). Then, the vacuum was reinstated over the course of 3 minutes, to an almost absolute vacuum of a measurable 0.00 hPa. Afterwards, the chamber was again filled with argon for 3 minutes up to atmospheric pressures. A vacuum was created again over the course of 3 minutes, after which the 0.00 hPa pressure was kept for one more minute to ensure a vacuum across the whole chamber. The total startup phase takes 15 minutes for each sample. The argon-vacuum flushing ensures almost no oxygen, water or other atmospheric elements are present within the chamber. If there is any gas present at all, they will mostly be replaced with inert argon gas. The vacuum is maintained throughout the whole sintering process. Any evolved gasses during sintering are removed.

3.4.4. Heating and Sintering

A DC pulse profile of 15:5:1:0 was used to heat the punch and die. This means a high rectangular wave of 15 ms, 66.67 Hz, combined with a lowering wave of 5 ms, 200 Hz. This is one pulse. The 1:0 indicates a single, 1, pulse every 0 seconds. This profile was used as it yields the most stable heating in previous experiments by the operator. The voltage and amperage are variable and pyrometer-temperature guided. These values are recorded. Voltage values were between 5 to 6 V. Amperage values were between 0.5 to 0.8 kA.

The sintering phase starts after the startup phase. The parameters of sintering are different between runs. They are presented in Table 3.1 and 3.2. A heating rate of 50 °C was used with all samples. The recorded sintering values were: temperature as measured by the pyrometer, actual value of the applied force, absolute piston travel, relative piston travel, absolute chamber pressure, applied voltage, applied amperage and energy usage. All recorded values were recorded with respect to time at a one second interval. An example of a sample sintering is presented in Figure 3.7b

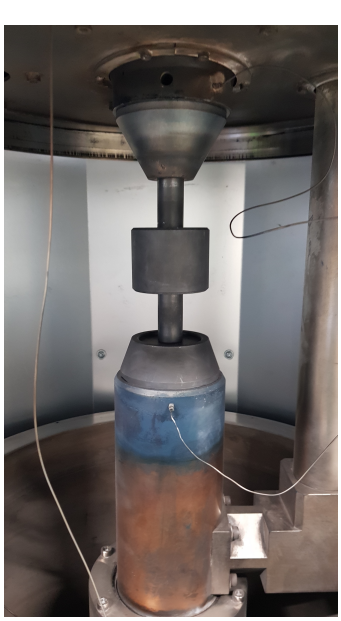

(a) The punch and die assembly within the opened SPS chamber. The material resides within.

(b) The punch and die assembly as seen through the chamber window. No isolating sleeve was applied. The punch and die glow red hot as temperatures are about 1000 °C to 1100 °C.

Figure 3.7: Example of how the SPS is loaded (a) and how it looks when in use (b).

3.4.5. End of Sintering and Sample removal

Near the end of the sintering phase, the applied pressure is released first, 5 minutes before the cooling phase. Afterwards the temperature is dropped and the sample cools in a controlled manner of 100 °C. This has been done to see the difference in effect between pressure and temperature with regards to sample length. Applied pressure has in an instantaneous and direct effect on the sample length, due to linear-elastic behaviour. After the pressure has reached the minimum of 5 kN, its effect can be assumed completed. For temperature, this is different. The coefficient of thermal expansion should result in an instantaneous effect. However, the sample will cool in-homogeneously and at a different rate opposed to the measured die surface temperature. Therefore, the effect of temperature on the sample length cannot be assumed complete after the temperature value reads the minimum. An example of the process is presented in Figure 3.8.

After both the temperature and pressure have been dropped, a 5 minute cooling phase starts. This lets of any residual heat of the sample that is undetectable by the pyrometer. After this, the chamber is flooded with air. The die still has a measurable temperature of around 80 to 140 °C at this point. It is removed from the device with heat proof gloves. The punch and die combination is put under a manual press on a 50 mm diameter hollow placeholder. First, one of the punches is removed from the bottom, by pressing the top. Next, the sample is removed by pressing again after removing the bottom punch. By this time, the sample has cooled to touchable temperatures (<50 °C). The graphite paper layer is removed if possible. The sample is weighed and put inside its specified low-moisture vial before transportation and testing.

The total end compaction was defined as the compaction at the end of sintering, minus the initial compaction at 00:00. These values were converted to percentages by the following formula:

$$\epsilon_{SPS} = 100 * \frac{\Delta_{SPS}}{\Delta_{SPS} + H_{end}}$$

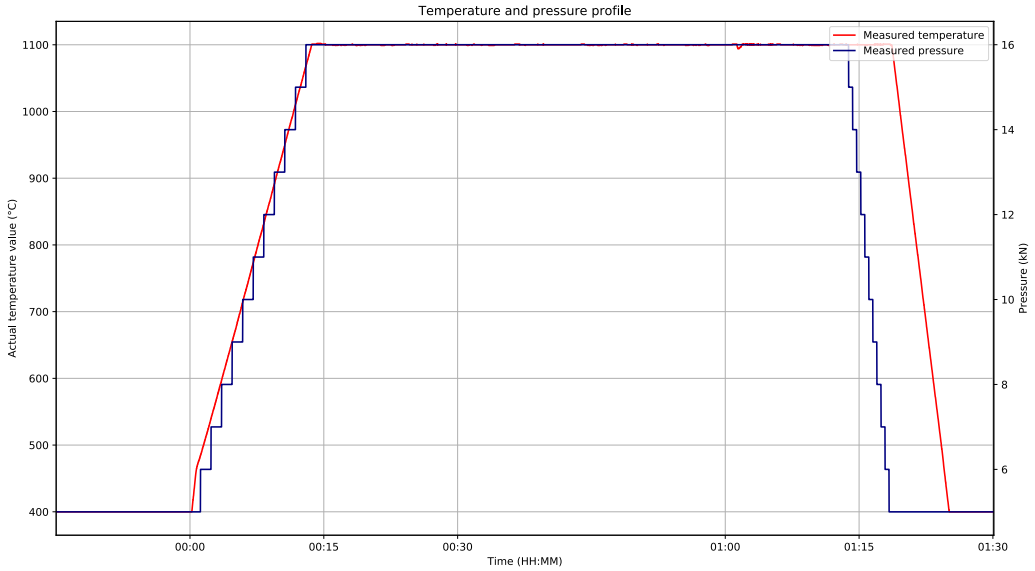

Figure 3.8: An example of an SPS profile. This is the profile for sample 17. Before the start of sintering at 00:00, the chamber environment is flushed with argon and made vacuum several times, the startup phase. At 00:00, heating and pressure is applied. With a heating rate of 50 °C, this duration is different per sample. The pressure is applied within the same time-frame. Unfortunately, the log data contained only integers for applied pressure, therefore the graph is jagged. The real pressure application was smooth. In this case, at 00:13, the maximum pressure and temperature have been reached. Now, the steady sintering stage begins. At 01:13, the pressure is released from the sample. At 01:18, the temperature is dropped at a controlled rate of 100 °C. Five more minutes of cooling are provided after this.

Where, ϵ_{SPS} is the percentage of compaction compared to the total initial height of the material, which is defined as the final height, H_{end} plus compaction, Δ_{SPS}.

3.5. Required Material Characteristics

Before choosing variables and tests, it should first be defined what a viable construction material for use on Mars requires. For a material to be used as a construction material, some properties should at least be sufficient. The most obvious property is strength. A material requires enough strength to be able to support its self-weight and any foreseen imposed loads. Determining a minimum strength of a material depends on several parameters. The structure aimed to be built is most important. A simple dome requires less strength than a multi-story building, as well as thick versus slender structural elements.

A potential structural design for Martian buildings is not defined yet. With this, the imposed loads are also undefined. Therefore, only a minimum strength is proposed. This minimum is enough to build a simple dome. Any strength higher than this, allows for larger and more slender structures to be built. The minimum strength is defined as the minimum reliable strength for a conventional burnt clay brick, which is 5 MPa [121]. As explained in Chapter 2.2, Mars has a lower gravitational constant. This minimum strength can be changed in order for it to be suitable on Mars. This results in a minimum strength of 1.9 MPa.

Another property of a construction material is stiffness, defined as the Young's modulus. A material should be stiff enough not to deform beyond a serviceability limit. A material that is too stiff has the trouble of not showing signs of failure before collapse. Similarly, brittleness and ductility come into play. A brittle structure shows little to no deformation before violently collapsing. Meanwhile, a ductile material shows clear signs of deformation before slowly collapsing. Absolute limits for both stiffness and ductility cannot be presented. Their limits depend highly on design. As an example, glass is very brittle and stiff, but due to design choices it can still be a suitable building material.

The thermal expansion coefficient is an important parameter, especially on Mars, where temperatures

range between 35 °C [56] and -140 °C [54, 55]. Again, these properties can be accounted for in design. Allowing for expansion within a structure is one such example. Multiple other properties, such as durability, hardness, fatigue, can also be of importance. These properties are important to study in further research, but are outside the scope of this thesis.

3.6. Experimental Design

In total, two groups of runs were performed. The first group, named group-1, has been setup in such a way as to find the influence of the four main sintering parameters [96]. These parameters are: particle size, temperature, sintering time and pressure applied. The results of this group would determine the design of the second group, group-2. In this second group, the main goal was to find the influence of differences in input material and preparation thereof. The measured values were deconvoluted for the Taguchi designs to obtain the results per variable. The code is presented in Appendix K.

3.6.1. Group-1

The Taguchi design for group-1 is an L9(3^4). This means that 9 runs are defined to test 4 variables, each with 3 levels. The design is presented in 3.1. Particle size, temperature, sintering time and pressure applied are chosen variables. Due to possible non-linearity, three levels are chosen for each variable.

Sample	**Particle size** (µm)	**Temperature** (°C)	**Sintering time** (min)	**Pressure** (MPa)
1	Full	1100	30	51
2	Full	1000	45	35
3	Full	800	60	16
4	<250	1100	60	35
5	<250	1000	30	16
6	<250	800	45	51
7	<53	1100	45	16
8	<53	1000	60	51
9	<53	800	30	35

Table 3.1: Taguchi design of group-1. 9 runs in total are presented. Each run has a different set of variables specific to the Taguchi design.

Particle size reduction was performed by sieving, as explained in 3.3. Sieve size should give a negative correlation according to literature [96], where a smaller grain size should yield higher density and strength values. The only foreseeable problem could be a difference in mineralogy per grain size. A grain size value of <600 µm denoted that no sieving or grinding has been performed. The grain size of the received material had a maximum of 600 µm. This was chosen to test if no material preparation could be feasible. A grain size value of <250 µm was chosen as near this value, a notable difference in mineralogy presented itself, see Chapter 4. A grain size value of <53 µm was chosen because this was the smallest sieve size available. Smaller sieving would have resulted in very minimal amount of material. Sieving at this size proved difficult, therefore a smaller sieve size was not considered. No sieving is preferred due to energy requirements and waste generation, but smaller particle sizes could result in better performance.

The temperature during sintering was varied. A positive correlation between was expected with respect to density and strength. A value of 800 °C was chosen because this yielded a minimally cohesive sample. Lower temperatures were tested in trails but proved to be too weak to handle. A temperature of 1000 °C was chosen as it proved to be the highest temperature before mineralogy changes occurred [122]. A temperature of 1100 °C was chosen as this was the highest temperature that did not result in a meltout during trails. Any higher temperatures would result in too much liquid forming and coming out of the die. Lower sintering temperatures are preferred due to energy requirements, but higher temperatures could result in better performance.

Sintering time was varied between 30, 45 and 60 minutes. A positive correlation with respect to density and strength was expected [96]. In trail runs, a 15 minute sinter time resulted in a very non-cohesive centre of samples, indicating that sintering had not been enabled there. A maximum of 60 minutes ensured that enough samples could be sintered for this study. Lower sintering times are preferred due to both lower energy requirements and shorter manufacturing times, but higher sintering times could result in better performance.

Pressure applied was varied between 16, 35 and 51 MPa. A positive correlation with respect to density and strength was expected. The value of 16 MPa corresponds to the minimum SPS applied pressure of 5 kN. The value of 35 MPa corresponds to normally used SPS parameters. The value of 51 MPa indicates the maximum safe pressure due to the graphite's compressive strength. An increase in pressure requires a

minimal increase in energy consumption, but can yield better performance.

3.6.2. Group-2

The Taguchi design for group-2 is an L8(2^7). This means that 8 runs are defined to test 7 variables, each with 2 levels. The design is presented in 3.2. Simulant type, particle size reduction method, grain size, drying, coating, temperature and pressure applied are chosen variables.

Sample	**Simulant**	**Method**	**Pressure** (MPa)	**Particle size** (µm)	**Coating**	**Temperature** (°C)	**Drying**
10	JEZ-1	Sieved	100	<250	-	1100	Dry
11	JEZ-1	Sieved	100	<53	BN	1000	Non-Dry
12	MGS-1	Sieved	51	<53	-	1000	Dry
13	MGS-1	Sieved	51	<250	BN	1100	Non-Dry
14	JEZ-1	Grinded	51	<250	-	1000	Non-Dry
15	MGS-1	Grinded	100	<250	BN	1000	Dry
16	MGS-1	Grinded	100	<53	-	1100	Non-Dry
17	JEZ-1	Grinded	51	<53	BN	1100	Dry

Table 3.2: Taguchi design of group-2. 8 runs in total are presented. Each run has a different set of variables specific to the Taguchi design.

The simulant type was varied between MGS-1 and JEZ-1. MGS-1 is the representative simulant for the average of Mars. JEZ-1 is the representative simulant for the newly proposed landing site in the Jezero crater. No expectations were present on the influence of this variation.

The particle size reduction method varied between the previously used sieving and the newly introduced ball milling. It was expected that ball milling results in better performance. For similar reasons as stated for run-1, particle size was varied. To test the difference of the particle size reduction method, no unprepared, <600 µm, material could be used. Therefore, only the previously mentioned <250 and <53 µm are used.

The effect of drying was varied to study the influence of adsorbed and absorbed water. Due to the oven drying preparation, bound water could evaporate. On Mars, this water should still be present. On Mars, it is also possible for ice crystals to be present. Therefore, water could be an important parameter. The only drawback is that on Earth, the moisture from the air can moisten the material more than it could ever be on Mars.

A coating between the graphite paper and the material was applied in some tests. This coating consists of Henze HeBoCoat 21E, a BN coating. This coating should eliminate any carbon ingression from the graphite sheets. It could also serve as a lubricant between the graphite sheet and the material.

Temperature was varied for similar reasons as in run-1. As a temperature of 800 °C resulted in a weak material and only two variables could be chosen. Therefore, 1000 °C and 1100 °C were chosen.

Due to the enormous benefit of pressure applied, see Chapter 5.1, compared to the minimal increase in energy consumption, the maximum pressure was chosen plus an even higher pressure. This higher pressure could only be applied after the graphite punch would be up to temperature, to prevent failure of the punch. Therefore, a step of 51 MPa was applied before going to 80 MPa. This is presented in Figure 3.9. 80 MPa was the highest possible pressure that could be safely applied at increased temperatures.

3.6.3. Extra Samples

Three extra samples were made and tested similar to group-2. This is presented in Table 3.3. Two of these runs, 10b and 11b, were identical to run 10 and 11, with the only difference being input mass. These extra runs were performed because the height of samples 10 and 11 was insufficient. Their height was 15 and 13 mm respectively. This is comparably low to the aimed height of 20 mm. Samples 10 and 11 were made with less input mass because of an overflowing die. Samples 10b and 11b were made with more input mass. This was achieved by compressing the input mass in 3 layers during filling of the die. Compression was done with a manual press up to 2.5 kN. With this increased input mass, the die was full again. The end height obtained was 16 and 17 mm for 10b and 11b respectively. Samples 10b and 11b were used for the Taguchi analysis instead of the original 10 and 11.

Run 18 was identical to run 1 from group-1, with the only difference being the simulant type. This was done to measure the influence of simulant type for a sieve size of <600 µm. It had been observed that it was possible to sinter MGS-1 at this sieve size, therefore the same was tested for JEZ-1. All samples are used in the strength-density and strength-compaction plots.

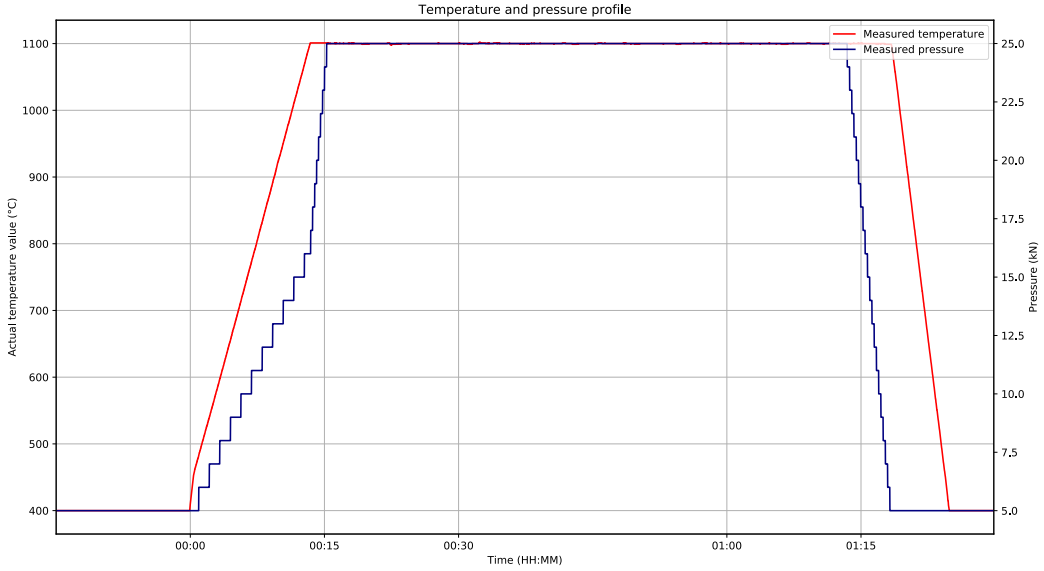

Figure 3.9: An example of an SPS profile with a bump in applied pressure. This is the profile for sample 10. Before the start of sintering at 00:00, the chamber environment is flushed with argon and made vacuum several times, the startup phase. At 00:00, heating and pressure is applied. With a heating rate of 50 °C, this duration is different per sample. The pressure up to 16kN is applied within the same time-frame. The pressure increase from 16 kN to 25 kN was applied in a 2 minute window at maximum temperature. Unfortunately, the log data contained only integers for applied pressure, therefore the graph is jagged. The real pressure application was smooth. In this case, at 00:15, the maximum pressure and temperature have been reached. Now, the steady sintering stage begins. At 01:13, the pressure is released from the sample. At 01:18, the temperature is dropped at a controlled rate of 100 °C. Five more minutes of cooling are provided after this.

Table 3.3: Overview of the extra samples made. Samples 10b and 11b were used for the Taguchi analysis instead of the original 10 and 11. Sample 18 was directly compared to sample 1.

Sample	**Particle size** (µm)	**Temperature** (°C)	**Sinter time** (min)	**Pressure** (MPa)
18	Full	1100	30	51

Sample	**Simulant**	**Method**	**Pressure** (MPa)	**Particle size** (µm)	**Coating**	**Temperature** (°C)	**Drying**
10b	JEZ-1	Sieved	100	<250	-	1100	Dry
11b	JEZ-1	Sieved	100	<53	BN	1000	Non-Dry

3.7. Compressive Strength

Samples were prepared for compressive testing by grinding until the top and bottom were flat and did not contain any graphite paper. This was achieved by grinding them with 4000 grit SiO paper. Only during grinding and actual testing were the samples taken out of their vials. The broken pieces were put back inside the vials.

Compressive testing was done on two devices. For the first group, an Instron 8872 with an Instron 8800 controller was used. For the second group, a Zwick Z100 was used. The former has a load capacity of 9 kN and a non-rotating crosshead. The latter has a load capacity of 100 kN and a rotating crosshead. The maximum capacity of the Instron proved insufficient for group-2. Therfore, two different divices were used. One notable difference between the two devices is the crosshead. A non-rotating crosshead requires almost absolute parallel surfaces of specimens. When this is not the case, some parts of the specimens may be subject to more force than others, resulting in only part of the specimen being loaded and tested in compression. A rotating crosshead ensures that non-parallel surfaces can be tested accurately in full compression, due to self-alignment. The samples made were not perfectly parallel, this has an influence on the tests. Therefore, both runs cannot be compared in absolute terms.

A loading rate of 0.001 mm/s was used. Loading was therefore displacement guided. The Instron tests were calibrated, thus the results should show absolute displacement. The Zwick had been calibrated using a compliance test performed on the same day, just after all tests were performed. This compliance test meant a run of the device without any sample. The displacement that resulted was subtracted from the displacements measured. For every sample force value, the respective compliance displacement at the same force level was subtracted from the measured displacement. For every non-perfect match of force, the compliance test displacement was linearly interpolated between the two force values closest to the sample force value. For every double force measurement in the compliance test, only the first occurrence was considered.

Obtained values for the Instron have an interval of 0.2 seconds. Load was measured with an accuracy of 0.01 N. Displacement was measured with an accuracy of 0.01 µm. Obtained values for the Zwick have an interval of 0.1 seconds. Load was measured with an accuracy of 0.0001 N. Displacement was measured with an accuracy of 0.001 µm. The presented values of stress and strain are the result of simple formulas. The stress is presented in MPa and is calculated by dividing the total load in Newton by the total area of that sample in mm^2. The strain is obtained by dividing the displacement minus the reported displacement at the initial zero-load, by the total length of the sample.

3.7.1. Size Effect

To analyse the results, the effect of differing sample height had to be taken into account. Both the diameter and height of samples vary. Therefore, results are calibrated using the Modified Size Effect Law (MSEL) [123]. All strength values are reported as the corrected strength. Strength values are also separately reported as a Mars-equivalent strength. As explained in Chapter 3.5, due to the gravity difference on Mars, structural application of materials is enhanced. Buildings build on Mars can be equivalent to a building on Earth, when using the Mars-equivalent strength as a characteristic value. The true strength of a material remains unchanged.

The following formula was used to obtain the corrected strength values [123]:

$$f_c' = \frac{f_0}{\frac{0.4}{\sqrt{1+(h-d)/50}} + 0.8}$$

Where:
f_0 is the measured compressive strength of a cylindrical concrete specimen with a height of h and diameter

of d in mm.
f'_c is the compressive strength of a standard cylinder.

3.7.2. Correlations

Strength measurements are often plotted against density measurements when sintering. This was also done for the measurements of this study. An attempt was made to fit the correlation to to a specific curve presented below. The fitting was performed by the least-squares method. No intersection coefficient has been applied on purpose. Applying a variable intersection could result in a relation with sub-zero strengths. It was found rational to assume a function that has 0 as an absolute lower limit.
The data was fitted to the following curve:
$y = a \times x + b \times x^2$
Where x is 0 at the lowest measured density.

Strength values were observed to be more correlated with compaction measurements. Therefore, the same curve was fitted to the strength-compaction data. This time, x is 0 at 0 compaction. The code for the curve-fitting is presented in I.

3.7.3. Young's Modulus

An attempt of estimating the Young's modulus was made. For actual measuring, the samples need to be subjected to multiple load cycles at 30% of the maximum strength. As only one sample was made per run, the maximum strength was unknown before compressive testing. Therefore, only an estimate of the Young's modulus could be attempted.

Due to the nature of the estimation, the results are not regarded as acceptable for the results and discussion chapters. If the results are of interest, they can be found in Appendix B. Furthermore, the determination of the Young's modulus was done by considering only the part of the stress-strain curves which showed most linearity. This is indicated in the figures. A linear regression was performed to estimate the slope and report the Young's modulus. Test results for group-2 were calibrated by performing a compliance run. This is a run without sample present. The results for the samples were then calibrated by subtracting the results of the compliance run in a specific manner. At every measured compressive force, the subsequent strain of the compliance run was subtracted from the measured strain in the sample. The code to make this possible is presented in Appendix H.

3.8. Density and Porosity

CT scans were made in a Phoenix Nanotom M. A rotation interval of 0.25°is applied. The sample to X-ray source distance resulted in a detectable voxel size of 15µmx15µmx15µm. The overall de-convoluted slice size is 1600x1600 pixels, or 24x24 mm. The measured height was 2140 pixels, or 32.1 mm. The grey values were obtained in 16-bit grey-scale. CT was only performed for group-1 due to time constraints.

Before testing, the graphite paper was removed by grinding with 1200 grit SiO paper. The samples were hot-glued to a glass cylinder and scanned in upright position. Removing the hot glue resulted in minimal abrasion of the sample surface. This loss of material is compensated for while grinding for flat and parallel surfaces. Samples were held in the vials as described in 3.3 between testing. The maximum duration exposed to normal air was around 1.5 hours.

The deconvoluted CT data was analysed with Fiji ImageJ [124]. Peak values for the surrounding air were measured, as well as maximum pixel value. These values were used to correct individual CT scan measurements and normalise the data. The peak value of the surrounding air was subtracted from the measured values. The maximum pixel values were used to linearly normalise the values after the aforementioned subtraction. Batch processing macros were written and are presented in Appendix J. To obtain the radial profiles, a plugin was used [125]. The measurements from the batch-processing are then used to plot the density distribution in Python. Calibrations are made by using the average pixel intensity of the air and the maximum pixel value possible. The calibrated intensity, analogue to density, of the samples with respect to its height and radial profile were plotted. The python code is presented in Appendix J. Voids were not considered part of the density of the samples in this regard.

Porosity measurements were performed by using the BoneJ plugin [126] on the described data. Macro porosity was measured this way. The volume of one voxel was 3375 μm^3. Because of noise, it is not reliable to measure pores of this volume. Therefore, a minimum of 30 voxels was determined as lower limit for pore

sizes. This equates to a volume of about 0.0001 mm^3. All detected pores below this limit were discarded. Python code for the analysis of the BoneJ data is presented in Appendix L.

All samples were also weighed and measured in volume, after performing CT scanning, if that was the case. The weighing was done on a Mettler Toledo AB304-S analytical balance, with a precision of 0.1 mg. This was done after removing all graphite paper. The height was measured five times, once in the middle and once for every 90°opposing side, using a HeidenHain ND 221 B, with a precision of 0.5 µm. Diameter was measured four times, once for every orthogonal diameter on both the bottom and top side. Average values were used to calculate the volume en subsequently envelope density. Comparing these values to the initial input mass per sample resulted in estimated mass loss during sintering.

3.9. Microstructure

Broken samples were prepared for microstructure analysis. Selection of the broken piece was done by two criteria. The first criterion was inclusion of important edges. It was considered important to be able to analyse the bottom edge of the sample, as well as the side edge. The second criterion was that as much of the intermediate material between these two edges was still present. This would result in pieces that contain all areas of interest: the bottom edge, a side edge and a portion of the inside of the sample.

The selected pieces were impregnated with epoxy. Conpox Resin BY 158 and Conpox Hardener HY 2996 were used. They were mixed in a 10:3 ratio. After a piece was held at vacuum for 15 minutes, epoxy would be added. The application of epoxy was done slowly to remove all air before the epoxy would touch the sample. The sample was held submerged for 10 minutes. During this time, bubbles were observed to come from the samples. This indicated that the 15 hold at vacuum was not enough to remove all air. The bubbles can also be the result of a reaction with the samples. After this time, the vacuum was released in a controlled manner. This would slowly push the epoxy inside the empty pores. After the pressure was released, the samples were removed and set to rest for at least 72 hours at room temperature. The epoxy would harden during this time.

The impregnated samples were ground with ever finer sandpaper. First, 220 grit SiO paper was used to grind the samples to roughly the desired shape. Then 300, 800, 2000 and 4000 grit SiO paper was used to grind the samples for 3 minute at each level. Only ethanol was used during grinding. Samples were put in an ultrasonic bath between each paper size. They were submerged in ethanol. After grinding, samples were polished with diamond paste. Sizes of 9 µm,6 µm,3 µm and 1/4 µm diamond paste were used. Polishing was done for one minute at each paste size. Samples were put in an ultrasonic bath between each polishing stage. They were submerged in ethanol.

SEM microscopy was performed on all polished samples with a Quanta FEG 650. Locations of interest were first determined by light microscope images. These images contained the whole sample and were stitched together from multiple smaller images made at a 300x magnification. The total image size was around 20000x20000 pixels, depending on sample sizes. Two light microscope images were made, one for coaxial light conditions and one for ring light conditions.

ESEM was used to mitigate the need of a conductive coating. A conductive coating could interfere with EDS imaging. A chamber pressure of 0.1 bar was used with water vapour as environmental discharge mechanism. Images were made at 15.00 kV. This was to ensure detection of iron in EDS. A spot size of 5.0 and working distance of 10 mm were used. Images were made in CBS mode. This resulted in an image where the grey-scale indicates the average atomic number of the elements present. Images with a resolution of 1536x1024 pixels were obtained. Different magnifications were used, ranging from 125x up to 20000x.

4
Material Characterisation

The resource of choice for this thesis is regolith. One problem with Martian regolith, is the variability with respect to location. Particle size distribution, as well as mineralogy differ from region to region. Another problem is the limited available knowledge. Although many Martian missions have identified soil characteristics [62, 63, 74, 75], they cannot compare to lab tests on Earth. Sample return missions have been planned to combat this, but for now, uncertainties in soil characteristics should be accepted.

Simulant characteristics compared to actual Martian regolith are presented in Table 2.9 of Chapter 2.5. Most material properties are readily provided by ExolithLab [29–31]. In Table 4.1, the mineralogy as reported as mixed is presented for both simulants. Reported properties are used throughout the study. The main difference between two simulants is the addition of smectite and magnesium-carbonate in JEZ-1 and differing ratios of other minerals. This difference resulted in JEZ-1 being visibly more pink than MGS-1.

Table 4.1: Mineralogy of used simulants as mixed, MGS-1 and JEZ-1 [29, 30].

Mineral	**MGS-1** (wt.%)	**JEZ-1** (wt.%)	**Chemical formula**
Anorthosite	27.1	16	$(Ca_{0.50(4)}Na_{0.50})(Al_{1.50}Si_{2.50})O_8$
Glass-rich basalt	22.9	13.5	SiO_2
Pyroxene	20.3	12	$(Mg_{1.01(15)}Ca_{0.80(11)}Fe_{0.19(19)})Si_2O_6$
Olivine	13.7	32	$(Mg_{1.15(5)}Fe_{0.85})SiO_4$
Mg-sulfate	4	2.4	$MgSO_4$
Ferrihydrite	3.5	2.1	$Fe_2O_3 \cdot 0.5\,H_2O$
Hydrated silica	3	1.8	$SiO_2 \cdot nH_2O$
Magentite	1.9	1.1	Fe_3O_4
Anhydrite	1.7	1	$CaSO_4$
Fe-carbonate	1.4	0.8	$FeCO_3$
Hematite	0.5	0.3	Fe_2O_3
Smecite	n.a.	6	Multiple
Mg-carbonate	n.a.	11	$MgCO_3$
Total	100	100	

ExolithLab manufactures MGS-1 and JEZ-1 by combining several mineral sources in ratios similar to those measured on Mars. Instead of sourcing 100% pure minerals and combining them in correct ratios, ExolithLab sources rocks comprised of possibly multiple minerals. These rocks are then carefully combined in the right ratios to achieve an accurate mineralogy [127]. This, however, results in some particles that consist of different minerals. During analysis, these particle types have been identified and named according to their features for MGS-1. In Table 4.2, the different categories are presented.

Bulk and tap densities have been measured for MGS-1. Bulk density was the density measured when material was loosely packed. This was 1334 kg/m^3 as received and 1434 kg/m^3 when dried. Tap density was the density measured when material was packed tightly due to 30 seconds of vibration. For MGS-1 this was 1755 kg/m^3 as riecieved and 1781 kg/m^3 when dried.

Table 4.2: Mineral types analysed. These are the types of mineral present within the simulant MGS-1 [29], that could accurately be differentiated from each other. Some groups consist of multiple mineral types, while others only represent a singular mineral type.

Name	Description
Mg-sulfate	Magnesium-sulfate ($MgSO_4$). Alteration was observed as a cracked particle, see Figure 4.3(a).
Ca-sulfate	Calcium-sulfate ($CaSO_4$). Also called anhydrite, it is the anhydrous form of gypsum. Average irregularly shaped particles.
Fe_1	Iron-bearing minerals with significant carbon, C, presence. Carbon was either present originally as iron-carbonate ($FeCO_3$) or as carbon from the applied carbon coating. A distinction can be made with Fe_2.
Fe_2	Pure iron oxides, Fe_yO_x. Sources can differ between hematite, magnetite or ferrihydrite.
Anorthosite	Impure form of anorthosite containing the only source of ilmenite ($FeTiO_3$), clearly visible in Ti spectrum. Main other constituent is plagioclase. See Figure 4.3(b).
Silicates	Silicate minerals, SiO_2. Quartz, glass and hydrated silica ($SiO_2 \cdot nH_2O$). Hydrated silica has distinct organic shapes, see Figure 4.3(c-e).
Plagioclase	$(Ca_{0.50}Na_{0.50})(Al_{1.50}Si_{2.50})O_8$. Average irregularly shaped particles.
Pyroxene	$(Mg_{1.01}Ca_{0.80}Fe_{0.19})Si_2O_6$ and $(Mg_{1.02}Fe_{0.88}Ca_{0.10})Si_2O_6$. Average irregularly shaped particles.
Olivine	$(Mg_{1.15}Fe_{0.85})SiO_4$. Average irregularly shaped particles.

4.1. DSC-TGA

DSC-TGA measurements have been performed for both MGS-1 and JEZ-1 simulants. Both simlants have been tested in both argon and air environment. The results are presented in Figures 4.1 and 4.2. The total mass loss of MGS-1 was 5.8% in argon and 5.1% in air. The total mass loss of JEZ-1 was 12.9% in argon and 12.3% in air.

In Figure 4.1, the DSC-TGA curve of MGS-1 is presented for both an argon and air environment. Up to 180 °C, 2% mass was lost. This is attributed to adsorbed and absorbed water. At a temperature of 400 °C, the heating rate changed. This resulted in a change in the DSC curve. Unfortunately, a simultaneous change in the TGA curve was observed. This change cannot be correctly analysed due to the unreliability of the DSC curve at this temperature. At 800 °C, about 2.8% total mass was lost in an argon environment. Mass loss increases and about 1.5% of mass was lost up to a temperature of 1000 °C, to a total loss of 4.8% in an argon environment. After around 1100 °C, heat flow starts to decrease sharply. This region was not of interest as the sintering temperatures only went up to 1100 °C. The total mass loss was 5.2% in an argon environment. Higher temperatures are not of interest for this study, as only a temperature of 1100 °C was obtained during sintering.

In Figure 4.2, the DSC-TGA curve of JEZ-1 is presented for both an argon and air environment. Up to 180 °C, 2% mass was lost. This is attributed to adsorbed and absorbed water. At a temperature of 400 °C, the heating rate changed. This resulted in a change in the DSC curve. From 500 °C to 750 °C, mass loss was significant and presents itself as two separate events. It was accompanied by a dip in the DSC curve, meaning it is endothermic. This can be the result of chemically bound water evaporating. At 800 °C, about 10.9% total mass was lost in an argon environment. Mass loss increases again from 950 °C. At 1000 °C, to a total loss of 11.8% was observed in an argon environment. After around 1100 °C, heat flow starts to decrease sharply. This region was not of interest as the sintering temperatures only went up to 1100 °C. The total mass loss was 12.8% in an argon environment. Higher temperatures are not of interest for this study, as only a temperature of 1100 °C was obtained during sintering.

Unfortunately, due to the heterogeneity of the material, the observed behaviour could not be untangled and addressed to certain mineral transitions, chemical reactions or other processes. The described processes above were of importance to the overall behaviour of the material during heating. The DSC-TGA results were specifically important to the theoretical energy calculation for sintering. This is presented in Chapter 5.8.

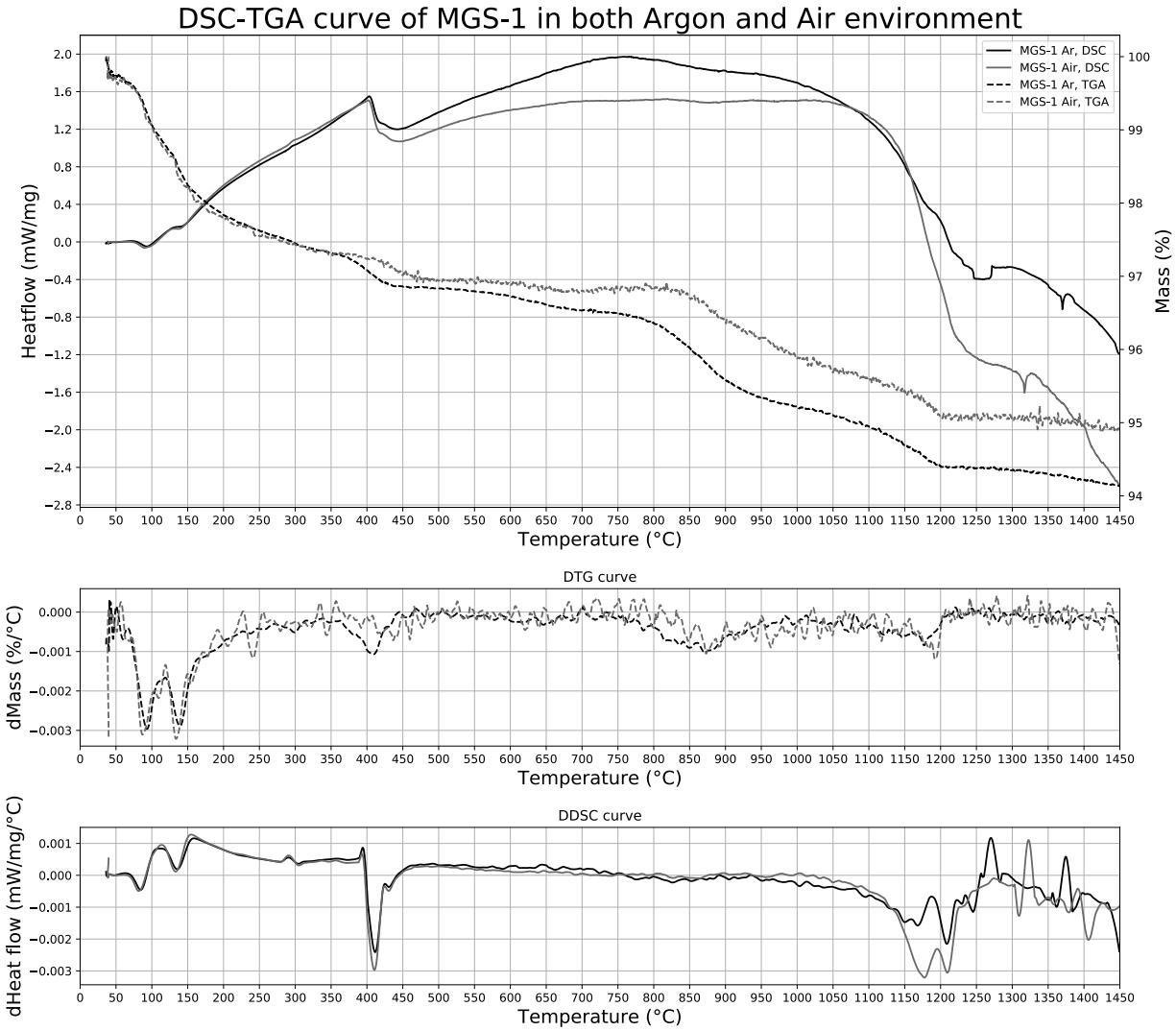

Figure 4.1: DSC-TGA curve of MGS-1 in both argon and air environment. The derivative functions for the DSC and TGA curve are presented as DDSC and DTG curves respectively.

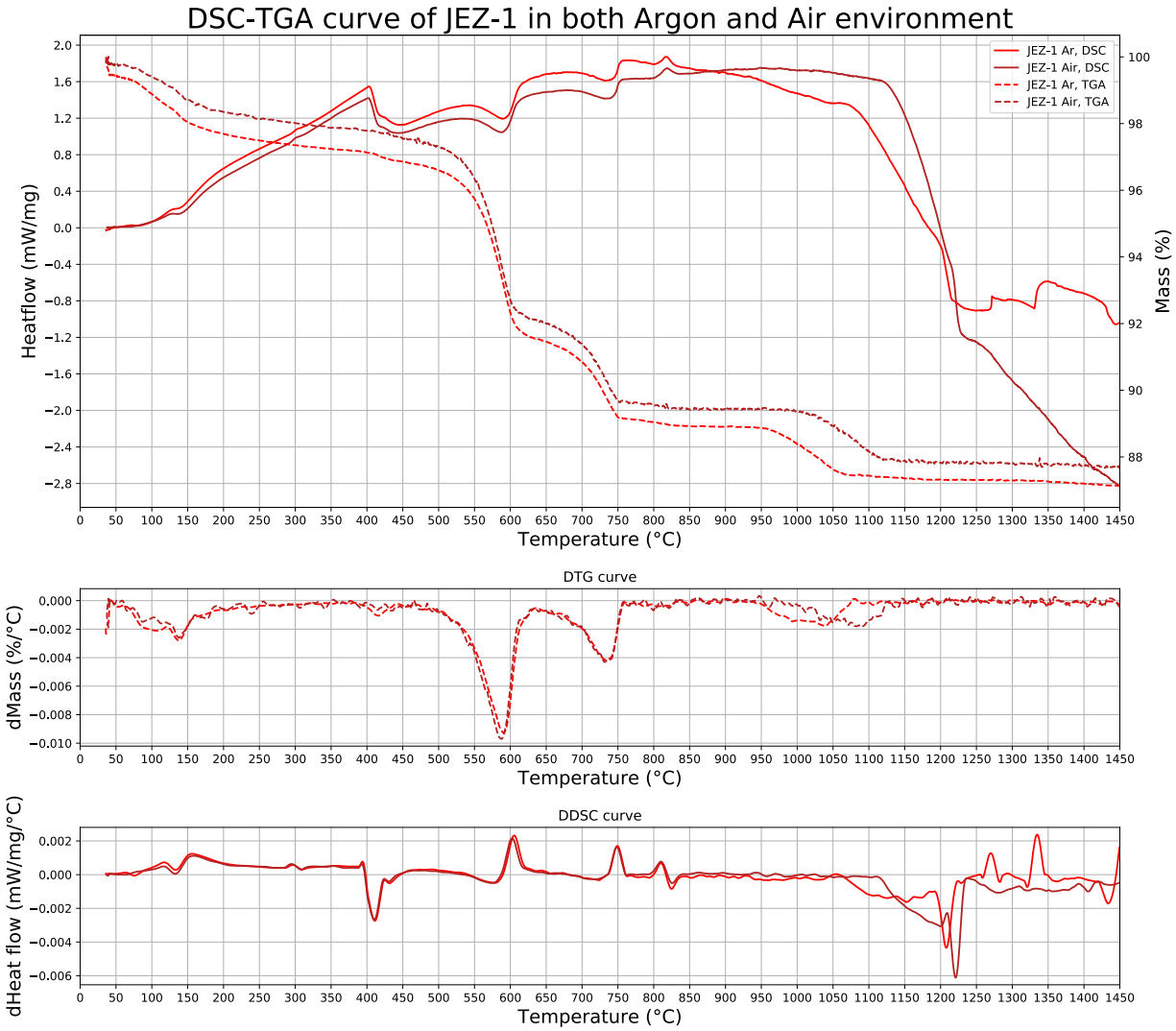

Figure 4.2: DSC-TGA curve of JEZ-1 in both argon and air environment. The derivative functions for the DSC and TGA curve are presented as DDSC and DTG curves respectively.

4.2. Mineralogy per Particle Size of MGS-1

One characteristic that was deemed important was the mineralogy per particle size. As material was sieved, a change in mineralogy ratios can present itself if the mineralogy per particle size is not evenly distributed. Mineralogy per particle size was determined for MGS-1.

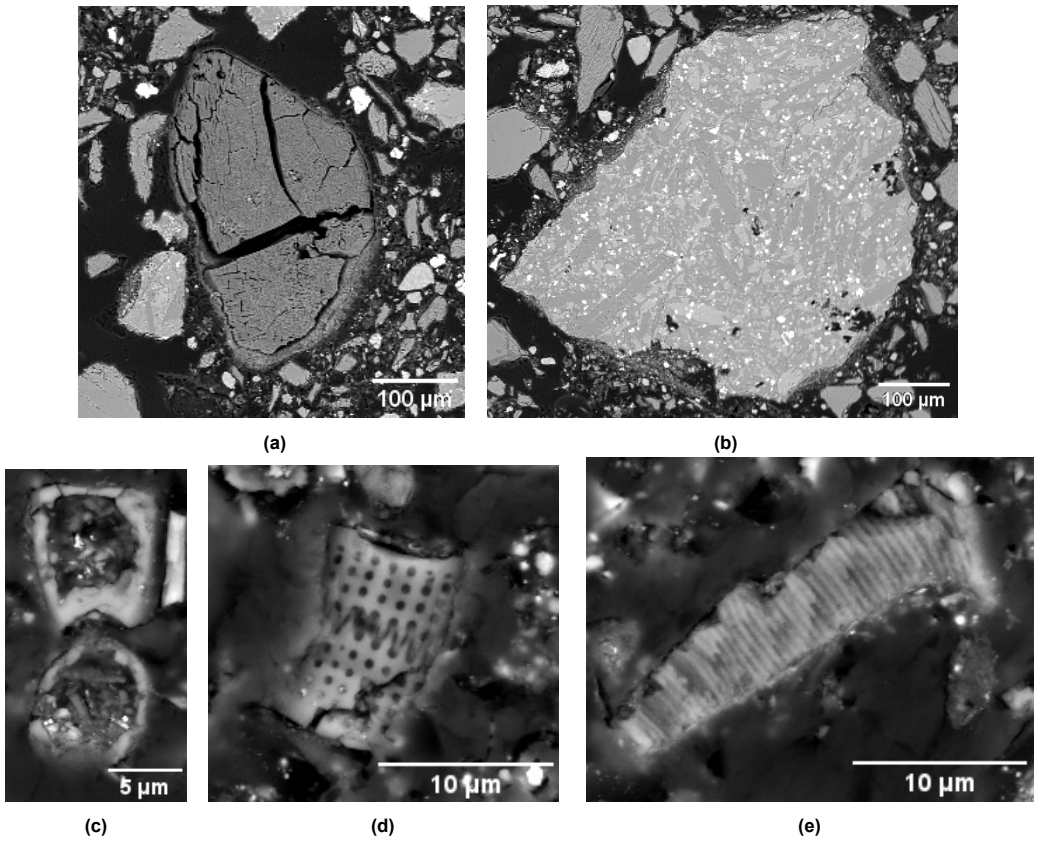

Figure 4.3: Unique types of particles. (a) Magnesium-sulphate particle with a cracked appearance. (b) Anorthosite particle with well defined ilmenite speckles (white). (c) Circular hydrated silica particles. (d) Comb-like cylindrical hydrated silica structure. (e) Ribbed hydrated silica structure.

Results are presented in Figure 4.4 as histograms of mineralogy per particle size for different magnifications, 125x, 500x and 2000x. This corresponds to a total analysed area for each magnification of 55 mm^2, 2.75 mm^2 and 0.139 mm^2, respectively. In Figure 4.5, results are presented per mineral type. Estimated particle size versus total area percentage is presented in both figures. This allows for easy sieve selection.

Figure 4.4, for a 125x magnification, shows a mostly uniform distribution of mineralogy across particle sizes. Only above a grain size of 200 µm can a difference be observed. Anorthosite, plagioclase, pyroxene and silicates show little variance across grain sizes. Olivine has a similarly low variance below 110 µm, but was sporadically present at larger particle sizes. Both iron-containing groups, Fe_1 and Fe_2, have a low constituent amount, but are still present across smaller particle sizes (<110 µm) with low variance. Calcium-sulphate was prominently present in the larger particle size bracket. Although present throughout this magnifications full particle size range, most of its presence was within particles larger than 200 µm. Mg-sulphate was mostly visible within smaller particle sizes (<170 µm).

Furthermore, this uniform trend continues within the 500x magnification range up until a particle size of around 30 µm. This was expected as there was overlap between magnifications. Below this particle size, there was an absence of silicate minerals, olivine and anorthosite. The decrease in plagioclase and increase in $MgSO_4$ was notable and explained in the next section. Fe_1 particles are uniformely present within the observed magnification.

Within the 2000x magnification, a largely different mineralogy was present. This magnification was dominated by plagioclase, silicate minerals and iron phases. A small amount of olivine and pyroxene can be observed. Absence of mgagnesium-sulphate and anorthosite is notable.

According to Dr. Zoe Landsman [127], chief scientist at ExolithLab, there are two distinct grain size distributions within the simulant. The bulk minerals, plagioclase, basalt, olivine and pyroxene should have similar large grain size distribution, while the other minerals are finer. This distinction has also been observed during analysis. As can be observed from Figure 4.4, from a magnification of 2000x, a different regime with respect to mineral types was present. Within the SEM images, particles observed at this magnification seemed to have less irregular broken rock like shapes, similar to Figure 4.3(a,b). Instead, hydrated silica particles are organic shapes, as presented in Figure 4.3(c-e). This also shows in Figure 4.5, where two distinct modes are present for silica minerals.

Due to their low constituent amounts, some minerals pose irregular particle size distributions. With a weight percentage of 1.7%, anhydrite ($CaSO_4$) was mainly present as larger types of particles. This is also visible from Figure 4.5, where, aside from one odd bar, Calcium-sulphate was almost exclusively present in larger sizes (>200 µm). Similarly, iron group Fe_2 shows a spiked distribution. This time, only smaller particles are detected. The sparsity of olivine is also notable, especially considering its supposed 13.7 wt.% mineralogy share.

Both iron-phase groups, Fe_1 and Fe_2, are only present as smaller particle sizes, where they seem to be uniformly distributed. With a total iron containing minerals content of 7.3%, they can play a significant role in the mineral mix.

4.2.1. Discussion

Results for $MgSO_4$ are inaccurate for smaller particles sizes. Due to their similarity in colour, the TWS classifier identified the edges of particles as $MgSO_4$. This was a problem for smaller particles, whose relative area around edges is proportionally larger. Thus more smaller particles were inaccurately identified as $MgSO_4$. That being said, $MgSO_4$ appeared to only be present as relatively larger particle sizes (>60 µm), based on visual evidence from SEM images. Using small sieve sizes could result in only sporadic presence of $MgSO_4$.

Although anhydrite ($CaSO_4$) was present throughout all grain sizes, this mineral was mainly concentrated as larger particle sizes (>200 µm). Sieving can result in a drastic decrease of this mineral. Plagioclase appears to be present throughout the simulant in all sizes. Sieving cannot drastically reduce or increase the content of this mineral. Sieving might result in an increase of this minerals relative content, due to the absence of other minerals at lower sizes. Pyroxene seems to be as uniformely distributed as plagioclase, as is suggested by Dr. Zoe Landsman [127]. A drop in pyroxene content has been observed for the smallest particle sizes, as is observed in Figure 4.5.

A drop in iron content can only be achieved by using particle sizes larger than 150 µm. Due to decreased sintering performance at larger particle sizes, this is not recommended. A similar story holds for silicates, with the only difference being a change in mineralogy and shape at smaller particle sizes. It can be useful to remove hydrated silica minerals, to prevent H_2O influences. This is achievable by sieving and removing particles that are smaller than 10 µm.

The absence of anorthosite for the larger magnifications was notable. It has been observed that these particles are relatively large and do not show a large grain size distribution. Because anorthosite consists of pyroxene and olivine minerals, combined with ilmenite, removal only excludes the main ilmenite source. This can be achieved by sieving out particles larger than 30 µm. A reason for the absence of anorthosite can be the crushing of particles. As only a small proportion consists of ilmenite, it is conceivable that anothosite breaks into separate minerals when crushed. This would result in separate ilmenite, pyroxene and olivine particles, hence explaining no anothosite particles at smaller sizes.

It is suggested to analyse three different sieve sizes. The first size is: <10 µm. This should result in only the very fine material being used. It has the advantage of better sintering performance due to small particle sizes [96]. There should also be limited amounts of $MgSO_4$, $CaSO_4$ and anorthosite present. This size bracket is mainly dominated by plagioclase. The effect of this different mineralogy is unknown. A significant drawback of this sieve size is the amount of waste created.

The next sieve size is the absence of the former mentioned sieve size, thus every particle larger than 10 µm. This results mainly in the omission of hydrated silica. The H_2O released by heating the hydrated silica could have an influence, which is mitigated by using this sieve size.

The last suggested sieve size is: <200 µm. This sieve size should not result in a significant difference in mineralogy, but will make the size distribution more optimal. The omission of larger particles in the matrix will result in a more homogeneous material. It is expected that a more homogeneous material has better performance, due to a decreased likelihood of defects.

As it was impractical to make grid-maps during SEM, quantitative data measuring total sizes, areas or

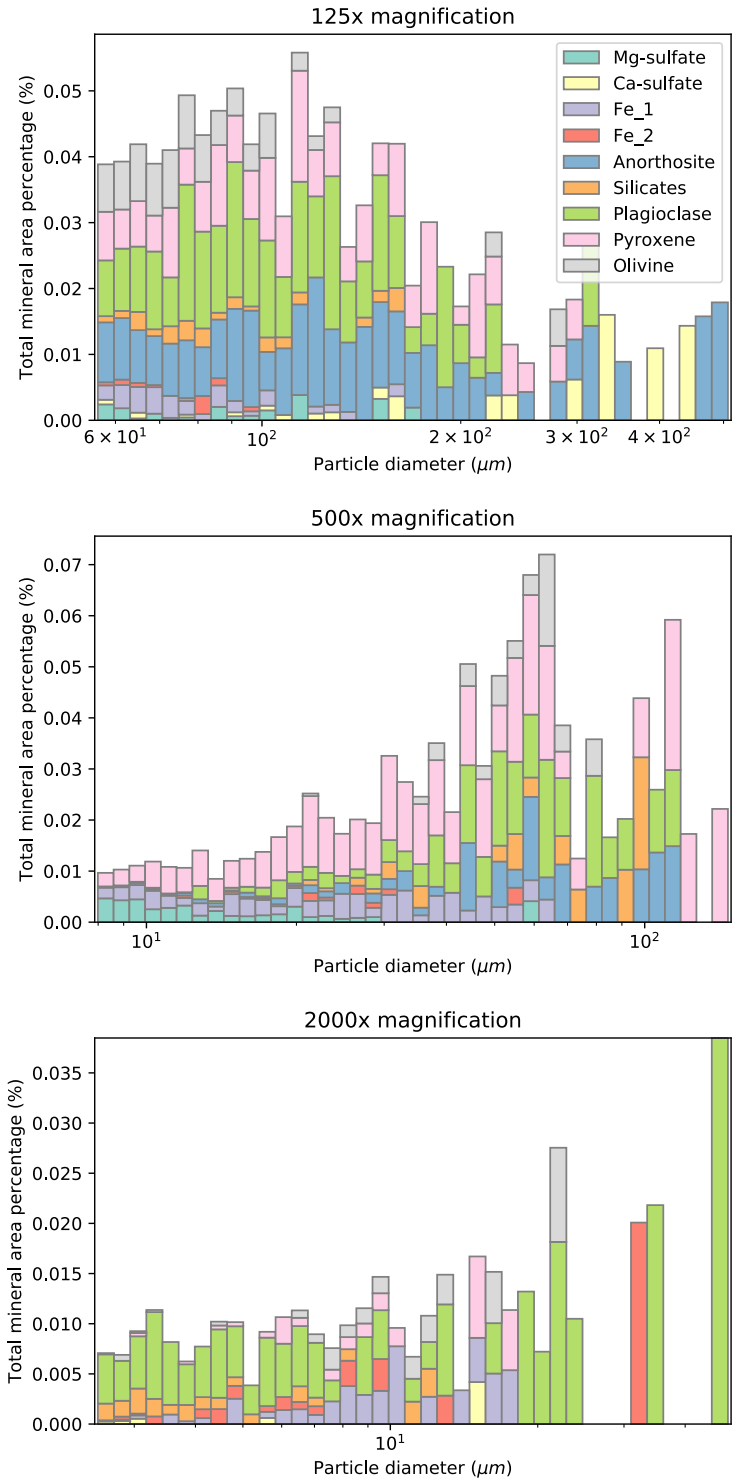

Figure 4.4: Histogram plots of relative particle areas per particle diameter for three analysed magnifications, 125x, 500x and 2000x. Particle diameter is plotted in log10. Upper ends of each graph are inconsistent due to boundary effects for image analysis. Some overlap between particle sizes was present. The relative total area percentage is based on the area of each image. It represents what percentage of the image is accounted for by each specific particle size bracket.

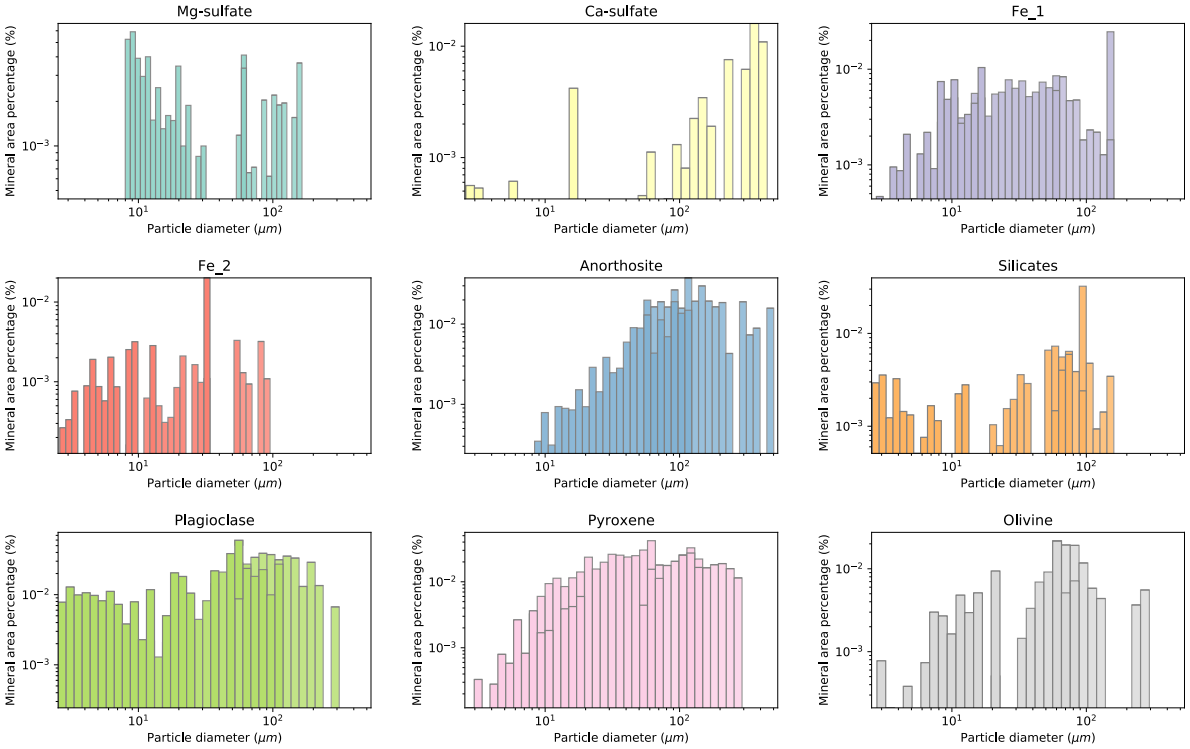

Figure 4.5: Histogram plots of relative particle areas per particle diameter per mineral. Both particle diameter and area percentage are plotted in log10. For each mineral, three magnifications are combined, 125x, 500x and 2000x. Each magnification is linearly scaled to make comparison possible. The relative total area percentage is based on the area of each theoretical image. It represents what percentage of the image is accounted for by each specific particle size bracket.

volumes are not accurate across magnifications. For larger magnifications, there should be more empty images, i.e. images containing almost zero particles analysable within a magnification range, per analysed image. Even so, this study aims to find a discernible difference in mineralogy per particle size, not to find the grain size distribution itself. These results are considered consistent across magnifications.

Any particle smaller than 5 μm^2 was excluded from analysis. From SEM images, particles smaller than this are observed. These particles are a magnitude finer than what was analysed. Efforts were made to create SEM images for these particles, but to no avail. Their size meant that they often were embedded a little below the epoxy, resulting in blurry images and incorrect EDS data. Due to the chaotic and blurry nature of these images, the image processing was not possible.

The act of casting particles in epoxy can have disturbed particles. Any particles that are lighter than epoxy could have floated. No particles were observed to float. Another problem with this method was the section taken for analysis. Small particles tend to sit at the bottom while larger particles only touch the bottom partly. When a section is taken too close to the bottom, this results in an increase in observed small particles. In this case, both smaller particles are present, as well as larger particles that only have a small cross section exposed. When the section is too far off the bottom, smaller particles tend to be lost, while larger particles have a more representative cross-section. The cross section was at least as high as halve of the largest particle size. To combat the loss of small particles, enough material was cast in epoxy, so any holes between large particles should have been filled with smaller particles, similar to bulk packaging.

The simple assumption of round particles to determine sieve sizes was incorrect. Angular particles will be able to pass through smaller sieve sizes. For this reason, any determined sieve size should be taken at an expected lower range. It was difficult to account for this angularity, due to the variability between particles.

Olivine and pyroxene have a similar chemical makeup. This makes distinction difficult. Although results should be accurate, interchangeability between pyroxene and olivine should be considered.

$MgSO_4$ seems to be the only mineral impacted by handling. Particles seem to have cracked and shrunk, as can be seen in Figure 4.3(a). Solubility of $MgSO_4$ in ethanol was assumed to be negligible. This leaves two options for the alteration. The $MgSO_4$ particles could have absorbed moisture from the air. This moisture might have dried during contact with ethanol, resulting in a particle with drying-like cracks. Another possibility is the interaction of $MgSO_4$ with epoxy.

The sieve sizes chosen for practical application in this study are different from the optimal sieve sizes discussed in this section. This has been explained in Chapter 3.6.

5
Results

To answer research question 4.b-c and 5.a-c, several physical properties were measured and analysed. The important properties were: uniaxial compressive strength, density, density distribution, macro porosity, total compaction, mass loss and energy consumption. In total, 20 runs were performed and tested. For group-1, 9 runs were performed to analyse the influence of the sieve size, temperature during sintering, duration of sintering and applied pressure during sintering. For group-2, 8 runs were performed to analyse the influence of simulant type, method of particle size reduction, applied pressure during sintering, resulting particle size after sieving or ball milling, the application of a BN coating, temperature during sintering and drying of the material before sintering.

Group-1 was tested for strength, density, compaction, mass loss, energy consumption, porosity and density distribution. Group-2 was tested for strength, density, compaction, mass loss and energy consumption. The influence of the manufacturing variables on these physical properties were investigated by analysing the Taguchi design. The combined variables of the individual samples were deconvoluted. This generated a clear overview of the influence of each individual variable on each physical property. The three extra runs were not included in the analysed Taguchi results. This is because the Taguchi design cannot be changed or be unbalanced. CT scans were only performed on group-1. Besides CT, all samples were measured with identical measures, as stated in Chapter 3. Each measurement was performed once, as no duplicate samples were made.

Three extra runs were performed and tested similar to group-2. Two of these runs, 10b and 11b, were identical to run 10 and 11, with the only difference being input mass. The other run, run 18, was identical to run 1 from group-1, with the only difference being the simulant type. See Table 3.1 and 3.2 for a complete overview of the research design. An example of a sample is presented in Figure 5.1.

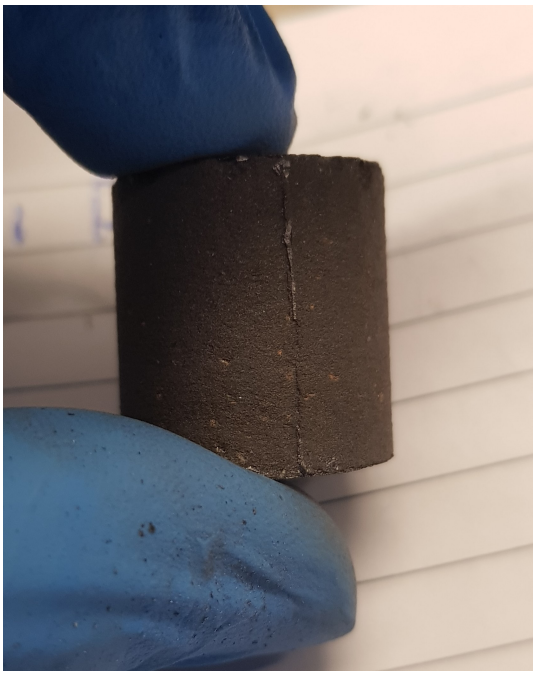

Figure 5.1: An example of a sample resulting from SPS. The sample has a size of 20 mm in diameter and about 20 mm in height.

5.1. Compressive Strength

To find the uniaxial compressive strength of the manufactured material, all samples were tested in uniaxial compression. Group-1 was tested with a different device compared to group-2, because the latter proved to be too strong for the compressive test bench of group-1. The implications thereof are stated in Chapter 3. All strength values are reported as the corrected strength, as is discussed in Chapter 3.7. In graphs, strength values are also reported as a Mars-equivalent strength. This is further explained in Chapter 3.7. Measurement results for strength, density and compaction are presented in Table 5.1. All samples had a sufficient hourglass failures shape, see Figure 5.2. This indicates that the failure mechanism was sufficient for compressive testing.

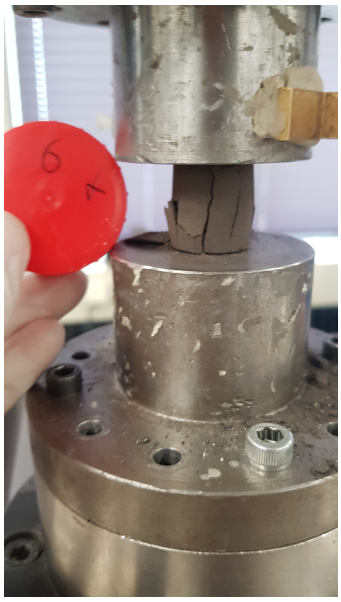

(a) Visible cracks after failure in compressive loading. The crack pattern is expected.

(b) An example of an hourglass failure shape after compressive testing. This is the bottom part.

Figure 5.2: Examples of failure in compressive testing. (a) shows the crack pattern at failure. (b) shows the resulting material after removal.

Table 5.1: Measurement results for strength, density and compaction. For an overview of variables used for every sample, see Chapter 3.6.

Sample	**Strength** (MPa)	**Density** (kg/m^3)	**Compaction** (%)
1	15.40	2309	0.18
2	6.79	2217	0.14
3	0.01	1860	0.04
4	8.29	2131	0.15
5	1.32	1950	0.05
6	2.75	2069	0.11
7	9.22	1815	0.13
8	17.30	1974	0.22
9	6.03	1801	0.13
10	111.49	2426	0.38
11	105.19	2109	0.44
12	23.04	2059	0.23
13	45.27	2411	0.26
14	40.73	2165	0.25
15	46.92	2478	0.25
16	102.66	2424	0.30
17	136.57	2460	0.40
18	68.75	2406	0.31
10b	124.07	2636	0.43
11b	98.13	2290	0.40

5.1.1. Relation of Strength with Density and Compression

It is common for sintering technique comparison to plot the strength versus the density [91, 122]. This generally results in a positive correlation. Density is used as an indication of sintering performance. This performance is often expressed as the measured density as a percentage of theoretical density. Figure 5.3 shows this plot for all samples. A clear positive correlation can be seen.

The data was fitted to the following curve:
$y = a \times x + b \times x^2$
Where x is 0 at the lowest density.

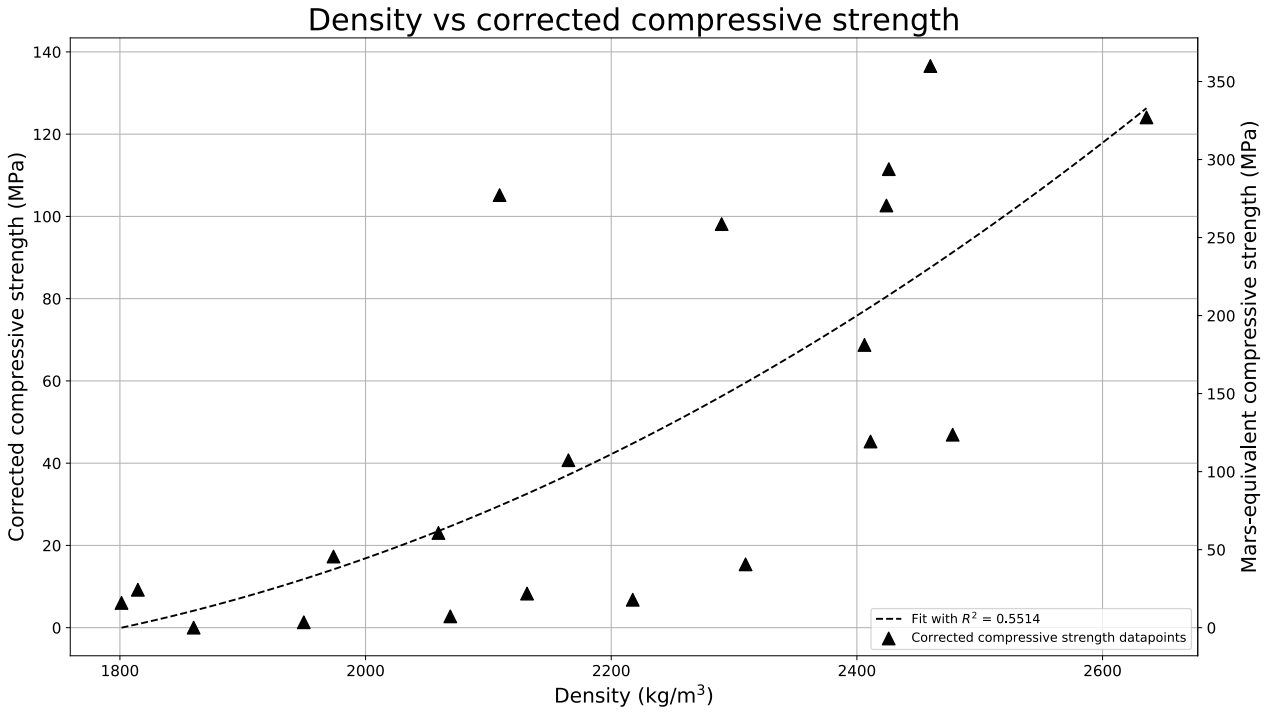

Figure 5.3: Density plotted against the corrected compressive strength, see Table 5.1. Datapoints are plotted as triangles. Strength is presented in MPa and in a Martian equivalent MPa. Compaction is presented as the percentage of compaction compared to the initial height. A second order polynomial curve is fitted with the formula: $y = a \times x + b \times x^2$. Where a and b are coefficients determined to be 0.06412 and 0.0001 respectively, as by least squares regression. The R^2 value was determined to be 0.55. This is significant enough to present correlation, but not enough to assume a correct relation. Typical sinter performance should have a positive correlation between density and strength, which was observed.

However, these plots are meant for single materials. The correlations and fitted curves should be separate for each type of material. In this thesis, two very similar materials have been used. They have been prepared by different methods, resulting in varying mineralogy for every sieve size and ball milling size. Both of these factors have made the density measurements less comparable. This, in turn, has made the strength-density plot more scattered. Therefore, this study suggest a better method to determine sintering performance. Although device specific, the most direct measurement of sintering performance is the actual compaction of the material during sintering. This has been normalised by calculating the compaction as a percentage of the initial input height. Compaction is explained more in Chapter 3.4.5 and compaction results are presented in Chapter 5.4.

The strength-compaction graph is presented in Figure 5.4. Data points are substantially less scattered compared to the strength-density graph in Figure 5.3. It can be observed that a significant fit can be made using the mentioned curve. An R^2 of 0.91 is close to a true relation. These results show that for a single type of sintering device, compaction is a better method of measuring sintering performance than density. It is applicable throughout variations of input material.

5.1.2. Group-1

Results after analysing the Taguchi design for group-1, are presented in Figure 5.5. The variables can be indicated from most to least influential as: pressure, temperature, particle size and time. From Table 5.1, it can be noted that sample 3 had an almost zero strength. This is due to the sample breaking while the machine attempted to make contact. A compressive strength of 0.001 MPa was applied at the time.

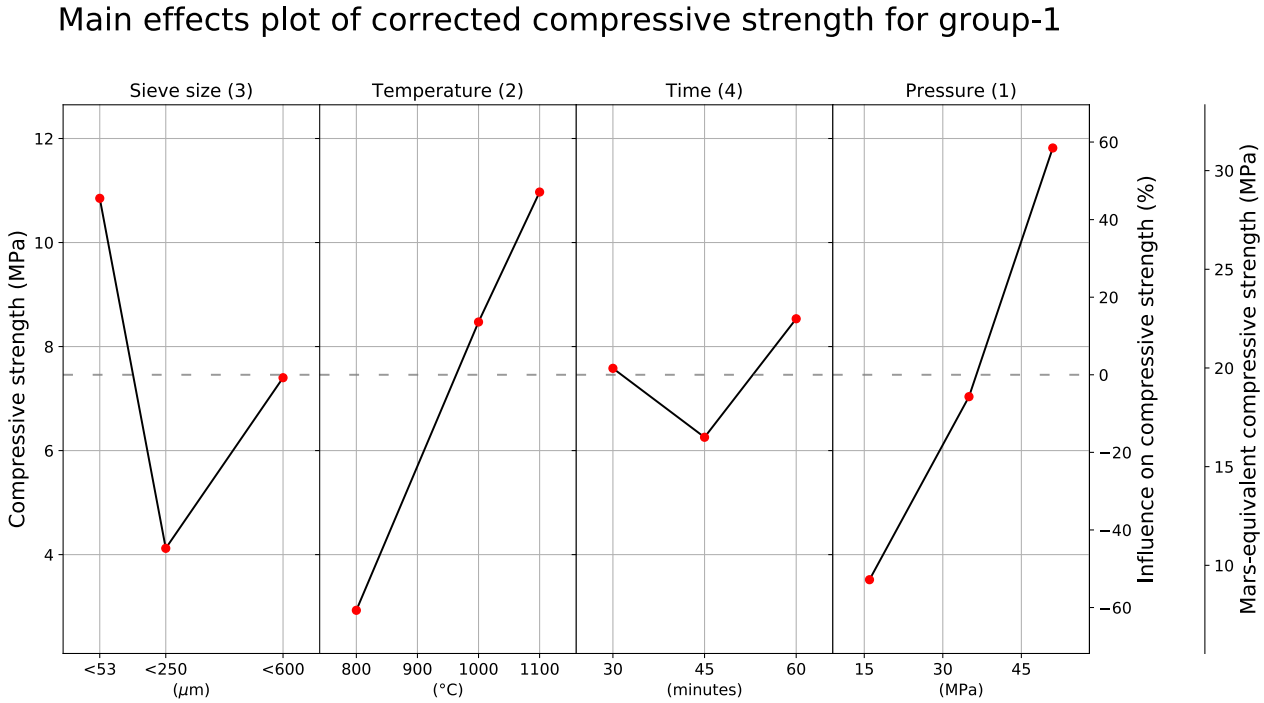

Figure 5.5: Compressive stength respective to each variable and variable level. The dotted grey line indicates the mean strenght. Measurement values are in MPa. The mean corrected compressive strength was 7.46 MPa. The numbers in brackets after the variable name indicate the rank of influence, from most influential (1), to least influential (4). On the left side, the strength is presented as corrected measurements. On the right side, the equivalent Martian strength is presented. The use thereof is explained in Chapter 3.7 The values are Taguchi deconvoluted values from the real measured values. Each dot does not indicate an individual measurement, but the average of three measurements. The values represent the values to be obtained, if only that variable was changed compared to the mean. The straight connected lines indicate linear interpolation. In reality, the true relation can differ. A higher strength can be obtained by taking the best-performing level of each variable. This is also visible in Table 5.2

Table 5.2: Strength values of the analysed Taguchi design, as plotted in 5.5. Values are in MPa, except for rank, which has no unit. The delta row indicates the difference between the maximum and minimum value for each column. This value is used to determine the rank. The rank indicates the variable with the most influence on the results, e.g. the largest delta. The level column indicates the set level of each variable from 1 to 3. For sieve size this is <53 µm, <250 µm and <600 µm respectively. For temperature this is 800 °C, 1000 °C and 1100 °C respectively. For time this is 30 minutes, 45 minutes and 60 minutes respectively. For pressure this is 16 MPa, 35 MPa and 51 MPa respectively.

Level	Sieve size	Temperature	Time	Pressure
1	10.85	2.93	7.58	3.52
2	4.12	8.47	6.26	7.04
3	7.40	10.97	8.53	11.82
Delta	6.73	8.04	2.28	8.30
Rank	3	2	4	1

Sieve size has a complex influence on uniaxial compressive strength. The smallest sieve size resulted in the greatest strengths. Instead of a single trend, the strength is lowest for the middle sieve size bracket of <250 µm, at an average strength of 4.12 MPa. While a sieve size of <600 µm resulted in near average strength of 7.40 MPa. The best average strength was achieved by using a <53 µm sieve size, resulting in 10.85 MPa. It is the third largest factor for compressive strength in group-1, with a delta of 6.73 MPa.

Temperature has the second largest influence on strength, with a delta of 8.04 MPa. The results show a linear and positive influence, which was expected. An influence of 0.0268 MPa, or 0.36% average strength

per °C was measured. A test run performed with a temperature of 700 °C confirmed that using too low temperatures results in almost zero strength. It was breakable by touch and not safely transportable. The weak characteristics of samples sintered at 800 °C resulted in only 1000 °C and 1100 °C being tested in group-2.

Time had an unexpected influence with no clear trend. Increasing sintering time from 30 to 45 minutes lowers the strength on average with 1.32 MPa, or 17.7%. A further increase to 60 minutes does increase the strength again to above the strength of a 30 minute run, at 8.53 MPa. With a delta of 2.28 MPa, sintering duration has the least influence on strength.

The applied pressure has the largest influence on the strength, with a delta of 8.30 MPa. The influence of pressure is positive and almost linear. Assuming linearity, the strength increased by 0.24 MPa, or 3.18% of the average, per MPa of pressure applied. A positive effect was expected. The significant influence resulted in the choice for higher applied pressures for group-2.

5.1.3. Group-2

Results after analysing the Taguchi design for group-2, are presented in Figure 5.6. The variables can be indicated from most to least influential as: pressure, temperature, grain size and time. The mean strength was 77.17 MPa, a 10-fold increase from group-1. Individual results are presented in Table 5.1.

Table 5.3: Strength values of the analysed Taguchi design, as plotted in 5.6. Values are in MPa, except for rank, which has no unit. The delta row indicates the difference between the maximum and minimum value for each column. This value is used to determine the rank. The rank indicates the variable with the most influence on the results, e.g. the largest delta. The level column indicates the set level of each variable from 1 to 2. For simulant this is MGS-1 and JEZ-1 respectively. For method this is ball milling and sieving respectively. For pressure this is 51 MPa and 80 MPa respectively. For particle size this is <53 µm and <250 µm respectively. For coating this is no coating and a BN coating respectively. For temperature this is 1000 °C and 1100 °C respectively. For drying this is dry and non-dry respectively.

Level	Simulant	Method	Pressure	Particle size	Coating	Temperature	Drying
1	54.47	81.72	61.40	90.10	72.62	52.21	82.65
2	99.87	72.63	92.95	64.25	81.72	102.14	71.70
Delta	45.40	9.09	31.55	25.85	9.10	49.94	10.95
Rank	2	7	3	4	6	1	5

Simulant of type JEZ-1 yields significantly higher strengths than MGS-1. With an increase of 45.40 MPa, 59% of the mean and an absolute increase of 83% compared to MGS-1, this is the second most influential factor. A difference between simulant types was expected. These results show that, for strength, it is better to use material from locations on Mars with soil characteristics similar to JEZ-1.

Ball milling also resulted in higher average strength of 9.09 MPa, or 12%, compared to sieving. However, this variable had the least influence of all variables.

The even higher application of pressure, compared to group-1, still results in a rise of strength of 31.55 MPa, or 40.88% of the mean. Assuming linearity, this is an increase of 1.41 MPa, or 1.09% of the mean, per MPa of applied pressure. In absolute terms, this is more than for group-1, but in relative percentages, it is less.

A larger particle size resulted lower strength of 25.85 MPa, or 33.5% of the mean. This is less than the results from group-1, where the difference between a <53 µm and <250 µm particle size was 90% of the mean. This is an average trend, it cannot be said for certain that this value is the same for both ball milled and sieved samples.

Applying a BN coating resulted in strengths that were 9.10 MPa higher. The temperature increase from 1000 °C to 1100 °C resulted in an increase of 49.94 MPa, or 65% of the mean. This was a larger influence than in group-1, with a delta of 2.5 MPa, or 34% of the mean. Drying shows a clear benefit in compressive strength with a delta of 10.95 MPa.

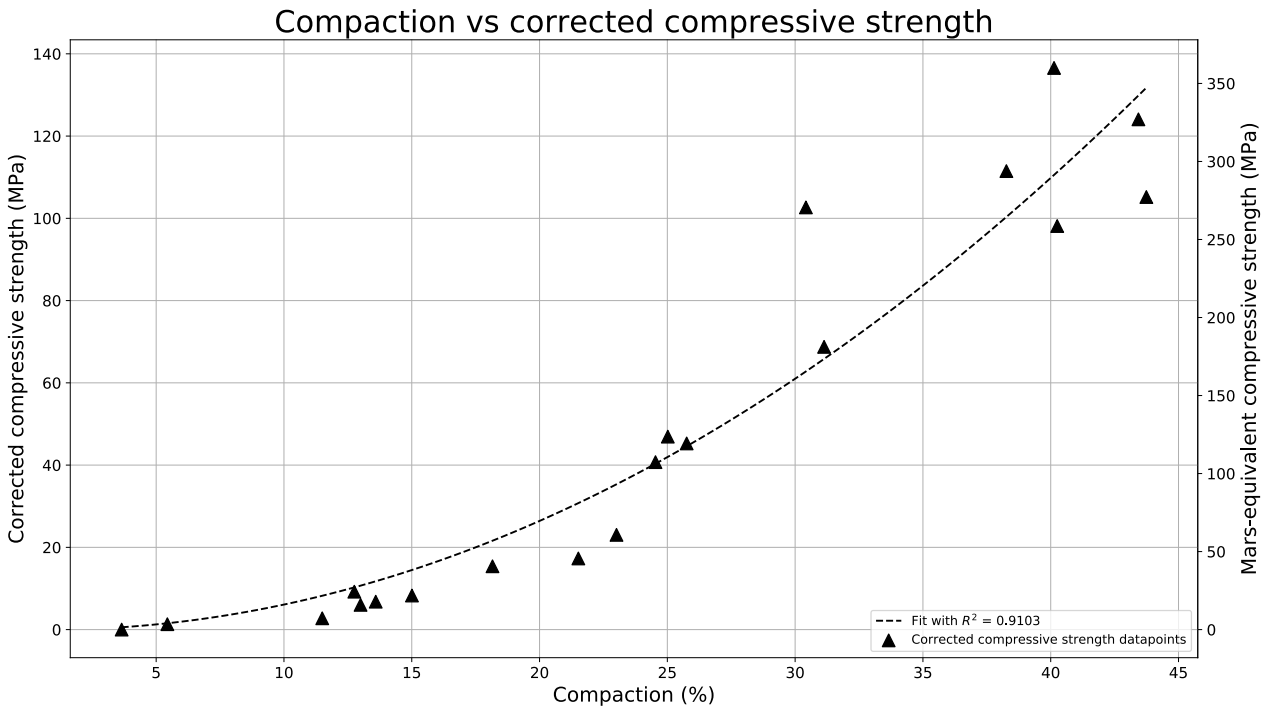

Figure 5.4: Compaction plotted against the corrected compressive strength, see Table 5.1. Datapoints are plotted as triangles. Strength is presented in MPa and in a Martian equivalent MPa. Compaction is presented as the percentage of compaction compared to the initial height. A second order polynomial curve is fitted with the formula: $y = a \times x + b \times x^2$. Where a and b are coefficients determined to be -0.1034 and 0.0712 respectively, as by least squares regression. The R^2 value was determined to be 0.91. This is significant enough to present correlation and also suggest a true relation.

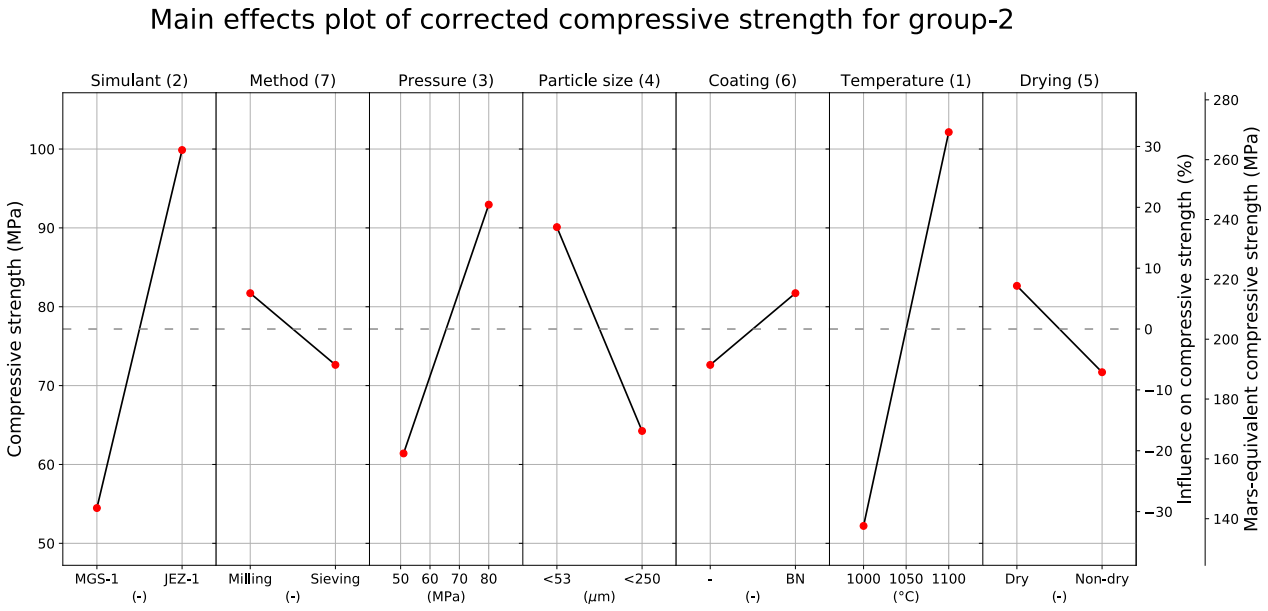

Figure 5.6: Compressive strength respective to each variable and variable level. The dotted grey line indicates the mean compressive strength. Measurement values are in MPa. The mean corrected compressive strength was 77.17 MPa. The numbers in brackets after the variable name indicate the rank of influence, from most influential (1), to least influential (7). On the left side, the strength is presented as corrected measurements. On the right side, the equivalent Martian strength is presented. The use thereof is explained in Chapter 3.7

The values are Taguchi deconvoluted values from the real measured values. Each dot does not indicate an individual measurement, but the average of four measurements. The values represent the values to be obtained, if only that variable was changed compared to the mean. The straight connected lines indicate linear interpolation. In reality, the true relation can differ. A higher strength can be obtained by taking the best-performing level of each variable. This is also visible in Table 5.3

5.2. Density

To find the density of the manufactured material, all samples were weighed and measured in volume. The mean density of all samples was 2200 kg/m^3. Individual measurements are presented in Table 5.1.

5.2.1. Group-1

Density results after analysing the Taguchi design for group-1, are presented in Figure 5.7. From most to least influential, as indicated by the number in brackets behind each variable name, the variables were: particle size, pressure, temperature and time. The mean density was 2014.1 kg/m^3.

Particle size had the largest influence on density, with a delta of 265.7 kg/m^3. It was expected that a smaller particle size would lead to a higher density, thus a negative correlation. The results show a positive correlation. This means that taking a larger sieve size resulted in higher densities after sintering. It does not necessarily mean that a larger particles size resulted in better sintering, as the mineralogy, packing and other properties were also changed due to sieving.

The second largest influence was the applied pressure, with a delta of 242.6 kg/m^3. The influence of pressure is almost linear, but does seem to follow a curve with a limit.

After this, temperature has an influence delta of 175 kg/m^3. Its effect appeared to be linear, suggesting higher temperatures could be preffered. Due to meltout problems at higher temperatures, the applied maximum temperature of 1100 °C is the effective maximum temperature.

Time has an unexpected, near-zero influence in the density. A decrease in density at longer sintering times is suggested. With a delta of only 45.2 kg/m^3, its influence was small.

5.2.2. Group-2

Results after analysing the Taguchi design for group-2, are presented in Figure 5.8. The variables can be indicated from most to least influential as: temperature, pressure, coating, particle size, drying, method and lastly the simulant type. The mean density was 2324.8 kg/m^3.

Simulant of type JEZ-1 yields marginally higher densities, 44.56 kg/m^3, than MGS-1. Ball milling also results in higher average densities with a delta of 32.72 kg/m^3.

The even higher application of pressure still results in a rise of density of 183.06 kg/m^3. This rise is proportionally almost equal to the total rise of 242.6 kg/m^3 from 16 to 51 MPa in group-1. It must be said that these results cannot directly be compared in terms of absolute values due to their differing process variables.

A larger grain size still results in larger densities of about 114.23 kg/m^3 from a sieve size of <53µm to <250µm. This is not consistent with a rise of 186.79 kg/m^3 for group-1. This is an average trend, so it cannot be said for certain that this is also the case for ball milled samples.

Applying a BN coating resulted in a rise in density of 88.62 kg/m^3. The temperature increase from 1000 °C to 1100 °C has had a larger influence than in group-1, with a delta of 234.60 kg/m^3, compared to only 38.13 kg/m^3 for group-1. Drying shows a clear benefit in acquired density with a delta of 85.67 kg/m^3.

5.2.3. Density Distribution

Figure 5.9 shows the density distribution of the sample height as a result of the CT scans. It can be noted that for most samples (1,2,4,6,7 and 8), the density is lower in the middle than on the top and bottom. For some samples (4, 7 and 8) the density is very unevenly distributed. These samples show a higher density at the bottom, sample 7, compared to the top or vice-versa, samples 4 and 8.

Results show two small dips at around 4.5 mm height in all samples. This is due to the nature of the CT-scanner. As indicated in 5.11, bands form due to the deconvolution process. These bands have a minimal influence on the results and overall trends should still be visible. These bands are also present at roughly the same locations for each sample, making them comparable.

Figure 5.10 shows the density distribution along the radial profile of the samples. An increase in density at the edges was expected, but it cannot be concluded for certain that it is the case. The increase along the edge, at around 10mm radius, can at least partially be attributed to CT-scanning and deconvolution issues. However, there is a visible downwards trend in all samples from the centre to the edges. This means that the centre of the sample is more dense than the edges.

The colours indicate the sieve size. Blueish indicates a sieve size of <600 µm. Yellow to reddish indicates a sieve size of <250 µm. Greenish indicates a sieve size of <53 µm. It was noted that the results are unintentionally grouped by sieve size. This is the case in both the height and radial profiles.

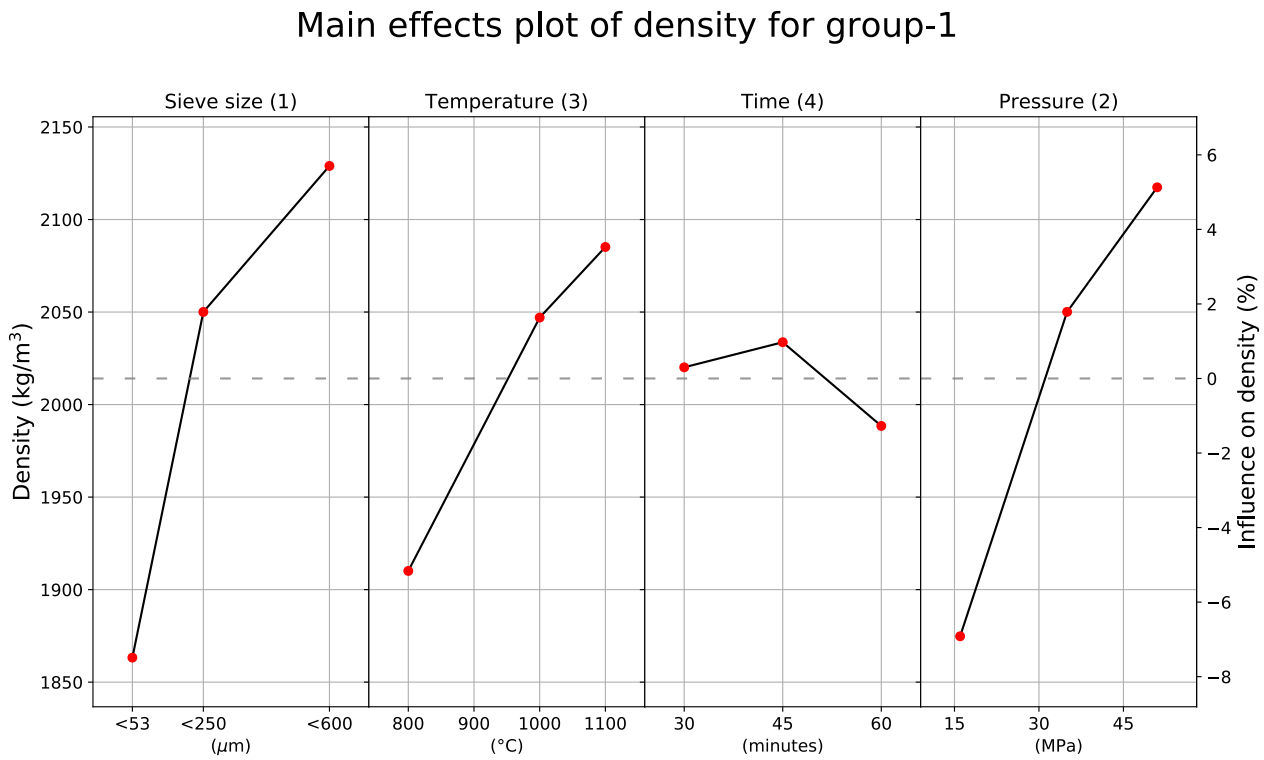

Figure 5.7: Density results respective to each variable and variable level. The dotted grey line indicates the mean density. Measurement values are in kg/m^3. The mean density was 2014.1 kg/m^3. The numbers in brackets after the variable name indicate the rank of influence, from most influential (1), to least influential (4).
The values are Taguchi deconvoluted values from the real measured values. Each dot does not indicate an individual measurement, but the average of three measurements. The values represent the values to be obtained, if only that variable was changed compared to the mean. The straight connected lines indicate linear interpolation. In reality, the true relation can differ. A higher density can be obtained by taking the best-performing level of each variable. This is also visible in Table 5.4

Table 5.4: Density values of the analysed Taguchi design, as plotted in 5.7. Values are in kg/m^3, except for rank, which has no unit. The delta row indicates the difference between the maximum and minimum value for each column. This value is used to determine the rank. The rank indicates the variable with the most influence on the results, e.g. the largest delta. The level column indicates the set level of each variable from 1 to 3. For sieve size this is <53 µm, <250 µm and <600 µm respectively. For temperature this is 800 °C, 1000 °C and 1100 °C respectively. For time this is 30 minutes, 45 minutes and 60 minutes respectively. For pressure this is 16 MPa, 35 MPa and 51 MPa respectively.

Level	Sieve size	Temperature	Time	Pressure
1	1863.27	1910.11	2020.13	1874.79
2	2050.06	2047.03	2033.70	2050.09
3	2128.97	2085.16	1988.46	2117.41
Delta	265.69	175.05	45.24	242.62
Rank	1	3	4	2

Table 5.5: Density values of the analysed Taguchi design, as plotted in 5.8. Values are in kg/m^3, except for rank, which has no unit. The delta row indicates the difference between the maximum and minimum value for each column. This value is used to determine the rank. The rank indicates the variable with the most influence on the results, e.g. the largest delta. The level column indicates the set level of each variable from 1 to 2. For simulant this is MGS-1 and JEZ-1 respectively. For method this is ball milling and sieving respectively. For pressure this is 51 MPa and 80 MPa respectively. For particle size this is <53 µm and <250 µm respectively. For coating this is no coating and a BN coating respectively. For temperature this is 1000 °C and 1100 °C respectively. For drying this is dry and non-dry respectively.

Level	Simulant	Method	Pressure	Particle size	Coating	Temperature	Drying
1	2343.10	2381.74	2273.85	2308.27	2321.07	2248.08	2408.22
2	2387.66	2349.02	2456.91	2422.49	2409.69	2482.68	2322.54
Delta	44.56	32.72	183.06	114.23	88.62	234.60	85.67
Rank	6	7	2	3	4	1	5

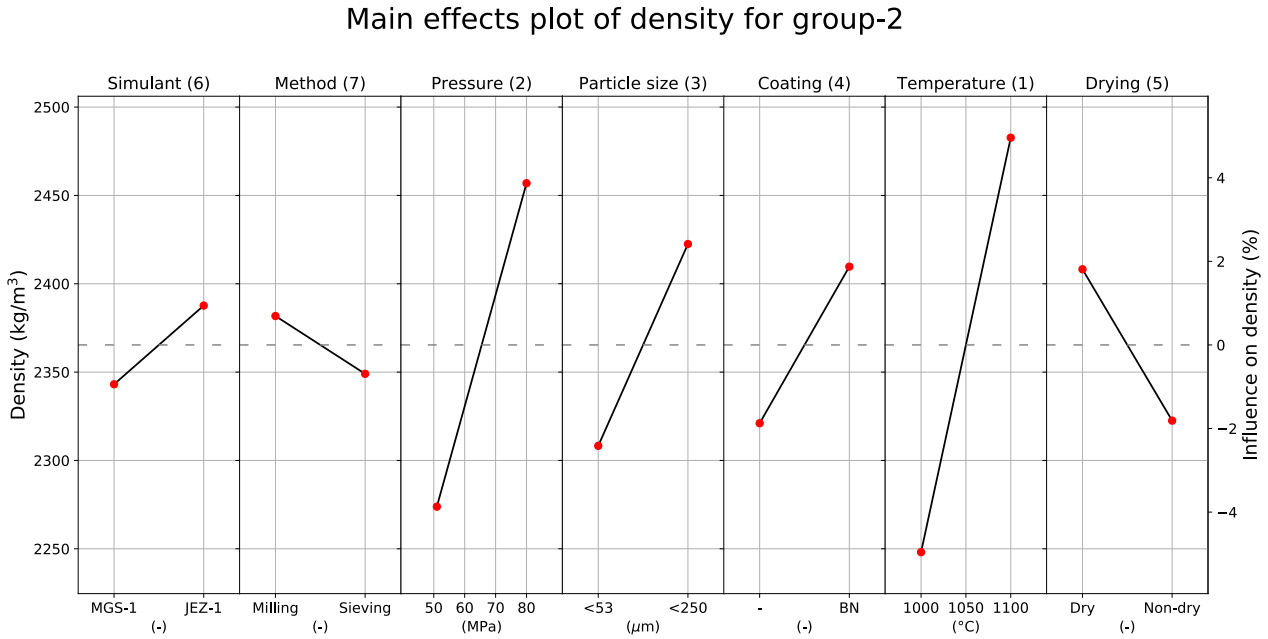

Figure 5.8: Density results respective to each variable and variable level. The dotted grey line indicates the mean density. Measurement values are in kg/m^3. The mean density was 2365.38 kg/m^3. The numbers in brackets after the variable name indicate the rank of influence, from most influential (1), to least influential (7).
The values are Taguchi deconvoluted values from the real measured values. Each dot does not indicate an individual measurement, but the average of four measurements. The values represent the values to be obtained, if only that variable was changed compared to the mean. The straight connected lines indicate linear interpolation. In reality, the true relation can differ. A higher density can be obtained by taking the best-performing level of each variable. This is also visible in Table 5.5

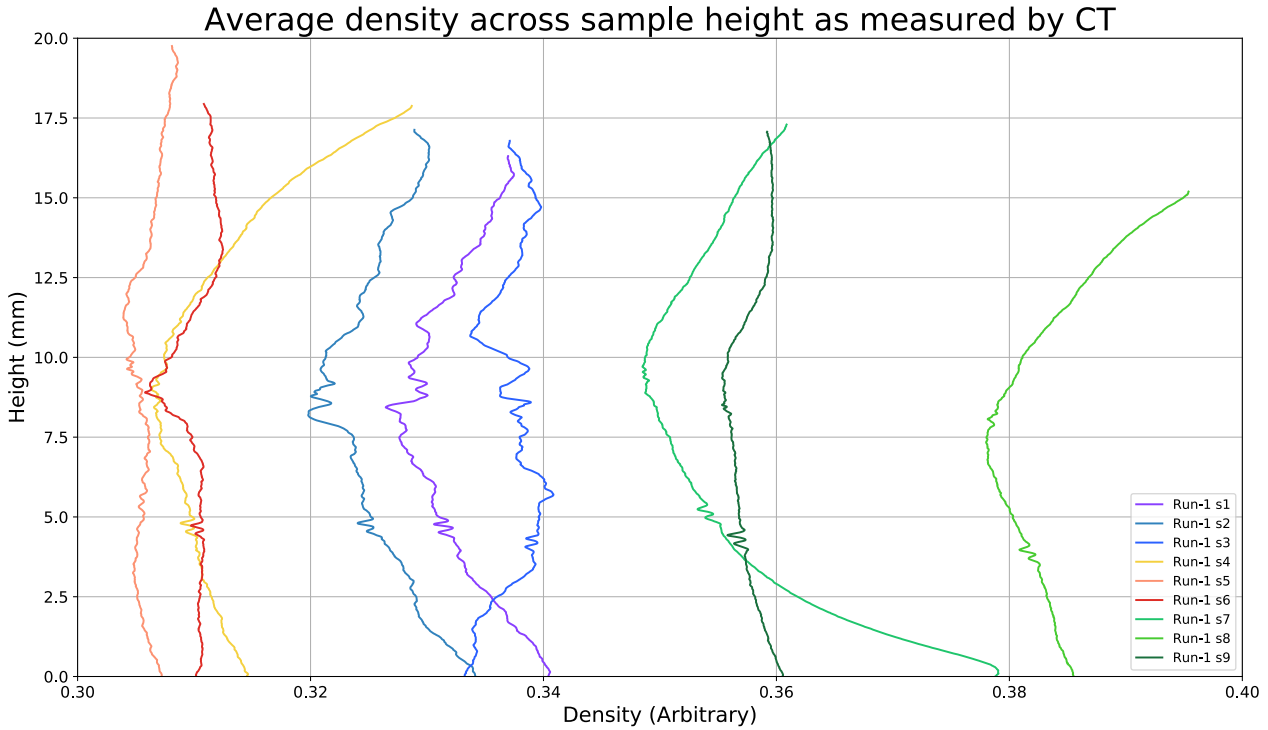

Figure 5.9: The density distribution across the height of the sample. Calculated as the average of each slice of the measured CT data. CT data pixel values were normalised according to maximum detectable pixel value and peak height of the surrounding air. The resulting values are the averages of the intensities of pixel values at every slice.
The colour type indicates the sieve size used for the respective sample, which is the most determining parameter for CT macro porosity. Blueish indicates a sieve size of <600 µm. Yellow to reddish indicates a sieve size of <250 µm. Greenish indicates a sieve size of <53 µm. At around 4.5 mm, a certain double peak pattern is present in every plot. This is the result of CT processing artefacts.

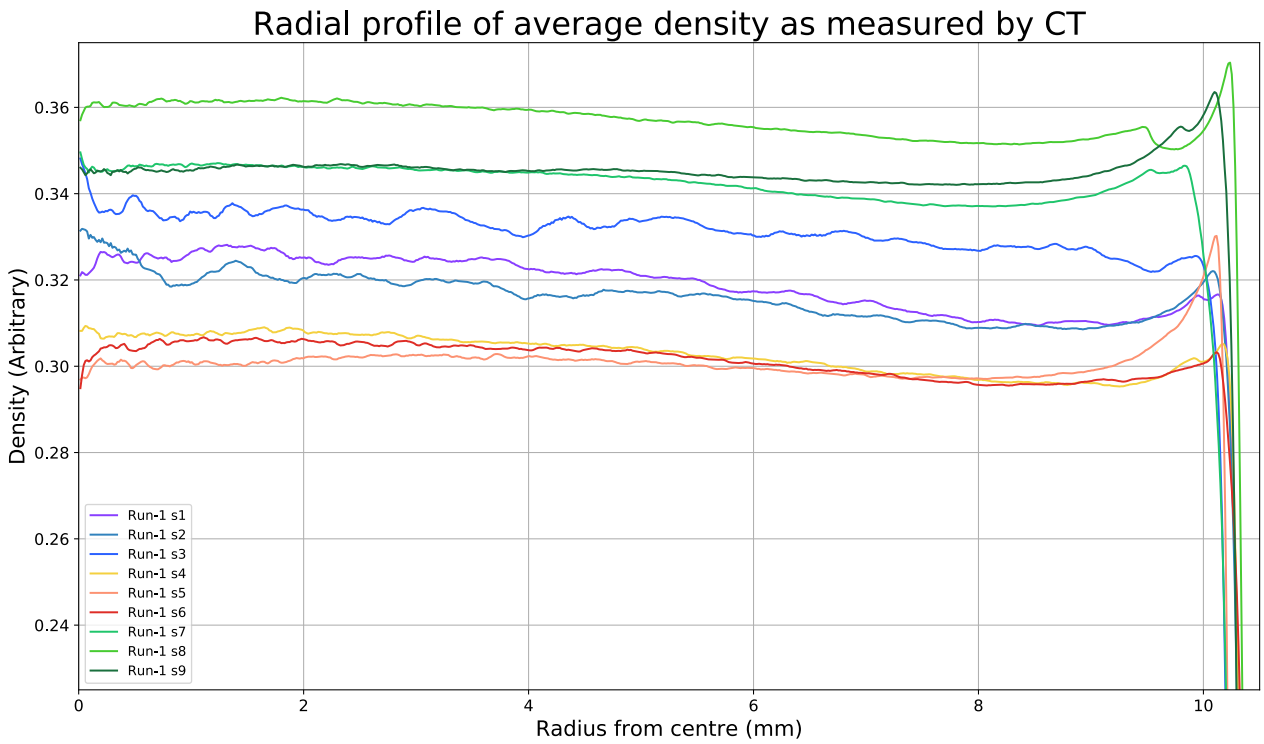

Figure 5.10: The density distribution across the radius of the sample. Calculated as the average across the height of the sample, averaged across a 360°rotating angle for each discrete distance to the centre. CT data pixel values were normalised according to maximum detectable pixel value and peak height of the surrounding air.
The colour type indicates the sieve size used for the respective sample, which is the most determining parameter for CT macro porosity. Blueish indicates a sieve size of <600 µm. Yellow to reddish indicates a sieve size of <250 µm. Greenish indicates a sieve size of <53 µm. At around 10 mm, an increase is detected and a sudden drop. This drop indicates the edge of the sample. The peak is due to CT processing artefacts.

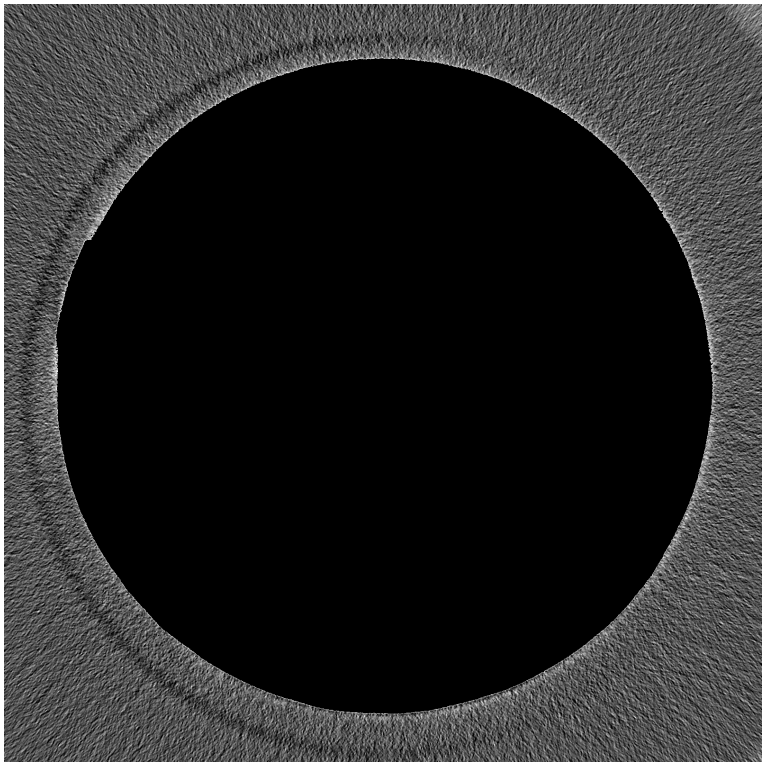

Figure 5.11: An example to the reason of the dips at 4.5 mm. The sample itself has been coloured black. The dip is created by the darker halo surrounding the sample, mainly at the left side. This halo slowly approaches the sample when scrolling through its height. When it touches the sample, the average values are lowered at the edges, resulting in the visible dips.

5.3. Macro Porosity

The macro porosity data as a result of CT scans is presented in Table 5.6. As the minimal detectable pore volume from CT was 0.0001 mm^3, equivalent to about 30 voxels with 15 micron sides, these results show macro porosity only. For the samples with a sieve size of <600 µm, significantly more macro porosity was measured. The average porosity was 0.22%. Per sieve size the average porosity was 0.00% for a sieve size of <53 µm , 0.11% for <250 µm for and 0.54% for <600 µm. Compared to a porosity for concrete of 2-4%, this is very low.

Table 5.6: Measurement results for macro porosity of group-1. Macro porosity constitutes pores that are larger than 0.0001 mm^3. For an overview of variables used for every sample, see Chapter 3.6.

Sample	**Porosity** (%)
1	0.4453
2	0.6644
3	0.5002
4	0.1062
5	0.2206
6	0.0061
7	0.0003
8	0.0000
9	0.0000

Porosity distributions for all samples are presented in Figure 5.13. The pore size bins, the x-axis logarithmic bins, are identical for all samples. The total pore volume per pore size, the y-axis, is the same for sample 1 to 3. For all other samples it differs due to differences in orders of magnitude. Sample 1 and 2 have a similar, Gaussian like, distribution. Sample 3 has a more uniform but also irregular distribution, with a relatively higher amount of small and large pores. The maximum pore size detected was 0.69 mm^3 for sample 3. Assuming perfectly spherical particles, this is 6.1 times the maximum particle size. Sample 4 and 5 have a similar pore size distributions, normally distributed. Sample 6 shows a different type of distribution, trading larger pore sizes for relatively more smaller pores. It was also noticeable that the total pore volumes were two magnitudes lower than results for similar sieve sizes, sample 4 and 5. The maximum pore size for this sieve size was 0.0011 mm^3. This is about 13.4 times the maximum particle size. Samples 7, 8 and 9 show almost no porosity. Only 31, 2 and 6 pores were detected for each sample respectively. The average pore count per sample for samples 1 to 6 was 11905 pores. The maximum detected pore sizes were 0.0085 mm^3, 0.00037 mm^3 and 0.00096 mm^3 respectively.

Porosity results after analysing the Taguchi design for group-1, are presented in Figure 5.12. The particle size was the main influence on macro porosity. At a sieve size of <53 µm, almost no macro porosity was present. At a sieve size of <250 µm, the average macro porosity increases to 0.111%. The largest jump is to a sieve size of <250 µm. At this sieve size, the average porosity is 0.537%.

Temperature variations resulted in a higher porosity at 1000 °C, while both 800 °C and 1100 °C showed similar macro porosity. The influence of time is almost zero, with a delta of only 0.02% of the total sample volume. Longer sintering times only marginally decreased porosity. An increase in pressure resulted in a decrease in macro porosity only after a pressure of 35 MPa.

Table 5.7: Porosity values of the analysed Taguchi design, as plotted in 5.12. Values are in percentages, except for rank, which has no unit. The delta row indicates the difference between the maximum and minimum value for each column. This value is used to determine the rank. The rank indicates the variable with the most influence on the results, e.g. the largest delta. The level column indicates the set level of each variable from 1 to 3. For sieve size this is <53 µm, <250 µm and <600 µm respectively. For temperature this is 800 °C, 1000 °C and 1100 °C respectively. For time this is 30 minutes, 45 minutes and 60 minutes respectively. For pressure this is 16 MPa, 35 MPa and 51 MPa respectively.

Level	**Sieve size**	**Temperature**	**Time**	**Pressure**
1	0.000	0.169	0.222	0.240
2	0.111	0.295	0.224	0.257
3	0.537	0.184	0.202	0.150
Delta	0.537	0.126	0.021	0.106
Rank	1	2	4	3

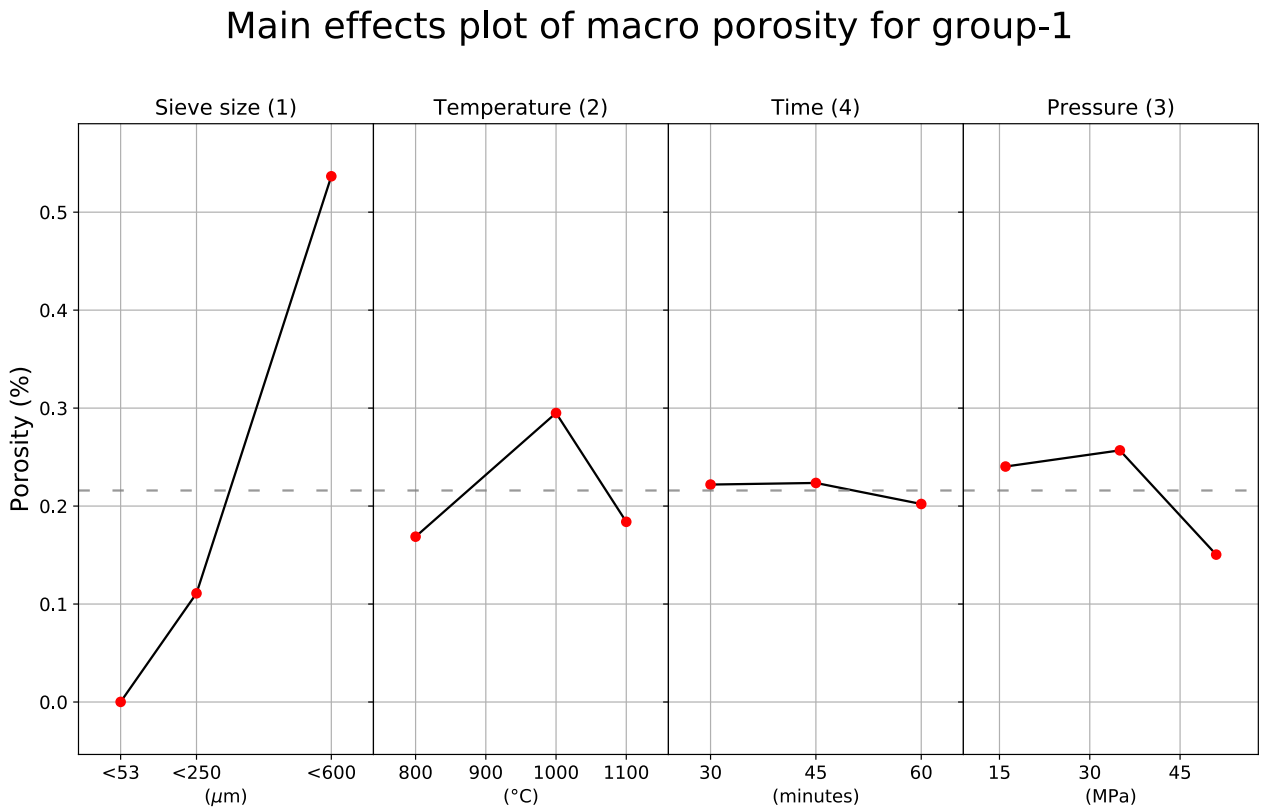

Figure 5.12: Porosity results respective to each variable and variable level. The dotted grey line indicates the mean porosity. Measurement values are in percentages. The mean porosity was 0.22%. The numbers in brackets after the variable name indicate the rank of influence, from most influential (1), to least influential (4).
The values are Taguchi deconvoluted values from the real measured values. Each dot does not indicate an individual measurement, but the average of three measurements. The values represent the values to be obtained, if only that variable was changed compared to the mean. The straight connected lines indicate linear interpolation. In reality, the true relation can differ. A lower porosity can be obtained by taking the best-performing level of each variable. This is also visible in Table 5.7

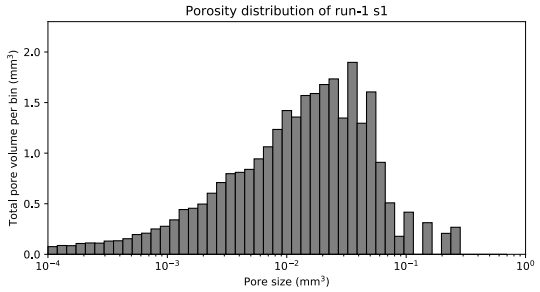

(a) Pore distribution for sample 1. A maximum pore size of 0.267 mm^3 was detected. The total porosity was 0.44%.

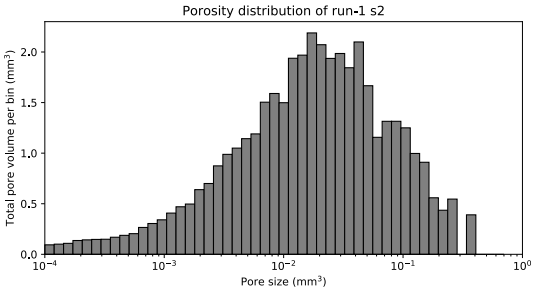

(b) Pore distribution for sample 2. A maximum pore size of 0.390 mm^3 was detected. The total porosity was 0.66%.

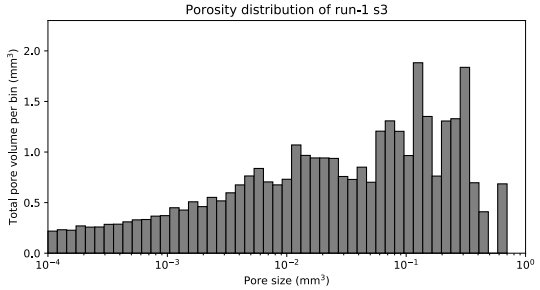

(c) Pore distribution for sample 3. A maximum pore size of 0.675 mm^3 was detected. The total porosity was 0.50%.

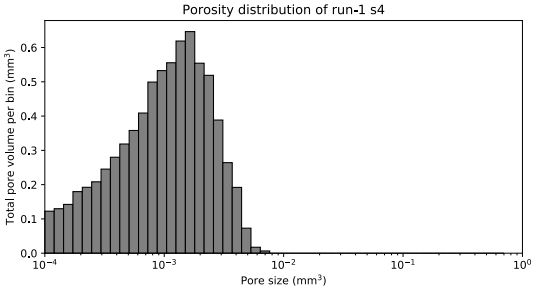

(d) Pore distribution for sample 4. A maximum pore size of 0.00656 mm^3 was detected. The total porosity was 0.11%.

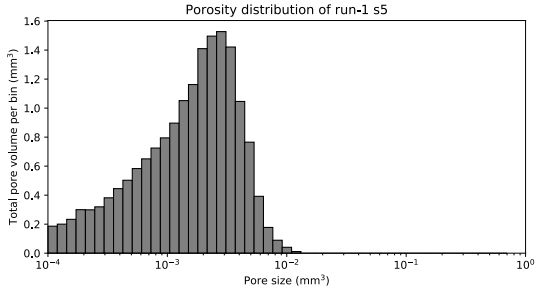

(e) Pore distribution for sample 5. A maximum pore size of 0.0113 mm^3 was detected. The total porosity was 0.22%.

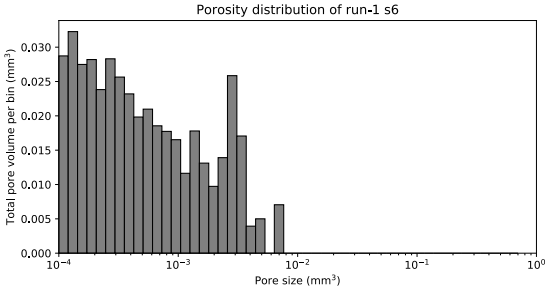

(f) Pore distribution for sample 6. A maximum pore size of 0.00705 mm^3 was detected. The total porosity was 0.0061%.

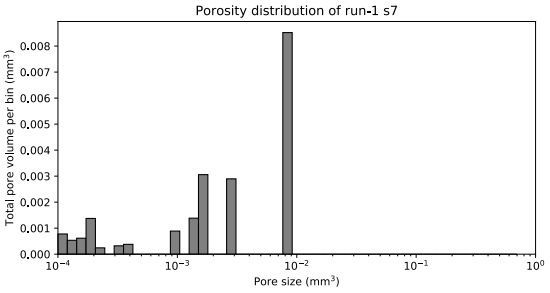

(g) Pore distribution for sample 7. A maximum pore size of 0.00852 mm^3 was detected. The total porosity was 1.38×10^{-4}%.

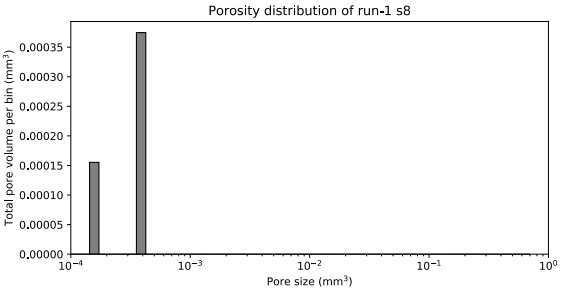

(h) Pore distribution for sample 8. A maximum pore size of 0.000375 mm^3 was detected. The total porosity was 8.67×10^{-6}%.

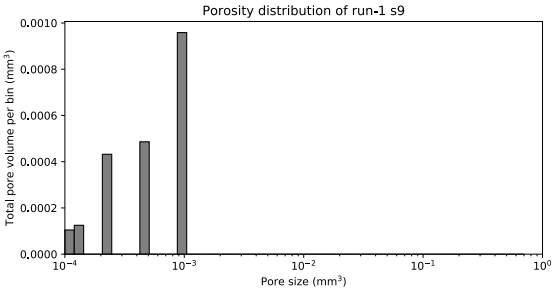

(i) Pore distribution for sample 9. A maximum pore size of 0.000958 mm^3 was detected. The total porosity was 3.98×10^{-6}%.

Figure 5.13: Porosity distribution plotted as a histogram. The x-axis indicates the pore size and is logarithmic. Similarly, the bin sizes are logarithmic. The y-axis indicates the total pore volume for each specific pore size bin. To obtain the pore volume for a larger fraction of pore sizes, e.g. all pores above 0.04 mm^3, one simply needs to add the values of all bars in the range of interest.

5.4. SPS Compaction

Compaction values in Table 5.1 are presented as percentages of the total initial height. In Chapter 5.1, the importance of SPS compaction data is elaborated on. In Figure 5.14, the compaction data from the SPS runs is presented.

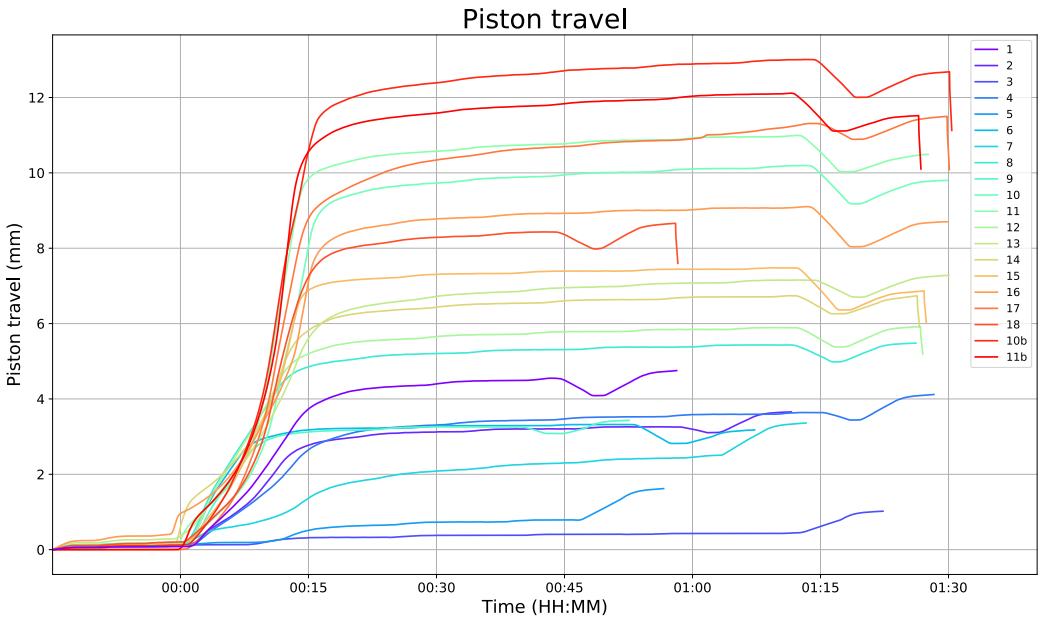

Figure 5.14: Plots of compaction of the samples during sintering. The number in the legend indicates the sample. As different runs had different lengths, some curves stop earlier. The phases of sintering and their effect on these curves is described in Chapter 5.4 and 3.4.

The initial start of sintering was subtracted from all subsequent measured values. This is at the indicated time of 00:00. This is because the previous compaction depends on non-controllable variables such as the effectiveness of the manual press and packing. At 00:00, the applied initial pressure makes sure that the samples are all compressed under similar conditions.

The initial compaction was defined as the compaction that occurred during the ramping up of the temperature and pressure. For all samples, the compaction during this phase accounts for most of the total compaction. The effects of this phase of sintering continue for a short time period. This is visible as the curve is still increasing rapidly, but at a lowering pace. An example is sample 16. It shows a decrease in speed around 00:15, but the effect still continues until about 00:17

The next phase of sintering shows compaction purely due to the sintering process. In this phase, temperature and applied pressure are constant. Compaction in this phase is minimal. Compaction is also semi-constant. It was observed that the compaction has a steady rate plus an incremental effect at regular intervals. This resulted in very small increases in compaction at regular intervals.

The next phase, at the sudden drop after a constant increase, shows the release of the applied pressure. This linear elastic effect results in a drop in compaction. The material expands due to force being released. The effect hereof is fully accounted for after the pressure has been dropped. Some samples did not have an increase in pressure, as their sintering pressure was equal to the minimum required pressure of 16 MPa. This can be seen for samples 3, 5 and 7.

Afterwards, the temperature is lowered at a fixed rate of 100 °C/min. Even though the effect of thermal expansion is linear, the measured temperature is not identical to the actual material temperature. Thus, the effect continues after the pyrometer detects the minimal temperature. The sample is then kept inside the chamber for 5 more minutes, after which the end compaction is measured. These results are indifferent of input height or input mass of material, as is described in Chapter 3.4. They represent the actual performance of sintering.

5.4.1. Group-1

Results after analysing the Taguchi design for group-1, are presented in Figure 5.15. The variables can be indicated from most to least influential as: pressure, temperature, particle size and time. Average compaction for group-1 was 12.73%.

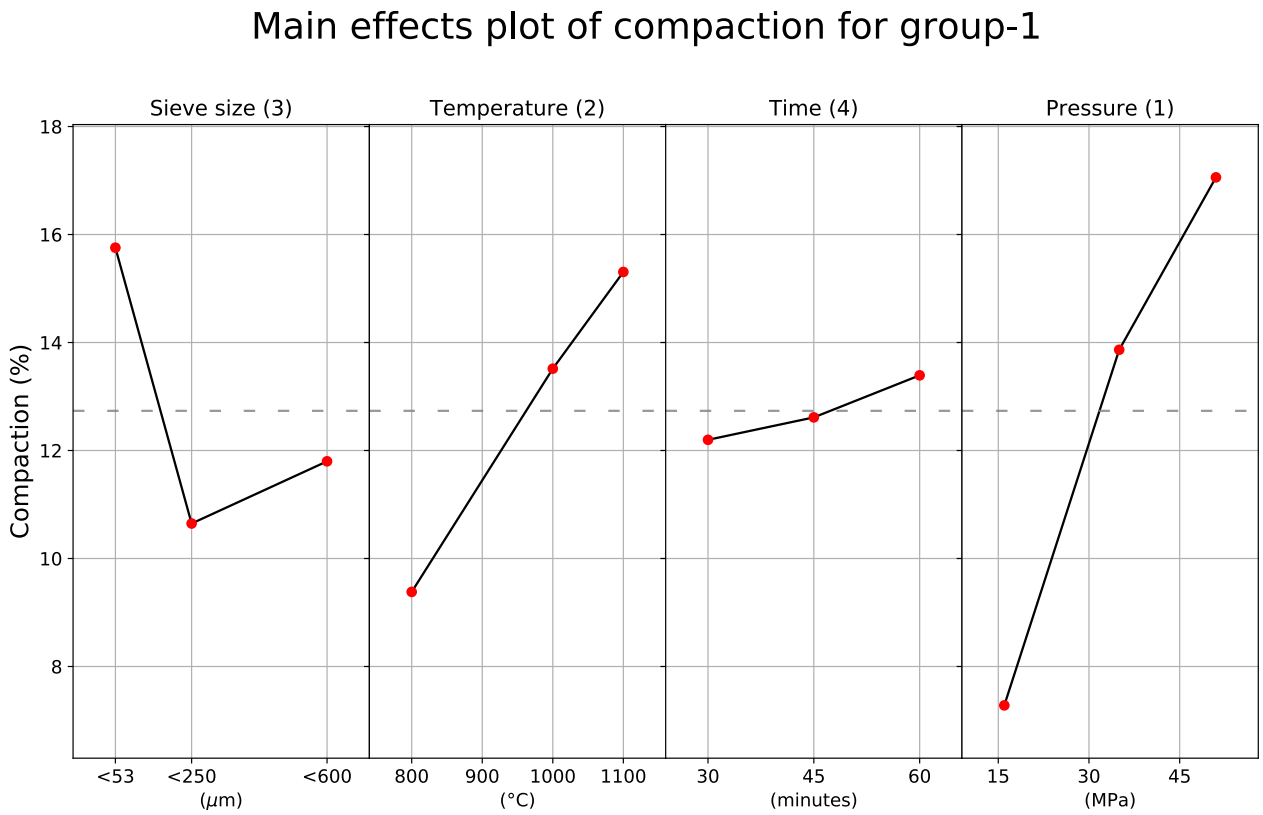

Figure 5.15: Compaction results respective to each variable and variable level. The dotted grey line indicates the mean compaction. Measurement values are in percentages. The mean compaction was 12.73%. The numbers in brackets after the variable name indicate the rank of influence, from most influential (1), to least influential (4).
The values are Taguchi deconvoluted values from the real measured values. Each dot does not indicate an individual measurement, but the average of three measurements. The values represent the values to be obtained, if only that variable was changed compared to the mean. The straight connected lines indicate linear interpolation. In reality, the true relation can differ. A higher compaction can be obtained by taking the best-performing level of each variable. This is also visible in Table 5.8

Table 5.8: Compaction values of the analysed Taguchi design, as plotted in 5.15. Values are in percentages, except for rank, which has no unit. The delta row indicates the difference between the maximum and minimum value for each column. This value is used to determine the rank. The rank indicates the variable with the most influence on the results, e.g. the largest delta. The level column indicates the set level of each variable from 1 to 3. For sieve size this is <53 µm, <250 µm and <600 µm respectively. For temperature this is 800 °C, 1000 °C and 1100 °C respectively. For time this is 30 minutes, 45 minutes and 60 minutes respectively. For pressure this is 16 MPa, 35 MPa and 51 MPa respectively.

Level	Sieve size	Temperature	Time	Pressure
1	15.76	9.38	12.20	7.28
2	10.65	13.52	12.61	13.87
3	11.80	15.31	13.39	17.06
Delta	5.11	5.93	1.19	9.78
Rank	3	2	4	1

The smallest sieve size of <53 µm resulted in 4.54 absolute percentage points more compaction than the average other sieve size. A sieve size of <600 µm resulted in more compaction than a sieve size of <250 µm.

Temperature had a linear effect on compaction. The effect was 0.0198 percentage points per °C. With a delta of 5.93 percentage points, it is the second biggest influence on compaction.

Time had a near linear influence on compaction. With a delta of 1.19 percentage points, it is the smallest effect. This effect was expected when comparing it to the data in Figure 5.14. In that figure, every SPS run

has a clear positive compaction with respect to time.

Applied pressure had the largest influence on compaction. With a delta of 9.78 percentage points, its influence is significant. The effect is nearly linear. The first section had an effect of 0.35 percentage points per MPa, the second section had an effect of 0.20 percentage points per MPa. Assuming linearity, the total effect was 0.28 percentage points per MPa.

5.4.2. Group-2

Results after analysing the Taguchi design for group-2, are presented in Figure 5.16. Average compaction for group-2 was 31.57%.

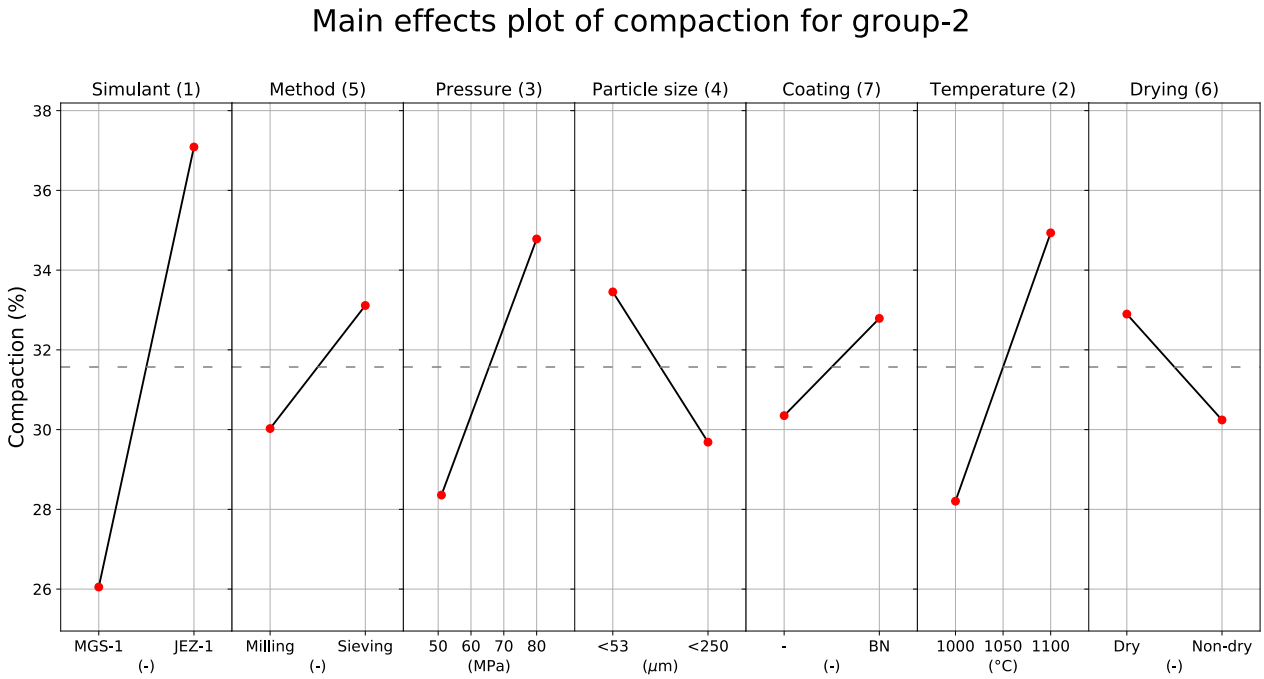

Figure 5.16: Compaction results respective to each variable and variable level. The dotted grey line indicates the mean compaction. Measurement values are in percentages. The mean compaction was 31.57%. The numbers in brackets after the variable name indicate the rank of influence, from most influential (1), to least influential (7).
The values are Taguchi deconvoluted values from the real measured values. Each dot does not indicate an individual measurement, but the average of four measurements. The values represent the values to be obtained, if only that variable was changed compared to the mean. The straight connected lines indicate linear interpolation. In reality, the true relation can differ. A higher compaction can be obtained by taking the best-performing level of each variable. This is also visible in Table 5.9

Table 5.9: Compaction values of the analysed Taguchi design, as plotted in 5.16. Values are in percentages, except for rank, which has no unit. The delta row indicates the difference between the maximum and minimum value for each column. This value is used to determine the rank. The rank indicates the variable with the most influence on the results, e.g. the largest delta. The level column indicates the set level of each variable from 1 to 2. For simulant this is MGS-1 and JEZ-1 respectively. For method this is ball milling and sieving respectively. For pressure this is 51 MPa and 80 MPa respectively. For particle size this is <53 µm and <250 µm respectively. For coating this is no coating and a BN coating respectively. For temperature this is 1000 °C and 1100 °C respectively. For drying this is dry and non-dry respectively.

Level	Simulant	Method	Pressure	Particle size	Coating	Temperature	Drying
1	26.05	30.03	28.36	33.45	30.35	28.20	32.90
2	37.09	33.11	34.78	29.69	32.79	34.93	30.24
Delta	11.04	3.09	6.42	3.77	2.44	6.73	2.66
Rank	1	5	3	4	7	2	6

Simulant JEZ-1 was most susceptible to compaction. The simulant type is the most important factor for compaction with a delta of 11.04 percentage points.

Sieving resulted in more compaction compared to ball milling. This result is the exactly opposite to density results in Figure 5.8 and strength results in Figure 5.6.

Applied pressure was still an important parameter, even at increased pressures. The delta of 6.42 percentage points is similar to the 6.59 percentage point increase due to a pressure increase from 16 to 35 MPa in group-1. The compaction increase per MPa of pressure increase was 0.22 percentage point per MPa. This is similar to the trend of 35 to 51 MPa from group-1, which had a 0.20 percentage point increase per MPa.

Decreasing the particle size increased compaction by an average of 3.77 percentage point. This is less compared to the purely sieved samples of group-1, which had a 5.11 percentage point increase from <250 µm to <53 µm sieve size.

The application of a BN coating increased compaction by 2.44 percentage points. Increasing the temperature from 1000 to 1100 °C, increased compaction with 6.73 percentage points. This is more than the increase in group-1 of 1.79 percentage point. Drying the material before sintering had a positive effect of 2.66 percentage points of compaction.

5.5. Mass Loss

Individual mass loss results are presented in Table 5.10. The percentage of mass loss proved an important factor. Mass loss is defined as the percentage of mass that was lost during sintering, compared to the initial input mass.

Table 5.10: Measurement results for mass loss. Measurements are in percentages of the initial mass.

Sample	**Mass loss** (%)
1	3.23
2	4.09
3	3.54
4	4.31
5	3.59
6	3.99
7	4.92
8	5.25
9	6.66
10	14.74
11	20.64
12	6.54
13	4.45
14	14.72
15	3.42
16	8.61
17	15.76
18	12.06
10b	16.06
11b	22.22

5.5.1. Group-1

Results after analysing the Taguchi design for group-1, are presented in Figure 5.17. The variables can be indicated from most to least influential as: pressure, temperature, particle size and time. Average mass loss for group-1 was 4.40%.

Table 5.11: Mass loss values of the analysed Taguchi design, as plotted in 5.17. Values are in percentages, except for rank, which has no unit. The delta row indicates the difference between the maximum and minimum value for each column. This value is used to determine the rank. The rank indicates the variable with the most influence on the results, e.g. the largest delta. The level column indicates the set level of each variable from 1 to 3. For sieve size this is <53 µm, <250 µm and <600 µm respectively. For temperature this is 800 °C, 1000 °C and 1100 °C respectively. For time this is 30 minutes, 45 minutes and 60 minutes respectively. For pressure this is 16 MPa, 35 MPa and 51 MPa respectively.

Level	**Sieve size**	**Temperature**	**Time**	**Pressure**
1	5.61	4.73	4.49	4.02
2	3.96	4.31	4.34	5.02
3	3.62	4.15	4.37	4.16
Delta	1.99	0.58	0.16	1.00
Rank	1	3	4	2

Mass loss is most prominently apparent at lower sieve sizes. The jump of 1.65 percentage points between a sieve size of <53 µm and <250 µm, constitutes a significant part of the total delta of 1.99 percentage points.

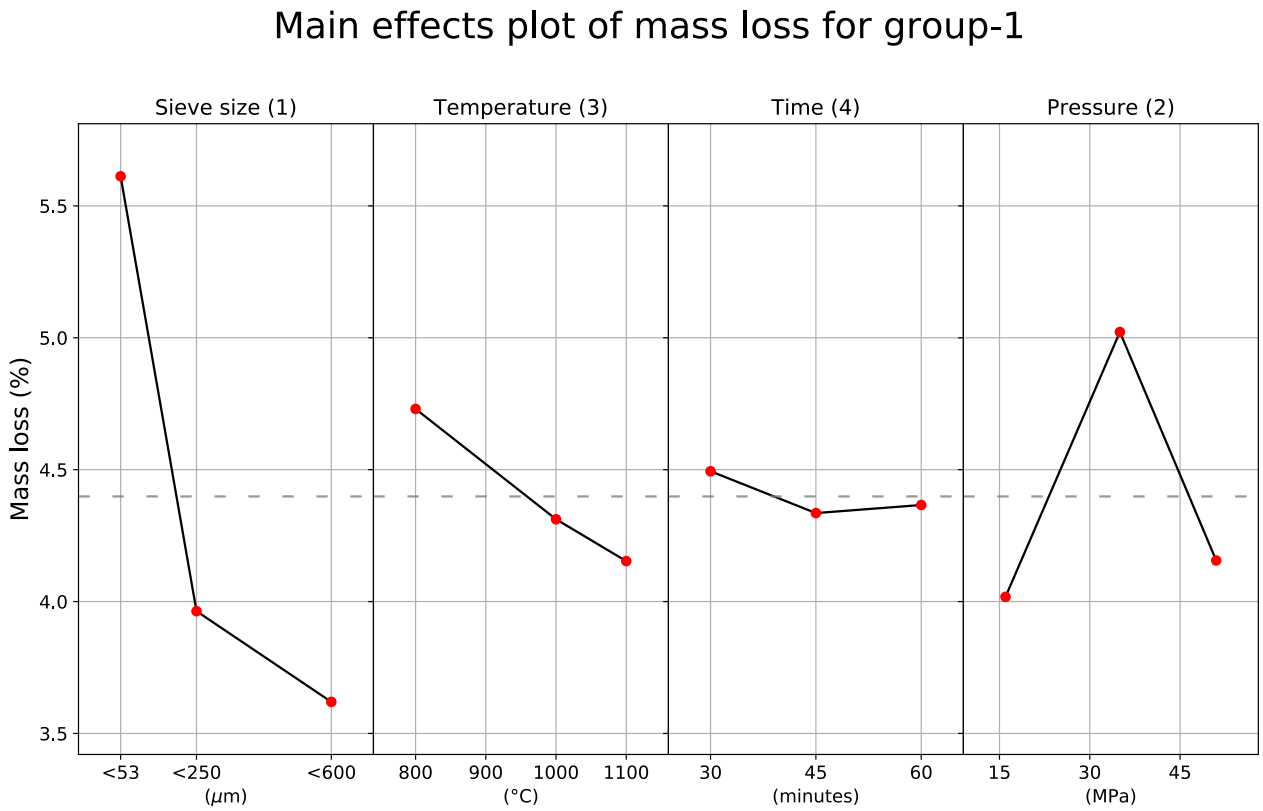

Figure 5.17: Mass loss respective to each variable and variable level. The dotted grey line indicates the mean mass loss. Measurement values are in percentages. The mean mass loss was 4.40%. The numbers in brackets after the variable name indicate the rank of influence, from most influential (1), to least influential (4).
The values are Taguchi deconvoluted values from the real measured values. Each dot does not indicate an individual measurement, but the average of three measurements. The values represent the values to be obtained, if only that variable was changed compared to the mean. The straight connected lines indicate linear interpolation. In reality, the true relation can differ. A lower mass loss can be obtained by taking the best-performing level of each variable. This is also visible in Table 5.11

Temperature linearly decreases mass loss with a delta of 0.58 percentage points. Time has little influence on mass loss. Only the jump in time from 30 to 45 minutes has a small but noticeable effect of 0.15 percentage point. The increase to 60 minutes only constitutes a meagre 0.03 percentage points. Applying pressure has an unconventional relation with mass loss. At the specific pressure of 35 MPa, mass loss is maximal.

5.5.2. Group-2

Results after analysing the Taguchi design for group-2, are presented in Figure 5.18. Average mass loss for group-2 was 11.47%.

Figure 5.18: Mass loss respective to each variable and variable level. The dotted grey line indicates the mean mass loss. Measurement values are in percentages. The mean mass loss was 11.47%. The numbers in brackets after the variable name indicate the rank of influence, from most influential (1), to least influential (7).
The values are Taguchi deconvoluted values from the real measured values. Each dot does not indicate an individual measurement, but the average of four measurements. The values represent the values to be obtained, if only that variable was changed compared to the mean. The straight connected lines indicate linear interpolation. In reality, the true relation can differ. A lower mass loss can be obtained by taking the best-performing level of each variable. This is also visible in Table 5.12

Table 5.12: Mass loss values of the analysed Taguchi design, as plotted in 5.18. Values are in percentages, except for rank, which has no unit. The delta row indicates the difference between the maximum and minimum value for each column. This value is used to determine the rank. The rank indicates the variable with the most influence on the results, e.g. the largest delta. The level column indicates the set level of each variable from 1 to 2. For simulant this is MGS-1 and JEZ-1 respectively. For method this is ball milling and sieving respectively. For pressure this is 51 MPa and 80 MPa respectively. For particle size this is <53 µm and <250 µm respectively. For coating this is no coating and a BN coating respectively. For temperature this is 1000 °C and 1100 °C respectively. For drying this is dry and non-dry respectively.

Level	Simulant	Method	Pressure	Particle size	Coating	Temperature	Drying
1	5.75	10.63	10.37	13.28	11.48	11.73	10.45
2	17.19	12.32	12.58	9.66	11.46	11.22	12.50
Delta	11.44	1.69	2.21	3.62	0.02	0.51	2.05
Rank	1	5	3	2	7	6	4

Simulant type has the largest influence on mass loss. With a delta of 11.44 percentage points, using JEZ-1 results in most mass loss. The method of lowering particle sizes has a little influence, with ball milling resulting in less mass loss with a delta of 1.69 percentage points.

Increasing the pressure increases mass loss. This is unexpected after the unconventional relation results from group-1. The increase is 2.21 percentage points. This is a significant amount compared to the total delta of 1.00 percentage points of group-1.

Decreasing the particle size results in more mass loss of 3.62 percentage points. Applying a coating has a near zero effect of 0.02 percentage points. Increasing the temperature has a negative effect similar to group-1. With a delta of 0.51 percentage points, this is more than the 0.16 percentage points of group-1 for the same temperature increase. Drying results in less mass loss. The difference in mass loss between dry and non-dry material was 2.05% of the total initial weight. This is the same as the expected mass loss for drying according to the DSC-TGA curves of 2%, see Chapter 4.1.

5.6. Microstructure

A difference of outside texture between samples was observed. Some samples, all samples in group-1 and samples 12 and 16 from group-2, had a matte texture. They had low particle cohesion. This manifested in the samples depositing a grey smear when touched, not unlike a coarse chalk stick. This is presented in Figure 5.19. Some samples, samples 10, 13, 15 and 17, had a glossy outside texture. This implies vitrification [96]. Other samples, samples 11, 14 and 16, had both characteristics. Their bottom was glossy while the top was matte. This is presented in Figure, 5.20. Here, the top and bottom of samples 16 is presented to indicate the differences.

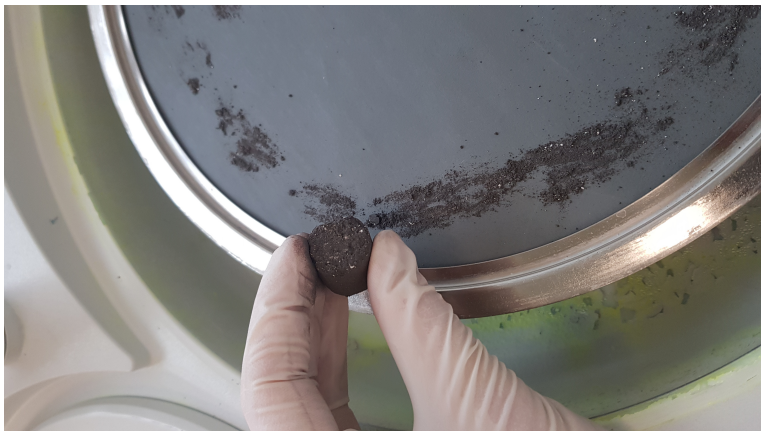

Figure 5.19: An exaggerated example of smearing. For all used samples, smearing was less significant. Smearing only happened when the material was exposed to friction.

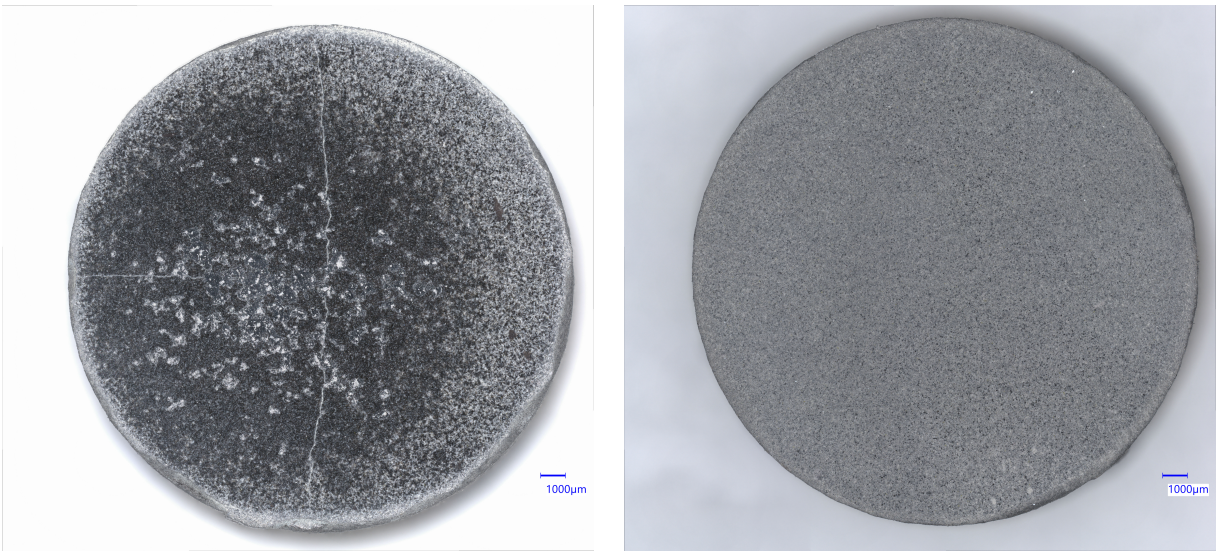

(a) The bottom side of sample 16. Vitrification is visible as a glassy texture. A crack pattern is also visible.

(b) The top side of sample 16. No vitrification is present. A matte texture is visible.

Figure 5.20: Comparison between the top and bottom side of sample 16. The bottom side shows vitrificaiton and cracks, while the top side is matte. Similar images have been made for all other samples.

In the same figure, cracks can be observed. These cracks are always in radial direction. Multiple cracks meet in the centre of the sample. These cracks are only visible on vitrified surfaces. CT-scans from, as presented in Figure 5.21, indicate that non-vitrified samples can also have these cracks. They are simply non-observable with the naked eye or light microscope for non-vitrified surfaces. These cracks were all observed before uniaxial compression tests.

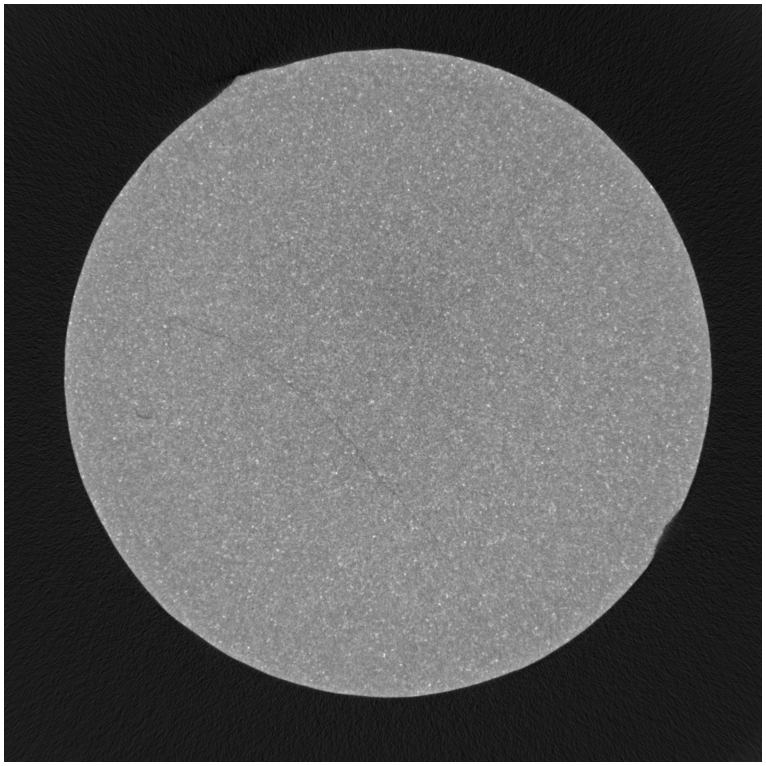

Figure 5.21: An example of cracks being observed inside a sample, which were not apparent from the outside.

5.6.1. SEM Microstructure Types

For MGS-1, SEM images revealed that all samples in group-1 were not liquid-sintered. Particles were observed to be tightly packed and were fused at the contact area, of which there were few. Particles were mostly angular. This structure is henceforth called M0, as in MGS-1 and zero sintering. An example is presented in Figure 5.22b. Some sintering had taken place, as the samples were cohesive, showed variation in compressive strength and had some fused contact areas.

Samples in group-2 showed locations were liquid sintering had happened. In these areas, individual particles were still recognisable, but a matrix of molten mineral had fused them. Particles were also still fused at contact areas. Particles were mostly rounded. This structure is called M1, see Figure 5.22a for an example. A transitional zone between the two structures has not been observed. It is a sudden change between M0 and M1. This is illustrated in Figure 5.22. An overview of the different observed microstructure types is given in Table 5.13.

SEM images revealed a stark difference between MGS-1 and JEZ-1 simulants. For JEZ-1, two distinct structures were observed, connected with a smooth transition. The first structure, henceforth named J0, was a coarse compact of intact angular particles connected by porous blobs, see Figure 5.23c. These blobs were determined to be mainly smectite clay, with the darker blobs being calcined magnesium-carbonate, see Figure 5.27. The second structure, J1, was a highly sintered mass where individual particles were hard to distinguish, see Figure 5.23a. Particles were mostly rounded. In contrast to M1, distinct grain boundaries were difficult to observe. Particles were often not connected to each other, but only connected by the matrix. Figure 5.23 shows an overview of this transition. An overview of the different observed microstructure types is given in Table 5.13.

The identification of diatomaceous earth particles is presented in Figure 4.3 of Chapter 4.2. In M0 diatomaceous earth was readily observed. In M1, no diatomaceous earth could be observed. In both J0 and J1, no

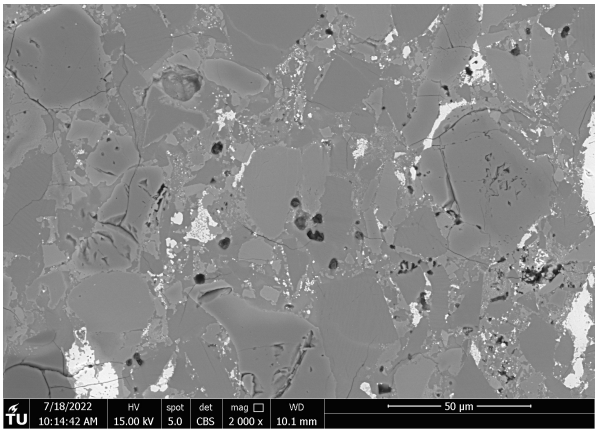

(a) An example of M1 structure. There is almost no porosity. It is difficult to distinguish the matrix from the particles. No diatomaceous earth is visible.

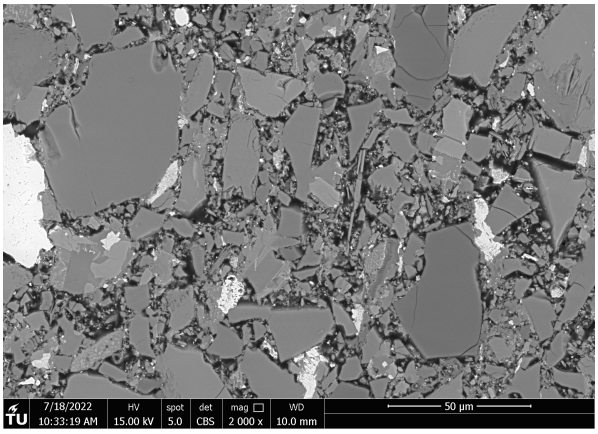

(b) The M0 structure. No molten particles particles are present. Very few particles appear to be fused together. Diatomaceous earth is visible.

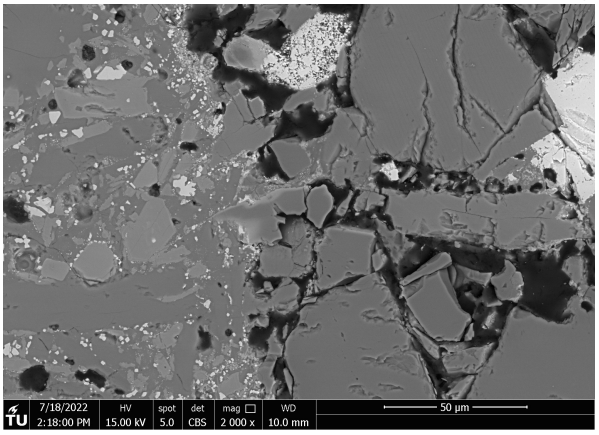

(c) An image where the full transition from M1 into M0 was observed from left to right.

Figure 5.22: Examples of the M1 and M0 structures. Image (c) presents an overview of the full transition in one image. Here, M1 is present on the left and M0 on the right.

Table 5.13: Overview of the microstructure types by defining appearances.

Simulant	**MGS-1**		**JEZ-1**	
Structure	M0	M1	J0	J1
Particle packing	Individual particles	Agglomerated	Individual particles	Agglomerated
Particle shape	Angular	Rounded	Angular	Rounded
Particle cohesion	Fused at contact area	Fused at contact area Bound by matrix	Fused by smectite	Bound by matrix Few contact areas
Interparticle porosity	High	Almost zero	High	Almost zero

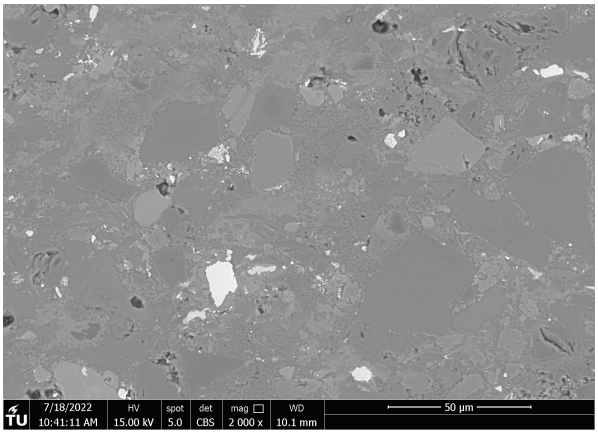

(a) An example of J1 structure. There is almost no porosity. It is difficult to distinguish the matrix from the particles. No smectite clay particles or diatomaceous earth is visible.

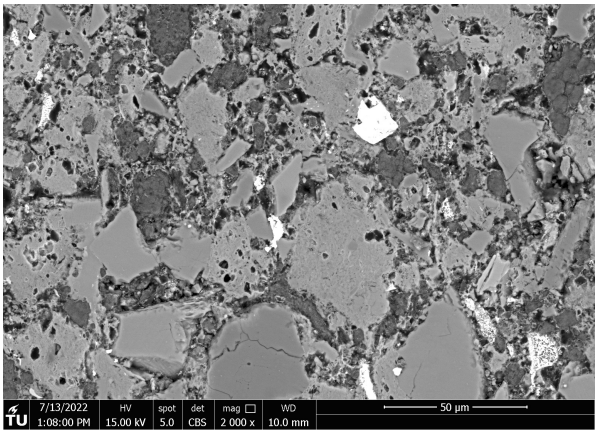

(b) The J1 structure becomes more porous towards the J0 structure. The matrix consists of porous blobs, which fuses with particles. Diatomaceous earth hardly visible.

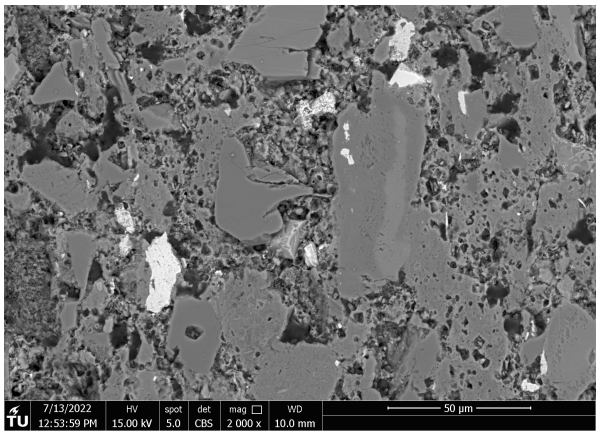

(c) The J0 structure. There are still visibly molten and fused particles. This is the least fused example present in samples of JEZ-1. Diatomaceous earth is visible

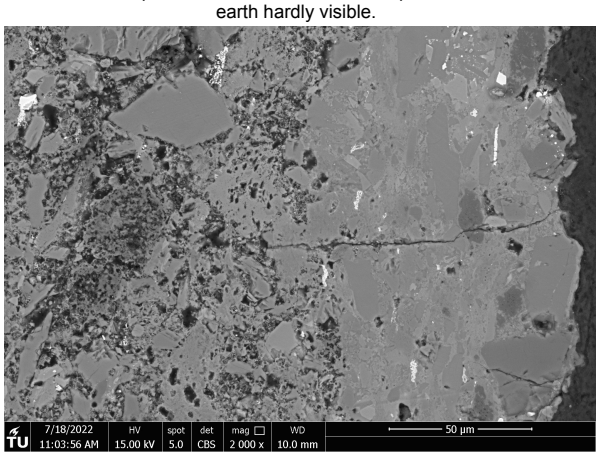

(d) An image where the full transition from J0 into J1, from left to right, was observed.

Figure 5.23: Examples of the smooth transition between J1 and J0 structures. From a to c, is equivalent as from J1 to J0. Image d presents an overview of the full transition in one image. Here, J0 is present on the left and J1 on the right.

diatomaceous earth had been observed. In J0, remnants of diatomaceous earth were thought to be present a void structures within the molten blobs.

5.6.2. SEM Effect of Sieving and Ball Milling

Sieving tended to skew the particle size distributions to larger sizes compared to ball milling. As is visible in Figure 5.24a, most of the space is occupied by a few large (> 25 µm) particles. Ball milling was observed to create a lot of nanoscale particles. As is visible in Figure 5.24b, most of the space is occupied by a a large quantity of very small (< 4 µm) particles. The previously mentioned Figures are for MGS-1 because the effect is better visible. The observations also hold for both JEZ-1. The effect is better visible for MGS-1 as the nanoparticles get stuck inside the smectite of JEZ-1. In Figure 5.25, the effect can be observed for JEZ-1.

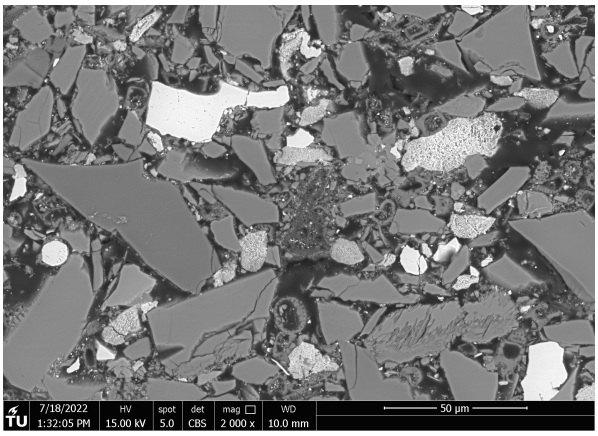

(a) An example of sieved MGS-1 to <53 µm. Different sizes of particles can be observed. The main size is about 25-65 µm. Both smaller and larger particles can be observed, but are less common.

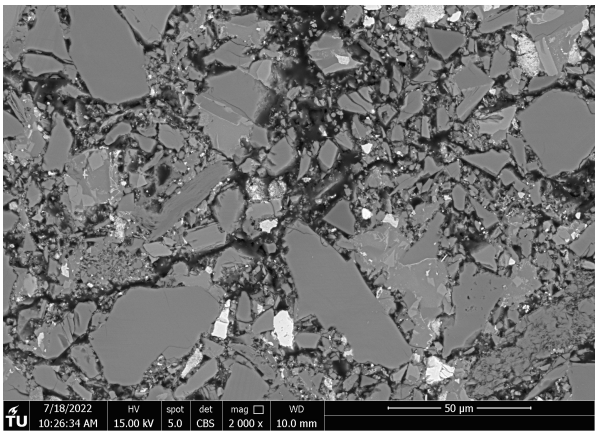

(b) An example of ball milled MGS-1 to <53 µm. Different sizes of particles can be observed. The main size is about 100 nm-4 µm.

Figure 5.24: Two similar samples of MGS-1, one sieved and one ball milled, both to the same particle size of <53 µm.

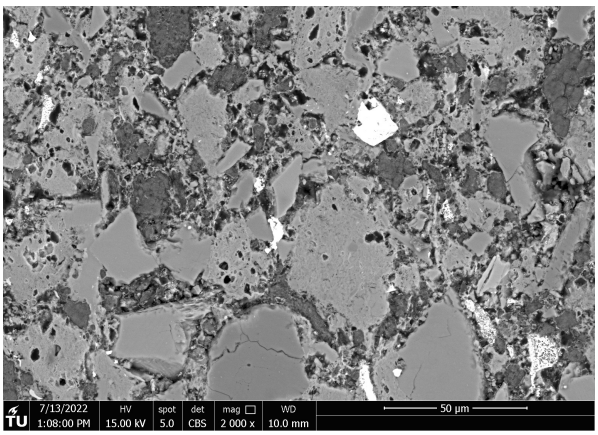

(a) An example of sieved JEZ-1 to <53 µm. Different sizes of particles can be observed. Particles are held together by the smectite and magnesium-carbonate J0 structure. The smecite and magnesium-carbonate blobs have a size, but consist of many individual smaller particles.

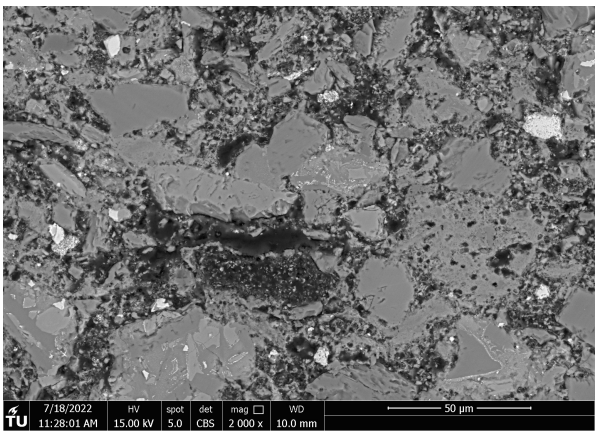

(b) An example of ball milled JEZ-1 to <53 µm. Overall, less smectite and magnesium-carbonate was observed. They are both distributed more and spread out. A lot of nanoparticles can be observed.

Figure 5.25: Two similar samples of JEZ-1, one sieved and one ball milled, both to the same particle size of <53 µm.

5.6.3. SEM Crack Formation

In Figure 5.26, crack formation is observed. The samples were analysed in SEM after compressive failure. Therefore, three crack types can be present. The main crack type is due to the compressive testing. They are located at specific locations, characteristic for cylindrical specimens. They consist of large cracks and microcracks. These types of cracks are indicated in Figures 5.26(a-d). The second type of crack is thermal

cracking. Samples have endured large temperature differences during sintering, from room temperature up to 1100 °C. With heating rates of 50 °C/min and cooling rates of 100 °C/min, thermal stresses can occur. These cracks are characterised by their crack pattern, as is visible in Figures 5.26(e-g). The third type of crack is due to the applied pressure during sintering. Samples do not break due to these stresses, but individual particles can break. This leads to cracks in particles which are uncorrelated to cracks in surrounding particles. They are visible in Figure 5.26h.

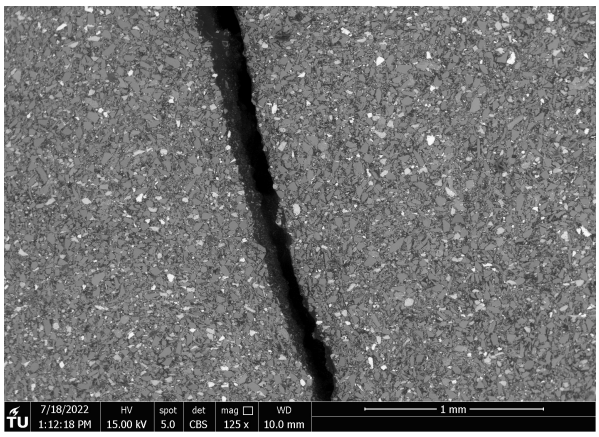

(a) An example of a crack due to compressive tesing in M0 structure. The crack simply separates the particles.

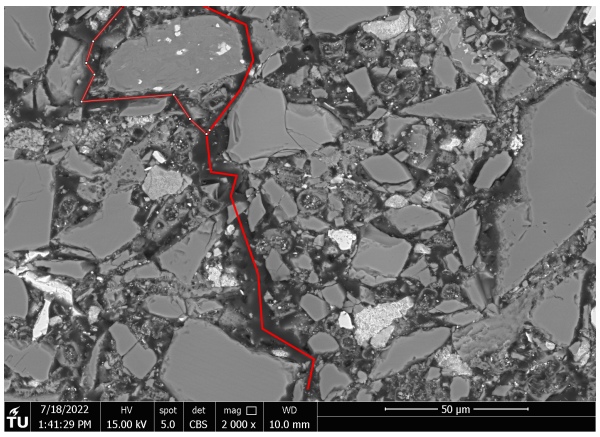

(b) An example of a crack tip due to compressive testing in M0 structure. The crack does not move through any particle. The crack tip is at the bottom of the image. The crack itself is indicated in red.

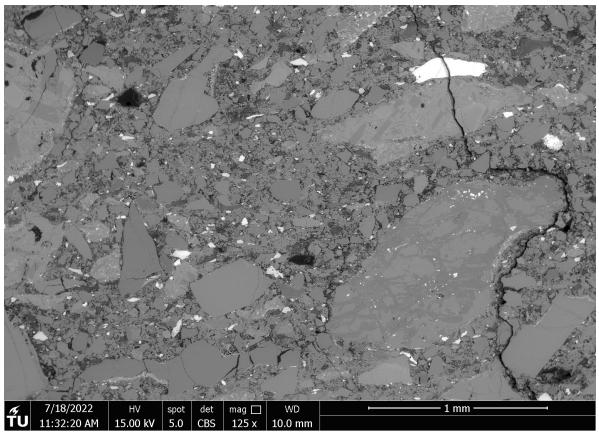

(c) An example of a crack due to compressive testing in J0 structure. The crack has propagated through some particles, but around others.

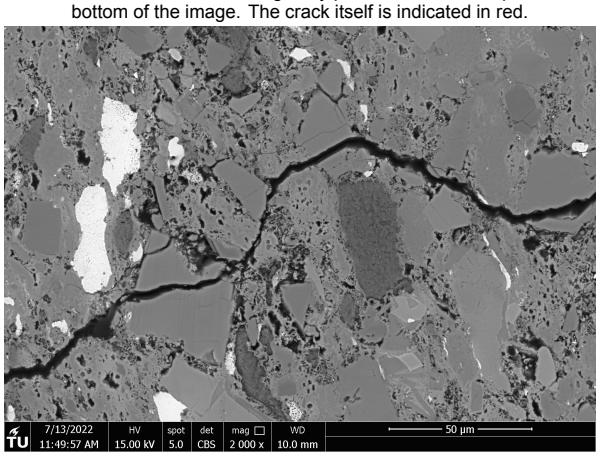

(d) An example of a crack due to compressive testing halfway the J0 to J1 structure. The crack has propagated without much regard for particles.

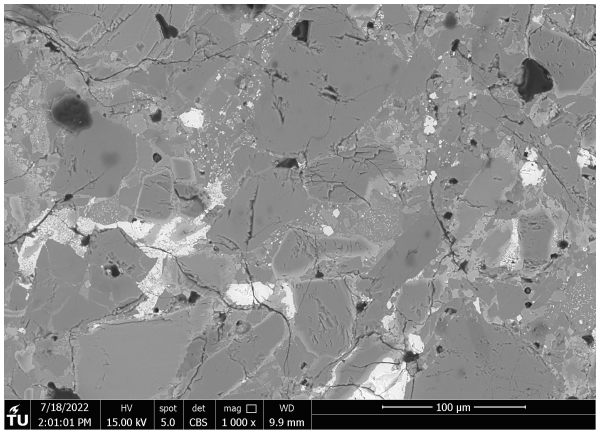

(e) An example of thermal cracking in M1 structure. The cracks tend to move through the matrix and particles without regard for either. This indicates that the matrix has the same strength as some particles.

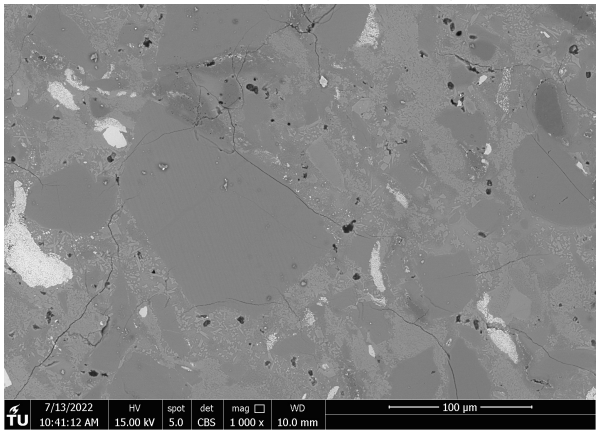

(f) An example of thermal cracking in J1 structure. The cracks tend to move through the matrix and particles. At some locations, the crack seems to move around the particles. in other locations, the crack moves straight through. This indicates that the matrix has the same strength as some particles.

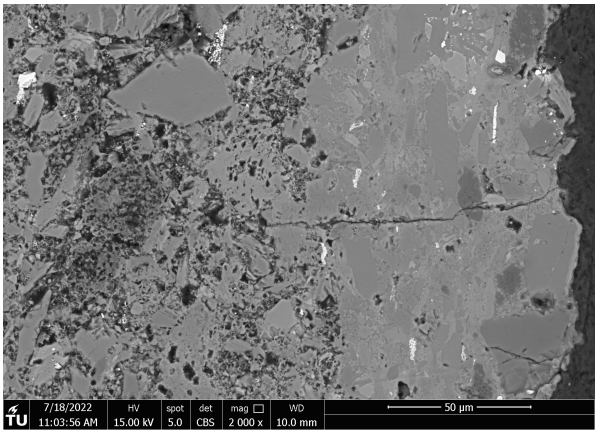

(g) An example of thermal cracking from J1 through J0 structure. The cracks tend to move through the matrix and particles. The crack stops at the J0 structure. This indicates that shrinkage occurred more in the J1 structure compared to the J0 structure.

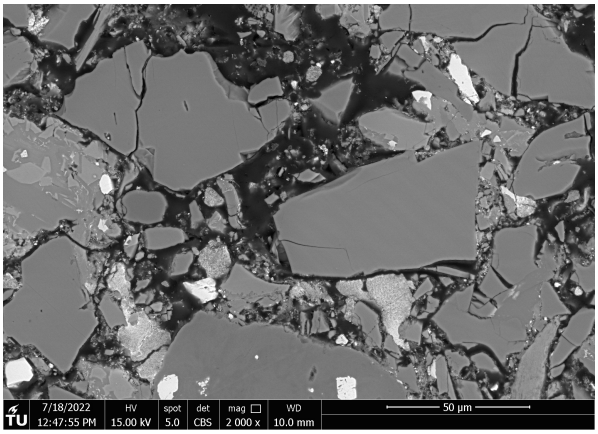

(h) An example of particle crushing in M0 structure. Particles clearly crack and can even become multiple smaller particles.

Figure 5.26: Examples of cracking. (a-d) indicate cracks as the result of compressive testing. (e-g) indicate thermal cracking. (h) is an example of particles crushing.

5.6.4. SEM-EDS

EDS analysis reveals the nature of the M1 and J1 matrix. In Figure 5.27, the EDS results for the J1 structure are presented. Only the relevant elements are shown. From these images, it is clear that smectite and magnesium-carbonate are the main components that make up the binding matrix. From the non-EDS images, this was also somewhat apparent. There, both smectite clay and magnesium-carbonate are visible in J0 structures, but not in J1 structures. More EDS-mapping images can be found in Appendix E.

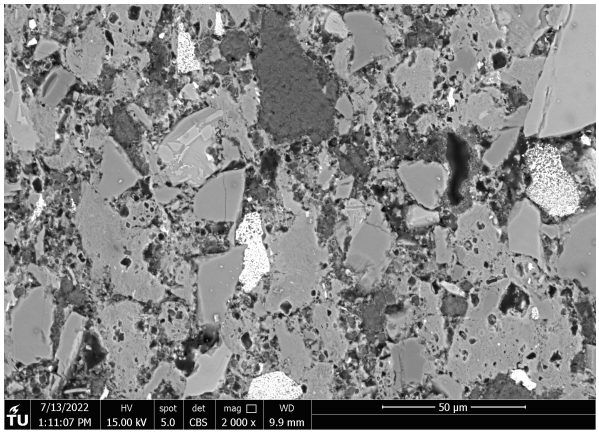

(a) The SEM image of the J0 structure. Smectite is visible as the porous deformed blobs. Magnesium-carbonate is visible as the dark particles.

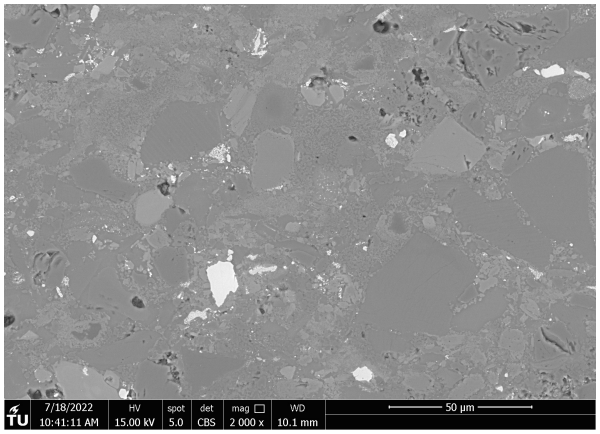

(b) The SEM image of the J1 structure. The matrix connecting the particles is heterogeneous and consist of fused smectite and magnesium-carbonate.

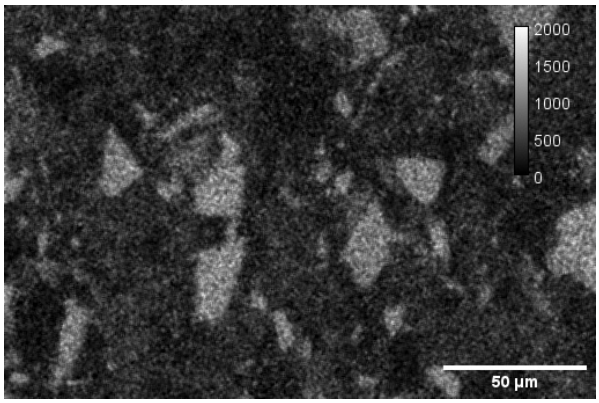

(c) Aluminium content in the J0 structure. The colour scale indicates the elemental percentage of Al atoms. The value is given as 100×percentage. Meaning a value of 10000 is the pure element.

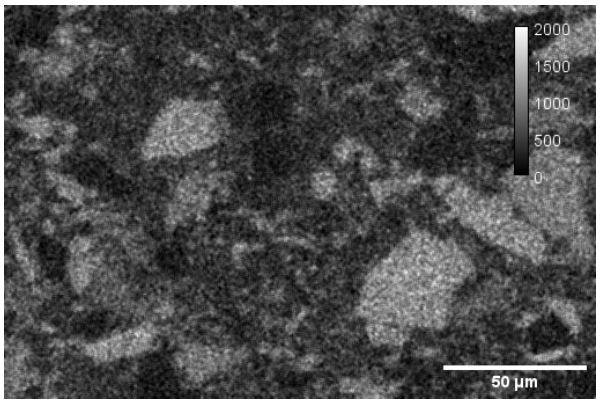

(d) Aluminium content in the J1 structure. The colour scale indicates the elemental percentage of Al atoms. The value is given as 100×percentage. Meaning a value of 10000 is the pure element.

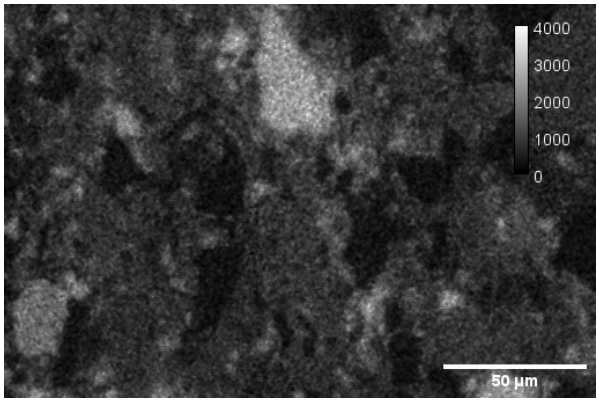

(e) Magnesium content in the J0 structure. The colour scale indicates the elemental percentage of Mg atoms. The value is given as 100×percentage. Meaning a value of 10000 is the pure element.

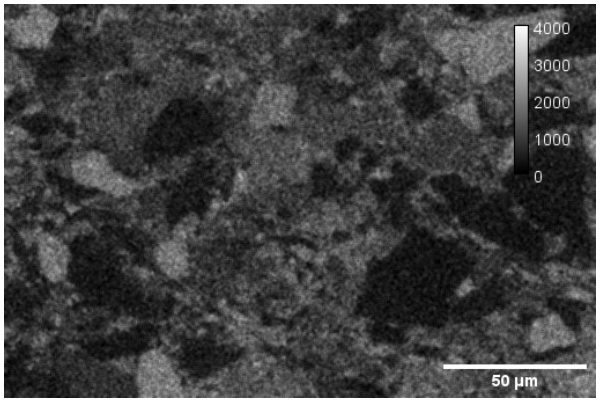

(f) Magnesium content in the J1 structure. The colour scale indicates the elemental percentage of Mg atoms. The value is given as 100×percentage. Meaning a value of 10000 is the pure element.

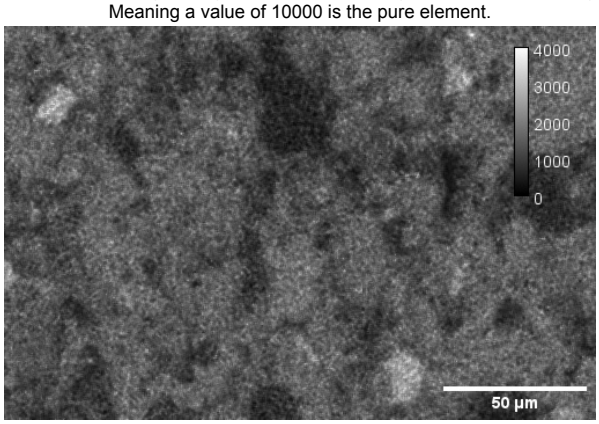

(g) Silica content in the J0 structure. The colour scale indicates the elemental percentage of Si atoms. The value is given as 100×percentage. Meaning a value of 10000 is the pure element.

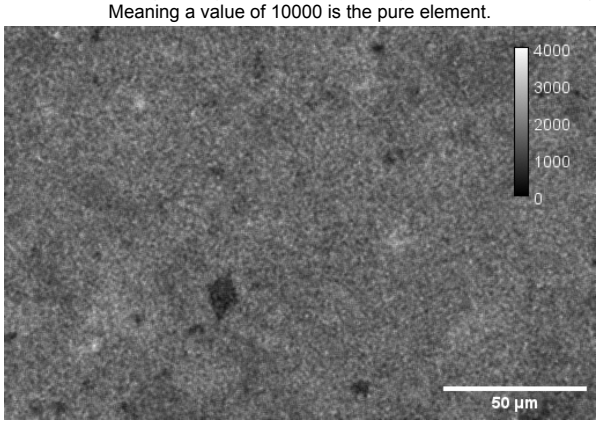

(h) Silica content in the J1 structure. The colour scale indicates the elemental percentage of Si atoms. The value is given as 100×percentage. Meaning a value of 10000 is the pure element.

Figure 5.27: Comparison of J0 and J1 structures in EDS for the elements: Al, Mg and Si. From the comparison, it is clear that the matrix in J1 structures consists mainly of smectite and magnesium-carbonate

5.7. Energy Use

The individual actual energy use per run is presented in Table 5.10. The values are measured by integrating the applied wattage of the SPS for a full run. The presented values are the absolute total energy use of each specific run. It is more useful to present energy use with respect to other important variables. The energy use per mass of material manufactured is one such measure. Another measure is the energy use per volume of material. Lastly the strength obtained per energy used is of importance. All these factors are important in colony design. Therefore, they are presented in Appendix F. In this section, the Taguchi analysis is performed for energy use per volume of material. In Chapter 5.8, the energy use to manufacture a Martian building is calculated. This calculation requires volumetric measurements. It can be noted that an increase in energy consumption did not necessarily lead to an increase in strength, density or compaction. Therefore, an optimum can be obtained.

Table 5.14: Energy use for all samples. Energy use per mass and volume of manufactured material are also presented, as well as obtained strength per energy used.

Sample	**Total energy** (MJ)	**Energy per mass** (MJ/kg)	**Energy per volume** (GJ/m^3)	**Strength per energy** (MPa/MJ)
1	12.74	806	1862	1.208
2	14.00	899	1993	0.485
3	12.76	808	1503	0.001
4	18.20	1161	2476	0.456
5	10.83	685	1335	0.122
6	8.85	564	1168	0.311
7	16.95	1341	2434	0.544
8	15.75	1254	2476	1.098
9	7.18	560	1009	0.839
10	21.12	1730	4197	5.278
11	15.94	1775	3743	6.598
12	19.30	1506	3102	1.194
13	19.31	1238	2985	2.344
14	15.14	1087	2354	2.690
15	15.49	983	2436	3.029
16	21.68	1453	3522	4.735
17	17.11	1254	3085	7.983
18	13.54	943	2269	5.079
10b	22.65	1653	4358	5.477
11b	14.90	1193	2731	6.585

5.7.1. Group-1

Results after analysing the Taguchi design for group-1, are presented in Figure 5.17. The variables can be indicated from most to least influential as: temperature, time, sieve size and pressure. Average energy consumption per volume for group-1 was 1806 GJ/m^3.

Table 5.15: Energy consumption per volume values of the analysed Taguchi design, as plotted in 5.28. Values are in GJ/m^3, except for rank, which has no unit. The delta row indicates the difference between the maximum and minimum value for each column. This value is used to determine the rank. The rank indicates the variable with the most influence on the results, e.g. the largest delta. The level column indicates the set level of each variable from 1 to 3. For sieve size this is <53 µm, <250 µm and <600 µm respectively. For temperature this is 800 °C, 1000 °C and 1100 °C respectively. For time this is 30 minutes, 45 minutes and 60 minutes respectively. For pressure this is 16 MPa, 35 MPa and 51 MPa respectively.

Level	**Sieve size**	**Temperature**	**Time**	**Pressure**
1	1973	1227	1402	1757
2	1659	1935	1865	1826
3	1786	2257	2152	1835
Delta	313	1030	750	78
Rank	3	1	2	4

The results were mostly as expected. Sieve size did not influence the energy use. A temperature increase linearly increased the energy use. Similarly, a longer sintering duration increases the energy use. It can be noted that applying pressure slightly decreases energy use.

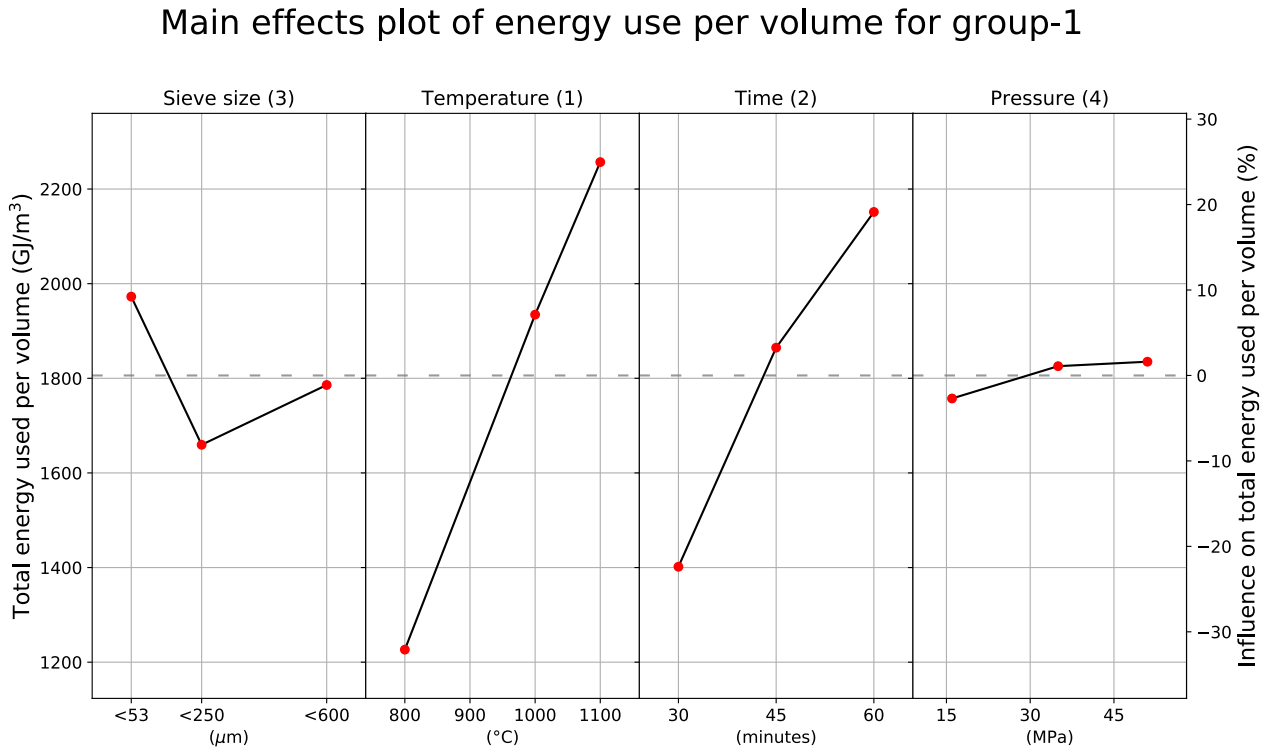

Figure 5.28: Energy consumption per volume respective to each variable and variable level. The dotted grey line indicates the mean energy use per volume. Measurement values are in GJ/m^3. The mean energy consumption per volume was 1806 GJ/m^3. The numbers in brackets after the variable name indicate the rank of influence, from most influential (1), to least influential (4).
The values are Taguchi deconvoluted values from the real measured values. Each dot does not indicate an individual measurement, but the average of three measurements. The values represent the values to be obtained, if only that variable was changed compared to the mean. The straight connected lines indicate linear interpolation. In reality, the true relation can differ. A lower total energy consumption can be obtained by taking the best-performing level of each variable. This is also visible in Table 5.15

5.7.2. Group-2

Results after analysing the Taguchi design for group-2, are presented in Figure 5.18. Average energy consumption per volume for group-2 was 3071 GJ/m^3. This is significantly higher than group-1. This mainly because of the use of a longer sintering duration of 60 minutes and only using higher temperatures of 1000 °C and 1100 °C.

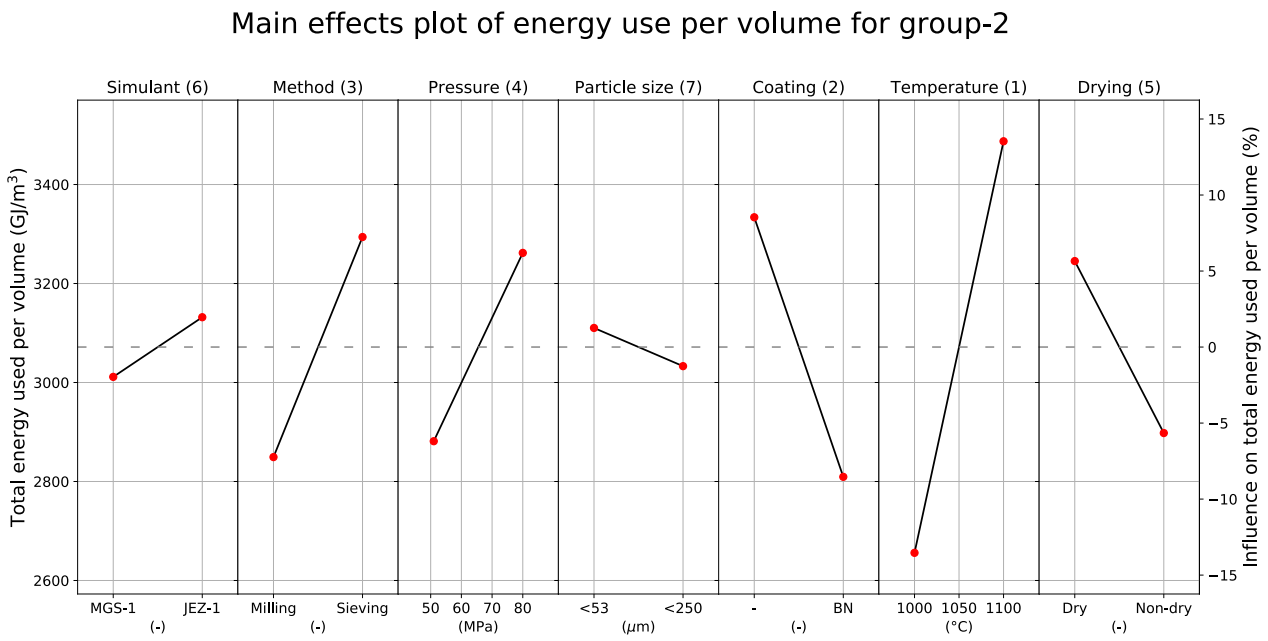

Figure 5.29: Energy consumption per volume respective to each variable and variable level. The dotted grey line indicates the mean energy use per volume. Measurement values are in GJ/m^3. The mean energy consumption per volume was 3071 GJ/m^3. The numbers in brackets after the variable name indicate the rank of influence, from most influential (1), to least influential (7). The values are Taguchi deconvoluted values from the real measured values. Each dot does not indicate an individual measurement, but the average of three measurements. The values represent the values to be obtained, if only that variable was changed compared to the mean. The straight connected lines indicate linear interpolation. In reality, the true relation can differ. A lower total energy consumption can be obtained by taking the best-performing level of each variable. This is also visible in Table 5.16

Table 5.16: Energy consumption per volume values of the analysed Taguchi design, as plotted in 5.29. Values are in GJ/m^3, except for rank, which has no unit. The delta row indicates the difference between the maximum and minimum value for each column. This value is used to determine the rank. The rank indicates the variable with the most influence on the results, e.g. the largest delta. The level column indicates the set level of each variable from 1 to 2. For simulant this is MGS-1 and JEZ-1 respectively. For method this is ball milling and sieving respectively. For pressure this is 51 MPa and 80 MPa respectively. For particle size this is <53 µm and <250 µm respectively. For coating this is no coating and a BN coating respectively. For temperature this is 1000 °C and 1100 °C respectively. For drying this is dry and non-dry respectively.

Level	Simulant	Method	Pressure	Particle size	Coating	Temperature	Drying
1	3011	2849	2881	3110	3334	2656	3245
2	3132	3294	3262	3033	2809	3487	2898
Delta	121	445	380	77	524	831	347
Rank	6	3	4	7	2	1	5

JEZ-1 simulant sintering requires more energy than MGS-1 per volume. Ball milling results in more energy efficient sintering.

A higher applied pressure resulted in a small increase in energy use per volume. The increase was significantly more than for group-1, at 12.4% compared to only 4.3% with respect to the means. The particle size was of almost no influence. Applying a coating significantly reduced the total energy use by 17.08%. Simillarly to group-1, a higher temperature resulted in more energy consumption per volume. Drying had a negative influence on energy use.

5.8. Production Feasibility Calculation

To find out if this production method is suitable for application on Mars, an important calculation must be made. It must be calculated how much time and energy it takes to manufacture enough material for a suitable structure. The chosen structure is a half-circle dome, as suggested by Agata Mintus [26]. In Figure 5.30, the process of manufacturing such a dome is presented.

The volume of such a dome can be calculated by making a lot of assumptions. Firstly, it was assumed that the walls should have a thickness of 0.5 metres. Due to the strength of the material, it might be possible to lower this requirement significantly. A thinner dome can be built on top of which regolith can be installed for radiation protection. Secondly, the size of the dome is assumed to be 20 meters long and have a diameter of 8 metres at the inside. This creates a living space of 502 m^3. With a wall thickness of 0.5 meters, the total volume of material required is 165 m^3.

Structures are proposed to be produced before humans land on Mars [7, 26, 114]. Both the most used value of 5 years and a value of 1 year for preparation is calculated with further. In this time-frame, robots are proposed to autonomously manufacture the structural materials and assemble them into buildings. This is indicated in step 2 in Figure 5.30.

The lowest energy use was for run 9 of group-1. It had an energy use per volume of 1009 GJ/m^3. This was the result of the lowest total energy use of 7.18 MJ to produce a mass of 12.83 grams, which corresponded to a volume of 0.007124 m^3. The strength of this sample was 6.03 MPa. This is sufficient to build with according to the requirements of this study. Multiplying the energy requirement by the volume of the proposed dome results in a total energy use of 166.74 TJ. This results in a constant energy supply of 5.29 MW and 1.06 MW for 1 and 5 years of preparation, respectively.

The best strength per energy used was obtained for sample 17, at 7.98 MPa/MJ. It coincidentally also has the highest absolute obtained strength at 137 MPa. This is more than sufficient to build with according to the requirements of this study. More advanced or slimmer structures can be built using this material. Some other runs had a higher energy use, but due to their lacking performance compared to sample 17, they are not logical to manufacture. Sample 17 had a energy use per volume of 3085 GJ/m^3. This was the result of a total energy use of 17.11 MJ to produce a mass of 13.64 grams, which corresponded to a volume of 0.005545 m^3. This results in a total energy use of 510.06 TJ. This results in a constant energy supply of 16.16 MW and 3.23 MW for 1 and 5 years of preparation respectively.

Another method of acquiring the energy use per weight of material is to analyse at the DSC-TGA graphs, presented in Chapter 4.1. The total specific heat capacity per both input and resulting mass, for both simulants, in both argon and air environments and for each sintering temperature were calculated and are presented in Table 5.17 and 5.18. The actual specific heat capacity can be calculated by dividing this value by the total temperature range used. Calculated values were higher for argon compared to air. Only argon values are used in the energy calculation. The oxygen that influences the reactions is not present on Mars, nor in the vacuum environment of the SPS. These values are only representative for non-sieved material (<600 µm) or ball-milled material.

The minimum viable energy requirement was at 1000 °C. At 800 °C, for the representative runs, the minimum required strength was not obtained. At this temperature, JEZ-1 had the lowest energy use at 6.48 J/mg for output mass. JEZ-1 samples sintered at 1000 °C had an average density of 2188 kg/m^3. The least advantageous total specific heat for this calculation was for MGS-1 in argon environment up to a temperature of 1100 °C. With a value of 7.79 J/mg for output mass. MGS-1 samples sintered at 1100 °C had an average density of 2218 kg/m^3.

The energy required to manufacture 1 m^3 of material then is between 14.17 and 17.27 GJ/m^3 for the most and least advantageous runs. Combining this with the densities, a continuous energy production between 74.30 and 90.54 kW for one year is necessary. For a preparation period of 5 years, these values become and 14.86 and 18.11 kW.

Table 5.17: Total specific heat capacity per output mass in J/mg. This is the total energy necessary to heat the specified simulant at the specified environment to the specified temperature per milligram of manufactured material. The actual specific heat capacity can be calculated by dividing this value by the total temperature range used.

Simulant	**MGS-1**		**JEZ-1**	
Environment	Argon	Air	Argon	Air
800	4.612	3.953	4.425	3.994
1000	6.856	5.798	6.478	6.062
1100	7.787	6.691	7.362	7.164

Table 5.18: Total specific heat capacity per input mass in J/mg. This is the total energy necessary to heat the specified simulant at the specified environment to the specified temperature per milligram of resource material. The actual specific heat capacity can be calculated by dividing this value by the total temperature range used.

Simulant	**MGS-1**		**JEZ-1**	
Environment	Argon	Air	Argon	Air
800	4.444	3.828	3.941	3.575
1000	6.528	5.559	5.725	5.417
1100	7.393	6.396	6.438	6.316

The calculated energy requirement according to actual energy used during sintering results in a total energy use that is not within the requirements of this study, which was 100 kW, see Chapter 2.6.11. All theoretical calculated values are less than the stated minimum of 100 kW, making them suitable. To put the energy requirement in perspective, an average wind turbine in the U.S. produces about 2.85 MW [128].

The duration to produce enough material depends on three factors: the duration of sintering, the amount of sintering devices and the volume of the sintered bricks. One device could sinter multiple bricks simultaneously, this is considered as multiple devices for this calculation.

With a total volume to be made of 165 m^3, only one sintering device and a sintering duration of 60 minutes, 8760 to 43800 bricks can be made for 1 to 5 years of preparation respectively. This results in a minimum brick volume of 0.0189 or 0.0038 m^3. For 1 year of preparation, a brick of 0.25x0.3x0.3 m will suffice. For 5 years of preparation, a brick of 0.125x0.25x0.125 m will suffice.

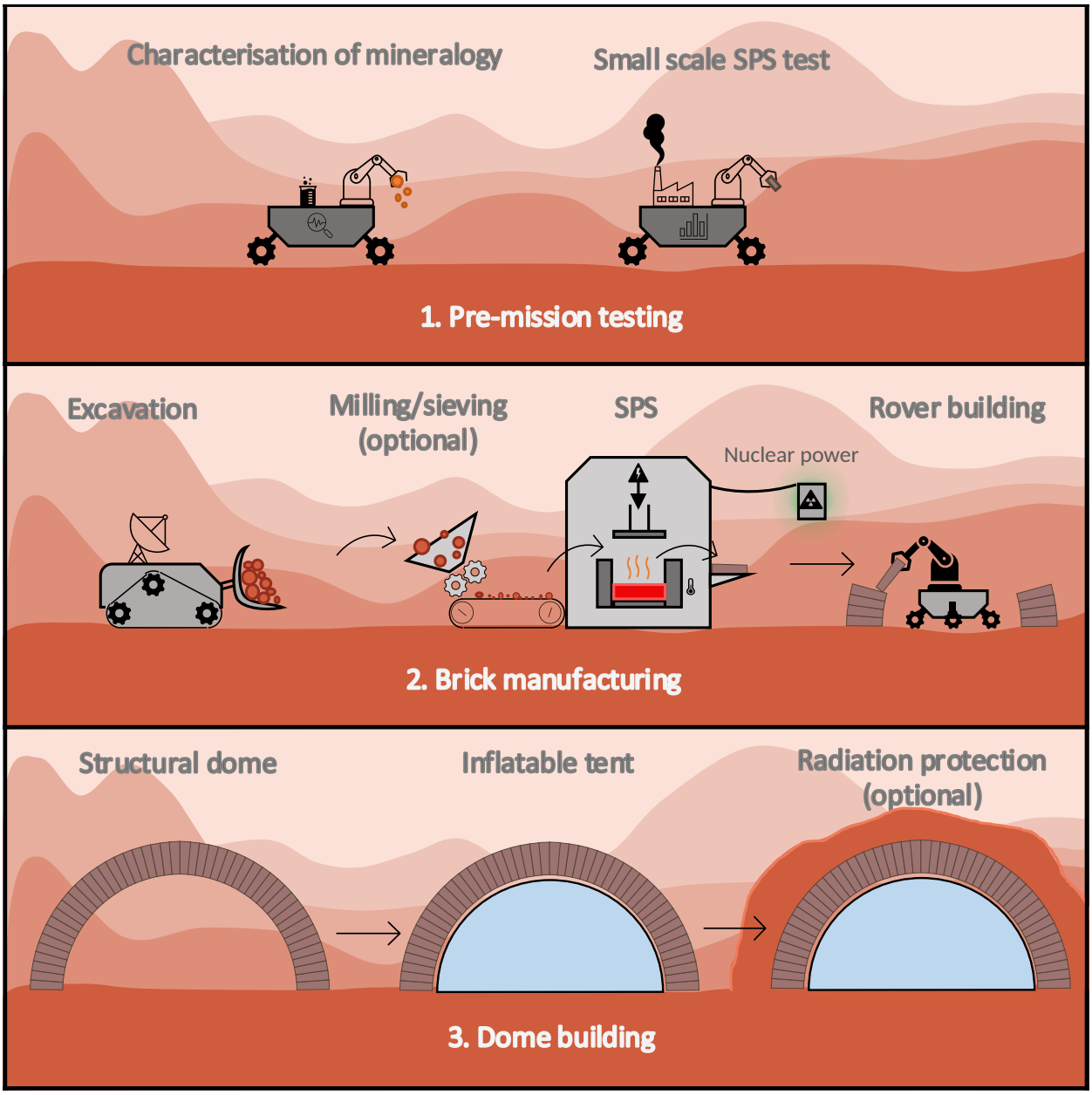

Figure 5.30: Example of a martian construction mission. In the first stage, the regolith at the actual landing location must be analysed. This will provide further information for optimising manufacturing. Next, a small scale SPS sample is manufactured. This sample will also be tested. Strength or three point bending could be tested by simply letting the rover drive over the sample. In the next phase, the actual rovers, tools and devices will be send to Mars for manufacturing the bricks. They are fine-tuned to the analysed data from step 1. Simultaneously, the dome will be build. This is done by autonomous rovers. After the dome is build, in step 3, the inflatable tent is set up. This will provide a living environment for the astronauts. They can now safely live on Mars. An optional step of applying a thick regolith layer is presented. This thick layer will serve as radiation protection. The strength of the manufactured bricks determines how thick this layer can be compared to the thickness of the dome. It is possibly more beneficial to manufacture stronger bricks at higher energy costs, because less of them are necessary. The extra strength will be used to support the regolith layer.

6
Discussion

6.1. Simulant Type

The simulant type had a large influence on the main properties of the manufactured material. JEZ-1 resulted in a significantly higher strength, moderately higher densities and a significantly higher compaction compared to MGS-1. It also resulted in a significantly higher mass loss. Because of the beneficial main properties, JEZ-1 is more suitable as a simulant for manufacturing construction materials. With an average mass loss of 17.2%, more raw JEZ-1 simulant is necessary to manufacture a similar weight of material compared to MGS-1. As discussed in Chapter 2.4.1, availability of regolith is not an issue on Mars. Therefore this is not seen as a drawback.

The difference between the two simulants is the addition of smectite and magnesium-carbonate in JEZ-1 and differing ratios of other minerals [29, 30]. This is described in Chapter 4. The addition of these elements resulted in significantly different microstructures. This is can be compared in Figures 5.22 and 5.23.

For MGS-1, particles were barely fused in the M0 structure. Only at a select number of locations, a fused contact area was observed. When a M1 structure was obtained, almost all voids were eliminated. The sudden transition indicates that this behaviour was the result of a threshold being surpassed. From 5.22, it can be observed that diatomaceous earth is clearly present in the M0 structure, but completely unrecognisable in the M1 structure. It is therefore hypothesised that diatomaceous earth has a large influence in the formation of an M1 structure.

For JEZ-1, particles were already fused in the J0 structure by the smectite. When a J1 structure was obtained, almost all voids were eliminated. The smooth transition indicates that the smectite and magnesium-carbonate slowly morphed to become the matrix. From 5.23, it can be observed that smectite and magnesium-carbonate are clearly present in the J0 structure, but can only be detected in the J1 structure's matrix by the mottled appearance of smectite. Furthermore, EDS analysis from Figure 5.27 proves that the matrix was similar to a mix of both smectite and magnesium-carbonate in terms of elements.

The M1 and J1 structures were either not present, or only at the edges of samples. This means that for most samples, the strength was determined by the M0 and J0 structure. As the M0 structure only relies on the sporadic fusion of contact area, it is logical that it was weaker than the almost completely fused J0 structure, where the smectite clay had fused with most particles. Considering this, it is concluded that smectite and magnesium-carbonate are the main constituents that lead to the increased performance of samples manufactured with JEZ-1. Diatomaceous earth was difficult to detect in the J0 structure, but should be present [30]. Therefore it is hypothesised that the pores inside the smectite are the result of embedded diatomaceous earth. Diatomaceous earth was not detected as a particle in the J1 structure, indicating that it also melted and contributed to the matrix formation.

Diatomaceous earth is suspected of having an influence on the sintering behaviour, especially with the MGS-1 simulant. It was observed to melt and enable liquid sintering. Unfortunately, diatomaceous earth is not expected to be present on Mars. This material is the result of biological Earth processes [127, 129]. That is also the reason for the shapes of the particles. Opal is the equivalent mineral present on Mars [127]. To keep costs of the simulant reasonable, ExolithLab had decided to substitute opal with diatomaceous earth [127]. The impact of this substitution should be minimal, as diatomaceous earth has been observed to turn into opal at high temperatures [129]. The only real difference between the two elements is structure. Diatomaceous earth has structure, such as holes and ribs, while opal is more solid. Both mineraloids are amorphous and contain similar amounts of chemically bound water. As diatomaceous earth has a structure with more surface area and holes, it has a higher capacity for adsorbed and absorbed water. For all samples that have been dried before sintering, this should not have an influence on the results.

No mass spectrometry results could be obtained for the mass loss of the simulants during DSC-TGA testing. It is still reasonable to assume that most mass loss during heating was due to water evaporation. Evaporation of adsorbed and absorbed water, dehydration of chemically bound water and dehydroxylation

are all expected to happen with both diatomaceous earth [129] and smectite [130]. The freed water can, and should, be captured from the evaporating gasses.

JEZ-1 had an small increased energy requirement per manufactured volume. While per mass the energy requirement was similar to MGS-1. This is the result of a increased compaction for JEZ-1. As JEZ-1 resulted in higher strength, the structural design can be altered compared to MGS-1. A thinner structure can be built. This would then reduce the energy cost again. It depends on the actual structural calculations and mission requirements if the end energy consumption of JEZ-1 is higher or lower than MGS-1.

For practical applications on Mars, it can be suggested to use a location with as much smectite, magnesium-carbonate and diatomaceous earth equivalents as possible. JEZ-1 has added smectite and magnesium-carbonate because it is expected to be present at the Jezero crater. Therefore, it is suggested to use this location, or a similar location containing even higher quantities of smectite, magnesium-carbonate and diatomaceous earth equivalents. Without discernible drawbacks, this drastically increases the physical performance of the manufactured material. The added benefit of water evaporation is something that should not be overlooked. Having more water available for use in the colony is a must, especially since water would otherwise be extracted through other, energy-intensive means [21, 27].

6.2. Particle Size

A smaller particle size resulted in improved performance in compaction, density, strength and porosity. This was expected according to theory, called Herring's Scaling Law [96, 131]. Not reducing the particle size was observed to yield better performance than sieving at a size of <250 µm. It is therefore suggested to either sieve to the smallest feasible particle size which is at least lower than <250 µm, but can be higher than <53 µm, or to not sieve the material at all. If ball milling is chosen as a means of particle size reduction, it is suggested to mill to the smallest feasible particle size.

The exact reason why sieving at <250 µm yields worse results than both <53 µm and <600 µm, is not known. A positive influence due to the particle size reduction can be expected [96, 131]. Therefore, other influences are of effect. One reason could be less effective packing for smaller particle sizes. This results in less contact area between particles and therefore less surface area to sinter.

Packing is somewhat irrelevant due to the applied pressures. These pressures ensure higher packing degrees than normally available. It can also break individual particles if stresses are too high. For particles with less contact area, synonym to worse packing, stresses are higher, as there is less area to transfer internal forces. It is unknown how great this effect is. It is hypothesised that the better packing of <600 µm outweighs the negative effects of the larger particle sizes.

More mass loss was observed for smaller particle sizes. This effect is attributed to an increase in diatomaceous earth and smectite at smaller particle sizes. An increase in mass loss results in lower yields. This is not expected to be a problem on Mars, as regolith is readily available on Mars. Mass losses were 8.9% on average and lost mass was suspected to contain valuable water that can be reclaimed.

The energy consumption per volume had a similar trend to the other parameters. It is hypothesised that the improved performance is the result of better sintering. This in turn means that more energy is used to diffuse molecules and relocate particles. This energy increase can be insignificant compared to the gain in performance.

6.3. Method of Particle Size Reduction

Ball milling resulted in higher densities than sieving. This is best explained by a difference in density between smaller and larger particles. Diatomaceous earth has a lower density, 2.25 kg/m^3 [129], compared to the average simulant density of 3 kg/m^3 [22, 29]. When sieving, only the lighter, smaller particles are kept. This lowers the average density of the material. Thus, they result in a lighter end material. When ball milling, the average density is kept constant, as all minerals are still present in the original ratio. Therefore, for the same compaction, ball milling results in a heavier material than sieving, for the same particle size.

Ball milling also resulted in higher strengths and compaction compared to sieving. It is hypothesised that ball milling introduced a more beneficial particle size distribution compared to sieving. Due to the violent nature of ball milling, it is hypothesised that a lot of nanoscale particles were created. This is reinforced by the SEM microscopy images. In these image, more very small (<1 µm) particles are visible between a ball milled and sieved sample, for the same maximum particle size. This is presented in Figures 5.24 and 5.25.

Ball milled samples required less energy to be manufactured. It is hypothesised that this is the result of increased surface area created. A part of the energy has already been spent with ball milling the material.

Therefore, depending on the actual mission design, the increased energy cost of ball milling might be of-set by a decrease in sintering energy consumption.

These factors results in ball milled material being similar to sieved material, but with the addition of many particles that are orders of magnitude smaller. For MGS-1 simulant, this only has an effect as is described in Herring's Scaling Law [96, 131]. For JEZ-1, there is relatively less smectite present when ball milling. The main particle size group that is present, is still similar to the sieved material and sinters similarly. Only now, there are also more nano-particles present. These particles don not contribute to sintering when embedded within smectite. They do, however, slightly increase sintering at locations where voids would otherwise be present. Therefore, the relative decrease in smectite has less impact.

Particle size reduction application depends on the actual practicalities of ball milling and sieving on Mars, such as energy cost, launch mass, complexity and chance of failure. The benefit of sieving was increased performance in strength at lower densities. Sieving is a relatively simple process but does produce waste. When sieving at a sieve size of <53 µm, only 44% of volume is retained [29]. With small particles clinging to larger particles, only 3.6% of mass is retained at this sieve size [29]. Waste itself is not an issue for an early Martian colony, but the increase in material to be extracted could pose an issue.

If sieving is performed on Mars, this study suggest using the smallest practical sieve size. The results suggest not sieving is better than sieving only at <250 µm, but sieving at <53 µm does yield a significant increase. It depends on the actual particle size distribution and mineralogy distribution per particle size on the colony site if sieving could pose a benefit. Ball milling has overall benefits in terms of physical properties. It is therefore suggested to use ball milling on Mars, irrespective of the soil conditions, but only if the added drawbacks of launch mass and other factors are smaller than the positive gain in performance.

To conclude, it is recommended to use small particle sizes for sintering. For the investigated simulants, a particle size of <53 µm is recommended. For real Martian regolith, this can be different. Application on Mars depends on the added complexity of particle size reduction and actual mission design. If possible, ball milling should be used, with sieving as second best and no particle preparation last. If a particle reduction method is used, it is recommended to use the smallest feasible particle size.

6.4. Drying

As expected, drying resulted in better density, compaction and strength. When using non-dried material, the adsorbed and absorbed water will escape when heated. This creates moisture. This moisture is already removed from the dry material. The added moisture can influence chemical reactions and aid in oxidation. The moisture can also create pores when it is trapped.

The increased compaction of dry material suggests that the added moisture of non-dry material is trapped. If it could freely escape, this would be identical to initially using less mass of the dried material. In turn, that would lead to a higher absolute piston travel. Therefore, compaction should increase for non-dried materials if the moisture was free to escape. It is not known what percentage of the extra moisture is trapped compared to escaped. It can be stated that the effect of trapped moisture outweighs the effect of escaped moisture in terms of compaction. Using dried material results in a lower relative mass loss, this is expected as there is less moisture to escape.

The increased energy consumption for dry material was unexpected. The evaporation due to non-dry material was hypothesised to cost more energy. Dried material resulted in better properties. Therefore it is hypothesised that more energy might have been expended for diffusion and compaction of particles. This energy increase might be more than the energy savings by using dry material.

It is recommended to dry material before sintering. The material needs to be heated regardless, which dries the material. If a drying step is implemented, where the temperature is held at 105 °C, this results in better performance. The extra energy required due to heat losses, can be minimised by applying isolating materials.

6.5. Temperature

Temperature had a large positive effect on strength, compaction and density. According to theory, this is due to the increased diffusion during sintering [96]. Temperature can also determine if a liquid will develop, causing liquid sintering, or a gas, causing pore formation or evaporation. The temperature can cause crystal structures to change and chemical reactions to take place. Increased diffusion should result in a smooth positive relation between temperature and physical properties [96]. The other described effects only happen at, or around, certain temperatures. These should lead to discontinuities in the relationship between temperature

and physical properties.

For a single constituent component system, the highest density, strength and compaction can be expected at the highest applicable temperature. For a heterogeneous material, like the ones used in this thesis, multiple discontinuities were expected. Phase change temperatures of matter, such as melting, sublimation and vaporisation, were expected to be the main reasons. Re-crystallisation or changes from amorphous material to crystalline material and vice versa were also expected. Another large influence was expected due to moisture. Evaporation of adsorbed and absorbed water, dehydration of chemically bound water and dehydroxylation all happen at specific temperature intervals and release moisture.

All of the above mentioned effects are difficult to attribute to certain temperatures. This is due to the sintering happening in a vacuum. Environmental pressure is known to influence many temperature-specific phenomena. The applied pressure on the material increases pressures within the material, but not necessarily the gas-pressure. If gasses can escape freely, gas pressure will stay at vacuum and the applied pressure is transferred solely through particles and grain boundaries. If gasses are trapped, pressures can build and effect temperature specific phenomena. This can result in decreased performance of material properties.

With all these effects in mind, it was expected that temperature results in a positively correlated trend with possible discontinuities for strength, compaction and density. The maximum strength might be obtained at a lower temperature than the maximum applicable temperature.

Temperature results show a linear behaviour. This linearity was not expected. Microstructure analysis suggested that some minerals had melted, which would result in liquid sintering. This would lead to a discontinuity at temperatures above the melting temperature. For group-1, microstructure analysis revealed that no liquid sintering had taken place. This explains why the three-level temperature variable for group-1 shows a linear trend. It can be said that the only significant effect of temperature, was increased diffusion. For group-2, only a two level temperature variable had been used. Therefore discontinuities could not be measured, but might have been present.

Temperature had a linear and negatively correlated trend with mass loss. This was unexpected. It was expected that an increase in temperature would result in more gasses forming. These gasses can escape the material due to the vacuum. Therefore more mass loss was expected at higher temperatures. One explanation is that using a higher temperature sinters the edges of the sample earlier on. This leads to a more dense and less permeable edge, which can trap gasses.

The energy consumption increases linearly with temperature. This is an expected result, as an increased sintering temperature results in more energy losses. The linearity is somewhat unexpected. Radiation losses increase with the temperature to the fourth power. This implies that energy losses are not mainly due to radiation losses, but due to more linear processes. The cooling of the punches is one such example, this is conduction which is linear with temperature. Another example is the heat transfer and storage due to the specific heat capacity of the material, punches and die.

The implication of the results is not easily concluded. Temperatures at and below 800 °C can result in infeasible materials. Temperatures above 1100 °C resulted in meltout with this specific setup. Temperatures in between this range are feasible. For the actual design of a Martian mission, the extra energy requirement of the increased temperature is a trade-of to be made. With this in mind, this study cannot conclude that one temperature is better than another. It can be stated that a higher temperature is recommended for increased material properties.

6.6. Time

As sintering duration is one of the basic variables of sintering, it was expected that a positive correlation between time and strength, compaction and density would be present [96]. In this study, time showed complex behaviour with respect to all measured variables.

Strength decreased with longer sintering from 30 minutes to 45 minutes, but increased again to the highest influence at 60 minutes of sintering. The exact opposite effect was observed for density. This means that, with only time as variable, strength-density graphs would be inverted. Sintering duration had little to no effect on macro porosity. Therefore it can be concluded that macro pore formation is not due to a time sensitive process within the scale of 30 to 60 minutes.

Compaction increased near linearly for longer sinter durations. This is expected when observing compaction graphs, see Figure 5.14. After initial fast compaction, compaction steadily increases during steady sintering parameters. The regular interval increases of compaction during this stage are hypothesised to be the result of friction releases. The material compacts due to sintering, but there is friction between the punch

and die. This friction increases with a rate similar to compaction. As the compaction rate is steady, friction increase is also steady. It is logical that there is a maximum friction possible, before the punch slips and moves inward. This therefore happens at regular intervals.

At its core, sintering time should have a positive influence on performance. Compaction visibly increases during sintering and shows no sign of a limit within 60 minutes of sintering. Compaction is a good indicator of strength. Therefore, longer sintering is still expected to positively influence material properties. Due to other time-sensitive effects, shorter sintering times can prove optimal.

The maximum sintering time was 60 minutes. It is possible that this was too short with respect to the time frame necessary for full sintering. This is suggested by the porous microstructure that persists. Only M1 and J1 microstructures showed proper sinter behaviour as is presented by literature [96]. A longer sintering duration increases energy use.

The energy consumption increased almost linearly with time. This is expected as heat transfer is a derivative of energy transferred over time.

With all this in mind, no concise recommendation can be presented for sintering duration. Longer sintering should be better, but the time-scales used in this study might fall short to prove this. Sintering shorter than 15 minutes had proven to yield insufficient results. Therefore a minimum sintering time of 30 minutes is recommended. The trade-of between energy requirement and performance should be made for future Mars missions. It must also be noted that sintering larger elements is expected to require longer sintering, as the heat needs to be properly conducted into the centre of the material.

6.7. Pressure

Applied pressure during sintering has had an expected influence. More pressure results in more compaction, higher densities, higher strengths and less porosity. Pressure is known to increase sintering performance [96]. It had a significant effect on all measured physical properties.

The applied pressure of 80 MPa was the maximum possible due to the limits of the punch and die material. As increased pressures increase performance, it is suggested to use stronger materials, such as steel or wolfram, as punch and die material. Changing the geometry of the punch can also help. Currently, the punch has a one sided hollow core so that the pyrometer can measure the temperature at the edge of the punch, closest to the material. If temperature measurements can be performed without this hollow core, or with a smaller hollow core, the area of the punch is larger. This increase in area means that more force can be applied for the same material.

The complex effect of pressure on mass loss could not be explained. For group-1, pressure showed the highest mass loss for the average pressure of 35 MPa. Two theories are possible. One theory is that an initial increase in pressure leads to more gasses being pushed out of the material, which leads to more mass loss. For even higher pressures, densification at the edges of the material might happen rapidly. Therefore, a less permeable layer is created before most gasses could escape, trapping them in the system. Another theory is that gasses are pushed out more at higher pressures. After a certain gas pressure, some gasses become fluids again. These fluids stay inside the material, resulting in less mass loss. A combination of both effects is also possible.

Applying pressure does not require much energy. The energy required for pressure application is equal to the work done by the force applied. When calculated, this was 4 to 315 Joules, an insignificant amount compared to the minimum 7.18 MJ applied for heating. The energy consumption increase due to pressure was minimal. This energy increase is not the energy required for the work done, but the additional energy required to heat the material. Thus, increasing the applied pressure is an easy and energy efficient method to significantly enhance sintering performance. It is therefore recommended to use the highest pressures available when sintering Martian regolith.

6.8. Applied Coating

The application of a BN coating shows a benefit in the compaction, density and strength results. No difference in mass loss was observed. This means that applying a BN coating has only a positive effect. Different reasons for this effect can be discussed.

Firstly, two chemical reasons can be hypothesised. The main reason for BN application was to limit the effect of carbon ingression due to the graphite sheets. If this is the only difference a coating has brought, these results would mean that it is beneficial to use other materials than carbon containing materials as the punch and die of the SPS. Currently multiple other materials can be used, such as steel and wolfram. Another

chemical reason could be the interaction of BN with the material. Although BN is known to not react with most materials, it could have acted as a flux, lowering melting temperatures or increasing the diffusion of materials.

SEM-EDS can detect boron. SEM-EDS images suggested that no BN has entered the material as no boron had been detected. However, the used voltage of 15 kV is sub-optimal for boron detection [132]. It is therefore still possible that boron had entered the material.

The last reason is a physical phenomenon. BN feels naturally smooth to the touch. It appeared to have a lower friction coefficient compared to graphite sheets. Therefore, it could have acted as a lubricant between the graphite sheets and the punch. This would mean that the punch would apply more of the pressure directly to the material. In the compaction graph, no discernible difference was observed for the steady stage of sintering, see Figure 5.14. Therefore, it is hypothesised that the coating did not have a lubricating effect.

The energy requirement to sinter a volume of material decreased significantly when a BN coating was applied. The reason for this can be that BN acted as a better heat conductor from the die to the material. Another reason can be that BN acted as a flux as described above.

The influence of the coating implies that the use of graphite paper is sub-optimal. It is therefore recommended to investigate alternative materials as a protective layer. It would be more beneficial to use a punch and die material that does not require a protective sheet. This means that no waste is created and no protective sheets should be imported from Earth. The best option would be a punch and die material which have properties similar to the BN coating, or better.

It is recommended to use a BN coating when using a similar SPS setup. This coating should be imported from Earth. This is not ideal when considering the ISRU requirement. As discussed, it is recommended to investigate alternative materials for the punch and die.

6.9. Strength

It was observed that plotting the strength versus the density resulted in a positive correlation. The correlation was highly scattered. All samples have a different set of variables due to the Taguchi design. Therefore, it was not possible to find one or more variables which resulted in clear separate trends. If no other indicator is available, density can be used to estimate performance.

The strength versus compaction graph shows a different result. It is highly correlated. Even the outliers from the strength-density graph now fit the strength-compaction relation. This means that compaction is a good indicator of sintering performance and strength results. This graph implies that it does not matter what pre-processing of material is performed, as long as it results in higher compaction. With an R^2 of 0.91, this study proposes a formula that accurately describes the relation between strength and compaction:

$$\sigma = -0.1034 \times \epsilon_{SPS} + 0.0712 \times \epsilon_{SPS}^2$$

Where σ is the corrected compressive strength of the material in MPa, with a compaction of ϵ_{SPS} in percentage. These factors need to be verified by different studies.

The implications of changing the compressive test bench were low. It is difficult to discern the used test bench in Figure 5.4. The difference between the Instron and Zwick test bench is described in Chapter 3.7. All samples below 20 MPa were tested on the Instron, which was group-1. All samples above 20 MPa were tested on the Zwick, which was group-2. The exact influence is unknown, but all samples follow the same strengt-compaction relation. If an influence is present, this can only be that the Instron reported lower strengths for identical samples compared to the Zwick. This is because the Zwick had auto levelling plates, They ensured a perfect connection when dealing with non-parallel surfaces. In theory, this increases the measured strength and makes measurements more reliable. It can be observed that an increase in strength for all Instron samples would result in these data points having a better fit with the proposed formula.

There is an absolute limit to strength that can be developed. If the material is sintered fully, meaning a 100% densification, the maximum theoretical strength should be obtained. In this case, the material contains no voids that impact strength behaviour. Therefore, there is an absolute limit to strength for a given input material. It was observed that this limit has not been reached. As the M1 and J1 microstructure suggest, liquid sintering did not happen throughout the material. M1 and J1 microstructure shows an almost zero porosity. Therefore, it is suspected that if this microstructure can be obtained throughout the whole sample, the strength will be near the maximum theoretically achievable.

By choosing the right variables, strong (>20 MPa) material can be manufactured without increasing complexity or energy requirements. This is sufficient for the proposed dome structure [26] and most other simple construction types. A high-performance material (>100 MPa) can be manufactured if necessary. JEZ-1 was more suitable for this, but MGS-1 also had this capability. A slight increase in complexity or energy requirement is necessary. This can be the use of smaller particle sizes (<53 µm), increasing the applied pressures to 80 MPa and/or increasing the temperature to 1100 °C. If two out of three conditions were met, a high-perfomance material resulted for JEZ-1 simulant. These material properties can be suitable for launch pads and larger structures.

The size effect must be accounted for when scaling results from this study to larger structural elements. Imperfections in a material result in the weakest points. The effect of imperfections does not increase evenly with regard to element size. This is called the size effect. The MSEL by Kim and Yi [123] was chosen to account for this effect. The reported compressive strengths were already corrected with this size effect in mind, see Chapter 3.7. This means that the strengths reported are characteristic for a standard cylinder. The same law can be used to calculate the strength of a larger element.

6.10. Density

It must be mentioned that density was measured by weighing the sample and measuring the volume, as described in Chapter 3.8. This was done after removing the graphite sheets if they were stuck to the sample. This removal might not have been perfect. Samples themselves might have not been cylindrically shaped. It does not matter if samples lost more mass due to improper graphite removal, as the volume itself would also become smaller. It does matter if the resulting shape was not cylindrical anymore.

Density distributions from Figure 5.9 show that some samples have a lower density in the middle than on the top and bottom. This can be explained by friction and internal pressures. The material experiences some friction with the die. This could results in lower pressures at the middle of the material compared to the edges. Some force might be transferred through the die.

Another reason could be a temperature difference between the punches and die. Concentration of electric field lines at the interface of the punch with the die can result in higher temperatures for the punch [110–112]. This could result in higher temperatures present at the contact surfaces of the top and bottom punch and the material. Due to conduction, the temperature in the middle does rise, but can be lower than at the top and bottom. A lower temperature can lead to less sintering and therefore a lower density.

A clear correlation of this effect with sintering parameters is not visible. The only discernible correlation is temperature. Both sample 3 and 9 were sintered at 1100 °C and did not show this behaviour. Sample 6 was also sintered at 1100 °C. It only showed a little decrease in density and only in middle most part. This is different compared to a gradual density decrease in other samples. Therefore, sample 6 does validate to this hypothesis. The odd sample 5 that also did not show the behaviour was sintered at 1000 °C. Therefore, all samples sintered at 800 °C showed this behaviour, most samples at 1000 °C did and only one sample at 1100 °C showed only a little sign of this behaviour. This concludes that a higher sintering temperature contributes to removing this behaviour.

Another theory could be trapped gasses. For gasses to escape from the middle of the material stack, it takes a longer path. This would result in more pores in the centre of samples. However, this theory does not explain why this behaviour is only present in some samples and not all, as there is no correlation with porosity.

6.11. Porosity

The measurements only show macro porosity. It was expected that this is lower for smaller sieve sizes. The resolution of the CT-scan is insufficient to accurately capture all porosity below 0.0001 mm^3, equivalent to about 30 voxels with 15 micron sides, this is explained in Chapter 3.8. A perfect spherical particle of 53 µm has a volume of 0.0000785 mm^3, just below the set limit. As voids between particles tend to be similar or smaller in size then their surrounding particles, especially after being sintered, it is only logical that almost no voids were detected. Therefore, sieve size was the most influential variable.

From Figure 6.1, three main sources of porosity can be distinguished. Firstly, some pores seem to present themselves without a clear reason, indicated with a ”1”. These can be due to the initial packing, but can also result from particles melting and leaching into the rest of the material or evaporating. The second type of pores are pores embedded within a certain particle type, indicated with a ”2”. These voids can be the result of certain minerals within the particles leaching out, either as a fluid or a gas, or they could be present within the particles to begin with. The third void type is clearly due to a certain particle type changing during sintering.

It is indicated with a ”3”. This particle type seems to have more shrinkage compared to the other particles. Cracks within these particles are clearly visible. This effect can be due to this particle type having a different coefficient of thermal expansion, compared to the other samples. The effect can also be due to the material partly leaching into the surrounding material or evaporating, causing shrinkage. A third reason could be that this particle type undergoes chemical or crystal change. The particle changes into a different mineral due to the sintering process. If this new mineral has a higher density, the particle shrinks.

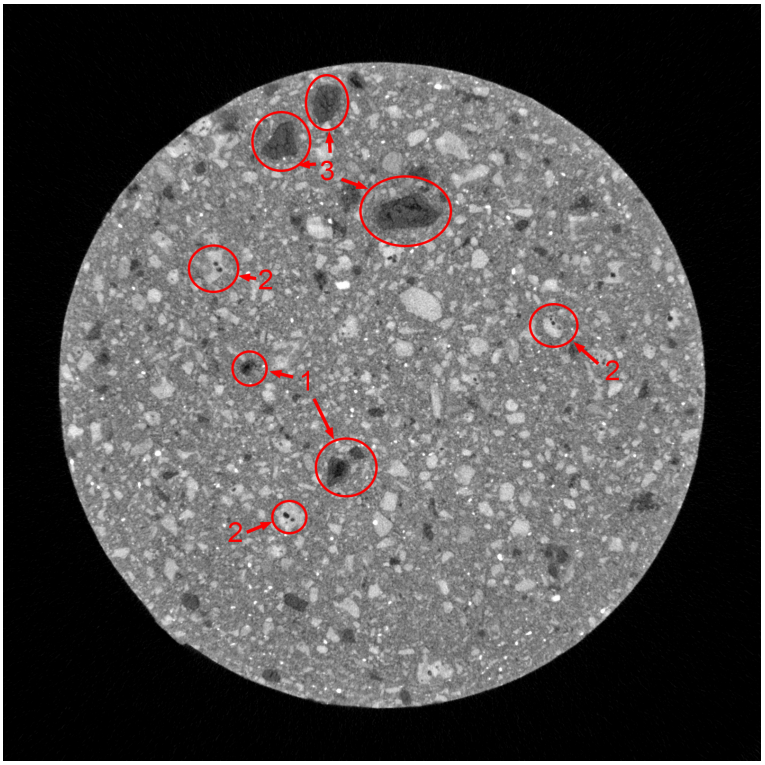

Figure 6.1: An example of a slice in from the CT data. This is a sample with a sieve size of <600 µm, sample 3. Number 1 represent normal pores. Number 2 indicates pores within a specific particle type. Number 3 indicates pores due to particle shrinkage.

6.12. Mass Loss

Mass loss can be attributed to four phenomena. The first and most important factor is mass evaporation. Due to high temperatures, some elements become volatile and escape the material as a gas. This effect is enhanced by the vacuum conditions. At lower temperatures, below 900 °C, it is hypothesised that the evaporation is mainly due to water and carbonates. Absorbed and adsorbed water, dehydration of chemically bound water and dehydroxylation all contribute to water evaporating and escaping. These effects are in order of temperature rise, with absorbed water releasing at the lowest temperatures, and dehydroxylation happening at the highest temperatures. Iron-carbonate decomposes when heated and magnesium-carbonate decomposes at 350 °C, both releasing CO_2 gas. At higher temperatures, it is not clear what causes evaporation. Some materials might boil and become a gas. Mass loss at higher temperatures can also be ascribed to the other phenomena below.

The second phenomenon is meltout. When a sufficient amount of fluid is present in the die, the applied pressure can push this fluid material, along with some small solid particles, out of the die. This is a direct mass loss. This phenomenon is easily discovered and has been noted. Only sample 17 showed this behaviour.

The third reason for mass loss is the direct loss after sintering. Due to the removal of the graphite sheets, some material is removed as well. Weight was measured after removal of the graphite sheets to ensure they had no influence. This mass loss should be similar across samples, but has variability.

The fourth reason is chemical reaction. Some chemical reactions loose mass. This happens in some exothermic reactions, where a small fraction of mass is converted into energy. From Figure 4.1 and 4.2, it can be noted that there is no clear large exothermic peak present. The conversion of mass results in enormous

amounts of energy. Therefore, the observed loss in mass would result in a significantly large exothermic peak. This was not observed.

6.13. Microstructure

Images of the microstructure show that for most samples, no liquid sintering had happened. It was also observed that most particles were intact and not fused to neighbouring particles. This both suggest sub-optimal sintering. If the material can be sinterd as structure M1 and J1 throughout the whole sample, this is expected to significantly increase all favourable properties. When this has happened, the material will behave as if it were a solid. No individual particles could break free and cracks would propagate through the sample as if it consisted of only one material. As strengths of up to 137 MPa have been reached with the sub-optimal sintered samples, it is not necessary to increase sintering for structural application. However, for other high-performance structures such as landing pads, this could prove beneficial. It is hypothesised that perfect sintering could result in strengths that are an order of magnitude larger than the maximum achieved strength of this study.

Microstructure analysis suggests that the matrix between individual particles has a similar strength to the particles. Cracks have been observed to move through the material irrespective of the difference between the matrix and particles. Some particles were observed to be stronger, resulting in cracks moving around them. The bonds between the matrix and particles is near perfect, as cracks have not been observed to solely propagate through this interface, but instead propagate through the matrix or particles itself. This means that the material can have very high peak performance, while still being heterogeneous. Only small gains can be achieved by changing the materials of the matrix or particles, as their strength is roughly equal.

Thermal cracks can reduce material performance. They have mainly been observed in M1 and J1 structures. Changing the heating rate during sintering is not expected to influence these results. Changing the cooling rate can influence thermal cracks [133]. The total thermal shrinkage will not change. A slower cooling rate can result in a more even distribution of heat. Thermal differences will be minimised, which can mitigate some thermal cracks. Thermal cracking due to differences in the thermal expansion coefficient cannot be mitigated. They can however become smaller when cooling slower. The gradual temperature decrease will lead to more, but smaller cracks forming [133]. Both of these effects are hypothesised to increase material performance. Therefore, it is suggested to use slower cooling rates for future studies.

6.14. Structural Application

Structural application of the sintered material is considered possible. The current shape is not suitable to build with. Prisms or cubes should be manufactured. These elements can be stacked to create buildings. The obtained compressive strengths are more than sufficient to build with on Mars. The size effect law must be considered when scaling the dimensions of the manufactured material. This is described in Chapter 6.9.

Individual structural elements are manufactured instead of being cast in place or 3D printed. Therefore, the elements must be stacked. This results in buildings that rely on compression only. Many such buildings can be built. A dome is a typical structure that is self-supporting through only compression. The Sagrada Família is a church build in Barcelona which relies mainly on compression to support itself [134–136]. For this study, the simple dome structure as proposed by Mintus [26] is used. This dome can protect humans from micrometeorite impacts, dust storms, radiation and the Martian atmosphere. The process of building such a dome is presented in Figure 5.30 from Chapter 5.8.

The stacking of bricks results in unavoidable gaps. The atmosphere within the building can escape though these gaps due to a pressure difference. One option is to fill these gaps with a seal. Acquiring such a seal can be difficult. It is logical to import this sealant from Earth. It must be noted that even a small failure chance of the sealant can have great effect due to the amount of gaps. If the sealant fails once every thousand applications, multiple failures are expected in a structure consisting of thousands of bricks. Even if a seal can correctly be applied, the permeability of the manufactured structural elements can prove detrimental. The permeability of the manufactured material should be studied further.

For those reasons, a separate internal tent is proposed [26]. This tent can be inflated inside the dome, providing a suitable living environment. The tent material should only be strong enough to withstand the pressure difference. All other structural protection will be enabled by the brick dome. This part should provide protection to all other hazards. Another similar option is to bring lining material. This can be used to line the inside of the dome with. This material should be airtight. At places where this lining is overlapped, an airtight connection is necessary. The advantage of this method is that the lining can be lighter than the proposed

tent. It does not have to withstand the cumulative tensile force of the atmosphere. It must only withstand the atmospheric pressure over small distances at gaps. It can also be brought as individual plates, instead of one singular tent. This decreases complexity and enhances repairability. The only drawback compared to a tent structure is the extra amount of connections between individual plates, increasing the chance of failure. Bringing plates that are as large as is feasible lowers this.

Manufacturing material with high compressive stresses is not necessary to create this building. However, it can prove vital to radiation protection. If a dome can be built with a strong material, the dome can be encapsulated by a thick layer of regolith. The stronger the dome, the thicker this layer can be. Thick structures are necessary to reduce radiation to safe levels [35, 58].

6.15. Production Feasibility

In Figure 5.30 from Chapter 5.8, the process of building a suitable structure on Mars is presented. The energy use necessary for such a building was estimated according to multiple assumptions. When using actual SPS data, the calculated energy requirement to build a dome within a 1 to 5 year mission was between 1.06 and 3.23 MW. This is significantly more than the proposed limit of 100 kW in Chapter 2.6.11.

When using DSC data, the calculated energy requirement to build a dome within a 1 to 5 year mission was between 14.86 and 18.11 kW. This is less than the proposed limit of 100 kW in Chapter 2.6.11. These values are theoretical. Often, efficiency of devices is around 50%. This means that this energy requirement must be doubled to be representative for real Martian application. Still, the values are below the 100 kW limit.

For a real Martian mission, the energy requirement is expected to be far less than the actual measured energy requirement of 1.06 to 2.23 MW. It is expected to be closer to the theoretical energy requirement multiplied by an estimated efficiency factor of 50%, resulting in an energy requirement of 29.74 and 36.22 kW. A few reasons are explained further.

First and foremost, the choice was made to run the SPS without an insulating sleeve. This was done to be able to see what happens and to spot a meltout before it could cause damage. This sleeve would have drastically reduced thermal radiation from the 1100 °C punch and die combination. A second decrease in energy consumption is expected due to larger volumes of material being sintered simultaneously. This means that there is less surface area per volume compared to this study. Less surface area per volume will decrease radiation losses in total and thus decrease energy consumption. However, larger volumes would also require longer sintering durations.

Modifying the production method will also yield lower energy requirements. In this study, the material and device were cooled completely before every new run. In reality, it is better to pre-heat the next batch of material with the cooling heat of the previous batch. Keeping the device hot and quickly loading new material will further decrease energy losses.

Another decrease in energy can be due to specialised equipment used. Different materials might result in less heat dissipation. The punches were actively cooled in this study, to prevent the loading ram from overheating. Equipment can be made that can withstand more heat, thus requiring less to no cooling at all. Extra insulation is also an easy measure to further decrease energy requirements.

Besides the mentioned measures, other device specific methods can be thought of, such as general insulation. It can be concluded that the overall energy requirement will be lowered before actual application. This means that either more structures can be built, less time is necessary to prepare a mission, or lower power energy generation is possible. As the energy required per cubic metre of material scales linearly with the total energy requirement, decreasing power consumption is a top priority.

Therefore, it is theoretically possible to manufacture the material with the specified energy limit. The actual energy requirement will be somewhere between the measured theoretical requirement and the actual energy use of the SPS device. The proposed optimisations above will bring the actual energy use closer to the theoretical energy use. The actual energy use can even be lower than the theoretical calculated value. Both the actual and theoretical energy requirement assumes only heating the material, after which the energy is lost with cooling. Some of this heat can be reclaimed. This can happen when the next batch of material is preheated with the dissipating heat of the previous batch.

The energy requirement is not directly related to higher strength materials. Therefore, with minimal energy increases, stronger materials can be manufactured. An increase in material strength can result in a decrease of the required thickness of the dome. Requiring less mass decreases the energy requirement. For this reason, it is vital that future missions are able to estimate the strength of the material. With this information, a structure can be designed and optimised.

With all of these factor in mind, it can be concluded that building a structure using the raw energy requirements of the SPS, is improbable. It can also be concluded that the theoretical power draw is well within the proposed limit of 100 kW. Therefore, when accounting for possible optimisations in manufacturing and building, it is expected that a Martian colony can feasibly be developed using SPS.

It is also presented that the time necessary to manufacture bricks depends on multiple undetermined variables. With the assumptions made, it can be concluded that the manufacturing process produces enough structural material within a reasonable time-frame.

The exact shape of bricks can be optimised for a dome structure. In the calculation, only prism shaped bricks were considered. When a trapezoidal prism is manufactured, the bricks can be stacked without having to cut them into desired shapes. Trapezoidal prisms are possible to manufacture with SPS.

Within the building of the dome, some structural parts were not considered. For example, a strong foundation is necessary to support the weight of the structure. The loose regolith can easily subside under such forces. The determination of such factors require more advanced mission designs. It is hypothesised that the manufactured material can possible also be suitable for foundations.

According to ESA's Science Advisor & Spaceship EAC Coordinator, Dr. Aidan Cowley, a more pressing problem is launch sites. On Mars, spacecraft should be able to land and launch from a solid launch pad, in order to enable a safe human return missions. The performance of launch site materials needs to be extraordinary. Exact parameters are still unknown, but challenges include: thermal shock, ablation, pressure and weight of the spacecraft, drive plume ventilation, temperature stability and dynamic loading. Investigating these properties can be difficult and requires specialised equipment. With the observed material properties in this study, the material might be suitable for such extreme conditions.

Another problem influencing the feasibility of this method is the durability of the devices used. The SPS should be able to operate fully autonomously. Similarly, the rovers used for gathering resources and building the structure should not fail either. Industrial application of SPS [120] indicates that it is possible to use SPS autonomously. On Earth, devices are built with maintenance in mind, this is not suitable for use on Mars. Materials should be durable to withstand thousands of production cycles. Dust on Mars can also enter the system when the vacuum is flushed as new material is loaded. It should be prevented that dust can built up on critical components.

It should be noted that the scalability of SPS is not seen as a problem [36, 37]. Numerous industrial applications are currently in use which use large sintering sizes [120]. Therefore, by using SPS, no new challenge is added for a future Martian mission. It is technologically feasible.

7
Conclusion

This study investigated answers for the main research question: *"What is a viable bulk construction material for use on Mars during early stages of colony development, manufactured using ISRU processes?"*

Different resources and manufacturing methods have been investigated. The most optimal manufacturing method and resource have been chosen for experimental research. In this thesis, it was hypothesised that a sufficiently strong and dense construction material can be manufactured using SPS, while using MGS-1 and JEZ-1 simulants as a substitute for Martian regolith. Due to the properties and scalability of SPS, it is suitable for manufacturing bulk construction material on the surface of Mars with low energy consumption. The studied properties of the manufactured material were hypothesised to show performance, suitable for construction materials. This was validated though experimental research. This resource and manufacturing process comply with the ISRU and early colony requirement.

The conclusion to this hypothesis is: **ISRU bulk construction material manufacturing on Mars, for early colony development, is possible by using regolith simulant and SPS.**

The minimum required compressive strength of 1.9 MPa was readily achieved with SPS. Only 2 out of the 20 samples did not reach this strength. A maximum compressive strength of 137 MPa was found with an average of 48.50 MPa. Combined with the possible shape geometries of SPS, the manufactured material is expected to be structurally applicable. The measured theoretical energy requirement was 17.07 GJ/m^3. The applied energy use was 2.72 TJ/m^3. A reference dome [26] requires a feasible theoretical 89.5 kW or infeasible applied 14.3 MW for one year. The latter value was elevated due to experimental factors. The actual energy requirement of a Martian mission is expected to be closer to the theoretical energy requirement. Water vapour was produced during sintering. This is a vital benefit to a Martian colony [21, 27]. Both the material used and the manufacturing method met the ISRU and early colony requirements.

The following sub-questions were answered in this thesis:

1. *Which raw resources are available on Mars?*
   Martian regolith was the resource of choice for this study, due to the answers to the sub questions a-f. Regolith was deemed viable for study in terms of ISRU, bulk availability and ease of extraction. As Martian regolith is not available on Earth, Martian simulants MGS-1 and JEZ-1 were acquired. Their high similarity with Martian regolith makes these two simulants the best option for testing Martian regolith [22, 29–31]. MGS-1 was chosen as it is representative of the average Martian regolith [29]. Therefore, results from the study are representative for most locations on Mars. JEZ-1 was chosen as it is representative for a future mission location, the Jezero crater [30]. Due to its differences in mineralogy compared to MGS-1, JEZ-1 could prove a better alternative.

   Other raw resources had sub-optimal properties within the sub questions a-f below. An important notion is that the use of water was not possible according to the set requirements [21, 27, 28]. This question has been more extensively answered in Chapter 2.4. There, results are presented for all raw resources that were considered, but were ultimately infeasible. Therefore, the following sub questions are only answered for Martian regolith.

   (a) *Where are they located?*
   Martian regolith is located across almost the entire planet [59]. The dust cover map in Figure 2.1 indicates locations where regolith is present. It is available at most landing sites of interest [7, 27], i.e. at the equator. MGS-1 is an accurate representative simulant of average Martian regolith [22, 29, 31]. JEZ-1 is an accurate representative simulant tailored towards the expected mineralogy in

the Jezero Crater [30].

(b) *In what quantities are they present?*
The regolith layer can be between 2 and 17 metres deep [60, 61]. Therefore, regolith is considered available in bulk. Due to its availability and abundance, regolith is generally considered as the most feasible material to manufacture bulk materials from [15, 22–24, 26, 31, 53, 64–67]

(c) *How can they be extracted and how difficult is this process?*
Regolith can easily be extracted with simple digging tools. The material is not consolidated and therefore easy to extract. Regolith can be sieved, ball milled or magnetically separated. This enables selective extraction of beneficial minerals.

(d) *What is their chemical composition?*
Regolith has a chemical composition that is similar to most rocks on Earth [62, 63]. A full overview is presented in Table 2.4. It was noted that the mineral composition is more important than the chemical composition.

(e) *What is their mineral composition?*
The mineral composition of Martian regolith consist mainly of commonly found minerals on Earth. Anorthosite, basalt, pyroxene and olivine are the main constituents [73]. A full overview is presented in Table 2.8. Here, the mineralogy for both Martian regolith and the simulants is presented and compared. Smectite and magnesium-carbonate are added to the JEZ-1 simulant [30]. The amount of olivine is also increased compared to MGS-1. This is representative for the expected mineralogy in the Jezero crater based on orbital observations [30].

(f) *What is their particle size distribution?*
The particle size distribution of regolith varies widely by location [75]. The used simulants have a well-graded distribution from 0.04 µm up to 600 µm [29, 30]. The particle size distribution per mineral was investigated and is presented in Chapter 4.2. With this data, it was concluded that sieving can result in differing mineral ratios, which could prove beneficial.

2. *What production processes are available to convert these raw materials into construction materials?*
Sintering was chosen as production process of choice for this study, due to the answers to the sub-questions 1.(a-d). The sub-questions 2.(a-d) determine whether a method is suitable for ISRU and early colony development. Two other feasible processes were full melting of regolith and cold-pressing. Sintering was chosen due to its significantly increased proposed strength compared to cold-pressing, while having a significantly lower energy requirement compared to melting. Sintering uses heat to fuse a green body [91, 96]. The material is not heated to melting temperatures. Diffusion of elements fuses particles together. This results in cohesive and strong materials [96].

   Some other processes did score better on certain sub questions, but ultimately failed one or more of the requirements. This question has been more extensively answered in Chapter 2.6. There, results are presented for all production processes that were considered. The following sub questions are only answered for the feasible processes: sintering, melting of regolith and cold-pressing.

   (a) *What is the energy requirement?*
   The energy requirement of sintering is a drawback. Material is heated up to 50-80 % of the melting temperature [15, 96]. Therefore, the energy requirement is lower than melting the material fully, but higher than cold-pressing.

   (b) *Is the process suitable for manufacturing bulk construction materials?*
   Sintering, melting and cold-pressing can all be scaled to any size. Multiple simultaneous production

lines can be used to speed up the process. Therefore, bulk construction materials can be manufactured.

(c) *What is the proposed strength of the material?*
Strengths for sintering techniques vary widely, but the process is shown to yield strengths of up to 232 MPa in compressive tests [98], and 53 MPa in flexural bending [53]. Melting has been shown to result in a compressive strength of 120 MPa [65], and tensile strength of 500 MPa [94] for Lunar regolith. It has not been investigated for Martian regolith. Cold-pressing can result in compressive strengths of up to 7.39 MPa [65, 66], and flexural strengths of up to 50 MPa [64].

(d) *Can the proposed material be utilised as a structural element?*
The sintering process can manufacture elements in a variety of shapes. The shapes are only limited by the green body. A green body can be made in almost any shape, as long as the particles stay cohesive before and during sintering.
Melting results in cast elements. Casting can be performed for any shape. A building can also be cast in-situ, similar to casting concrete. Therefore, the structural material is suitable as a structural element.
Cold-pressing is limited to the compression direction. Therefore, the basic process can only make shapes whose third dimension is a stretched 2D shape. This means that conventional bricks and beams can be manufactured. Complex shapes can be cold-pressed with more advanced methods [26]. Although the shape is sufficient to manufacture structural elements, the strength limits this. The proposed strengths are sufficient to build a minimal construction. Therefore cold-pressing is just sufficient to manufacture structural elements.

3. *Which of these processes should be subject to further study and tested in experimental research?*
This question has been answered with the answers given in the previous question, namely sintering was chosen. A specific sintering technique was determined to be most suitable. This was SPS. SPS uses heat and applied pressure to consolidate material [96]. Instead of a seperate green body, SPS compresses unconsolidated material into a green body while directly sintering it. This limits the element shape to stretched 2D shapes. The additional compression during sintering significantly increases performance [91, 96].

   SPS was chosen to manufacture a structural material from Martian simulant MGS-1 and JEZ-1. The controllable environment of the SPS chamber made vacuum operation possible. This is more representative as the Earth's atmosphere is proven to decrease sintering performance of MGS-1 [26, 53]. More information about the Martian environment and its influences is presented in Chapters 2 and 3.3.

   (a) *Are the answers given to 1.(a-f) sufficient for this specific production process?*
   The SPS process is compatible with the Martian simulants. This has been proven for MGS-1 [122] and was expected to hold for JEZ-1.

   (b) *Are the answers given to 2.(a-d) sufficient for the proposed structural requirements? (See 1.2.1 for the definitions of sufficient.)*
   SPS is suitable for the early stages of colony development and ISRU requirements. It is capable of bulk production of sufficiently strong structural elements. The actual energy requirements should be investigated to conclusively answer this question. This has been done in question 4.(c).

   (c) *Is the production process suitable for lab-scale testing?*
   SPS is suitable for lab testing. It is scalable, meaning that lab tests can be applied on industial scales [36, 37, 120]. Due to the vacuum chamber, the Earth environment in a lab does not have an influence.

   (d) *How could Martian conditions influence the production process?*
   Oxidation can happen naturally in the Earth environment and not on Mars [26, 53]. The decreased

oxidation in a Martian or vacuum environment results in better performance while sintering [26, 53]. Due to the controllable environment of SPS, oxidation has been minimised. However, oxidation might still have happened during storage and handling. The moisture content of the Earth's atmosphere is expected to have negatively influenced results. Therefore, material properties are expected to be better on Mars.

The lower gravity on Mars is not an issue for SPS. The SPS process is contained and applies internal pressures on its own, even exceeding the gravitational forces on Earth. The Martian atmosphere is not an issue when manufacturing on Mars itself, as the process is performed in a vacuum. The dust present in the atmosphere might pose a problem to the durability of the device.

4. *What are the properties of the production process?*
The SPS process has many variables. Most importantly, the input material can be changed or modified. Different simulants can be used. They can be sieved or ball milled to reduce the particle size to different levels. The material can also be dried before use. The profile of temperatures, pressures, chamber conditions and more, can be set up, this makes the device variables endless.

   Both simulant types were subject to three modifications: particle size used, particle size reduction method and drying. Four SPS parameters have been analysed: temperature, duration, applied coating and applied pressure.

   (a) *What influences the physical properties of the manufactured material and how?*
   It was discovered that the following variables influenced the physical properties of the manufactured material: simulant type, particle size, particle size reduction method, temperature, sintering time, drying, coating, and pressure.

   Without discernible drawbacks, JEZ-1 drastically increased the physical performance of the manufactured material compared to MGS-1. Mass loss was reported to be higher for JEZ-1. This is not an issue as regolith is readily available in bulk on Mars [59–61]. An added benefit of this mass loss is the generation of water. It was suspected that most of the mass loss was due to evaporation of adsorbed and absorbed water, dehydration of chemically bound water and dehydroxylation. All of these processes release moisture. Increasing the available of water for the colony is beneficial. Otherwise, water needs to be extracted through other energy-intensive means [21].

   For practical application on Mars, it is suggested to use a location with as much smectite, magnesium-carbonate and diatomaceous earth equivalents as possible. These minerals have been observed to be responsible for most of the increase in material property performance and the release of water.

   Smaller particles sizes increase sintering performance [96]. When sieving, it was observed that a particle size of <53 µm yielded the best results. Sieving for <250 µm resulted in worse material performance and sieving for <600 µm maintained better results than <250 µm, but still significantly worse than <53 µm. This effect is attributed to three phenomena. A smaller particle size results in better sintering. A smaller particle size includes more of the favourable diatomaceous earth upon sieving. Larger sieve sizes have better packing, resulting in increased contact area for sintering. For JEZ-1, sieving to smaller particles sizes includes more smectite in addition to diatomaceous earth.

   Ball milling yielded better results than sieving when using <53 µm and <250 µm particle sizes. Application on Mars depends on the added complexity of particle size reduction and actual mission design. If possible, ball milling should be used, with sieving as second best and no particle preparation last. If a particle reduction method is used, it is recommended to use the smallest feasible particle size.

   Drying the material before sintering increases sintering performance. The material needs to be heated regardless, which will dry the material. If a drying step is implemented, where the temperature is held at 105 °C or higher, better performance is achieved. The extra energy required due to heat losses, can be minimised by applying isolating materials.

   The implication of the temperature results are not easily concluded. Temperatures of ≤800 °C can result in infeasible materials. Temperatures of >1100 °C resulted in meltout with this specific setup. Temperatures in between this range were feasible. For the actual design of a Martian mission, the

extra energy requirement of the increased temperature is a trade-of to be made. With this in mind, this study cannot conclude on the optimal temperature. Higher temperatures did increase material properties significantly.

No concise conclusion can be presented for sintering duration. Longer sintering should be better [96], but the maximum 60 minute sintering duration of this study might fell short to prove this. Compaction was observed to slowly increase over time. Sintering shorter than 15 minutes yielded insufficient results. Therefore, a minimum sintering time of 30 minutes is recommended. The trade-of between energy requirement and performance should be made for future Mars missions. It must also be noted that sintering larger elements is expected to require longer sintering, as the heat must be properly conducted into the centre of the material.

The application of pressure resulted in significantly improved material performance upon higher pressures. Applying pressure does not require much energy. The energy requirement for pressure application is equal to the work done by the force applied. This was 4 to 315 Joules for the lowest and higher pressures used. This is an insignificant amount compared to the minimum 7.18 MJ applied for heating. Thus, this is an easy and energy efficient method to significantly enhance sintering performance. Therefore, it is recommended to use the highest pressures available when sintering Martian regolith. Stronger punch and die material will help to increase the limit of the applied pressure.

The application of a BN coating shows a benefit in the compaction, density and strength results. No difference in mass loss was observed. This means that applying a BN coating has a positive effect on all of the measured properties. It is recommended to use a BN coating when using a similar SPS setup. This coating should be imported from Earth. This is not ideal when considering the ISRU requirement. It is recommended to investigate alternative materials for the punch and die to obtain this effect without a coating.

(b) *Does the process yield enough material?*
The average mass loss during sintering was 4.82% for MGS-1 and 17.2% for JEZ-1. Due to the abundance of regolith [59–61], enough bulk material can be manufactured even with these mass losses.

Due to the scalability of the SPS process, one device or multiple devices can be used on Mars that manufacture enough material for construction. Depending on actual sintering time, brick size and number of devices, it was concluded feasible to use one device to manufacture all structural material.

(c) *What is the energy consumption of the process and is this feasible?*
According to the energy draw of the non-optimised lab-setup of SPS, an energy production of 1.06 to 3.23 MW is necessary to build a simple dome structure. These values are for 1 to 5 years of preparation, respectively. This is infeasible according to the requirement of this study of 100 kW energy generation. According to the theoretical energy draw measured using DSC, the power draw is between 14.86 and 18.11 kW for 1 to 5 years of preparation. This is feasible according to the limit of this study, which was 100 kW.

The real feasibility depends on the actual improvements made to the SPS process before use on Mars. It is expected that the energy requirement will get closer to the theoretical power draw for a well-designed mission. Building a structure using the raw energy requirements of the SPS, is improbable. however, the theoretical power draw is well within the proposed limit of 100 kW. It is most probable that the actual energy requirement is about twice the theoretical, when accounting for inefficiencies. Therefore, when accounting for possible optimisations in manufacturing and building, it is expected that a Martian colony can feasibly be developed using SPS.

5. *What are the physical properties of the manufactured construction material?*
The manufactured material was tested for uniaxial compressive tests, density, porosity, compaction and microstructure. Below, the results of each test is concluded on.

(a) *What is the strength of the material and is it sufficient?*

Corrected compressive strength results show that strengths between 0.001 MPa and 137 MPa were obtained. Only 2 out of the 20 samples had strengths below 1.9 MPa, depending on the parameters described above. The strength showed a high correlation with measured compaction. Therefore the following relation was suggested (R^2 = 0.91):

$$\sigma = -0.1034 \times \epsilon_{SPS} + 0.0712 \times \epsilon_{SPS}^2$$

Where σ is the corrected compressive strength of the material in MPa, with a compaction of ϵ_{SPS} in percentage.

The factors need to be verified by different studies. A minimum strength of 1.9 MPa was set as a requirement to be able to build a construction on Mars, see Chapter 3.5. Only 2 out of the 20 samples manufactured did not reach this threshold. By choosing the right variables, strong (>20 MPa) material can be manufactured without increasing complexity or energy requirements. This is sufficient for the proposed dome structure [26] and most other simple construction types.

A high-performance material (>100 MPa) can be manufactured if necessary. JEZ-1 was more suitable for this, but MGS-1 also had this capability. A slight increase in complexity or energy requirement is necessary. This can be the use of smaller particle sizes (<53 µm), increasing the applied pressures to 80 MPa and/or increasing the temperature to 1100 °C. If two out of three conditions were met, a high-perfomance material resulted for JEZ-1 simulant. This material can be suitable for launch pads or larger structures. Increased strength is also more suitable for regolith covered structures which provide high radiation protection [35, 57, 58].

(b) *What is the microstructure of the manufactured material?*
SEM microstructure images showed two distinct microstructure types for both simulants. The first was a more open structure. For MGS-1, this consisted of individual angular particles fused at their contact areas, this microstructure was named M0. For JEZ-1, this consisted of individual angular particles fused by smectite clay and sporadic contact areas, named J0. The second was a solid, almost zero porosity, structure. For MGS-1, this consisted of agglomerated rounded particles that were fused at numerous contact areas, with a binding matrix in between. This structure was named M1. For JEZ-1, this consisted of agglomerated rounded particles that were bound by a solid matrix of and fused only at sporadic contact areas. This structure was named J1.

It is suspected that even higher strengths are possible. The aforementioned J1 and M1 structures were suspected to cause a significant strength increase. They were only present on the edges of the samples. If this can be obtained throughout the whole material, compressive strength is expected to increase with an order of magnitude.

(c) *What is the density of the material?*
Densities of the manufactured material ranged from 1800 to 2636 kg/m^3, depending on the parameters used. Density showed a positive correlation with strength, but no clear relation could be obtained.

The density of the material is an important factor for radiation protection [35, 57, 58]. Various factors influence radiation protection, of which density can give a rough estimation. Moreover, density is important for structural application as it determines the self-weight of the building.

(d) *What is the density distribution inside the material?*
The density distribution shows that some samples had a lower density halfway, compared to the top and bottom. This suggested that sintering had not been performed equally throughout the samples. Temperature was the most important influencing factor for this phenomenon.

Results also showed that along the radial profile, the centre of the cylinders was most dense. The density steadily decreased towards the edges. At the edge, density was higher again, but this might have been influenced by the CT.

(e) *What is the macro porosity of the material?*
Macro porosity was detected by CT-scans. Macro porosity was defined as pores larger than 0.0001 mm^3, equivalent to about 30 voxels with 15 micron sides. The macro porosity depended significantly on the sieve size used. Macro porosity's of 0.000%, 0.111% and 0.537% were observed for the sieve sizes <53 µm, <250 µm and <600 µm, respectively. Sintering temperature also showed an influence in the porosity distribution. Above 1100 °C, the porosity distribution was skewed toward smaller pores.

It was discovered that some types of particles induce macro porosity. A better performance may be obtained through the removal of these particles. They might be responsible for liquid sintering. In which case, removing them will have the opposite effect.

(f) *Is the manufactured material applicable as a structural element and how should it be applied?*
The manufactured material consists of individual elements. A structural elements' 3D shape is obtained through the stretching of a 2D shape in the 3^{rd} dimension. The strength was sufficient to stack the material high enough for structural applications.

It is possible to build (large) structures with the manufactured material. Stacking simple structures such as domes and arches is possible without binder. Roads and launchpads can be built. Application of the manufactured material was discussed for the reference design of Mintus [26]. This dome can protect humans from micrometeorite impacts, dust storms, radiation and the Martian atmosphere. An inflated structure as internal lining is necessary to create a liveable environment. The unknown gas permeability and gaps between bricks would otherwise result in egression of the living atmosphere and a drop in pressure.

A material resistant to high compressive stresses is not necessary to create this building type. However, it can prove vital to radiation protection. If a dome can be built with a strong material, it can be encapsulated by a thick layer of regolith. The stronger the dome, the thicker this layer can be. Thick structures are necessary to reduce radiation to safe levels [35, 58]. This is presented as an optional stage in Figure 5.30.

8
Recommendations

During the study, several interesting results have been obtained. Some of these results require more attention or are compelling to study further in and of itself. Therefore, several recommendations are made for further study.

1. EDS maps and EDS point analysis have been performed to investigate the process of sintering. The goal was to analyse the individual minerals before and after sintering, to determine the exact minerals that contribute to sintering. This proved very difficult. EDS-maps result in element or oxide percentages detected. The minerals present in the simulants have great similarities in terms of elemental and oxide percentages. Also, the crystallinity could not be determined. For identical elemental composition this can result in several different minerals. An example is α-quartz, β-quartz, cristoballite, tridymite, amorphous glass and more. All these different minerals have the exact same elemental composition but result in greatly different properties.

   Therefore, a more thorough and focused study is recommended to analyse this. This study should accurately determine the individual minerals and their complex interaction during sintering. More than just EDS analysis should be performed, such as electron crystallography and XRD. With those technologies, not only the composition can be determined but also the mineralogy with respect to crystal structure. EDS-mapping is still required to analyse where the change has taken place and if that influences the material properties. Due to the heterogeneity of the simulants, it is recommended to also separate minerals and study their effect individually.

   If each specific minerals effect on sintering is analysed, optimisations can be made. On Mars, minerals could then be separated to greatly increase sintering performance. The results should also explain the complex DSC-TGA curves observed. If the influences presented in these curves can be attributed to certain minerals and processes, a more founded approach for optimising sintering can be used.

2. Another microscopy study can be performed that systematically quantifies the fused area of the particles. The systematic approach would consist of a constant and large amount of SEM images equally distributed over the cut surface area. Where the cut surfaces should be similar between samples. The samples should not be broken in compressive testing for this analysis. The contact area of particles is a consistent measure of material properties [96].

   This study can be extended by making samples though controlled fusion of every constituent component of the simulants. In this case, the sintering behaviour between particles of different chemical and mineral composition can be determined. Varying the particle sizes can result in accurate models of sintering of Martian simulants.

3. Mercury Intrusion Porosimetry (MIP) had been performed to analyse the micro porosity in complement to the analysed macro porosity. Due to unfortunate events, MIP was unavailable for all but one sample. Therefore, it is recommended to investigate micro porosity further. It can be discovered that a certain porosity distribution is more beneficial than another. This can explain differences between material inputs, present more insights in the specific mechanisms of sintering and can also serve as a guide on how to improve performance.

4. Advanced theoretical models can be made to analyse the behaviour of the material during sintering. A base model for the heat and stress distribution throughout the sample, die and punch is a first step towards this goal. As the sintering process is dependent on the actual behaviour of the material, this

should also be modelled. Making the model closer to reality will lead to more accurate results. This means adding more and more complex interactions to the model. With this model, predictions can be made for material properties. This model can also explain certain results, such as the density distribution in the sample. The complexity of interactions and verification make the development of such a model difficult. Therefore, it is recommended to first study the interactions and behaviour of sintering with real tests.

5. The observed M1 and J1 structures showed signs of good sintering performance. It is therefore recommended to investigate the conditions under which these microstructures form. CT of all samples could indicate the exact amount of M1 and J1 present in the samples. For this study, CT had only been performed for the group that did not show this microstructure. With these values, the optimal sintering parameters can be determined for manufacturing as much M1 and J1 as possible within a sample.

6. In this study, only the uniaxial compressive strength has been investigated. For the proposed structure, this is sufficient. Tensile tests and three point bending tests are recommended to investigate. These results can influence the possibility of structures. Other properties should also be investigated before a complete structural design can be made. Density and mass loss have been investigated in this study. The Young's modulus, coefficient of thermal expansion, radiation resistance and gas permeability have yet to be analysed.

7. The magnetic properties of Martian regolith have not been investigated in this study, but could prove useful. It was determined that after sintering, magnetic properties remained. The samples could be picked up by a weak standard refrigerator magnet. The simulant material itself showed static properties as it tended to stick to plastic surfaces. This can be either due to magnetic properties or static charge. The former implies the presence of ferromagnetic particles.

   The effect of ferromagnetic particle content on the SPS process can be investigated through removal of these particles with a magnet before sintering. Both the magnetic property as well as the high conductivity of metals can have an effect on sintering [96]. The former due to induction heating and the latter due to Joule heating.

8. The simulants used had a large (4-6%) content of conductive metallic material. For conductive materials, the heat distribution in SPS is different, materials heat up from the inside [110–112]. It is not known to what degree the conductivity of the simulants influences the heat distribution. Therefore, this should be analysed.

   If a significant amount of heat is applied from inside the material, then scaling SPS for Martian regolith does not increase sintering time. This result would be beneficial for the potential energy consumption on Mars as well as the time-frame to manufacture the material.

9. Testing of properties during this study had been done at room temperatures. As indicated in 2.3.2, the actual temperature on Mars is low and fluctuates significantly. Therefore, it is recommended to study the influence of cryogenic testing on the material properties.

10. For actual application on Mars, the durability of the material is important. The materials properties should be sufficient throughout the expected lifetime. Repairability is also an important factor. This can extend the lifetime of a material. The total lifetime of the material should minimally be the expected Mars mission duration of 5 years [7]. A longer lifetime results in growth, as the previous structure can still be used while newer buildings are completed. Durability should at least be tested for temperature cycling and a low pressure Martian environment.

11. The durability of the SPS process should be investigated. On Mars, the device should run autonomously for many years without possible repairs. The many heat-cycles the punch and die have to endure can degrade their performance. Dust accumulation can also cause parts to break. If it is known exactly where, how and how much this happens, the design might be altered to allow for zero maintenance, or replacement parts can be build-in. This is a challenging mechanical engineering problem.

12. Before actual Martian application, the process of sintering should be optimised. This study investigated the feasibility of sintering and provided a rough guideline for process design. This process should be fine-tuned. When the aforementioned recommendation have been studied, the complete capabilities of sintering Matian regolith should be known. These properties should be optimised for by testing several different sintering conditions, sintering devices, methods and materials. The results can then be used to accurately design structures for future Martian missions.

    The optimisation should also be investigated for variability in properties and size. The material properties should not vary too much. The size is especially important for building domes and arches. The key-stone should fit perfectly and will determine if the structure is safe.

13. It was mentioned that according to ESA's Science Advisor & Spaceship EAC Coordinator, Dr. Aidan Cowley, landing pads are a very pressing challenge for future Martian missions. With the high possible performance of the manufactured material in this study, it could be suitable for such uses. This requires further testing. Thermal shock resistance, ablation resistance, dynamical loading from the spacecraft, drive plume ventilation and temperature stability should be investigated.

14. Improving the efficiency of sintering would be very beneficial to the feasibility of sintering on Mars. It would also be benificial for a Martian mission as a whole if better methods of energy production are possible locally. Therefore, it is recommended to study both energy consumption efficiency and energy generation improvements.

15. The influence of the size effect of this specific material is unknown. Generally, the larger the element size used, the weaker is becomes [123]. As real application will use larger size elements. It is important to know their properties.

16. The effect of sintering different shapes than cylinders should be investigated. 90°corners might have an influence on the heat distribution due to the applied electricity. It might also have an effect on the heat- and pressure distribution in the sample. It should also be investigated what the optimal shape is for Martian construction. With trapezoidal prisms, domes can easily be built.

17. Residual stresses due to the heating and subsequent cooling of the material can play an important role in material properties. Their effect in relation to several sintering parameters, such as temperature, heating rate, cooling rate and applied pressure during cooling should be investigated.

References

[1] NASA; JPL-Caltech; ASU; MSSS. *Perseverance Captures Image of Kodiak*. Figure. 2021.

[2] R. M. Zubrin. “The economic viability of Mars colonization”. In: *Science and Technology Series* 92 (1997), pp. 239–256.

[3] Jason G. Matheny. “Reducing the Risk of Human Extinction”. In: *Risk Analysis* 27.5 (2007), pp. 1335–1344. ISSN: 0272-4332. DOI: https://doi.org/10.1111/j.1539-6924.2007.00960.x.

[4] Dr Shubov. “Feasibility Study For Hydrogen Producing Colony on Mars”. In: *arXiv preprint arXiv:2110.10795* (2021).

[5] Steve Garber. *The Space Exploration Initiative*. Web Page. 2010.

[6] THE UNITED STATES OF AMERICA (U.S.A). *National Space Policy of the United States of America*. Government Document. 2020.

[7] NASA. *Human Exploration of Mars Design Reference Architecture 5.0*. Report. NASA, 2014.

[8] NASA. *Journey to Mars*. Generic. 2015.

[9] Piero Messina et al. *The Aurora Programme*. Report. ESA, 2006.

[10] Bernhard Hufenbach, Thomas Reiter, and Elisabeth Sourgens. “ESA strategic planning for space exploration”. In: *Space Policy* 30.3, Part B (2014), pp. 174–177. ISSN: 0265-9646. DOI: https://doi.org/10.1016/j.spacepol.2014.07.009.

[11] Webster Mort et al. *Avoiding dangerous climate change*. Cambridge, UK: Cambridge University Press, 2006. ISBN: 0521864712 9780521864718.

[12] ESA. *Terrae Novae 2030+ Strategy Roadmap*. Generic. 2021.

[13] *Mars & Beyond. THE ROAD TO MAKING HUMANITY MULTIPLANETARY.* Web Page. 2021.

[14] Joseph Gottlieb. “Space Colonization and Existential Risk”. In: *Journal of the American Philosophical Association* 5.3 (2019), pp. 306–320. ISSN: 2053-4477. DOI: 10.1017/apa.2019.12.

[15] M. Z. Naser. “Extraterrestrial construction materials”. In: *Progress in Materials Science* 105 (2019). DOI: 10.1016/j.pmatsci.2019.100577.

[16] Gerald B. Sanders and William E. Larson. “Integration of In-Situ Resource Utilization into lunar/Mars exploration through field analogs”. In: *Advances in Space Research* 47.1 (2011), pp. 20–29. ISSN: 0273-1177. DOI: https://doi.org/10.1016/j.asr.2010.08.020.

[17] Kurt Sacksteder and Gerald Sanders. “In-situ resource utilization for lunar and mars exploration”. In: *45th AIAA Aerospace Sciences Meeting and Exhibit*, p. 345.

[18] ERNST A STEINHOFF. “The use of Mars and phobos to advance interplanetary flight”. In: *Advances in Space Science and Technology*. Vol. 8. Elsevier, 1966, pp. 347–383. ISBN: 0065-3365.

[19] George C Lordos, Jeffrey A Hoffman, and Sarah E Summers. “Towards a Sustainable Industrial Development of Mars: Comparing Novel ISRU/ISM Architectures Using Lifetime Embodied Energy”. In: *2018 AIAA SPACE and Astronautics Forum and Exposition*, p. 5125.

[20] Dale C Arney et al. “Sustaining Human Presence on Mars Using ISRU and a Reusable Lander”. In: *AIAA Space 2015 Conference and Exposition*, p. 4479.

[21] Angel Abbud-Madrid et al. “Mars water in-situ resource utilization (ISRU) planning (M-WIP) study”. In: *Report of the Mars Water In-Situ Resource Utilization (ISRU) Planning (M-WIP) Study* 90 (2016).

[22] David Karl et al. “Clay in situ resource utilization with Mars global simulant slurries for additive manufacturing and traditional shaping of unfired green bodies”. In: *Acta Astronautica* 174 (2020), pp. 241–253. ISSN: 0094-5765.

[23] Hui Li et al. “Development of a novel material and casting method for in situ construction on Mars”. In: *Powder Technology* 390 (2021), pp. 219–229. ISSN: 0032-5910. DOI: https://doi.org/10.1016/j.powtec.2021.05.054.

[24] Lin Wan, Roman Wendner, and Gianluca Cusatis. “A novel material for in situ construction on Mars: experiments and numerical simulations”. In: *Construction and Building Materials* 120 (2016), pp. 222–231. ISSN: 0950-0618. DOI: https://doi.org/10.1016/j.conbuildmat.2016.05.046.

[25] Yonathan Reches. “Concrete on Mars: Options, challenges, and solutions for binder-based construction on the Red Planet”. In: *Cement and Concrete Composites* 104 (2019), p. 103349. ISSN: 0958-9465. DOI: https://doi.org/10.1016/j.cemconcomp.2019.103349.

[26] Agata Mintus. “Building on Mars: Experimental research on efficient and sustainable production process and construction method”. Thesis. 2019.

[27] Robert Collom, David B Bussey, and Richard Davis. “Mars Human Landing Sites Study (HLS2)”. In: *42nd COSPAR Scientific Assembly* 42 (2018), B4. 2-29–18.

[28] Vashan Wright et al. “A minimally cemented shallow crust beneath InSight”. In: (2022).

[29] Exolith Lab. *MGS-1 Mars Global Simulant | Fact Sheet*. Online Database. 2021.

[30] Exolith Lab. *JEZ-1 Mars Global Simulant | Fact Sheet*. Online Database. 2021.

[31] Kevin M. Cannon et al. “Mars global simulant MGS-1: A Rocknest-based open standard for basaltic martian regolith simulants”. In: *Icarus* 317 (2019), pp. 470–478. ISSN: 0019-1035. DOI: https://doi.org/10.1016/j.icarus.2018.08.019.

[32] Tanmay Kadam. *Shunned By European Space Agency, Russian ROSCOSMOS To Go Ahead With Solo Mars Mission Sans ESA Rover*. Newspaper Article. 2022.

[33] The State Council Information Office of the People’s Republic of China. *China’s Space Program: A 2021 Perspective*. Government Document. 2022.

[34] Pallava Bagla. “India eyes a return to Mars and a first run at Venus”. In: *Science. doi: 10.1126/science. aal0781. Retrieved 1 May 2017* (2017).

[35] Yulia Akisheva et al. “Regolith and Radiation: The Cosmic Battle”. In: (2021). ISSN: 1803550791.

[36] Eugene A Olevsky et al. “Fundamental aspects of spark plasma sintering: I. Experimental analysis of scalability”. In: *Journal of the American Ceramic Society* 95.8 (2012), pp. 2406–2413. ISSN: 0002-7820.

[37] Eugene A Olevsky et al. “Fundamental aspects of spark plasma sintering: II. Finite element analysis of scalability”. In: *Journal of the American Ceramic Society* 95.8 (2012), pp. 2414–2422. ISSN: 0002-7820.

[38] Robert Shishko et al. “Mars Colony in situ resource utilization: An integrated architecture and economics model”. In: *Acta Astronautica* 138 (2017), pp. 53–67. ISSN: 0094-5765. DOI: https://doi.org/10.1016/j.actaastro.2017.05.024.

[39] Genichi Taguchi. *Introduction to quality engineering: designing quality into products and processes*. 1986. ISBN: 9283310845.

[40] Konstantin E) Циолковский Константин (Tsiolkovsky. “Exploration of outer space by means of rocket devices (Исследование мировых пространств реактивными приборами)”. In: *The Science Review* 5 (1903).

[41] Cyrus Foster. *NASA Ames Research Center Trajectory Browser*. Web Page. 2022.

[42] Caltech. *Rockets and Space Transportation*. Online Database. 2007.

[43] Victor R Baker. “Water and the evolutionary geological history of Mars”. In: *BOLLETTINO-SOCIETA GEOLOGICA ITALIANA* 125.3 (2006), p. 357. ISSN: 0037-8763.

[44] A. Treiman. *Venus*. Pamphlet. 2019.

[45] A. Buis. *The Atmosphere: Earth’s Security Blanket*. Generic. 2019.

[46] V. Dehant et al. “Planetary Magnetic Dynamo Effect on Atmospheric Protection of Early Earth and Mars”. In: *Space Science Reviews* 129.1 (2007), pp. 279–300. ISSN: 1572-9672. DOI: 10.1007/s11214-007-9163-9.

[47] Heather B. Franz et al. “Initial SAM calibration gas experiments on Mars: Quadrupole mass spectrometer results and implications”. In: *Planetary and Space Science* 138 (2017), pp. 44–54. ISSN: 0032-0633. DOI: https://doi.org/10.1016/j.pss.2017.01.014.

[48] US Standard Atmosphere. *US standard atmosphere*. National Oceanic and Atmospheric Administration, 1976.

[49] Thomas E Müller and Walter Leitner. *CO2 chemistry*. Generic. 2015.

[50] D. R. William. *Mars Fact Sheet*. Online Database. 2020.

[51] R. M. Haberle. "SOLAR SYSTEM/SUN, ATMOSPHERES, EVOLUTION OF ATMOSPHERES | Planetary Atmospheres: Mars". In: *Encyclopedia of Atmospheric Sciences (Second Edition)*. Ed. by Gerald R. North, John Pyle, and Fuqing Zhang. Oxford: Academic Press, 2015, pp. 168–177. ISBN: 978-0-12-382225-3. DOI: https://doi.org/10.1016/B978-0-12-382225-3.00312-1.

[52] J. W. Ashley et al. "Evidence for mechanical and chemical alteration of iron-nickel meteorites on Mars: Process insights for Meridiani Planum". In: *Journal of Geophysical Research: Planets* 116.E7 (2011). ISSN: 0148-0227. DOI: https://doi.org/10.1029/2010JE003672.

[53] David Karl et al. "Sintering of ceramics for clay in situ resource utilization on Mars". In: *Open Ceramics* 3 (2020), p. 100008. ISSN: 2666-5395. DOI: https://doi.org/10.1016/j.oceram.2020.100008.

[54] NASA. *Mars Facts*. Electronic Article.

[55] A. Eydelman. *Temperature on the Surface of Mars*. Web Page. 2004.

[56] NASA and JPL-Caltech. *Extreme Planet Takes Its Toll*. Electronic Article. 2007.

[57] Trent J Perrotto, Deb Schmid, and B Dunbar. *Radiation measured by NASA's curiosity on voyage to Mars has implications for future human missions*. Generic. 2013.

[58] K. Johnson. "Radiation Shielding Analysis of Martian Regolith Simulant MGS-1 and Polymers". Thesis. 2021.

[59] Steven W. Ruff and Philip R. Christensen. "Bright and dark regions on Mars: Particle size and mineralogical characteristics based on Thermal Emission Spectrometer data". In: *Journal of Geophysical Research: Planets* 107.E12 (2002), pp. 2-1-2–22. ISSN: 0148-0227. DOI: https://doi.org/10.1029/2001JE001580.

[60] N. Warner et al. "Near Surface Stratigraphy and Regolith Production in Southwestern Elysium Planitia, Mars: Implications for Hesperian-Amazonian Terrains and the InSight Lander Mission". In: *Space Science Reviews* 211 (2017). DOI: 10.1007/s11214-017-0352-x.

[61] N.H. Warner et al. "REGOLITH THICKNESS ESTIMATES FROM THE SIZE FREQUENCY DISTRIBUTION OF ROCKY EJECTA CRATERS IN SOUTHWESTERN ELYSIUM PLANITIA, MARS". In: *47th Lunar and Planetary Science Conference*.

[62] Doug W Ming and R. V. Morris. "Chemical, Mineralogical, and Physical Properties of Martian Dust and Soil". In.

[63] R. V. Morris et al. "Mössbauer mineralogy of rock, soil, and dust at Meridiani Planum, Mars: Opportunity's journey across sulfate-rich outcrop, basaltic sand and dust, and hematite lag deposits". In: *Journal of Geophysical Research: Planets* 111.E12 (2006). ISSN: 0148-0227. DOI: https://doi.org/10.1029/2006JE002791.

[64] Brian J. Chow et al. "Direct Formation of Structural Components Using a Martian Soil Simulant". In: *Scientific Reports* 7.1 (2017), p. 1151. ISSN: 2045-2322. DOI: 10.1038/s41598-017-01157-w.

[65] Yoji Ishikawa, Tetsuo Sasaki, and Tetsumi Higasayama. "Simple and efficient methods to produce construction materials for lunar and Mars bases". In: *Engineering, Construction, and Operations in space-III: Space'92* 2 (1992), pp. 1335–1346.

[66] Yoji Ishikawa. "Utilization of Regolith for Manufacturing Construction Material on Mars". In: *Mars*. Springer, 2009, pp. 543–550.

[67] Robertc Boyd, Patricks Thompson, and Bentonc Clark. "Duricrete and composites construction on Mars". In: *The case for Mars III: Strategies for exploration- General interest and overview(A 90-16651 05-12). San Diego, CA, Univelt, Inc., 1989* (1989).

[68] R. B. Hargraves et al. "The Viking Magnetic Properties Experiment: Primary mission results". In: *Journal of Geophysical Research (1896-1977)* 82.28 (1977), pp. 4547–4558. ISSN: 0148-0227. DOI: https://doi.org/10.1029/JS082i028p04547.

[69] R. B. Hargraves et al. “Viking Magnetic Properties Experiment: Extended mission results”. In: *Journal of Geophysical Research: Solid Earth* 84.B14 (1979), pp. 8379–8384. ISSN: 0148-0227. DOI: https://doi.org/10.1029/JB084iB14p08379.

[70] S. F. Hviid et al. “Magnetic Properties Experiments on the Mars Pathfinder Lander: Preliminary Results”. In: *Science* 278.5344 (1997), pp. 1768–1770. DOI: doi:10.1126/science.278.5344.1768.

[71] P. Bertelsen et al. “Magnetic Properties Experiments on the Mars Exploration Rover Spirit at Gusev Crater”. In: *Science* 305.5685 (2004), pp. 827–829. DOI: doi:10.1126/science.1100112.

[72] Morten B Madsen et al. “Overview of the magnetic properties experiments on the Mars Exploration Rovers”. In: *Journal of Geophysical Research: Planets* 114.E6 (2009). ISSN: 2156-2202.

[73] C. N. Achilles et al. “Mineralogy of an active eolian sediment from the Namib dune, Gale crater, Mars”. In: *Journal of Geophysical Research: Planets* 122.11 (2017), pp. 2344–2361. ISSN: 2169-9097. DOI: https://doi.org/10.1002/2017JE005262.

[74] Nathalie A. Cabrol et al. “Soil sedimentology at Gusev Crater from Columbia Memorial Station to Winter Haven”. In: *Journal of Geophysical Research: Planets* 113.E6 (2008). ISSN: 0148-0227. DOI: https://doi.org/10.1029/2007JE002953.

[75] Catherine M. Weitz et al. “Sand Grain Sizes and Shapes in Eolian Bedforms at Gale Crater, Mars”. In: *Geophysical Research Letters* 45.18 (2018), pp. 9471–9479. ISSN: 0094-8276. DOI: https://doi.org/10.1029/2018GL078972.

[76] B. Levrard et al. “Recent formation and evolution of northern Martian polar layered deposits as inferred from a Global Climate Model”. In: *Journal of Geophysical Research: Planets* 112.E6 (2007). ISSN: 0148-0227. DOI: https://doi.org/10.1029/2006JE002772.

[77] Michael Morris et al. “Mars Ice House: Using the physics of phase change in 3D printing a habitat with H2O”. In: *AIAA SPACE 2016*. 2016, p. 5528.

[78] Sebastian Emanuel Lauro et al. “Multiple subglacial water bodies below the south pole of Mars unveiled by new MARSIS data”. In: *Nature Astronomy* 5.1 (2021), pp. 63–70. ISSN: 2397-3366. DOI: 10.1038/s41550-020-1200-6.

[79] S. W. Squyres et al. “The Opportunity Rover’s Athena Science Investigation at Meridiani Planum, Mars”. In: *Science* 306.5702 (2004), pp. 1698–1703. DOI: doi:10.1126/science.1106171.

[80] Anupam K. Misra et al. “Possible mechanism for explaining the origin and size distribution of Martian hematite spherules”. In: *Planetary and Space Science* 92 (2014), pp. 16–23. ISSN: 0032-0633. DOI: https://doi.org/10.1016/j.pss.2014.01.020.

[81] Scott M McLennan et al. “Provenance and diagenesis of the evaporite-bearing Burns formation, Meridiani Planum, Mars”. In: *Earth and Planetary Science Letters* 240.1 (2005), pp. 95–121. ISSN: 0012-821X.

[82] AL Schneider et al. “Compositional constraints on hematite-rich spherule (blueberry) formation at Meridiani Planum, Mars”. In: (2007).

[83] Michael H. Carr. “Volcanism on Mars”. In: *Journal of Geophysical Research (1896-1977)* 78.20 (1973), pp. 4049–4062. ISSN: 0148-0227. DOI: https://doi.org/10.1029/JB078i020p04049.

[84] G. Neukum et al. “Recent and episodic volcanic and glacial activity on Mars revealed by the High Resolution Stereo Camera”. In: *Nature* 432.7020 (2004), pp. 971–979. ISSN: 1476-4687. DOI: 10.1038/nature03231.

[85] Eric AK Middlemost. “A simple classification of volcanic rocks”. In: *Bulletin Volcanologique* 36.2 (1972), pp. 382–397. ISSN: 1432-0819.

[86] GJ Flynn and DS McKay. “Meteorites on Mars”. In: *Mars Sample Return Science*.

[87] PA Bland and TB Smith. “Meteorite accumulations on Mars”. In: *Icarus* 144.1 (2000), pp. 21–26. ISSN: 0019-1035.

[88] John E Chappelow and Virgil L Sharpton. “Atmospheric variations and meteorite production on Mars”. In: *Icarus* 184.2 (2006), pp. 424–435. ISSN: 0019-1035.

[89] Carlton C Allen et al. “Martian regolith simulant JSC Mars-1”. In: *Lunar and planetary science conference*, p. 1690.

[90] The Martian Garden. *MOJAVE MARS SIMULANT*. Online Database.

[91] Kevin W. Farries et al. “Sintered or melted regolith for lunar construction: state-of-the-art review and future research directions”. In: *Construction and Building Materials* 296 (2021), p. 123627. ISSN: 0950-0618. DOI: https://doi.org/10.1016/j.conbuildmat.2021.123627.

[92] Dennis Tucker, Ed Ethridge, and Houssam Toutanji. “Production of glass fibers for reinforcement of lunar concrete”. In: *44th AIAA aerospace sciences meeting and exhibit*, p. 523.

[93] J Mackenzie and R Claridge. “Glass and ceramics from lunar materials”. In: *4th Conference on Space Manufacturing Facilities Princeton University*, p. 1381.

[94] Michael Magoffin and John Garvey. “Lunar glass production using concentrated solar energy”. In: *Space Programs and Technologies Conference*, p. 3752.

[95] Juergen Schleppi et al. “Manufacture of glass and mirrors from lunar regolith simulant”. In: *Journal of Materials Science* 54.5 (2019), pp. 3726–3747. ISSN: 1573-4803. DOI: 10.1007/s10853-018-3101-y.

[96] Mohammed N. Rahaman. *Sintering of Ceramics*. CRC Press, Taylor & Francis Group, 2007, p. 388.

[97] Charles H Simonds. “Sintering and hot pressing of Fra Mauro composition glass and the lithification of lunar breccias”. In: *American Journal of Science* 273 (1973).

[98] Thomas Gualtieri and Amit Bandyopadhyay. “Compressive deformation of porous lunar regolith”. In: *Materials Letters* 143 (2015), pp. 276–278. ISSN: 0167-577X. DOI: https://doi.org/10.1016/j.matlet.2014.11.153.

[99] Stephen J. Indyk and Haym Benaroya. “A structural assessment of unrefined sintered lunar regolith simulant”. In: *Acta Astronautica* 140 (2017), pp. 517–536. ISSN: 0094-5765. DOI: https://doi.org/10.1016/j.actaastro.2017.09.018.

[100] A. Meurisse et al. “Influence of Mineral Composition on Sintering Lunar Regolith”. In: *Journal of Aerospace Engineering* 30.4 (2017), p. 04017014. DOI: doi:10.1061/(ASCE)AS.1943-5525.0000721.

[101] John J. Moore et al. “The combustion synthesis of advanced materials”. In: *JOM* 46.11 (1994), pp. 72–78. ISSN: 1543-1851. DOI: 10.1007/BF03222640.

[102] Nan Su and Yaw-Nan Peng. “The characteristics and engineering properties of dry-mix/steam-injection concrete”. In: *Cement and Concrete Research* 31.4 (2001), pp. 609–619. ISSN: 0008-8846. DOI: https://doi.org/10.1016/S0008-8846(01)00460-4.

[103] Kai-tuo Wang et al. “Development of near-zero water consumption cement materials via the geopolymerization of tektites and its implication for lunar construction”. In: *Scientific reports* 6.1 (2016), pp. 1–8. ISSN: 2045-2322.

[104] Kai-tuo Wang et al. “Lunar regolith can allow the synthesis of cement materials with near-zero water consumption”. In: *Gondwana Research* 44 (2017), pp. 1–6. ISSN: 1342-937X. DOI: https://doi.org/10.1016/j.gr.2016.11.001.

[105] Geoffrey A. Landis. “Meteoritic steel as a construction resource on Mars”. In: *Acta Astronautica* 64.2 (2009), pp. 183–187. ISSN: 0094-5765. DOI: https://doi.org/10.1016/j.actaastro.2008.07.011.

[106] Shaun Moss. “Steelmaking on Mars”. In: *Mars Society Australia, June* (2006).

[107] R. Volger et al. “Mining moon & mars with microbes: Biological approaches to extract iron from Lunar and Martian regolith”. In: *Planetary and Space Science* 184 (2020), p. 104850. ISSN: 0032-0633. DOI: https://doi.org/10.1016/j.pss.2020.104850.

[108] Xirui Wang et al. “One pot facile transformation of CO2 to an unusual 3-D nano-scaffold morphology of carbon”. In: *Scientific Reports* 10.1 (2020), p. 21518. ISSN: 2045-2322. DOI: 10.1038/s41598-020-78258-6.

[109] Jiawen Ren et al. “One-Pot Synthesis of Carbon Nanofibers from CO2”. In: *Nano Letters* 15.9 (2015), pp. 6142–6148. ISSN: 1530-6984. DOI: 10.1021/acs.nanolett.5b02427.

[110] Devesh Tiwari, Bikramjit Basu, and Koushik Biswas. “Simulation of thermal and electric field evolution during spark plasma sintering”. In: *Ceramics International* 35.2 (2009), pp. 699–708. ISSN: 0272-8842.

[111] M Suárez et al. “Challenges and opportunities for spark plasma sintering: a key technology for a new generation of materials”. In: *Sintering applications* 13 (2013), pp. 319–342.

[112] Sree Koundinya. “Modelling and FEM simulation of electric field assisted sintering of tungsten carbide (WC)”. In: (2016).

[113] Sydney Do et al. “An independent assessment of the technical feasibility of the Mars One mission plan–Updated analysis”. In: *Acta Astronautica* 120 (2016), pp. 192–228. ISSN: 0094-5765.

[114] Robert W Moses and Dennis M Bushnell. *Frontier in-situ resource utilization for enabling sustained human presence on mars*. Report. 2016.

[115] CO Ujah et al. “Optimisation of spark plasma sintering parameters of Al-CNTs-Nb nano-composite using Taguchi Design of Experiment”. In: *The International Journal of Advanced Manufacturing Technology* 100.5 (2019), pp. 1563–1573. ISSN: 1433-3015.

[116] Xiang Zhang et al. “Spark plasma sintering of a lunar regolith simulant: effects of parameters on microstructure evolution, phase transformation, and mechanical properties”. In: *Ceramics International* 47.4 (2021), pp. 5209–5220. ISSN: 0272-8842.

[117] Reza Norouzbeigi and Mohammad Edrissi. “Preparation of nano alumina powder via combustion synthesis: porous structure optimization via Taguchi L16 design”. In: *Journal of the American Ceramic Society* 94.11 (2011), pp. 4052–4058. ISSN: 0002-7820.

[118] M Yousefieh, M Shamanian, and A Saatchi. “Optimization of experimental conditions of the pulsed current GTAW parameters for mechanical properties of SDSS UNS S32760 welds based on the Taguchi design method”. In: *Journal of materials engineering and performance* 21.9 (2012), pp. 1978–1988. ISSN: 1544-1024.

[119] Ignacio Arganda-Carreras et al. “Trainable Weka Segmentation: a machine learning tool for microscopy pixel classification”. In: *Bioinformatics* 33.15 (2017), pp. 2424–2426. ISSN: 1367-4803.

[120] FCT Systeme GmbH. *OUR PRODUCTS*. Catalog.

[121] *Eurocode 6 - Ontwerp en berekening van constructies van metselwerk - Deel 1-1: Algemene regels voor constructies van gewapend en ongewapend metselwerk Eurocode 6 - Design of masonry structures - Part 1-1: General rules for reinforced and unreinforced masonry structures*. Legal Rule or Regulation. 2013.

[122] Willem Hoekman. “Creating Structural Material From Martian Regolith Using Spark Plasma Sintering: Understanding the effect of additives and the possibility to lower the energy requirement”. In: (2022).

[123] Jin-Keun Kim and Seong-Tae Yi. “Application of size effect to compressive strength of concrete members”. In: *Sadhana* 27.4 (2002), pp. 467–484. ISSN: 0973-7677.

[124] Johannes Schindelin et al. “Fiji: an open-source platform for biological-image analysis”. In: *Nature methods* 9.7 (2012), pp. 676–682. ISSN: 1548-7105.

[125] Philippe Carl. *Radial Profile Extended*. Computer Program. 2020.

[126] Richard Domander, Alessandro A Felder, and Michael Doube. “BoneJ2-refactoring established research software”. In: *Wellcome Open Research* 6 (2021).

[127] Zoe Landsman. *MGS-1 Structured particle discovery and questions about mineralogy*. Personal Communication. 2022.

[128] United States Geological Survey (USGS). *How many homes can an average wind turbine power?* Dataset. 2020.

[129] Arianit A Reka et al. “Diatomaceous Earth: Characterization, thermal modification, and application”. In: *Open Chemistry* 19.1 (2021), pp. 451–461. ISSN: 2391-5420.

[130] CM Earnest. “Thermal analysis of selected illite and smectite clay minerals. Part II. Smectite clay minerals”. In: *Thermal analysis in the geosciences*. Springer, 1991, pp. 288–312.

[131] Conyers Herring. “Effect of change of scale on sintering phenomena”. In: *Journal of Applied Physics* 21.4 (1950), pp. 301–303. ISSN: 0021-8979.

[132] Jana Berlin. “Analysis of boron with energy dispersive x-ray spectrometry”. In: *Imaging Microsc* 13 (2011), pp. 19–21.

[133] Qiuhong Wu et al. “On the tensile mechanical characteristics of fine-grained granite after heating/cooling treatments with different cooling rates”. In: *Engineering Geology* 253 (2019), pp. 94–110. ISSN: 0013-7952.

[134] Santiago Huerta. “Structural design in the work of Gaudi”. In: *Architectural science review* 49.4 (2006), pp. 324–339. ISSN: 0003-8628.

[135] Jos Tomlow. “Gaudí’s reluctant attitude towards the inverted catenary”. In: *Proceedings of the Institution of Civil Engineers-Engineering History and Heritage* 164.4 (2011), pp. 219–233. ISSN: 1757-9449.

[136] Rodrigo Makert and Gilfranco Alves. “Between designer and design: Parametric design and prototyping considerations on Gaudí’s Sagrada Familia”. In: *Periodica Polytechnica Architecture* 47.2 (2016), pp. 89–93. ISSN: 1789-3437.

A

Reported Measured Data Table

Table A.1: A table containing all reported measurement data. More measurements were made than is presented. Some measurements presented are composites of other measurements.

Sample	Corrected strength (MPa)	Measures strength (Mpa)	Measured force (N)	Density (kg/m^3)	Weight in (g)
1	15.40	18.44	6.00	2309.37	16.34
2	6.79	8.09	2.55	2217.49	16.24
3	0.01	0.01	0.00	1860.03	16.36
4	8.29	9.87	3.19	2131.47	16.38
5	1.32	1.56	0.50	1949.71	16.40
6	2.75	3.27	1.06	2068.98	16.34
7	9.22	11.01	3.52	1814.62	13.29
8	17.30	20.82	6.79	1973.88	13.25
9	6.03	7.19	2.33	1801.31	13.75
10	111.49	136.10	44.14	2425.98	14.32
11	105.19	129.41	41.25	2109.11	11.32
12	23.04	27.72	8.87	2059.32	13.71
13	45.27	54.33	17.42	2411.10	16.33
14	40.73	48.81	15.40	2165.15	16.33
15	46.92	56.33	17.89	2477.95	16.32
16	102.66	123.72	40.02	2424.03	16.33
17	136.57	165.67	53.54	2459.82	16.19
18	68.75	82.90	26.42	2406.17	16.32
10b	124.07	150.85	47.90	2635.77	16.32
11b	98.13	113.58	16.84	2289.89	16.07

Sample	Weight out(g)	Mass loss (%)	Height (mm)	Initial compaction (mm)	End compaction (mm)
1	15.81	0.03	21.05	0.08	4.75
2	15.58	0.04	22.32	0.15	3.66
3	15.79	0.04	23.50	0.13	1.02
4	15.67	0.04	22.77	0.1	4.12
5	15.81	0.04	25.39	0.16	1.62
6	15.69	0.04	23.48	0.13	3.18
7	12.64	0.05	21.76	0.18	3.36
8	12.56	0.05	19.51	0.13	5.48
9	12.83	0.07	21.96	0.15	3.43
10	12.21	0.15	15.52	0.18	9.8
11	8.98	0.21	13.36	0.1	10.49
12	12.81	0.07	19.44	0.11	5.92
13	15.60	0.04	20.18	0.28	7.28
14	13.93	0.15	20.39	0.11	6.74
15	15.76	0.03	20.02	0.19	6.87
16	14.92	0.09	19.03	0.38	8.7
17	13.64	0.16	17.16	0	11.5
18	14.35	0.12	18.71	0.2	8.66
10b	13.70	0.16	16.37	0.12	12.69
11b	12.50	0.22	17.10	0	11.52

Sample	Total compaction (mm)	Compaction (%)	Porosity (%)	Surface area pores (mm^2)
1	4.67	0.18	0.4453	1456
2	3.51	0.14	0.6644	1502
3	0.89	0.04	0.5002	1070
4	4.02	0.15	0.1062	21
5	1.46	0.05	0.2206	796
6	3.05	0.11	0.0061	371
7	3.18	0.13	0.0003	0
8	5.35	0.22	0.0000	0
9	3.28	0.13	0.0000	1
10	9.62	0.38		
11	10.39	0.44		
12	5.81	0.23		
13	7	0.26		
14	6.63	0.25		
15	6.68	0.25		
16	8.32	0.30		
17	11.5	0.40		
18	8.46	0.31		
10b	12.57	0.43		
11b	11.52	0.40		

B

Supplementary Data for Compressive Testing and Young's Modulus

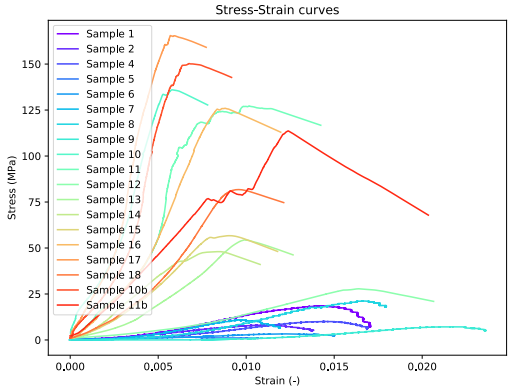

(a) The combined stress-strain curves for all samples.

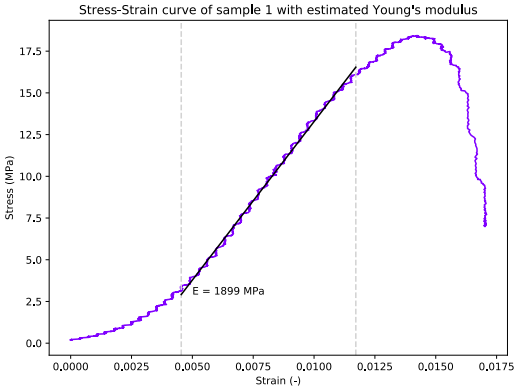

(b) The stress-strain curve for sample 1. An estimation of the Young's modulus is performed and indicated.

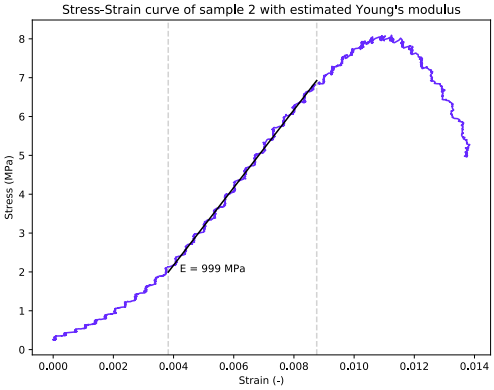

(c) The stress-strain curve for sample 2. An estimation of the Young's modulus is performed and indicated.

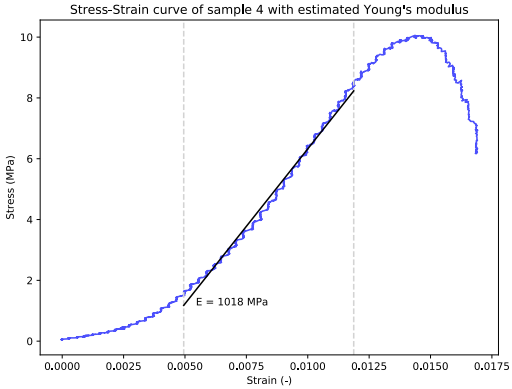

(d) The stress-strain curve for sample 4. An estimation of the Young's modulus is performed and indicated.

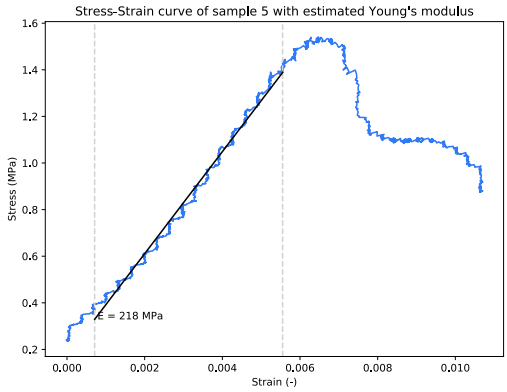

(e) The stress-strain curve for sample 5. An estimation of the Young's modulus is performed and indicated.

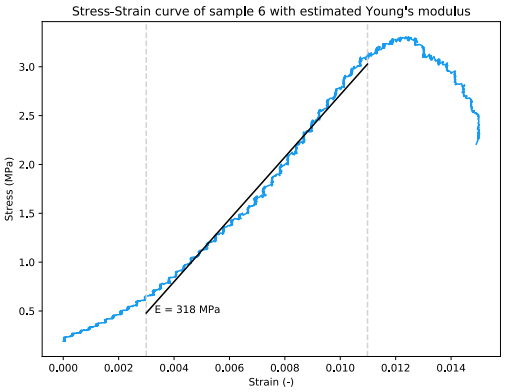

(f) The stress-strain curve for sample 6. An estimation of the Young's modulus is performed and indicated.

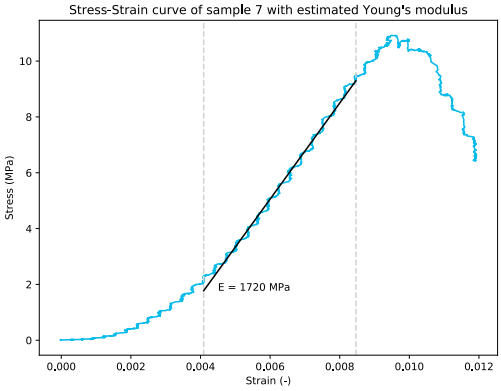

(g) The stress-strain curve for sample 7. An estimation of the Young's modulus is performed and indicated.

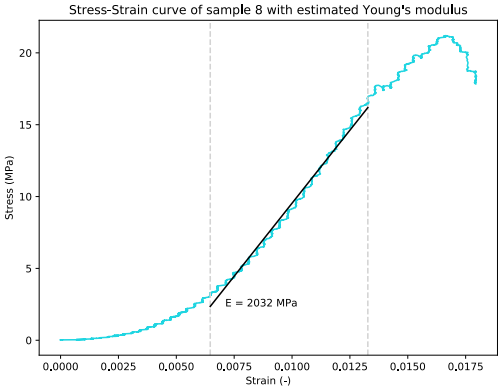

(h) The stress-strain curve for sample 8. An estimation of the Young's modulus is performed and indicated.

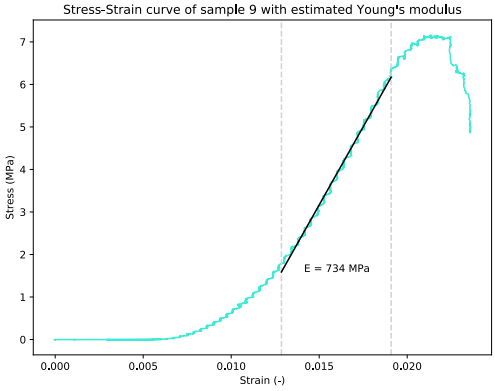

(i) The stress-strain curve for sample 9. An estimation of the Young's modulus is performed and indicated.

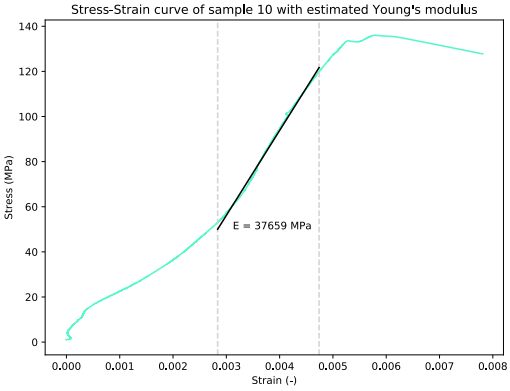

(j) The stress-strain curve for sample 10. An estimation of the Young's modulus is performed and indicated.

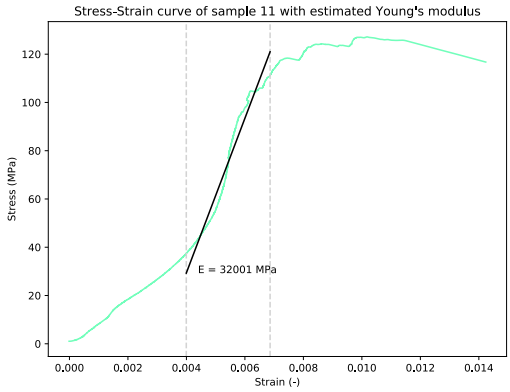

(k) The stress-strain curve for sample 11. An estimation of the Young's modulus is performed and indicated.

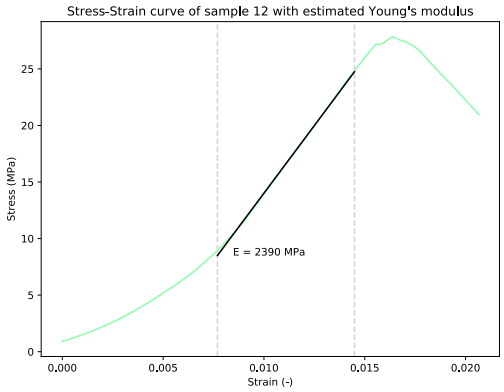

(l) The stress-strain curve for sample 12. An estimation of the Young's modulus is performed and indicated.

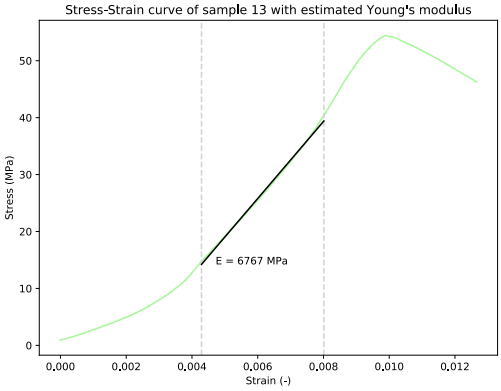

(m) The stress-strain curve for sample 13. An estimation of the Young's modulus is performed and indicated.

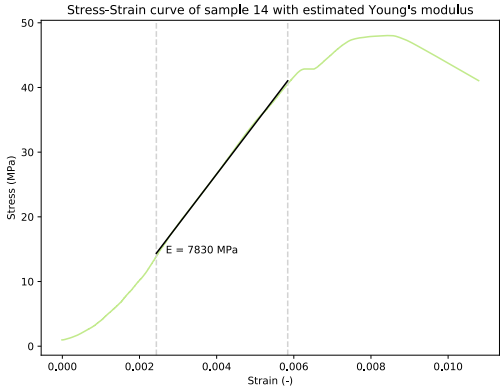

(n) The stress-strain curve for sample 14. An estimation of the Young's modulus is performed and indicated.

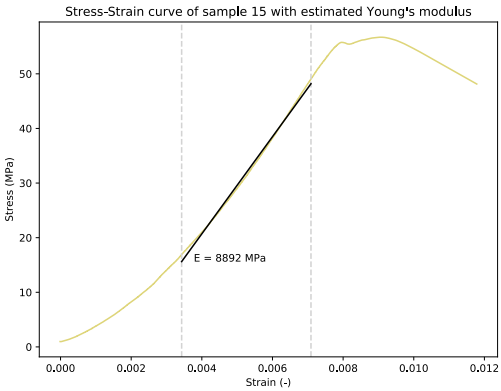

(o) The stress-strain curve for sample 15. An estimation of the Young's modulus is performed and indicated.

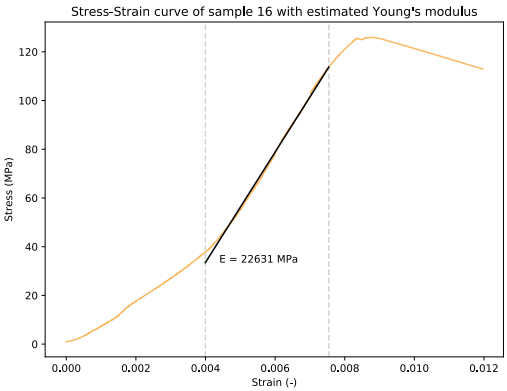

(p) The stress-strain curve for sample 16. An estimation of the Young's modulus is performed and indicated.

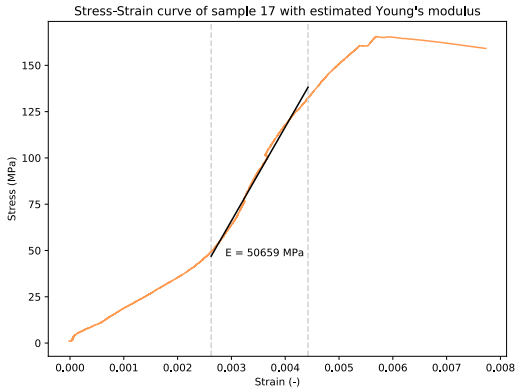

(q) The stress-strain curve for sample 17. An estimation of the Young's modulus is performed and indicated.

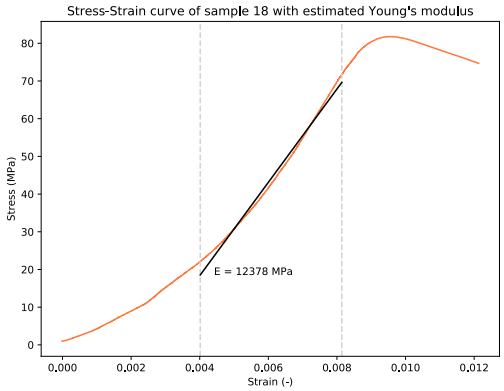

(r) The stress-strain curve for sample 18. An estimation of the Young's modulus is performed and indicated.

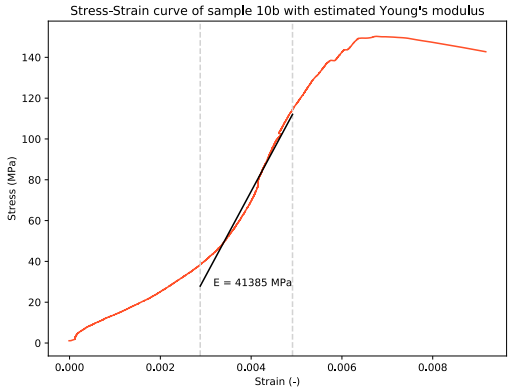

(s) The stress-strain curve for sample 10b. An estimation of the Young's modulus is performed and indicated.

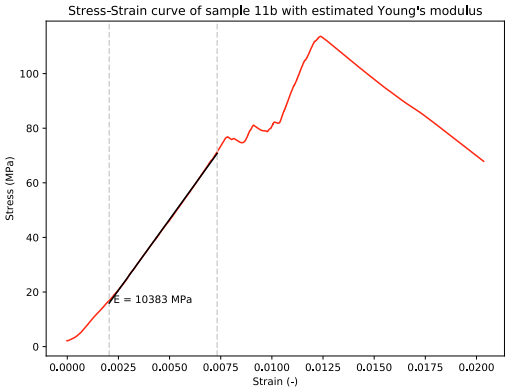

(t) The stress-strain curve for sample 11b. An estimation of the Young's modulus is performed and indicated.

Figure B.1: Stress-strain relations of all samples with estimations of Young's moduli. Due to the switch in testing device, the stress-strain curves of group-1 cannot be directly compared to those of gourp-2. See Chapter 3.7.

C

Supplementary Data of Light Microscopy

(a) Sample 10b bottom side.

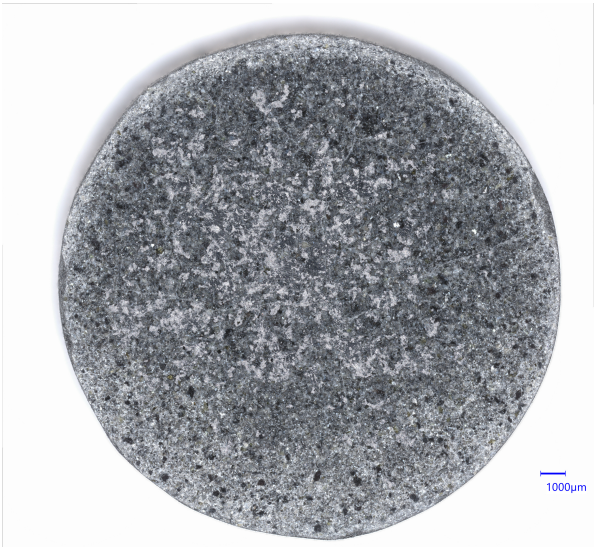

(b) Sample 10b top side.

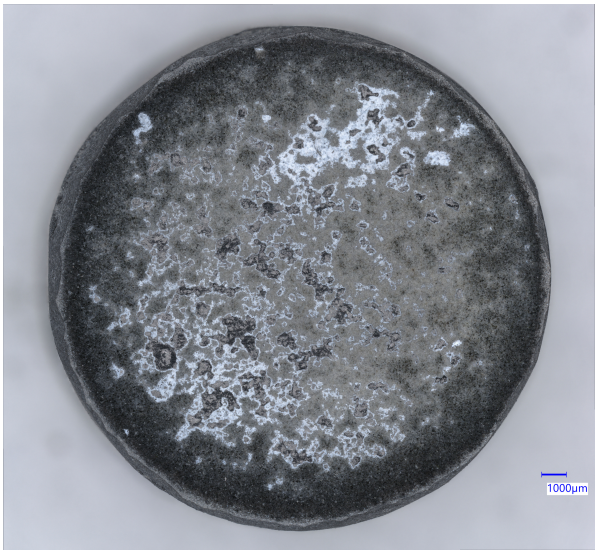

(c) Sample 11b bottom side.

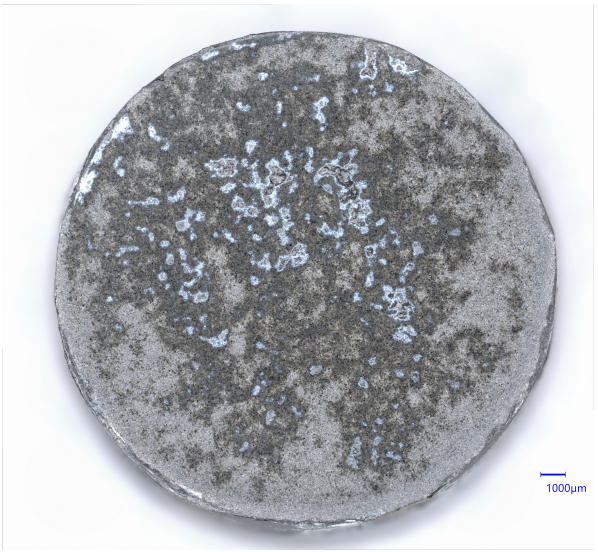

(d) Sample 11b top side.

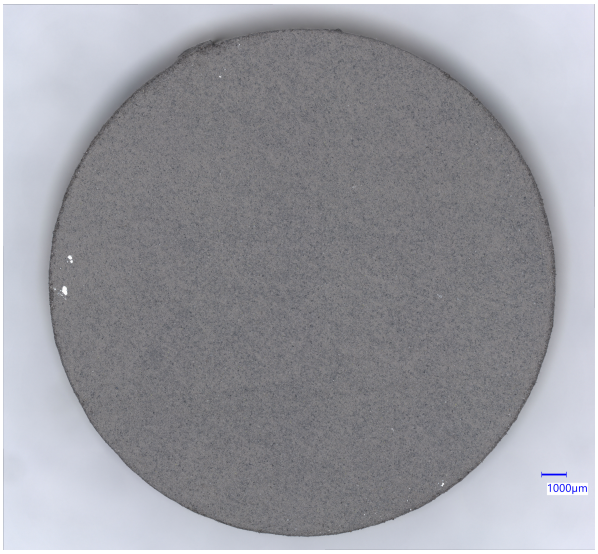

(e) Sample 12 bottom side.

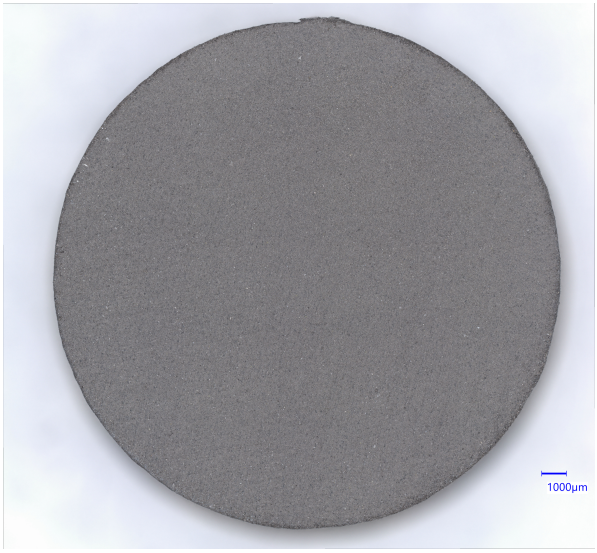

(f) Sample 12 top side.

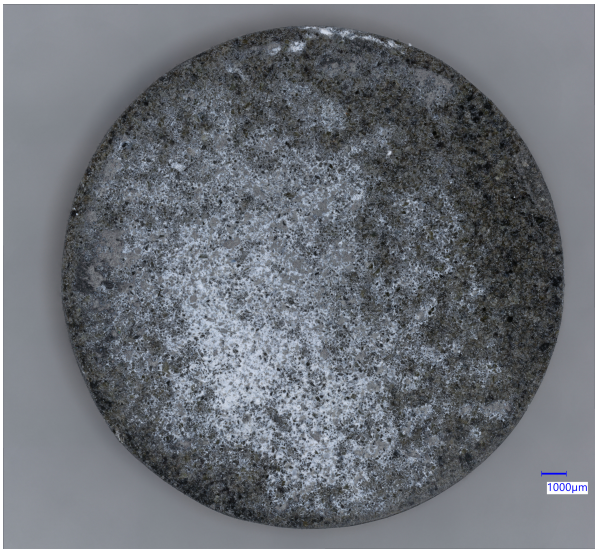

(g) Sample 13 bottom side.

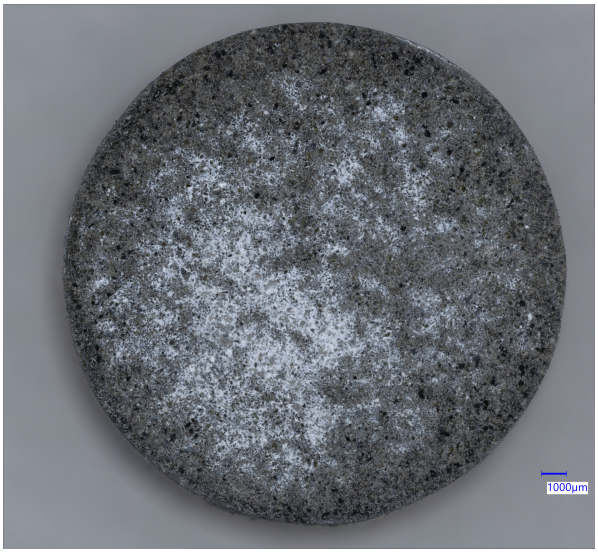

(h) Sample 13 top side.

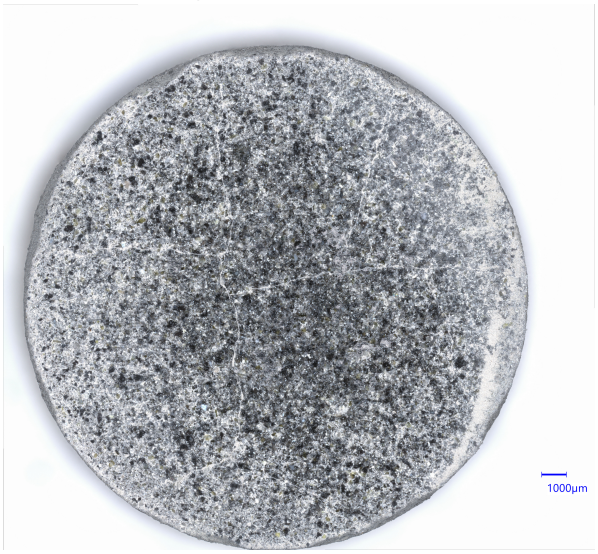

(i) Sample 14 bottom side.

(j) Sample 14 top side.

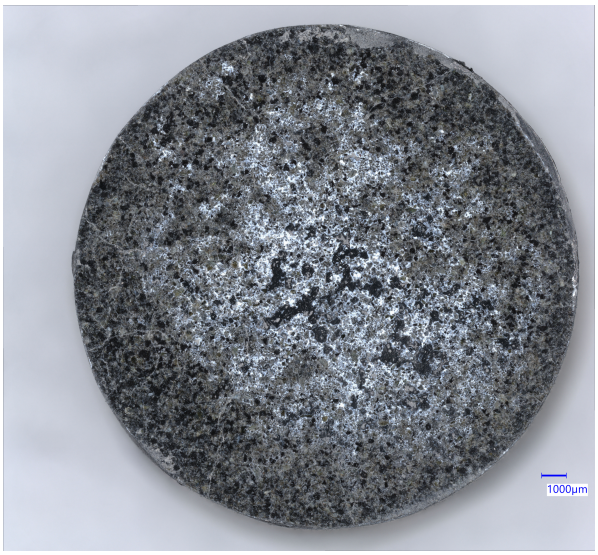

(k) Sample 15 bottom side.

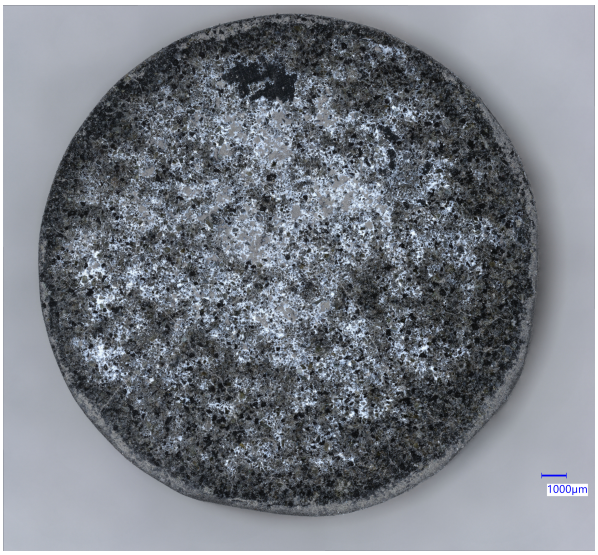

(l) Sample 15 top side.

(m) Sample 16 bottom side.

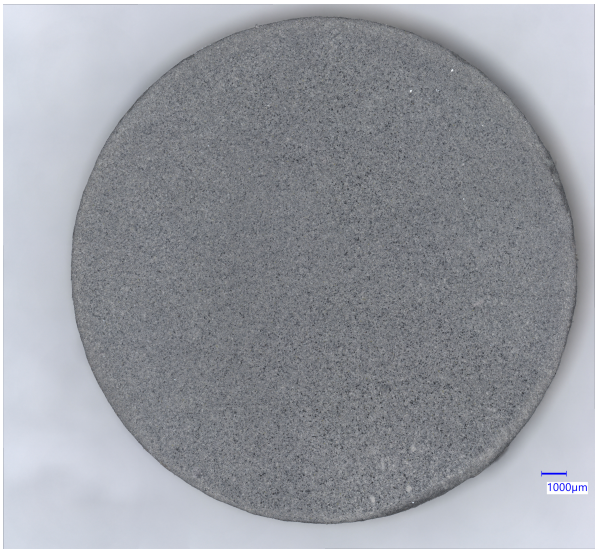

(n) Sample 16 top side.

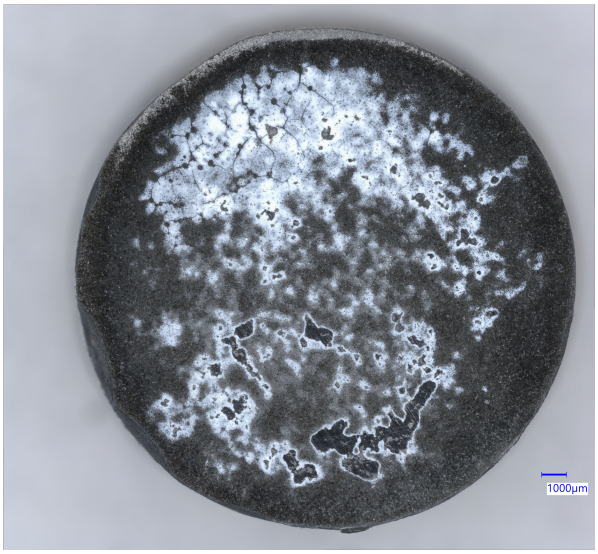

(o) Sample 17 bottom side.

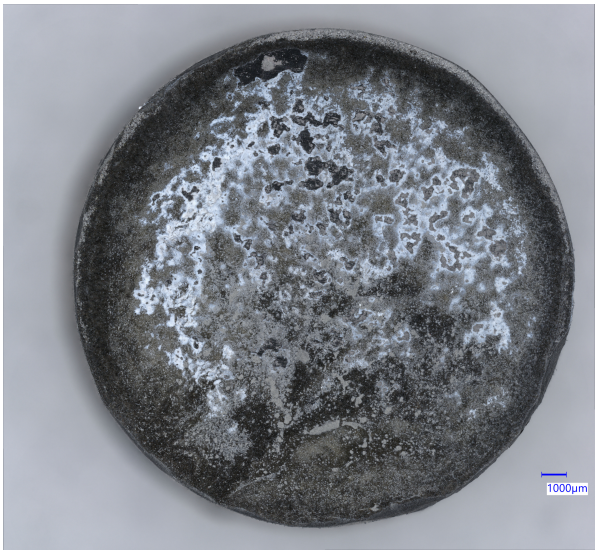

(p) Sample 17 top side.

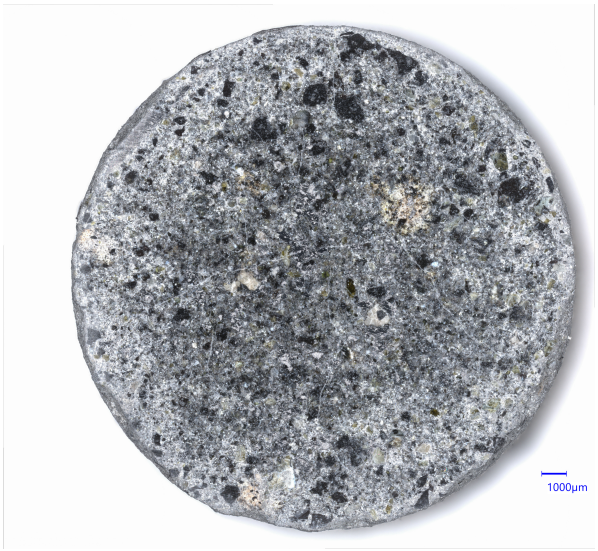

(q) Sample 18 bottom side.

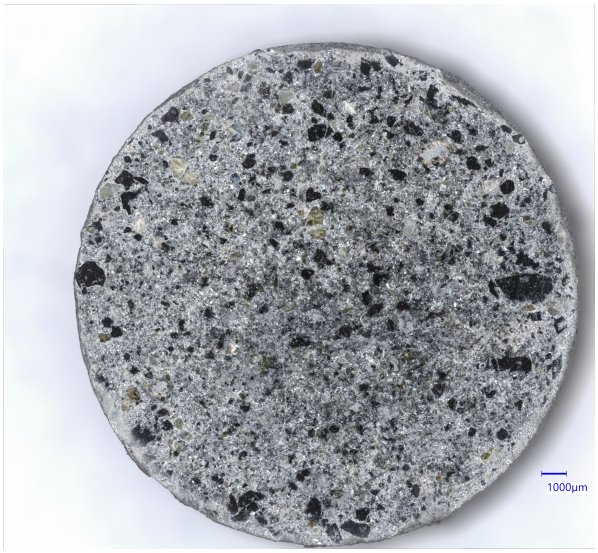

(r) Sample 18 top side.

D

Supplementary Data of SEM Analysis

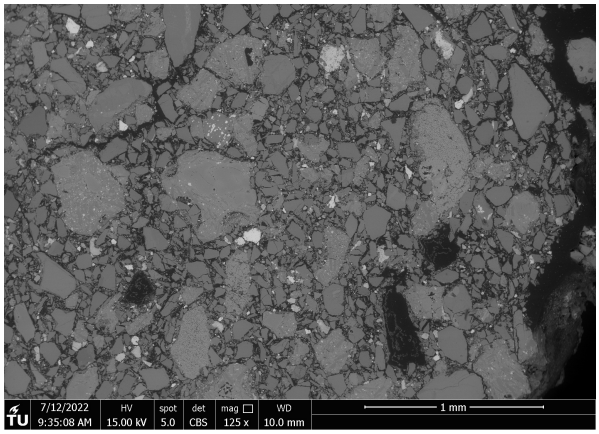

(a) Sample 1.

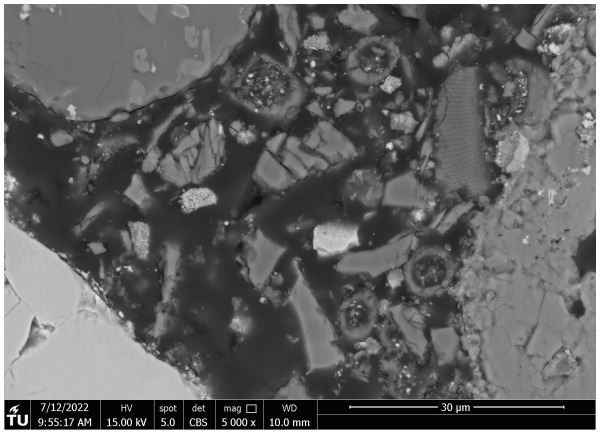

(b) Sample 1.

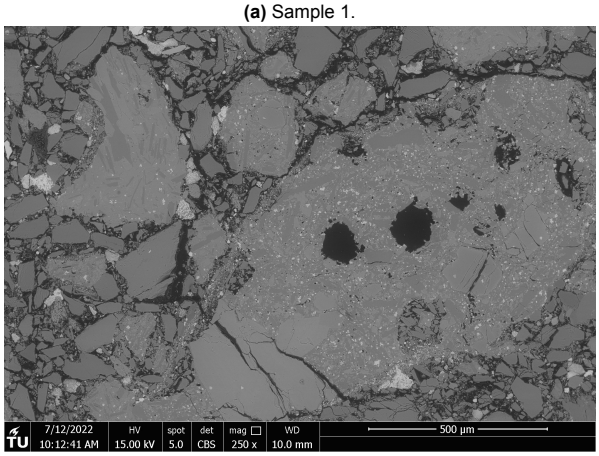

(c) Sample 1.

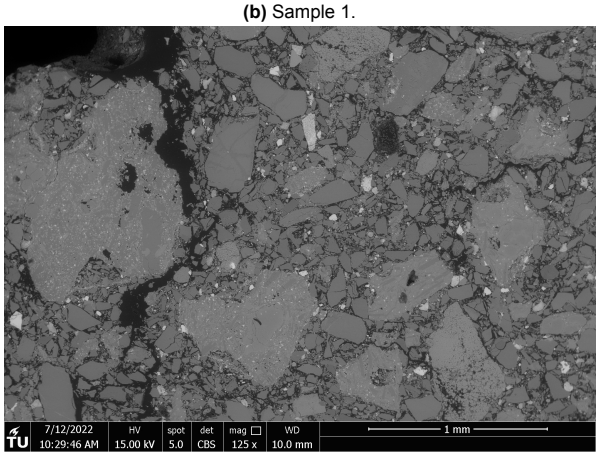

(d) Sample 1.

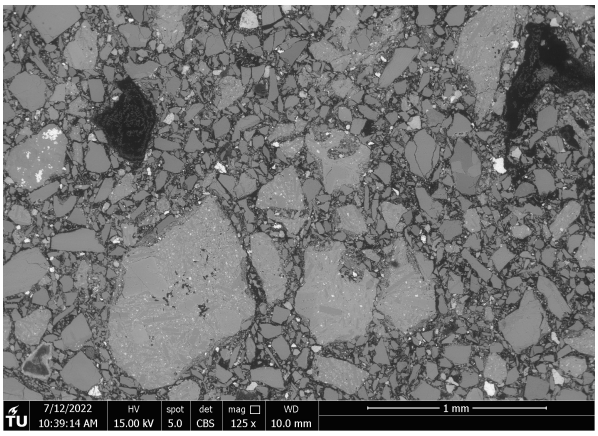

(e) Sample 2.

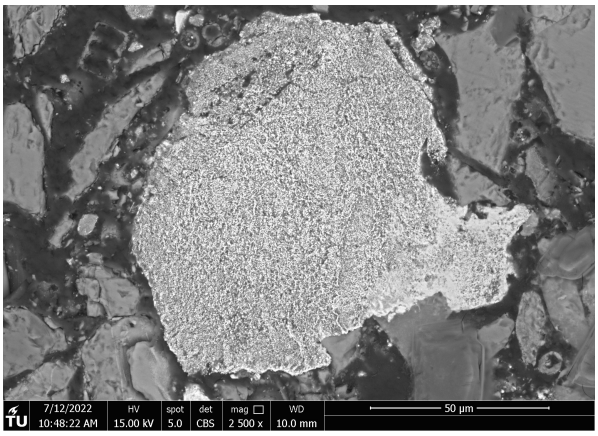

(f) Sample 2.

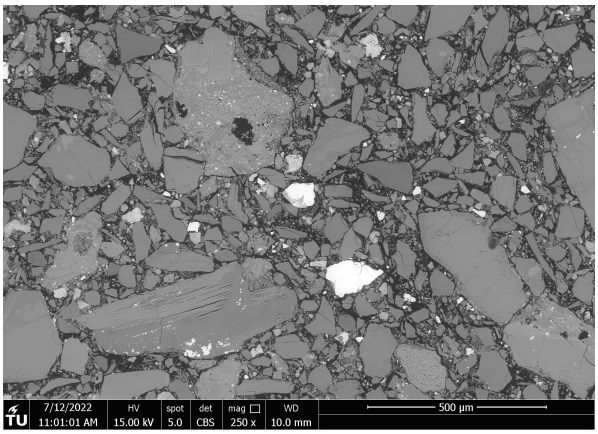

(g) Sample 2.

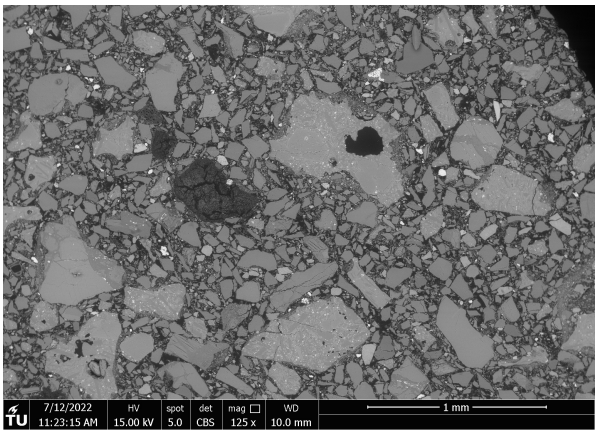

(h) Sample 3.

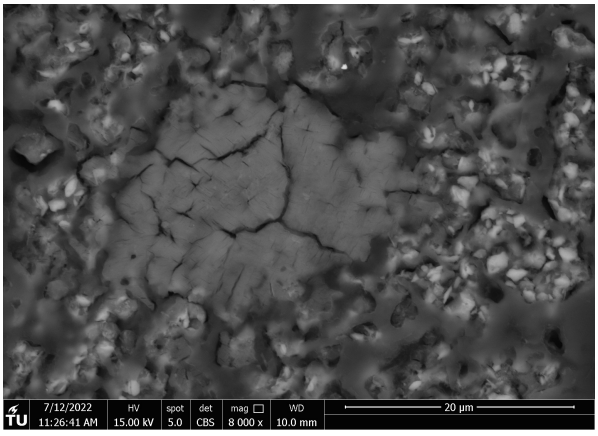

(i) Sample 3.

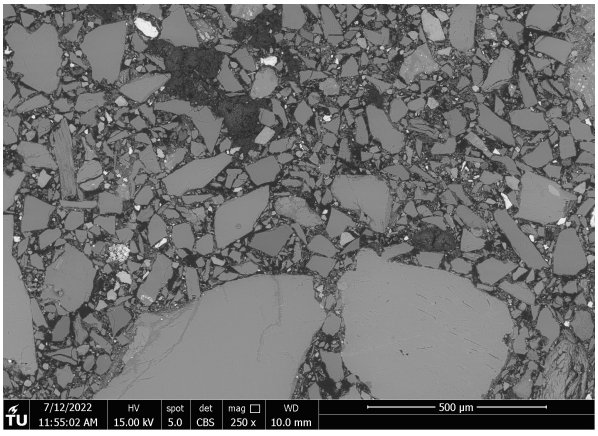

(j) Sample 3.

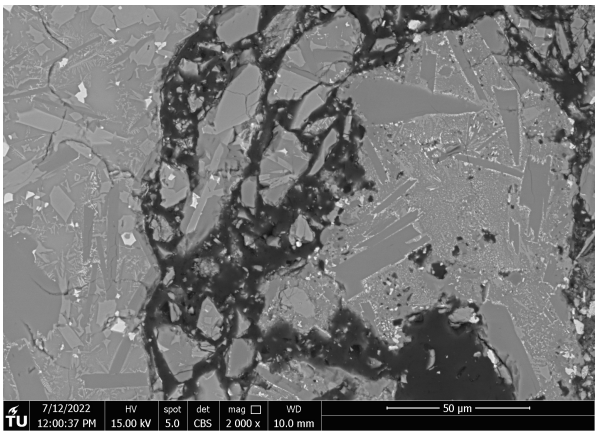

(k) Sample 3.

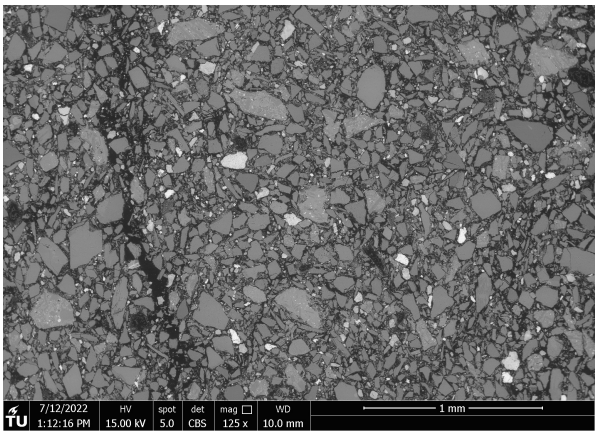

(l) Sample 4.

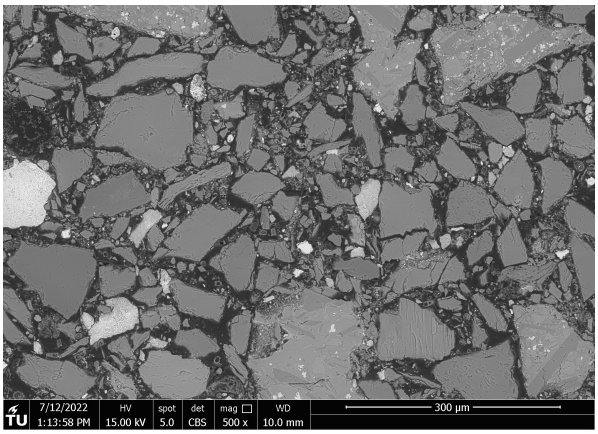

(m) Sample 4.

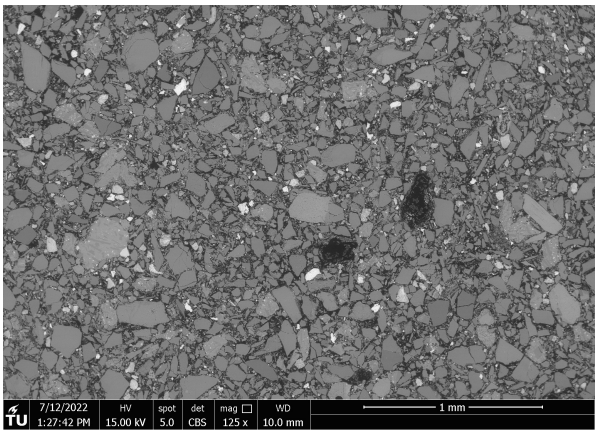

(n) Sample 4.

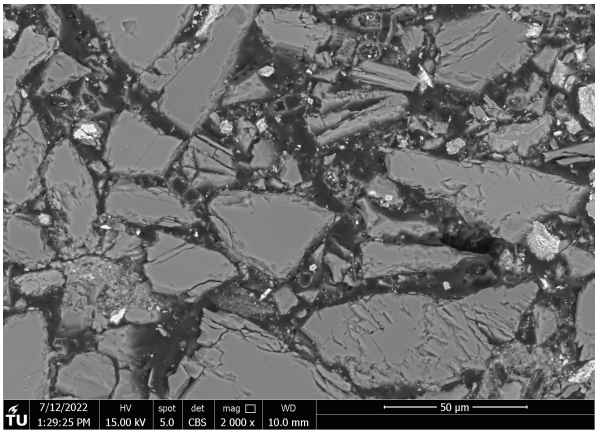

(o) Sample 4.

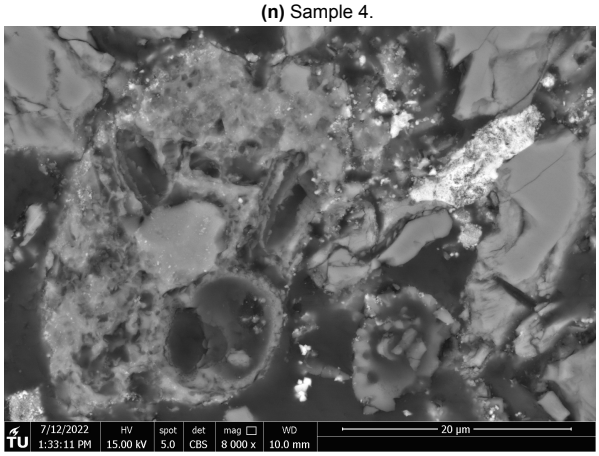

(p) Sample 4.

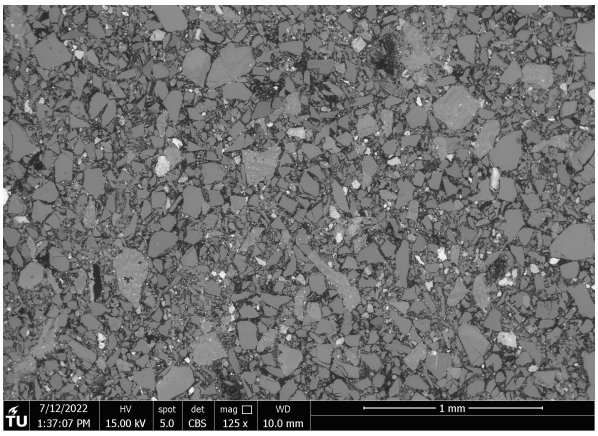

(q) Sample 4.

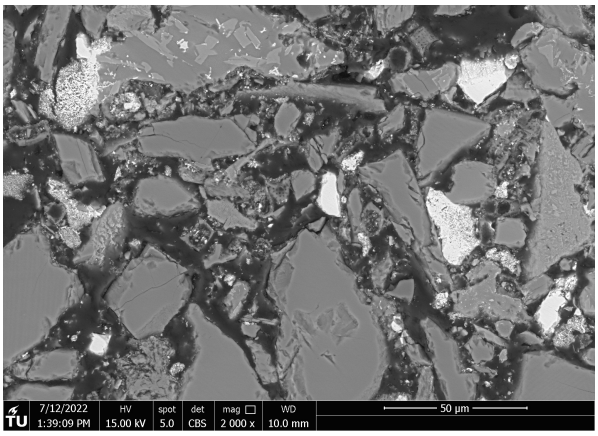

(r) Sample 4.

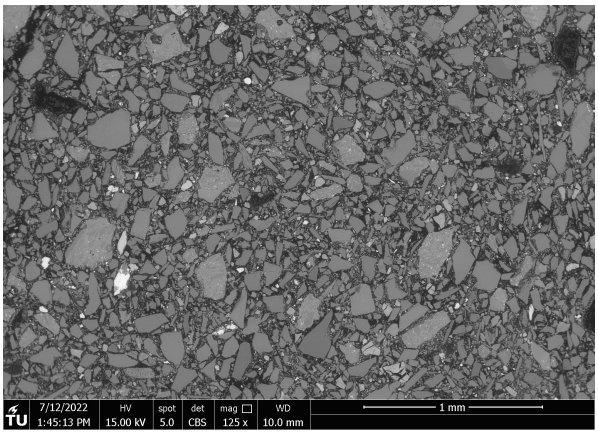

(s) Sample 5.

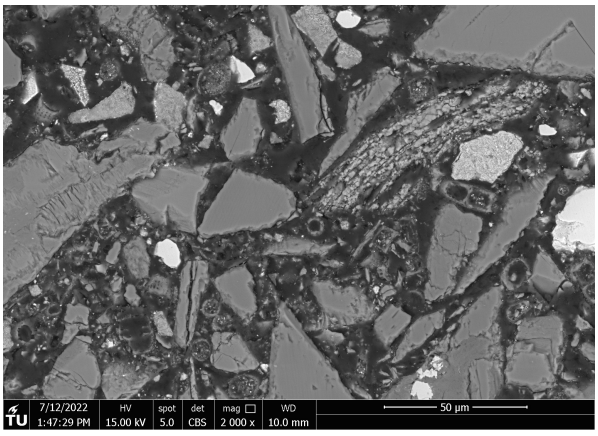

(t) Sample 5.

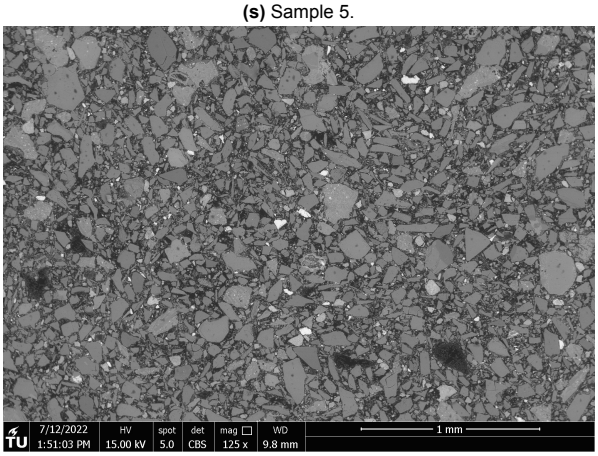

(u) Sample 5.

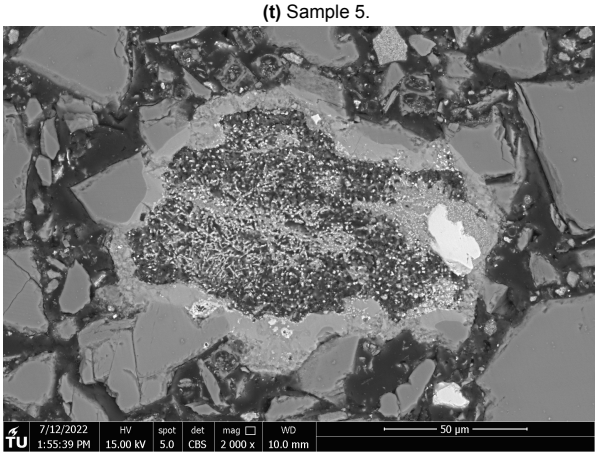

(v) Sample 5.

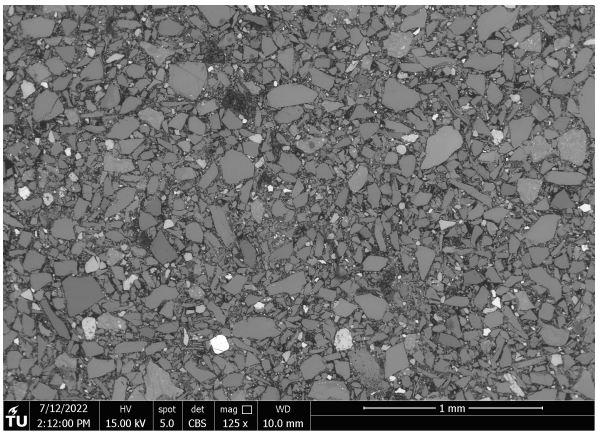

(w) Sample 6.

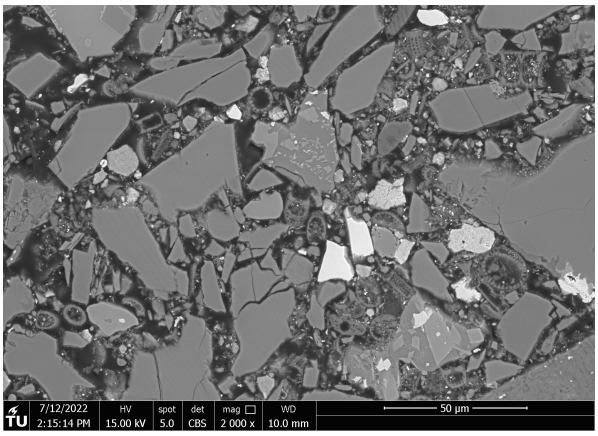

(x) Sample 6.

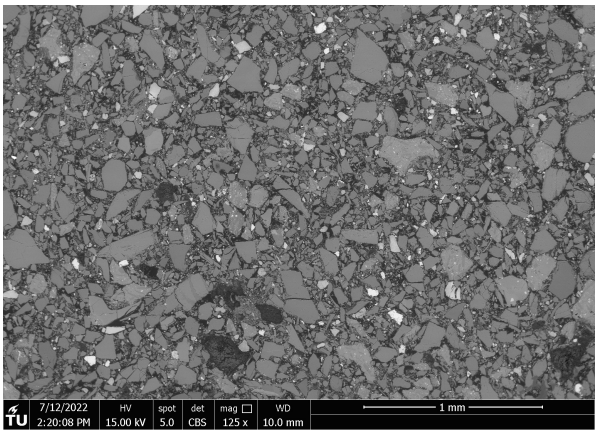

(y) Sample 6.

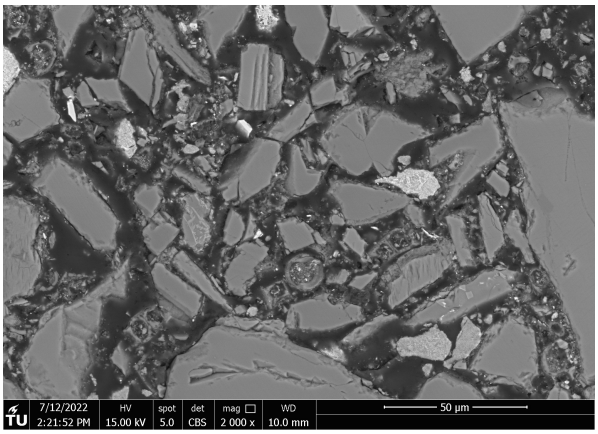

(z) Sample 6.

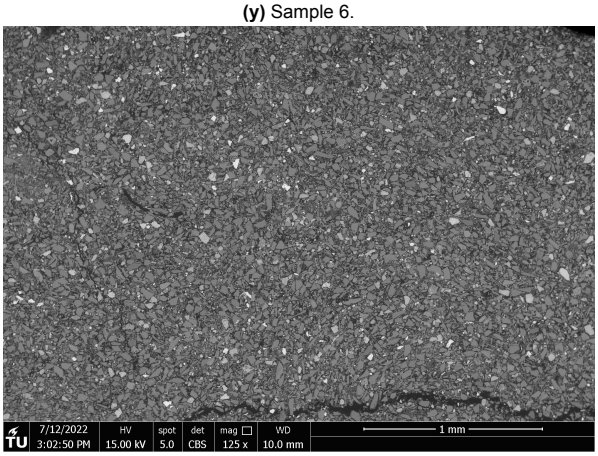

(aa) Sample 7.

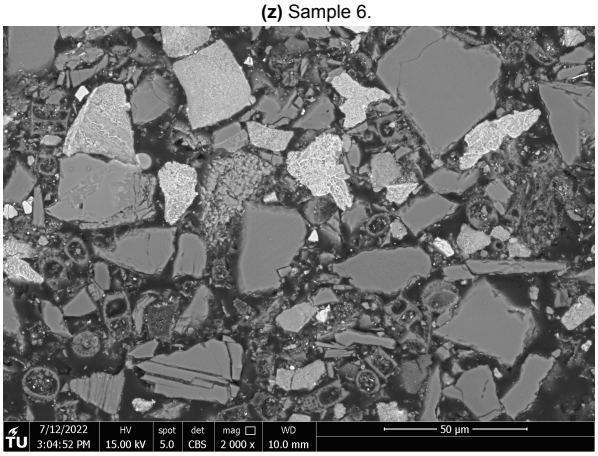

(ab) Sample 7.

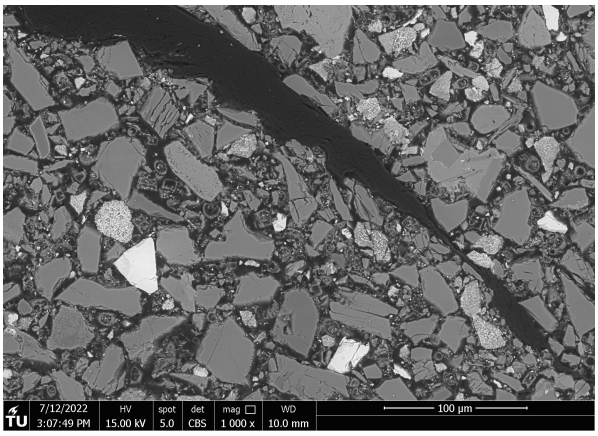

(ac) Sample 7.

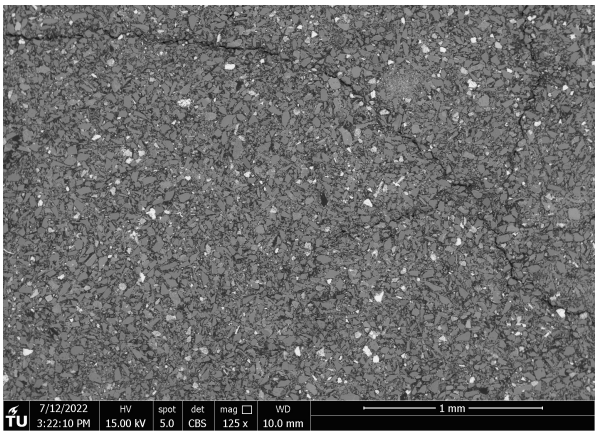

(ad) Sample 7.

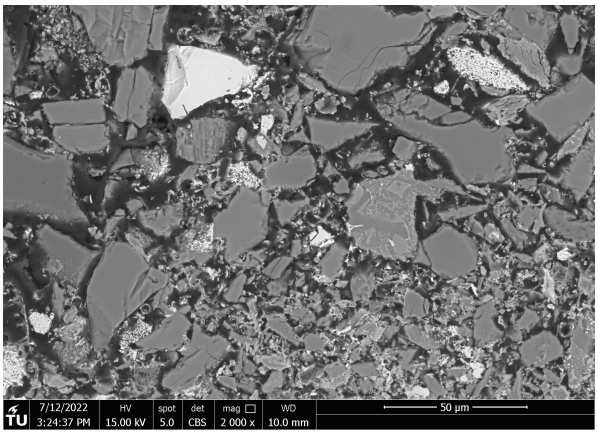

(ae) Sample 7.

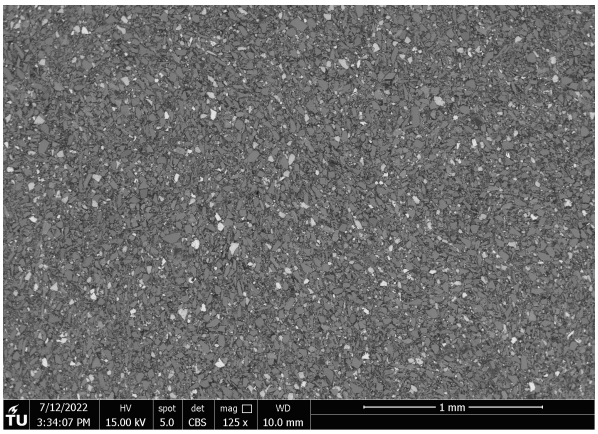

(af) Sample 8.

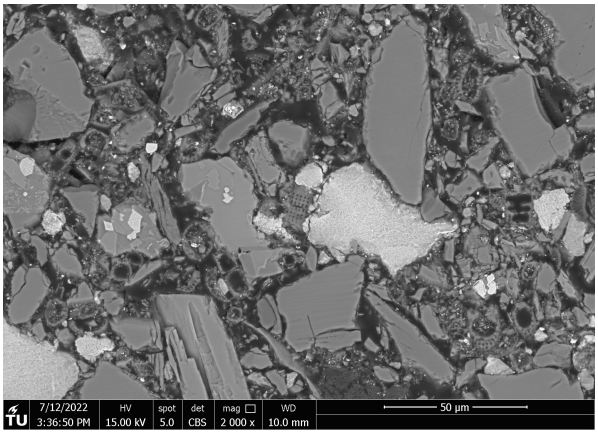

(ag) Sample 8.

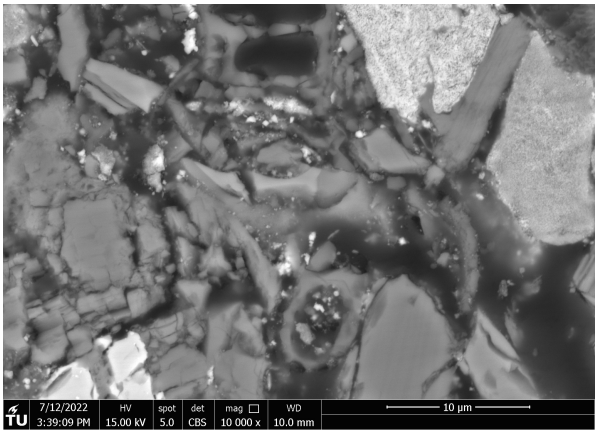

(ah) Sample 8.

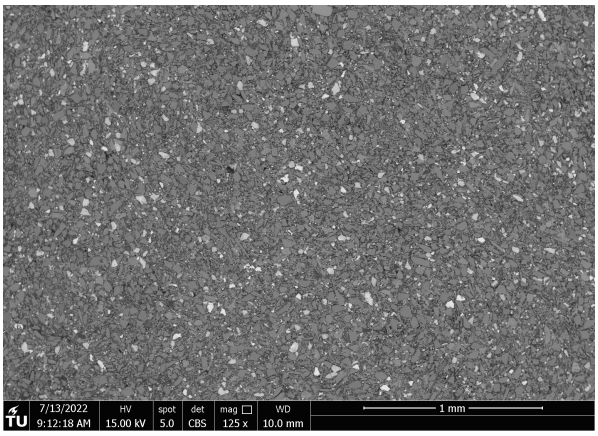

(ai) Sample 8.

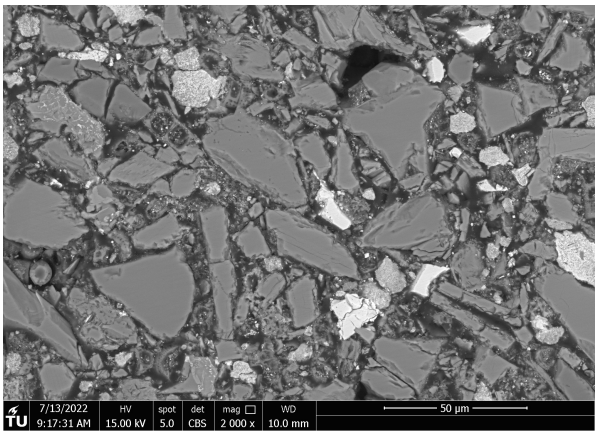

(aj) Sample 8.

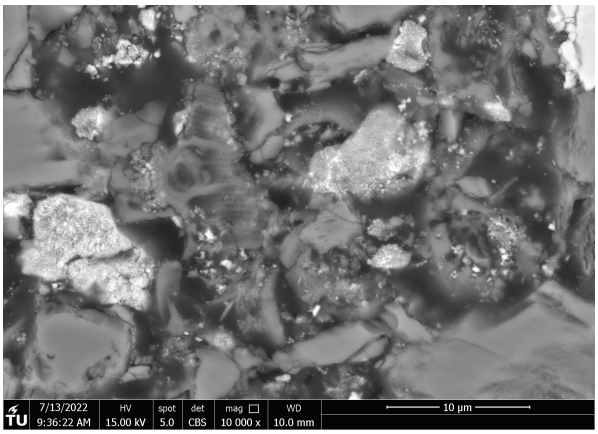

(ak) Sample 8.

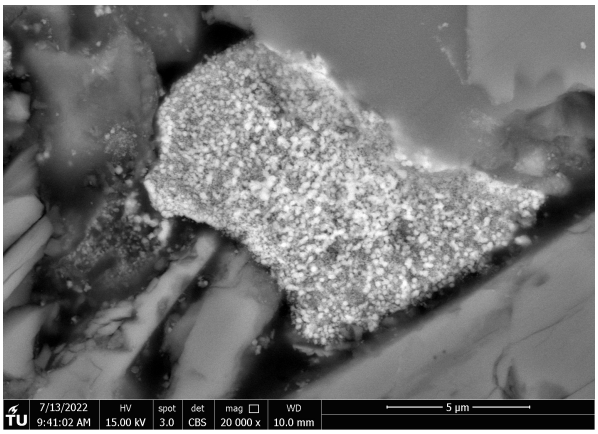

(al) Sample 8.

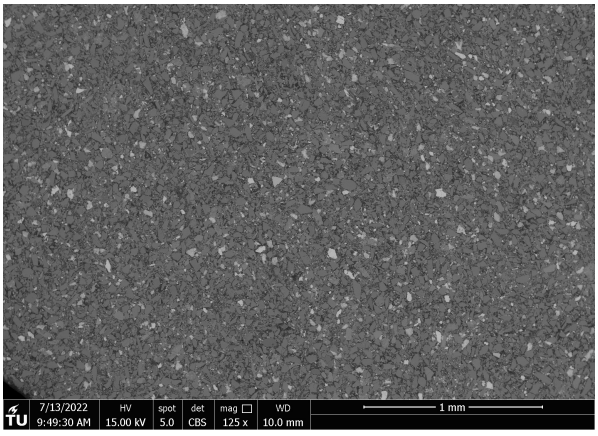

(am) Sample 8.

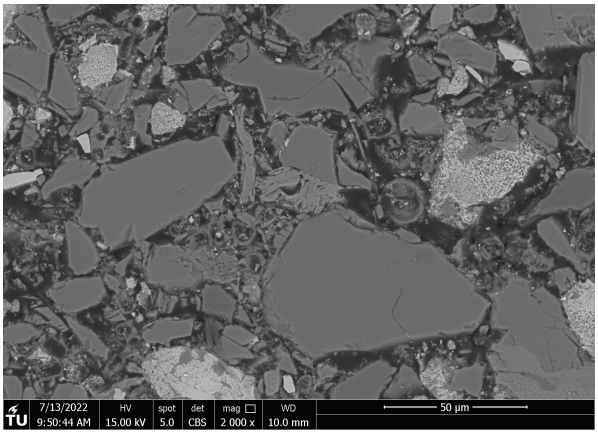

(an) Sample 8.

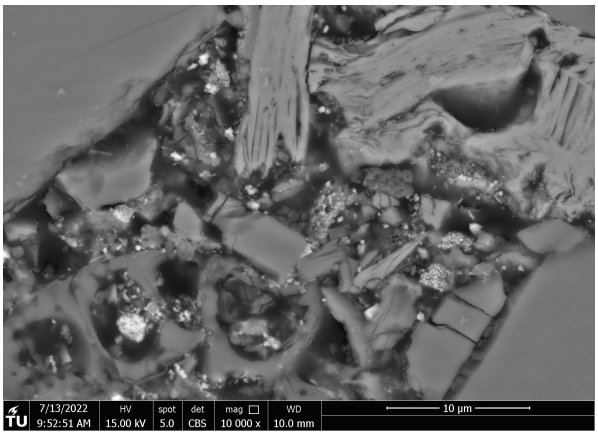

(ao) Sample 8.

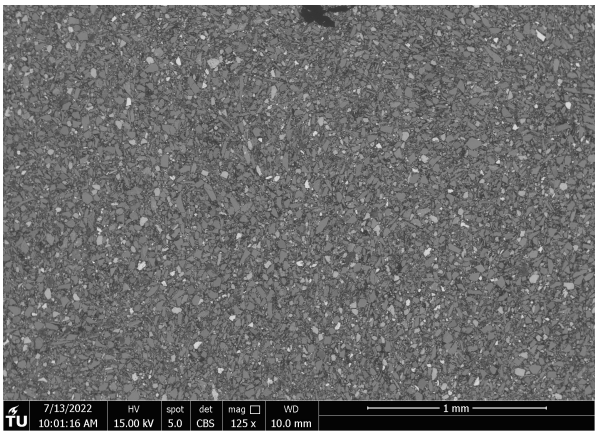

(ap) Sample 9.

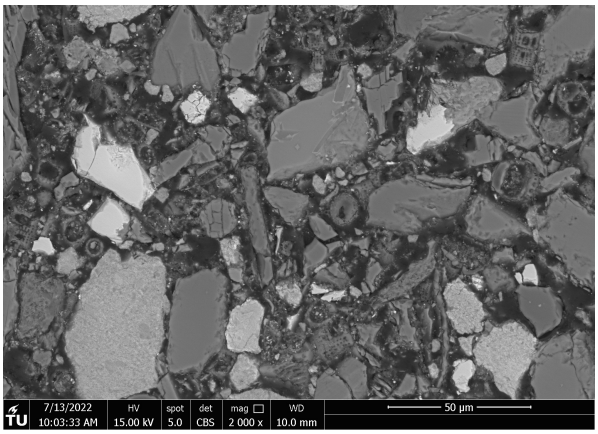

(aq) Sample 9.

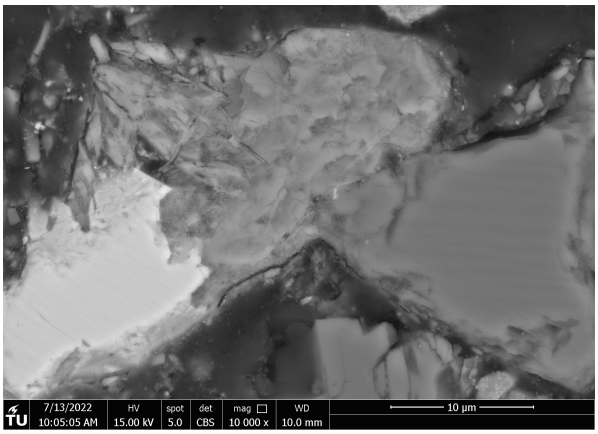

(ar) Sample 9.

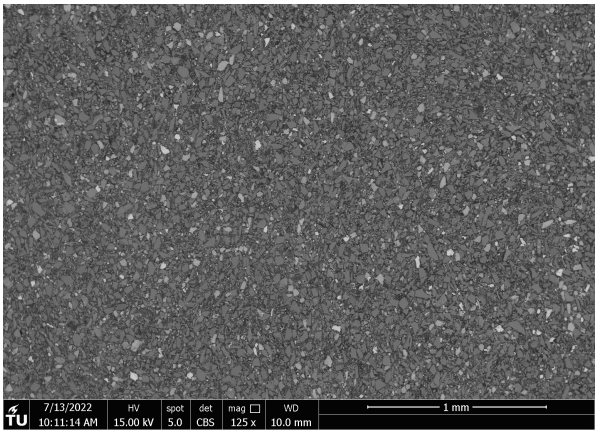

(as) Sample 9.

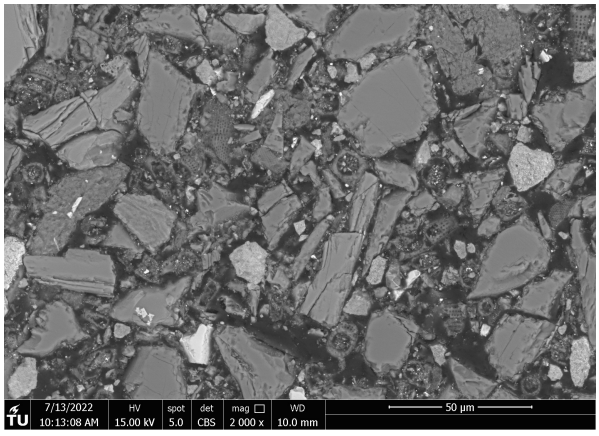

(at) Sample 9.

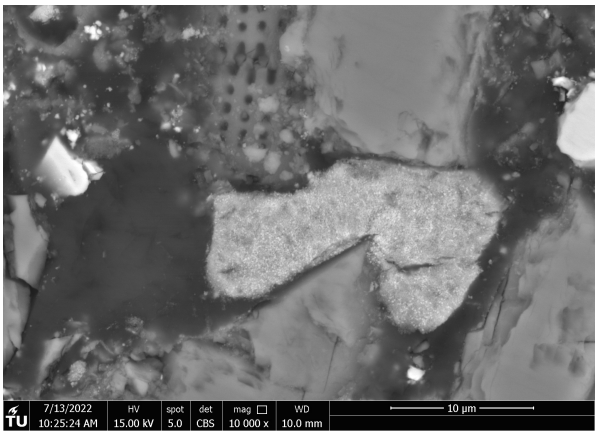

(au) Sample 9.

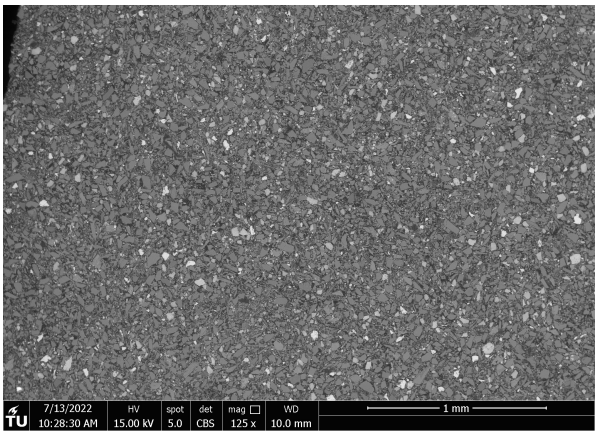

(av) Sample 9.

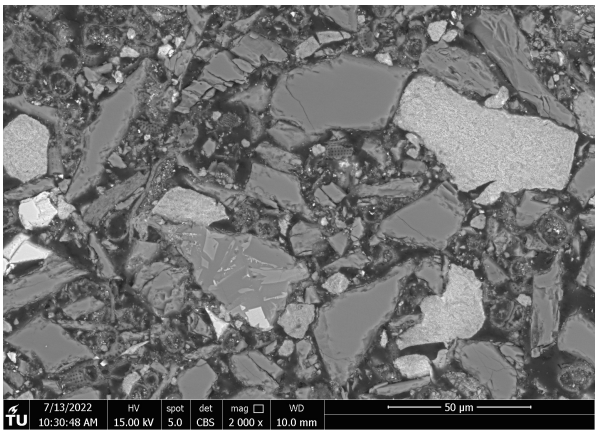

(aw) Sample 9.

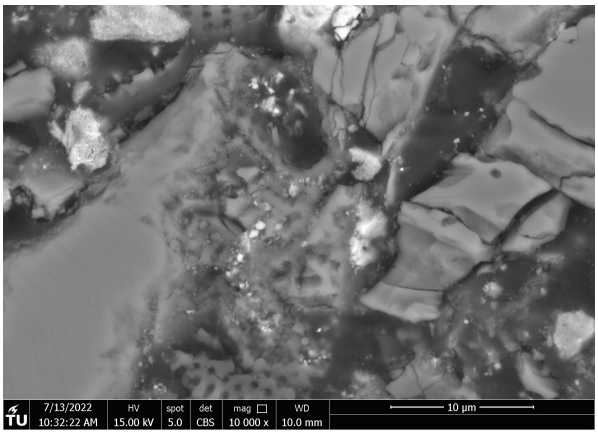

(ax) Sample 9.

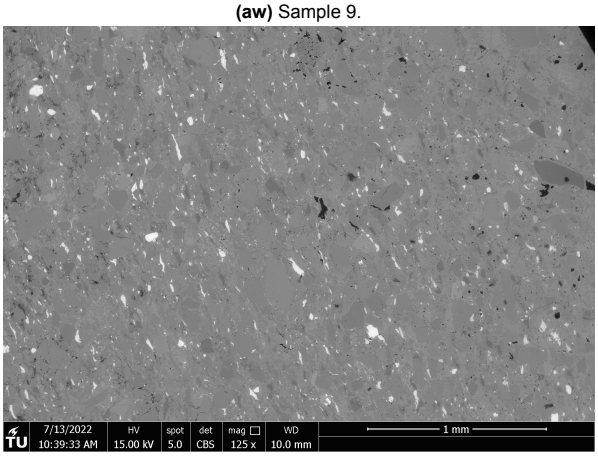

(ay) Sample 10.

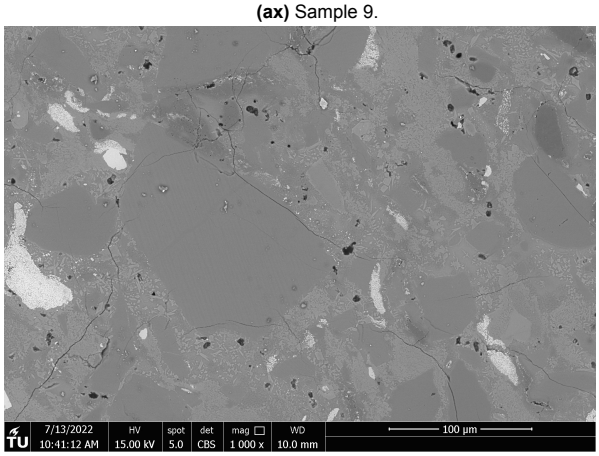

(az) Sample 10.

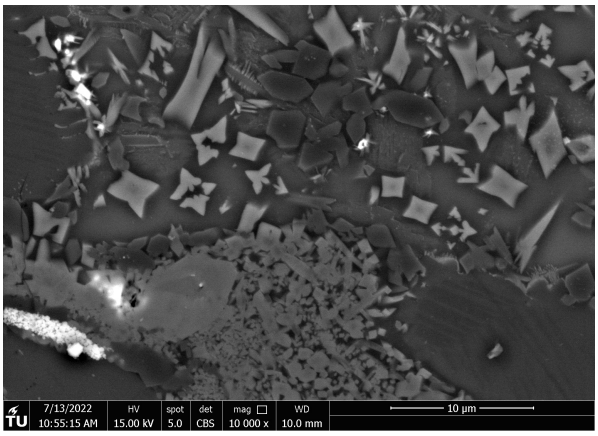

(ba) Sample 10.

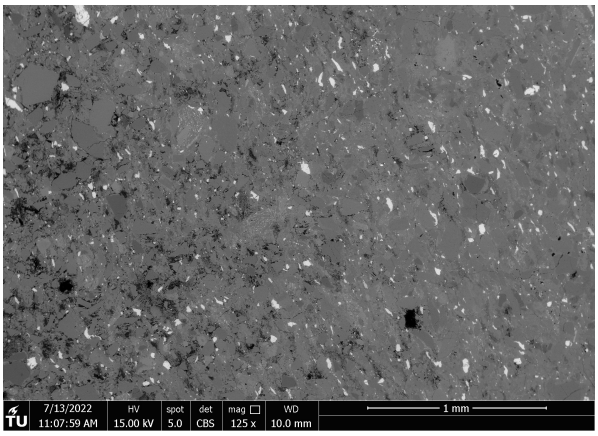

(bb) Sample 10.

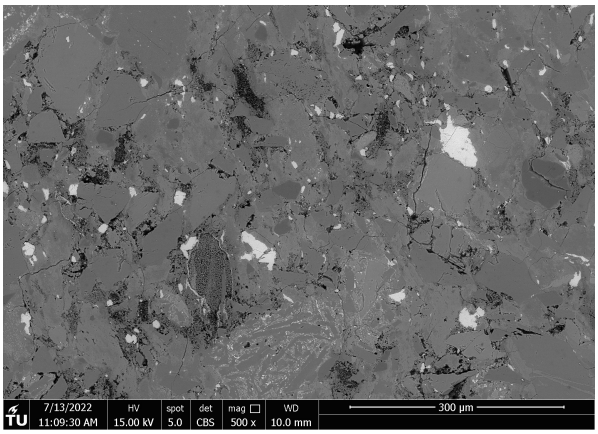

(bc) Sample 10.

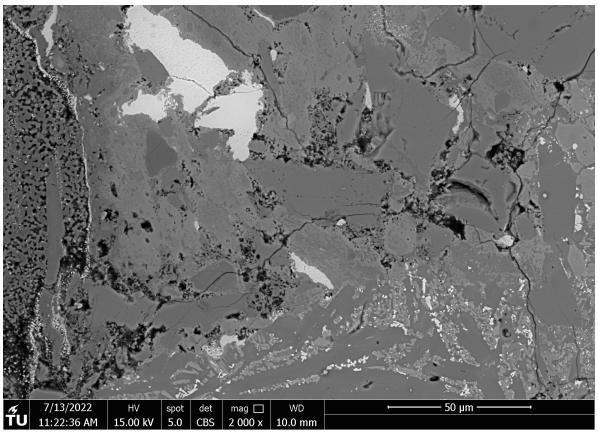

(bd) Sample 10.

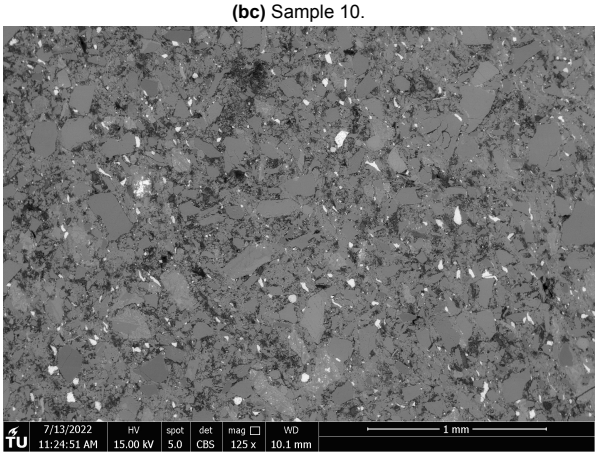

(be) Sample 10.

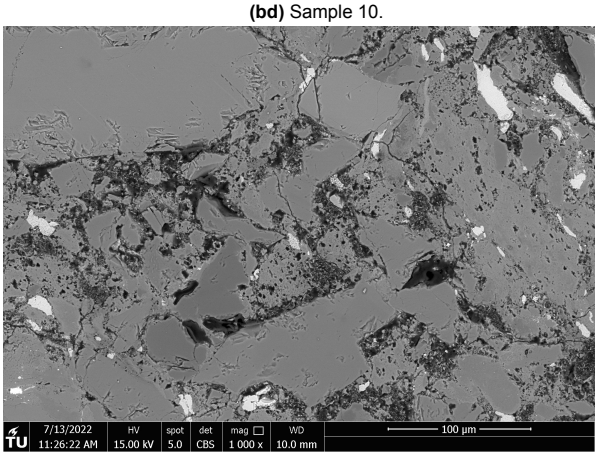

(bf) Sample 10.

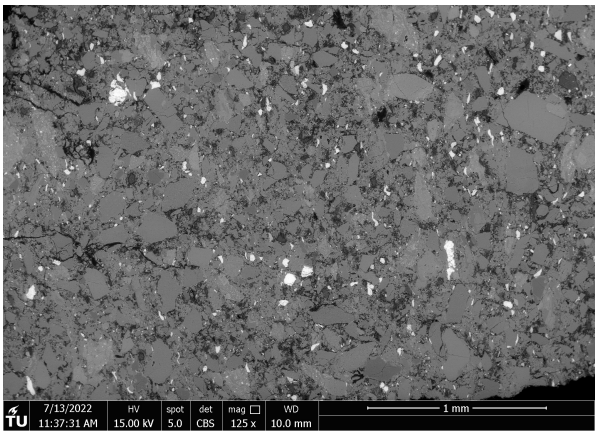

(bg) Sample 10.

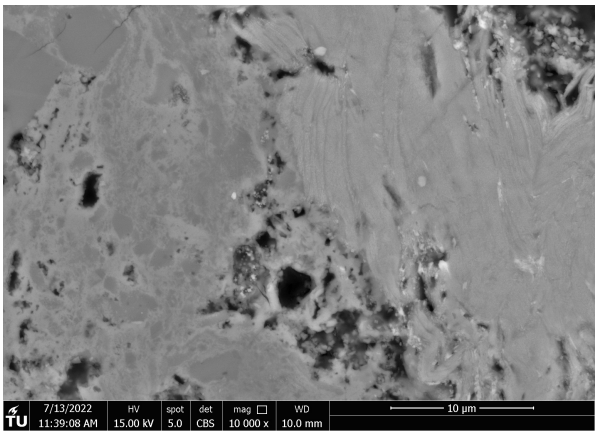

(bh) Sample 10.

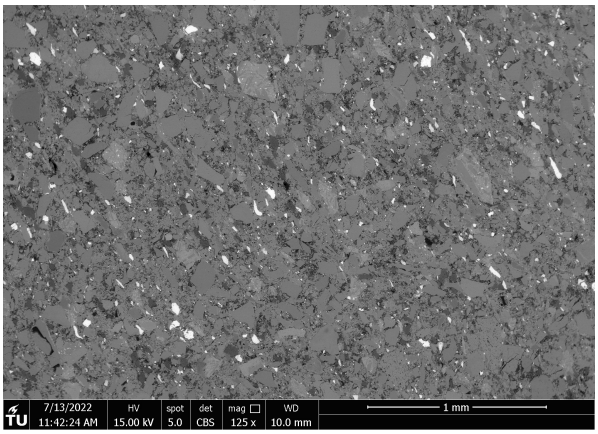

(bi) Sample 10.

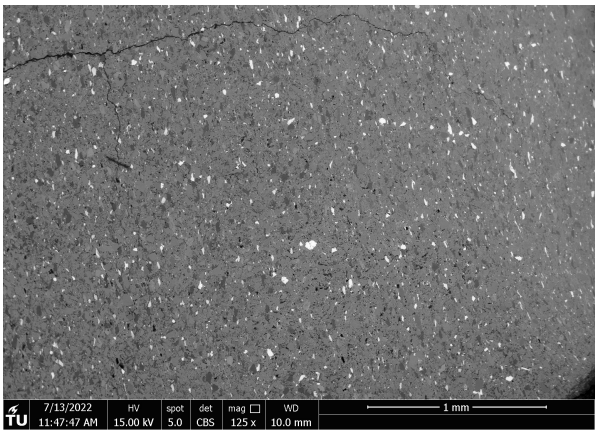

(bj) Sample 11.

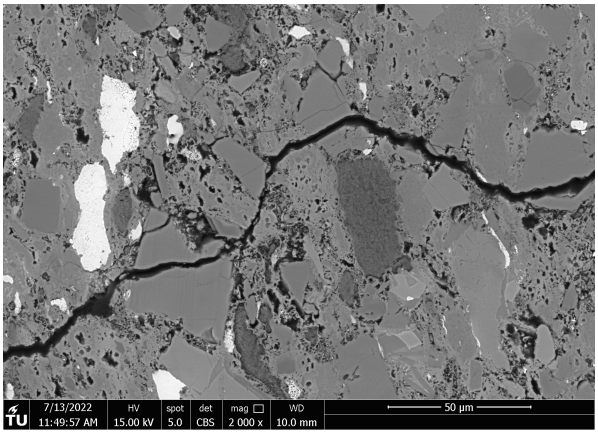

(bk) Sample 11.

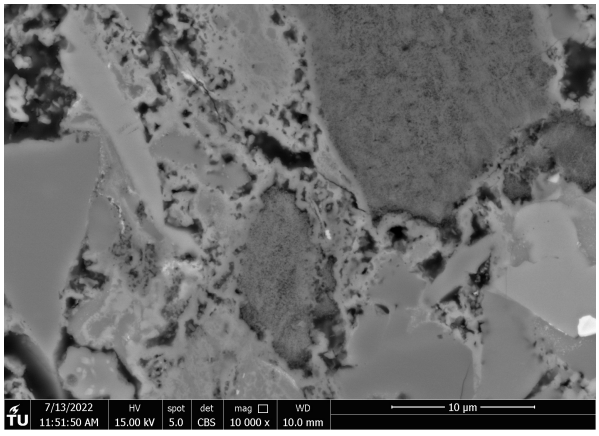

(bl) Sample 11.

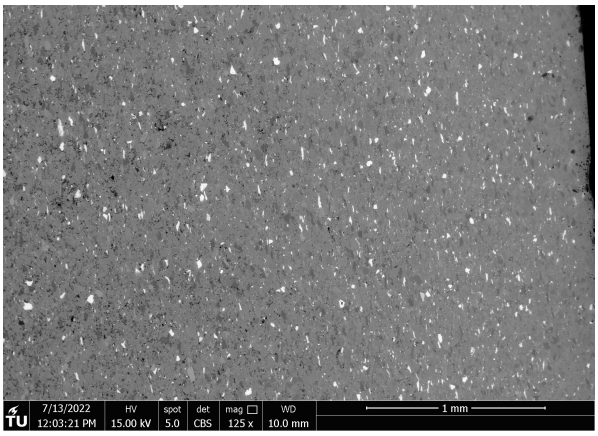

(bm) Sample 11.

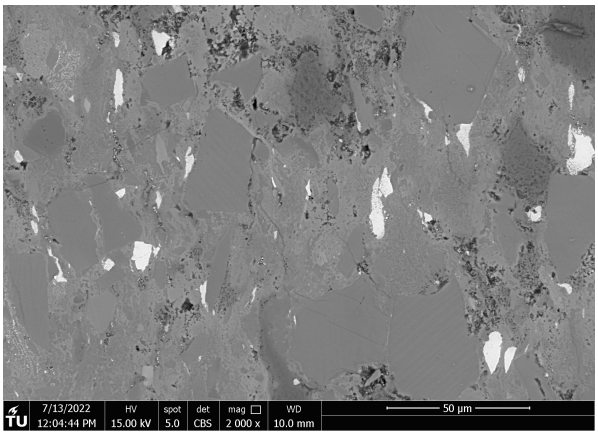

(bn) Sample 11.

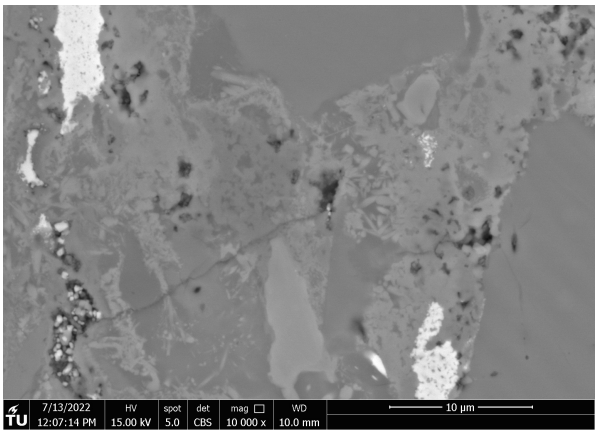

(bo) Sample 11.

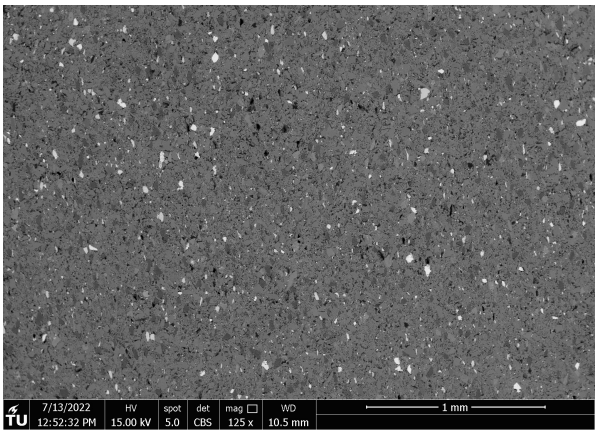

(bp) Sample 11.

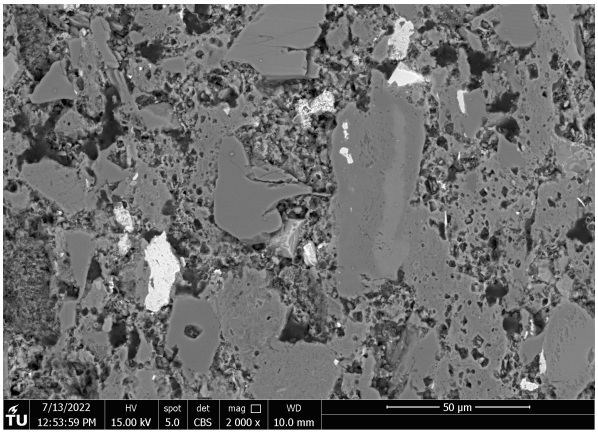

(bq) Sample 11.

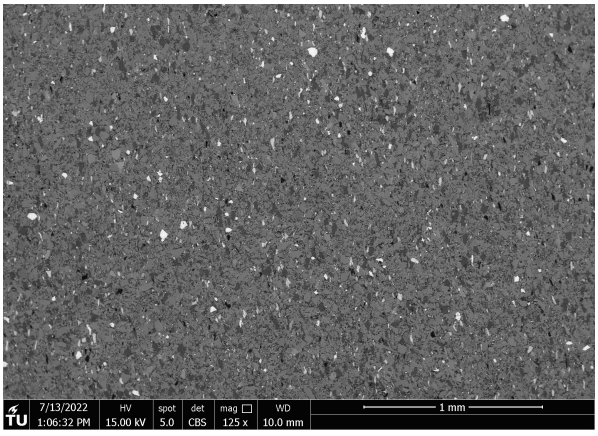

(br) Sample 11.

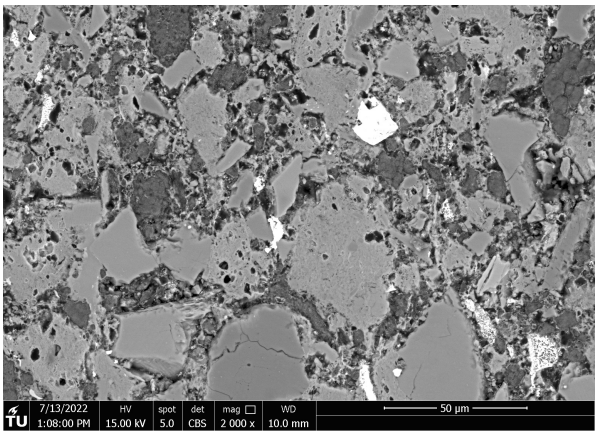

(bs) Sample 11.

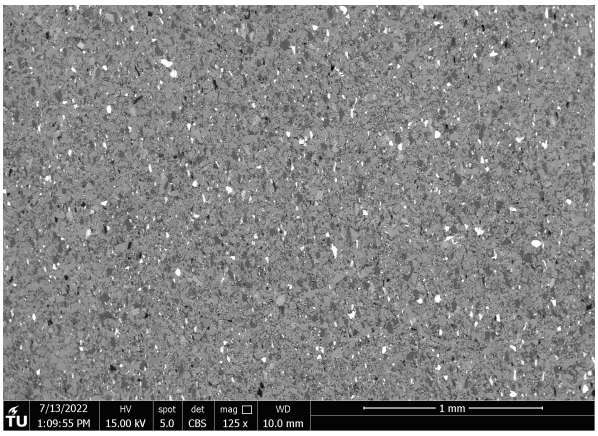

(bt) Sample 11.

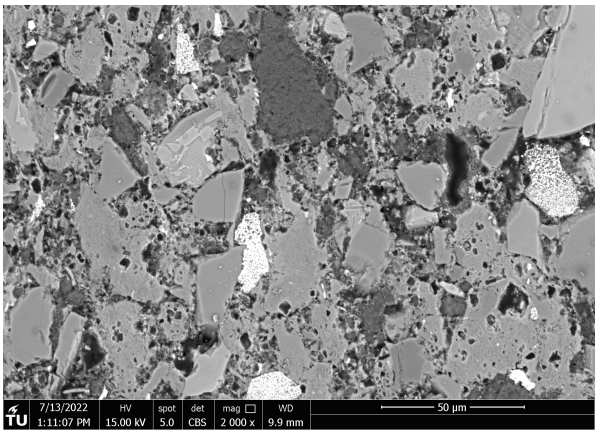

(bu) Sample 11.

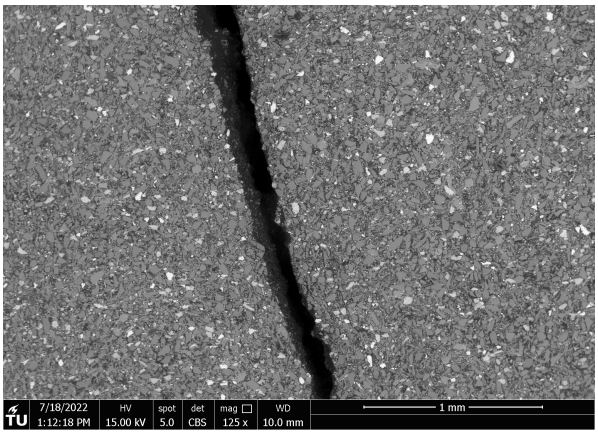

(bv) Sample 12.

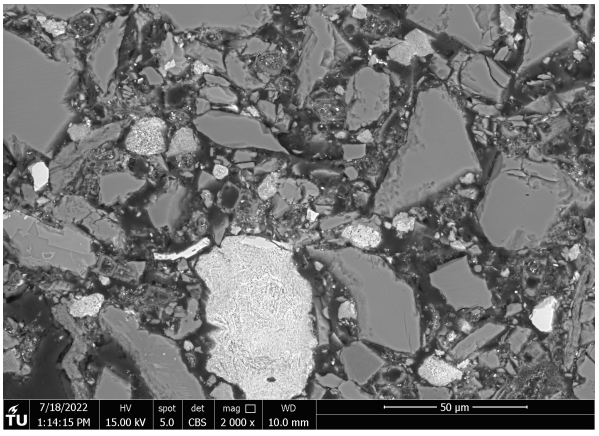

(bw) Sample 12.

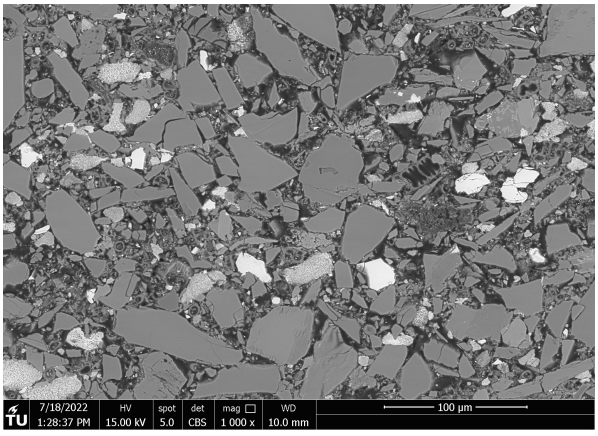

(bx) Sample 12.

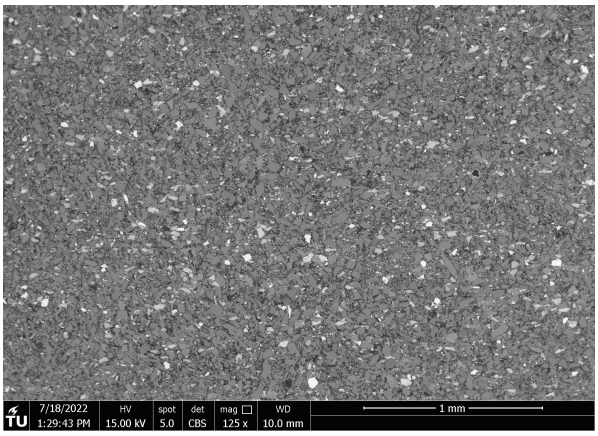

(by) Sample 12.

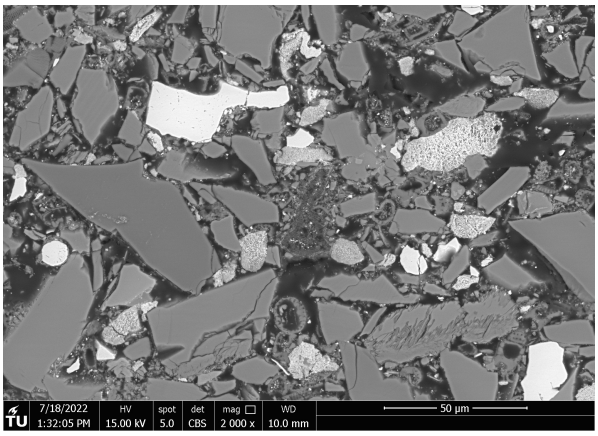

(bz) Sample 12.

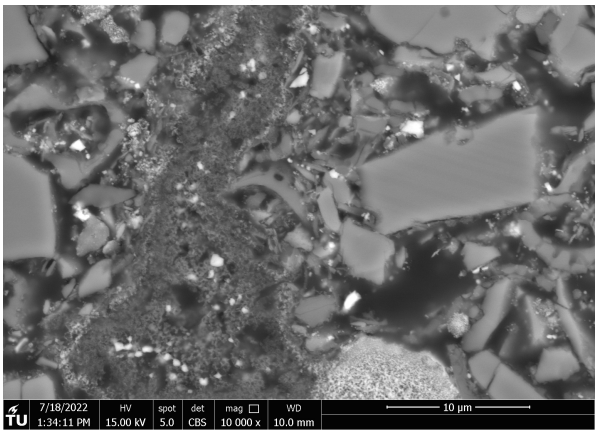

(ca) Sample 12.

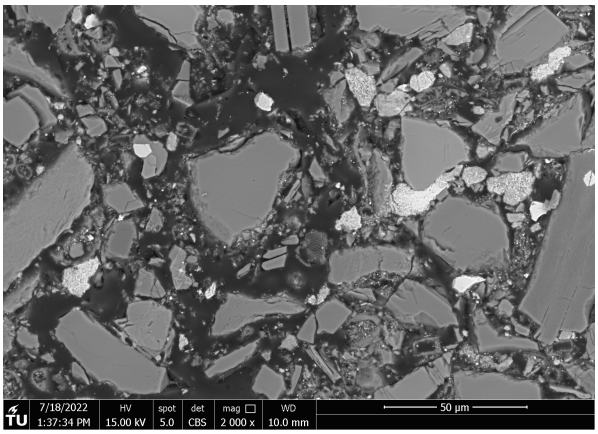

(cb) Sample 12.

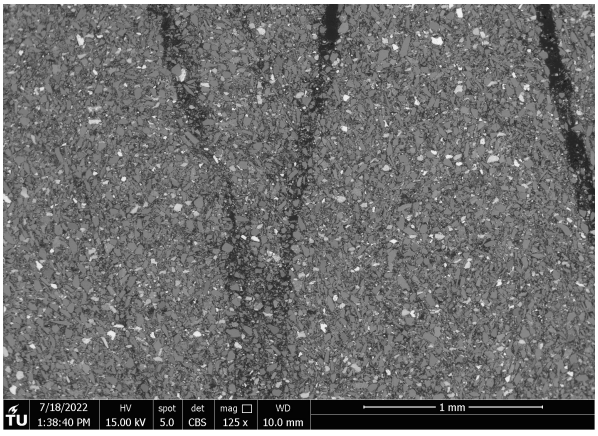

(cc) Sample 12.

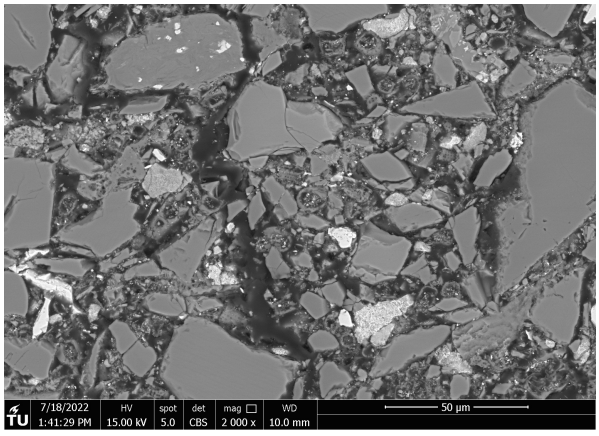

(cd) Sample 12.

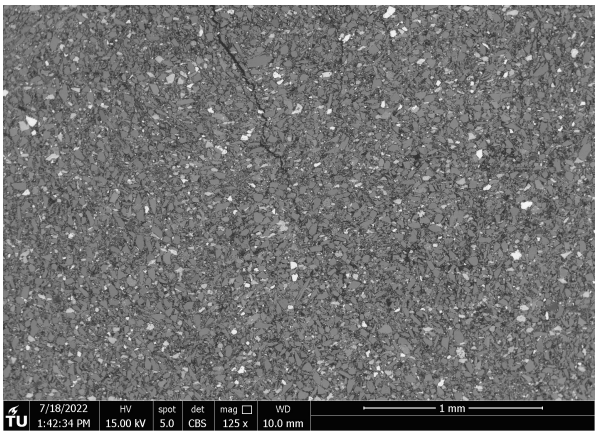

(ce) Sample 12.

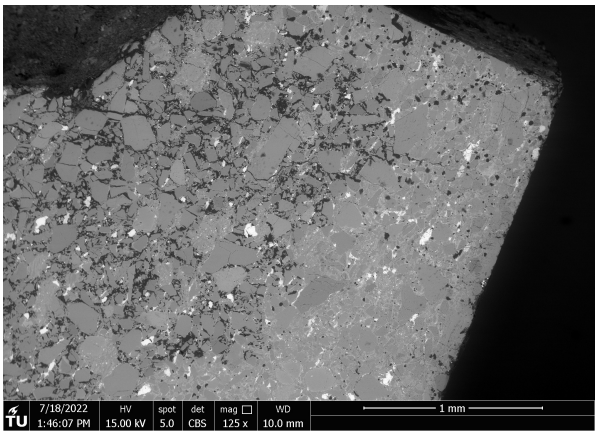

(cf) Sample 13.

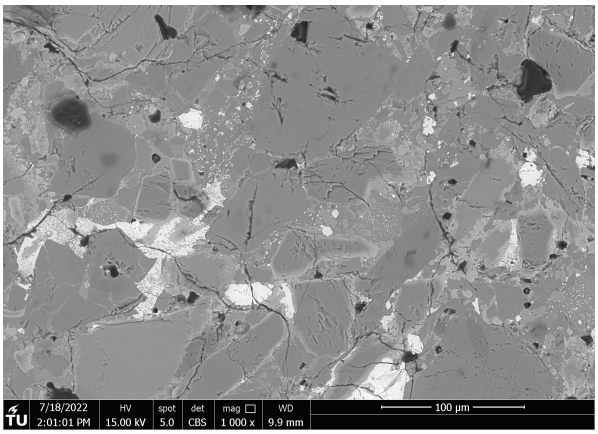

(cg) Sample 13.

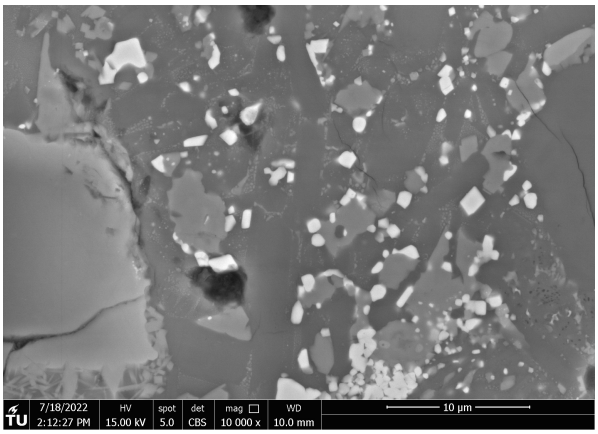

(ch) Sample 13.

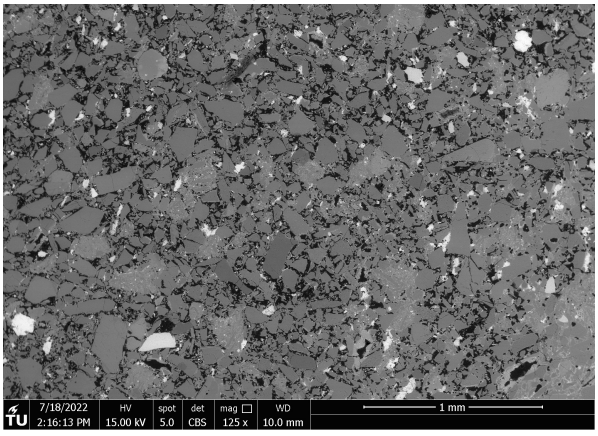

(ci) Sample 13.

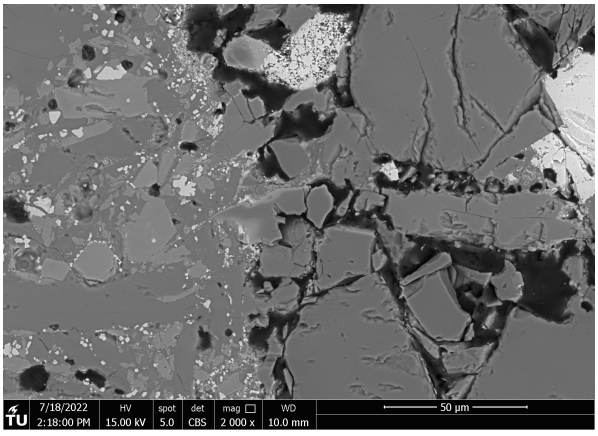

(cj) Sample 13.

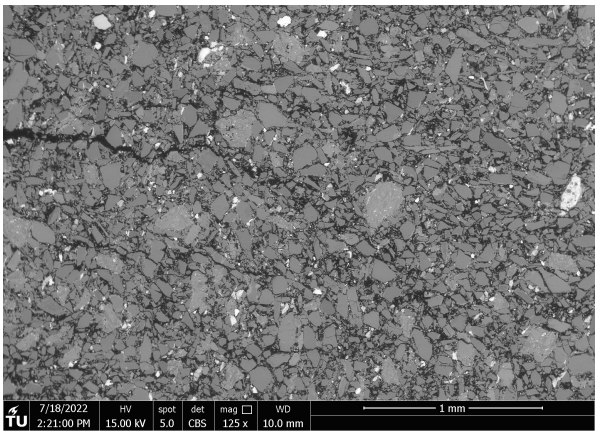

(ck) Sample 13.

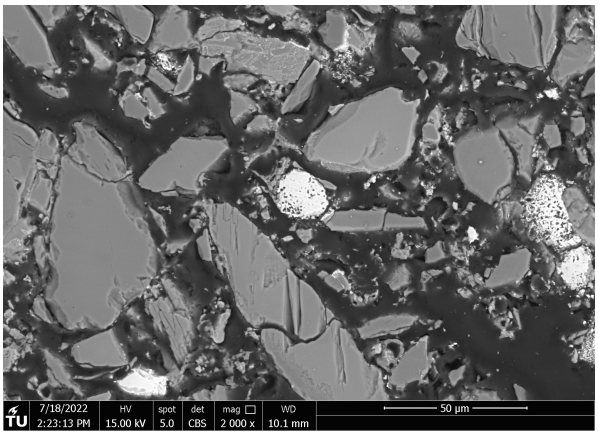

(cl) Sample 13.

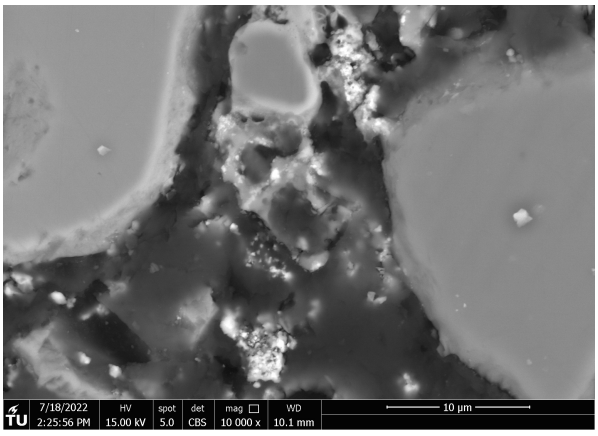

(cm) Sample 13.

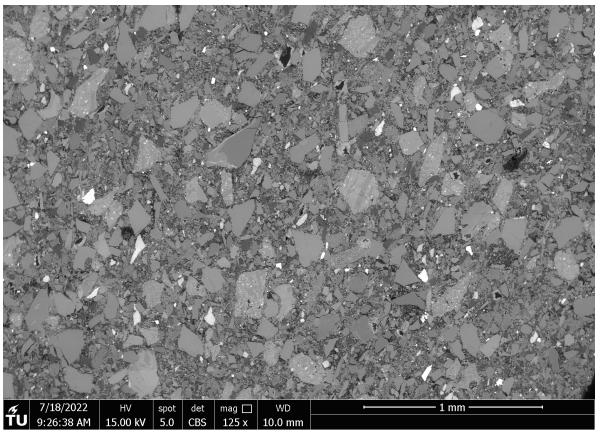

(cn) Sample 14.

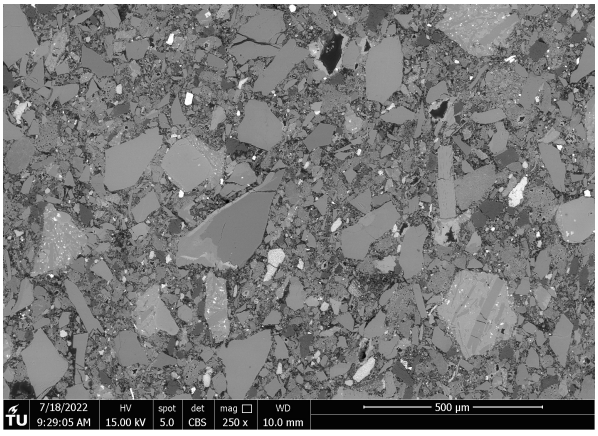

(co) Sample 14.

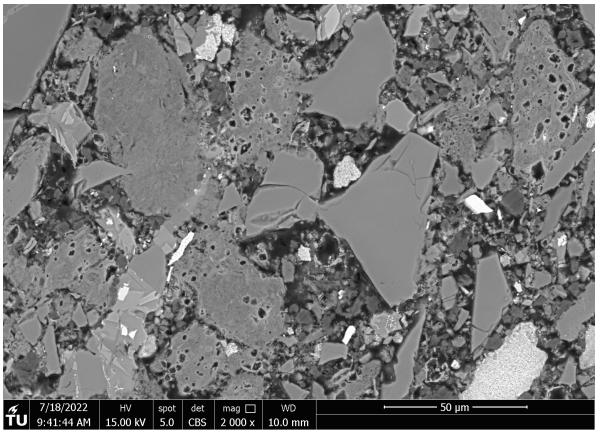

(cp) Sample 14.

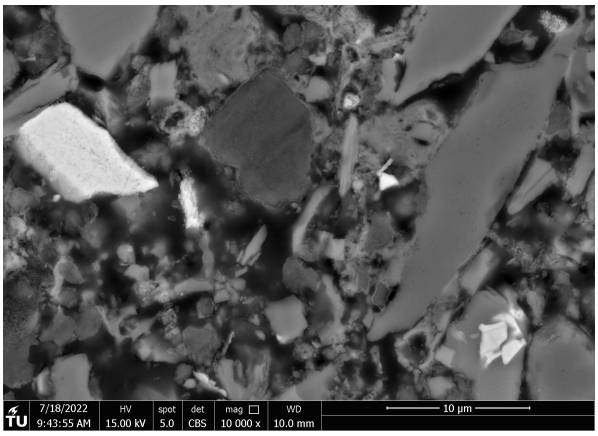

(cq) Sample 14.

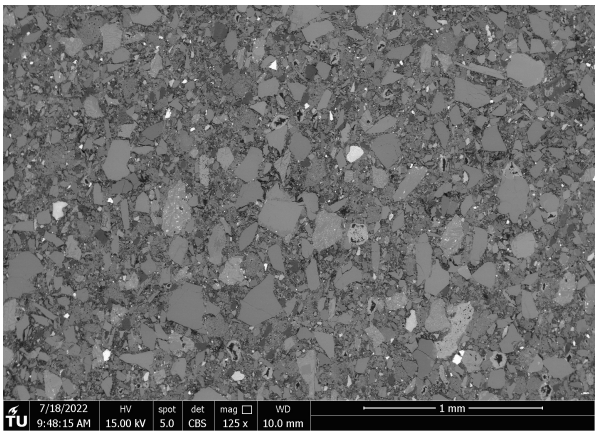

(cr) Sample 14.

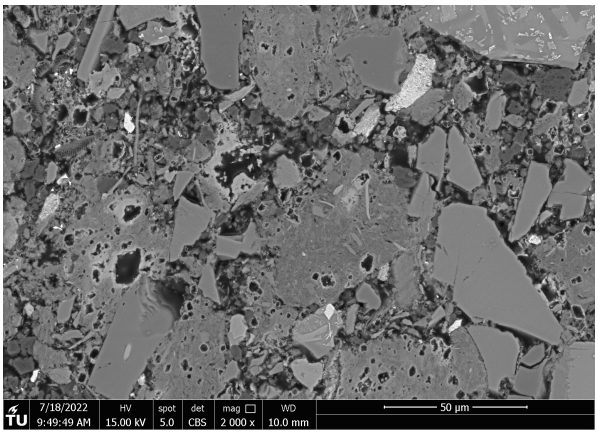

(cs) Sample 14.

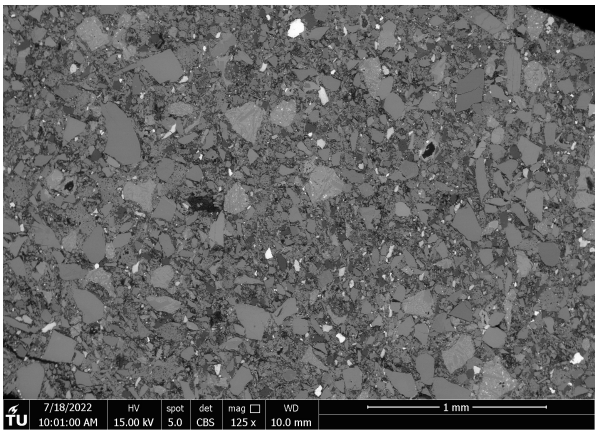

(ct) Sample 14.

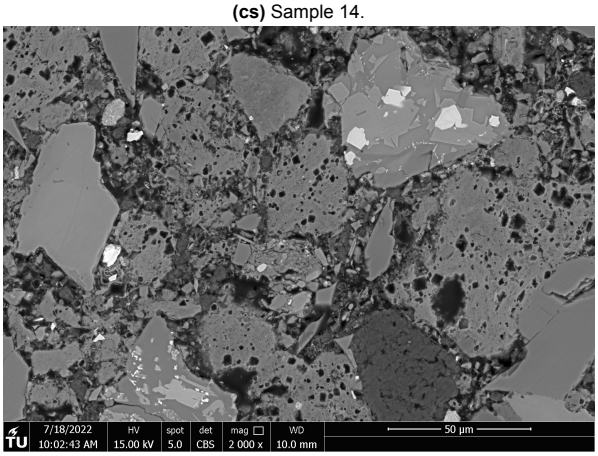

(cu) Sample 14.

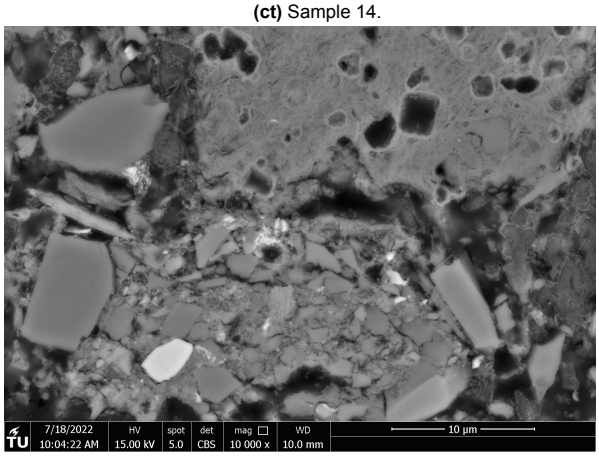

(cv) Sample 14.

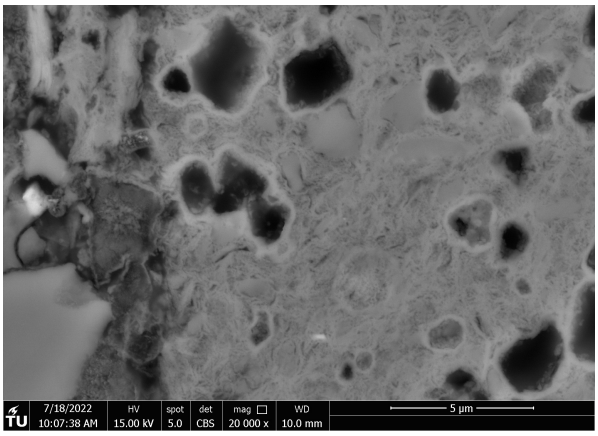

(cw) Sample 14.

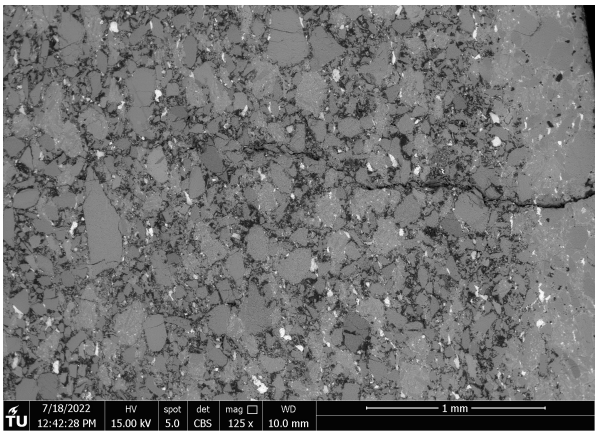

(cx) Sample 15.

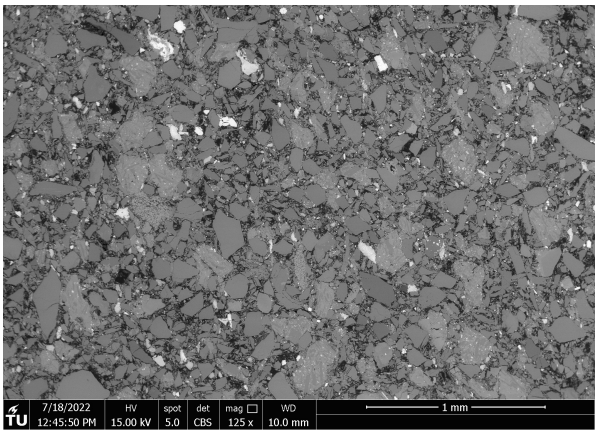

(cy) Sample 15.

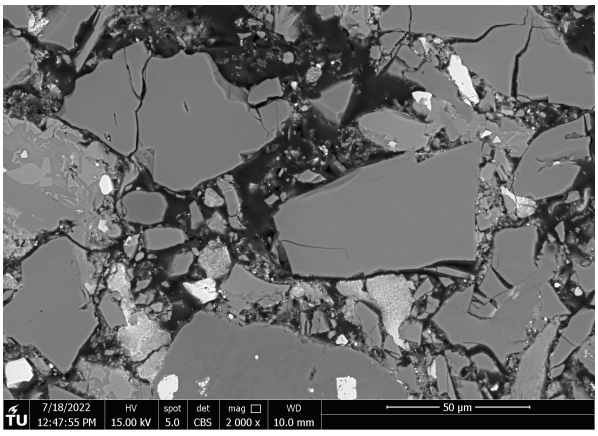

(cz) Sample 15.

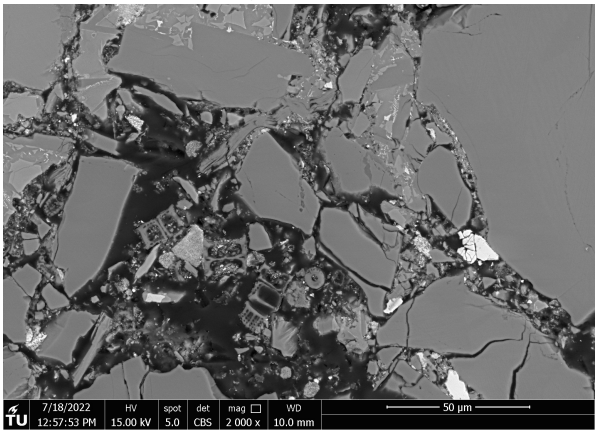

(da) Sample 15.

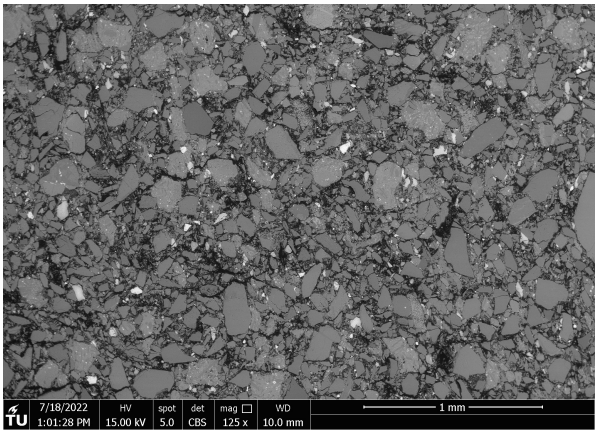

(db) Sample 15.

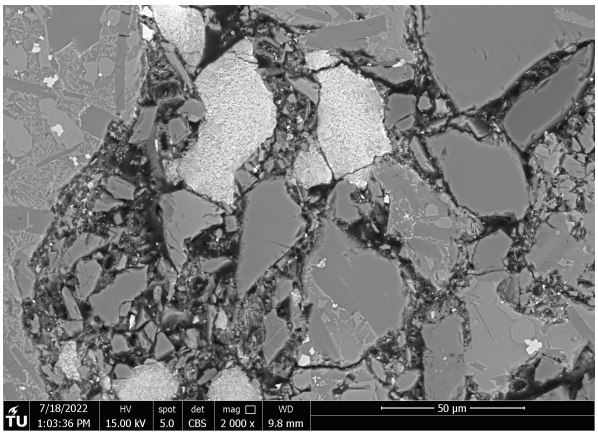

(dc) Sample 15.

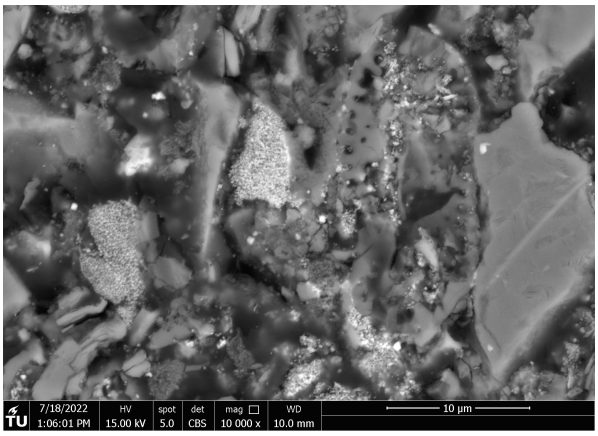

(dd) Sample 15.

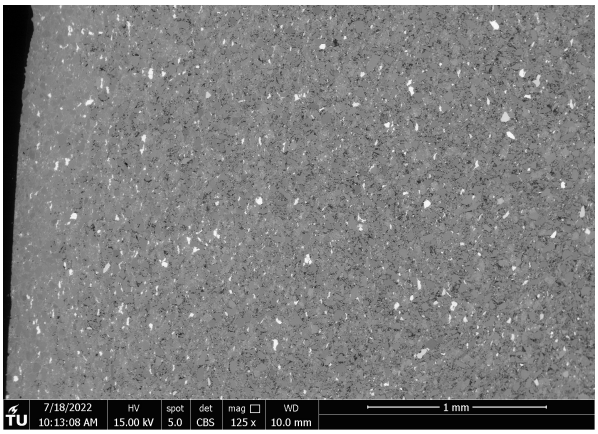

(de) Sample 16.

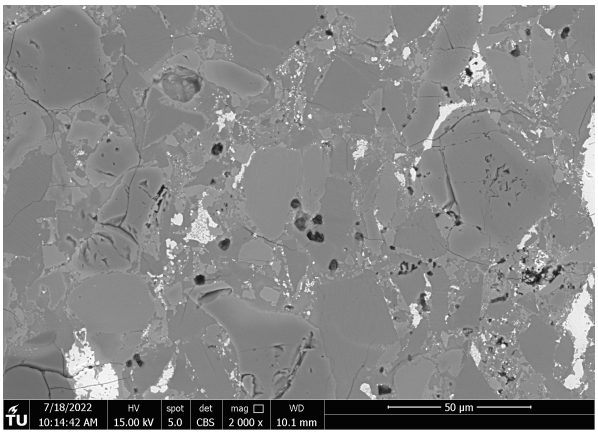

(df) Sample 16.

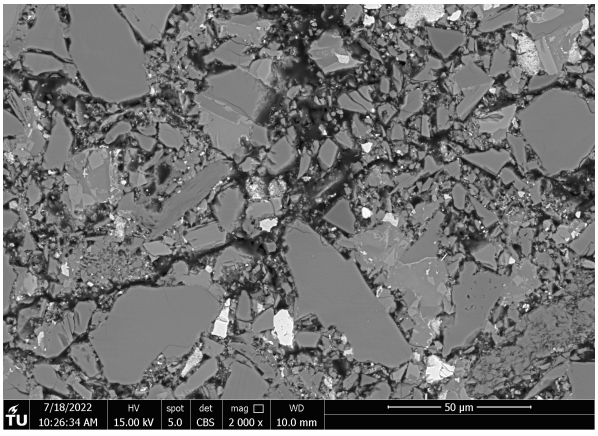

(dg) Sample 16.

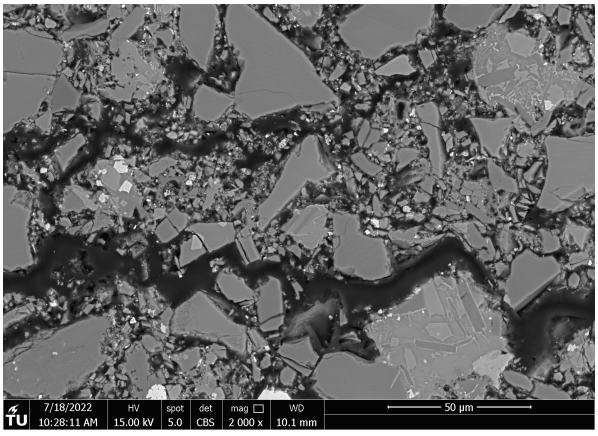

(dh) Sample 16.

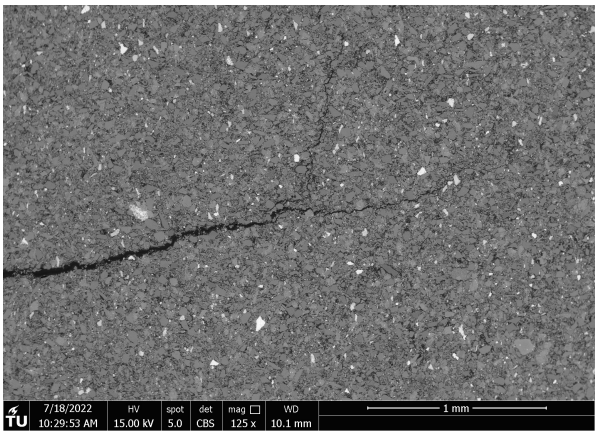

(di) Sample 16.

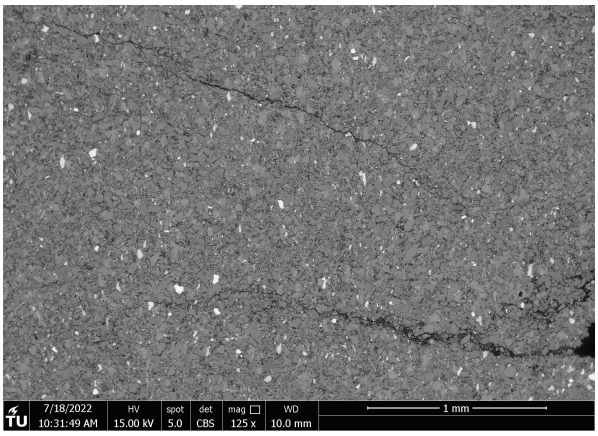

(dj) Sample 16.

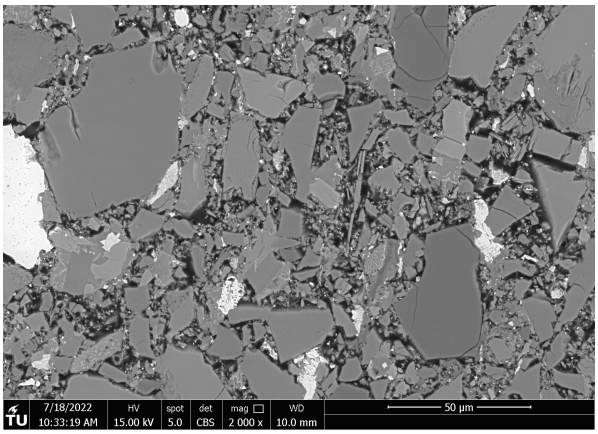

(dk) Sample 16.

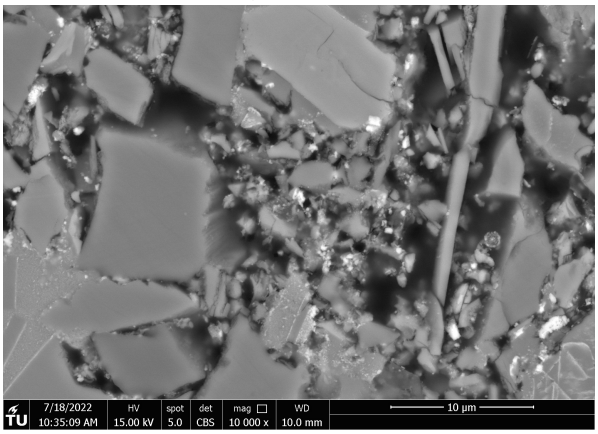

(dl) Sample 16.

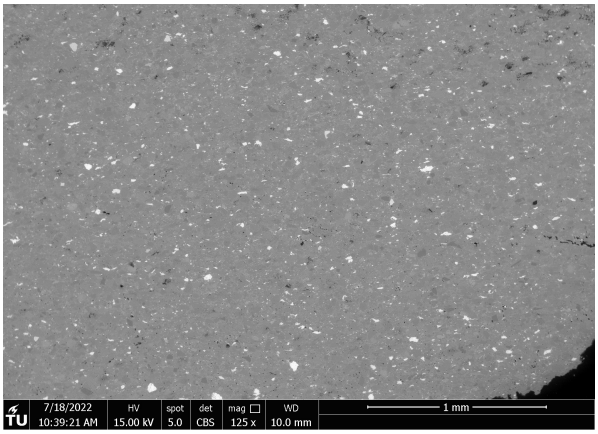

(dm) Sample 17.

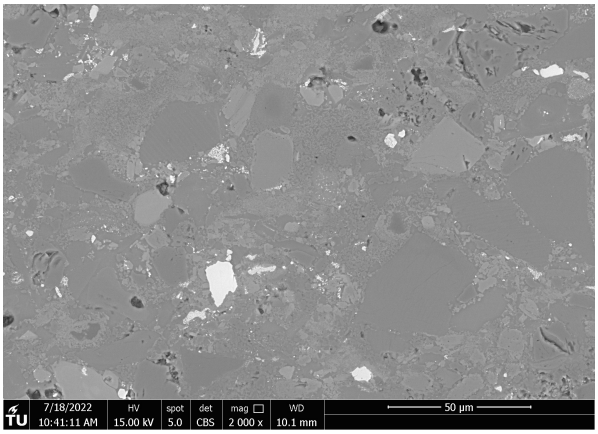

(dn) Sample 17.

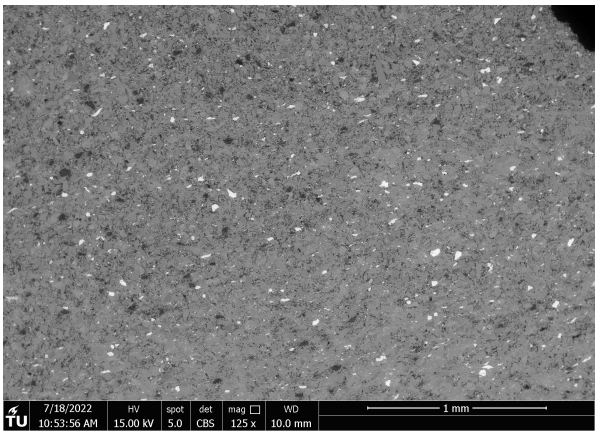

(do) Sample 17.

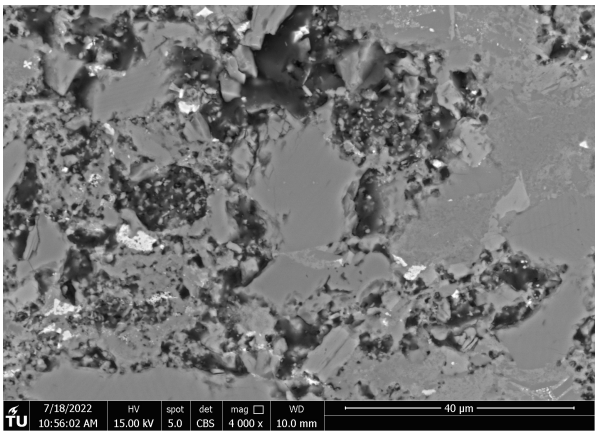

(dp) Sample 17.

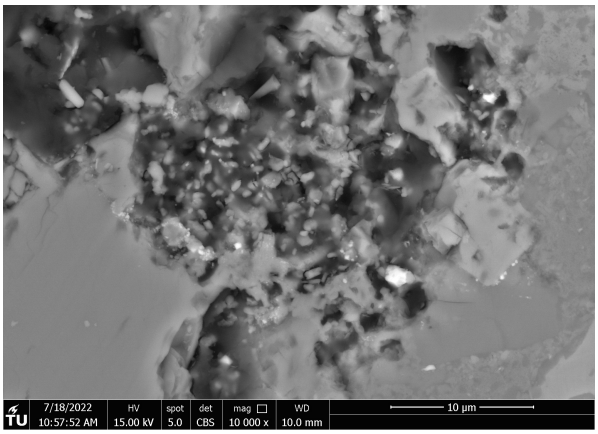

(dq) Sample 17.

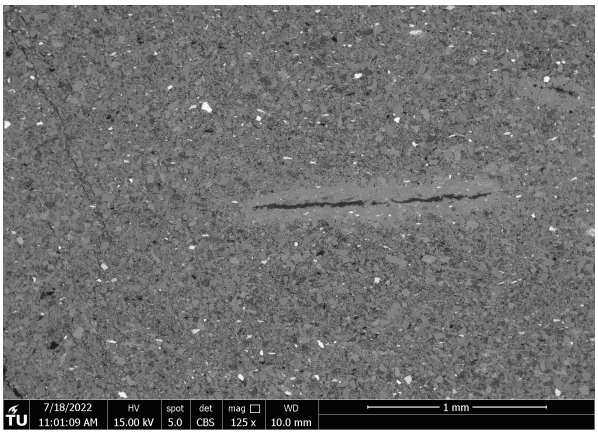

(dr) Sample 17.

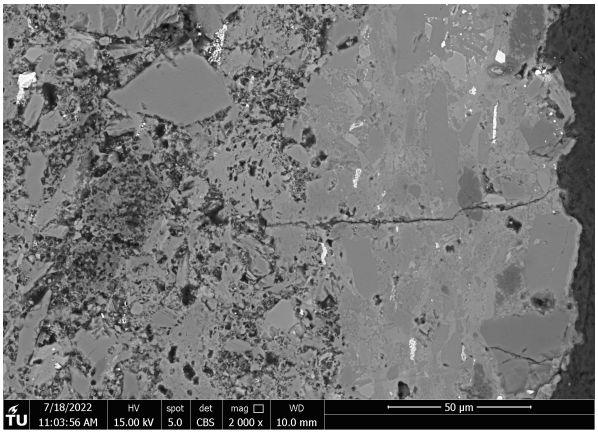

(ds) Sample 17.

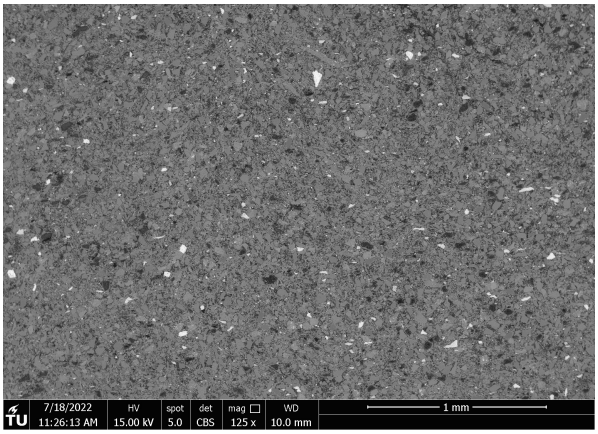

(dt) Sample 17.

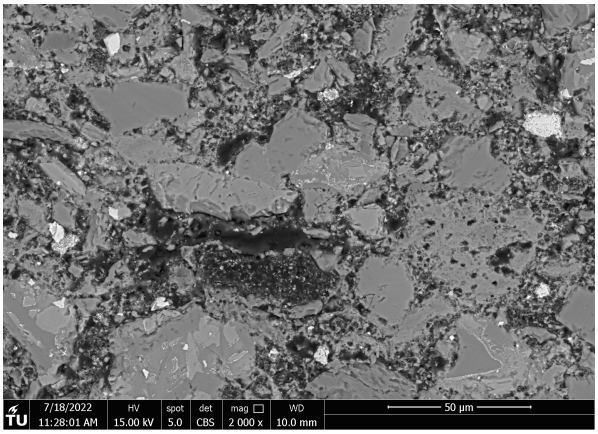

(du) Sample 17.

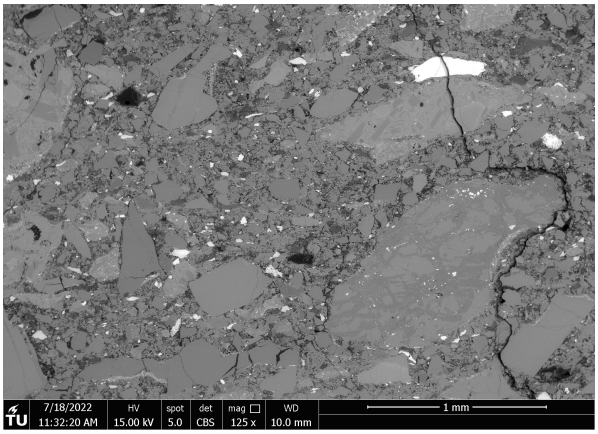

(dv) Sample 18.

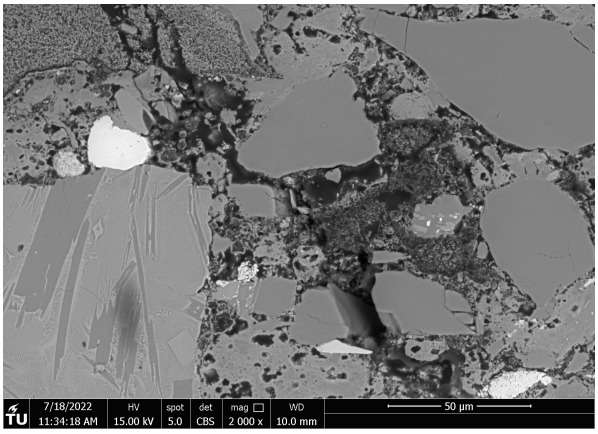

(dw) Sample 18.

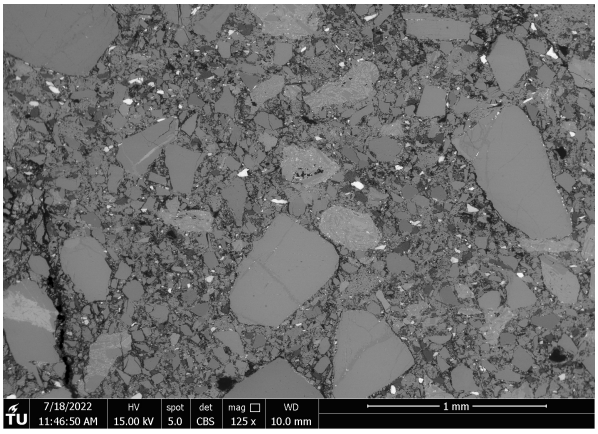

(dx) Sample 18.

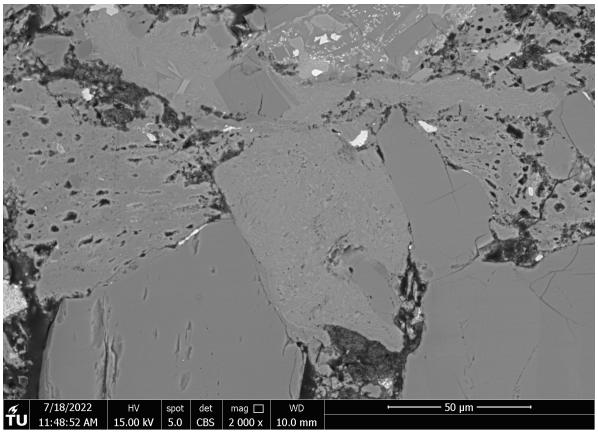

(dy) Sample 18.

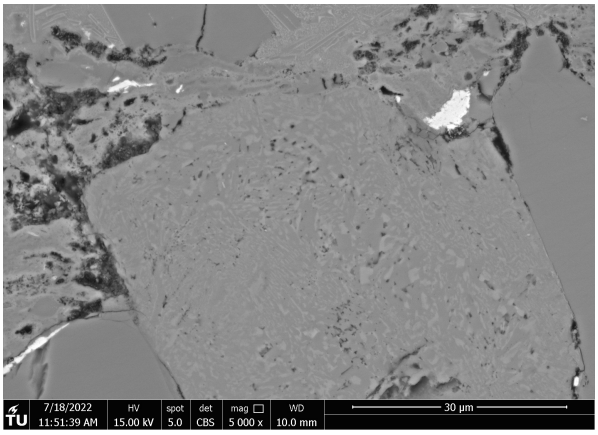

(dz) Sample 18.

Figure D.1: SEM images of all samples.

E

Supplementary Data of EDS Analysis

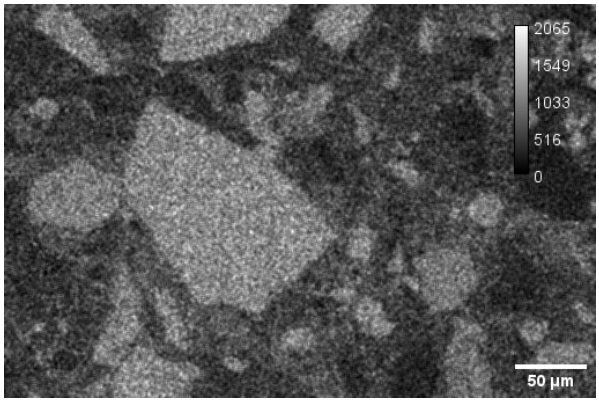

(a) Aluminium content in the J1 structure in sample 10. The colour scale indicates the elemental percentage of Al atoms. The value is given as 100×percentage. Meaning a value of 10000 is the pure element.

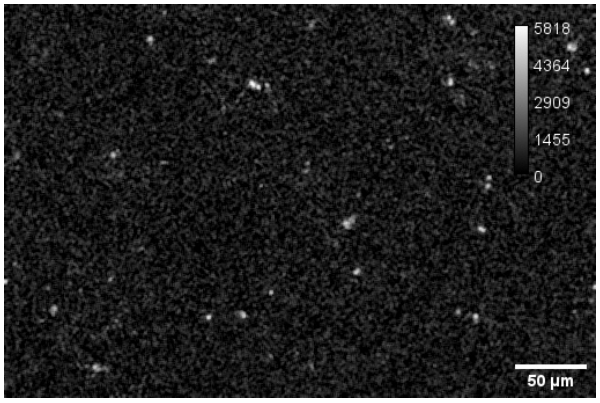

(b) Carbon content in the J1 structure in sample 10. The colour scale indicates the elemental percentage of C atoms. The value is given as 100×percentage. Meaning a value of 10000 is the pure element.

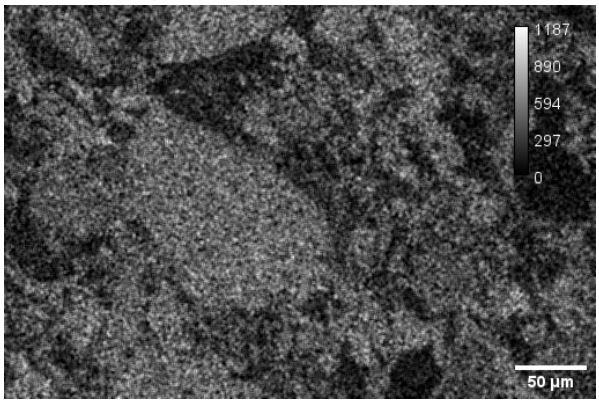

(c) Calcium content in the J1 structure in sample 10. The colour scale indicates the elemental percentage of Ca atoms. The value is given as 100×percentage. Meaning a value of 10000 is the pure element.

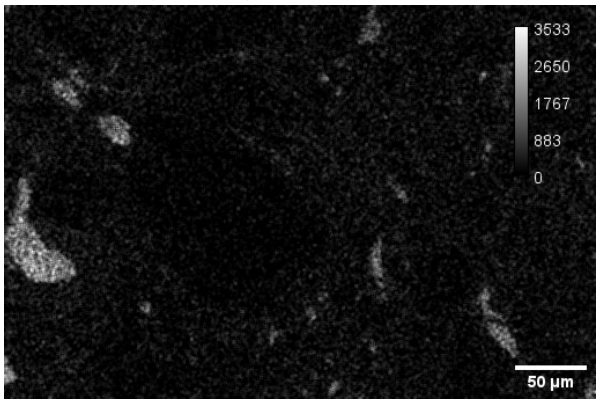

(d) Iron content in the J1 structure in sample 10. The colour scale indicates the elemental percentage of Fe atoms. The value is given as 100×percentage. Meaning a value of 10000 is the pure element.

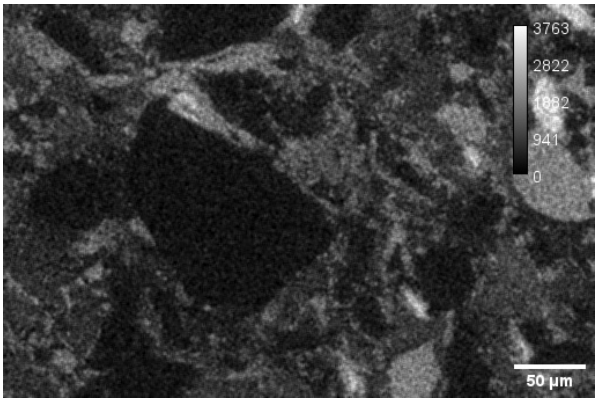

(e) Magnesium content in the J1 structure in sample 10. The colour scale indicates the elemental percentage of Mg atoms. The value is given as 100×percentage. Meaning a value of 10000 is the pure element.

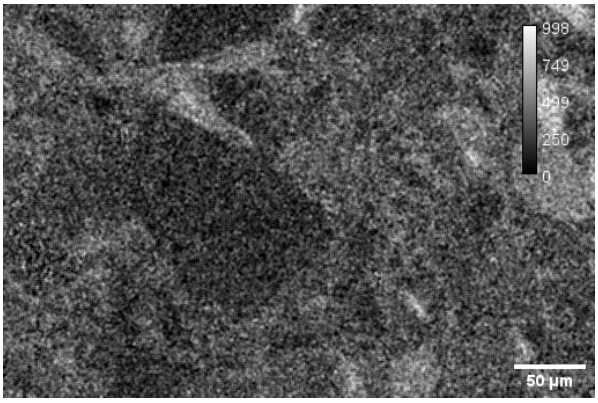

(f) Sodium content in the J1 structure in sample 10. The colour scale indicates the elemental percentage of Na atoms. The value is given as 100×percentage. Meaning a value of 10000 is the pure element.

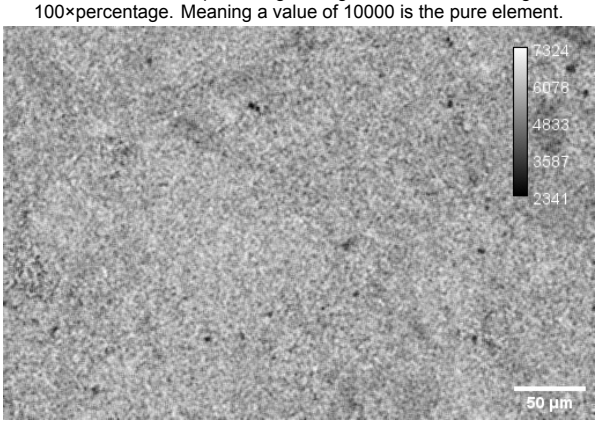

(g) Oxygen content in the J1 structure in sample 10. The colour scale indicates the elemental percentage of O atoms. The value is given as 100×percentage. Meaning a value of 10000 is the pure element.

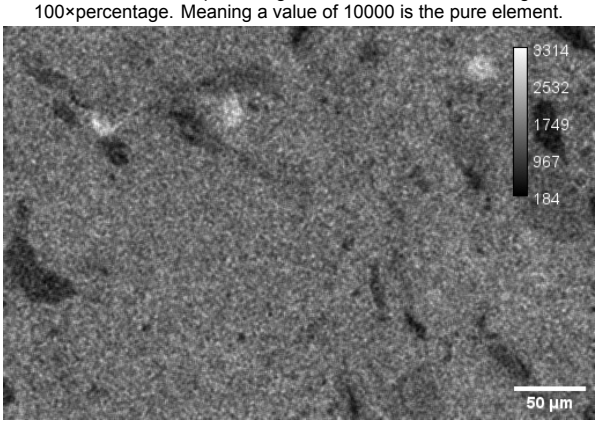

(h) Silica content in the J1 structure in sample 10. The colour scale indicates the elemental percentage of Si atoms. The value is given as 100×percentage. Meaning a value of 10000 is the pure element.

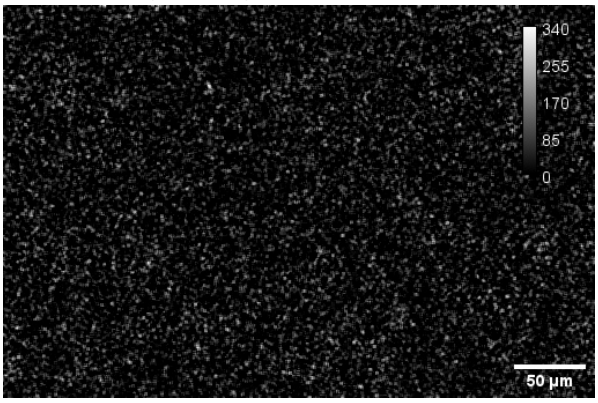

(i) Titanium content in the J1 structure in sample 10. The colour scale indicates the elemental percentage of Ti atoms. The value is given as 100×percentage. Meaning a value of 10000 is the pure element.

Figure E.1: EDS of sample 10 with thermal cracking in the J1 structure.

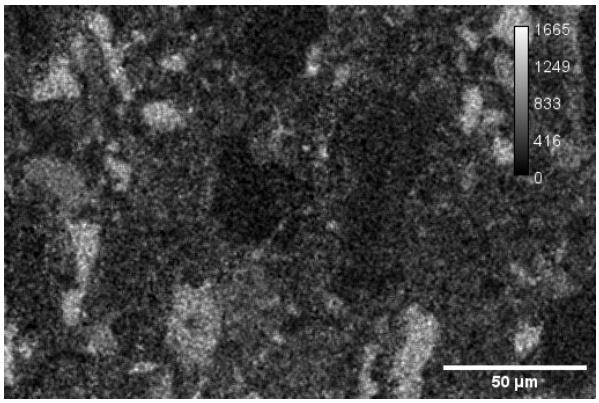

(a) Aluminium content in the J0 structure in sample 11. The colour scale indicates the elemental percentage of Al atoms. The value is given as 100×percentage. Meaning a value of 10000 is the pure element.

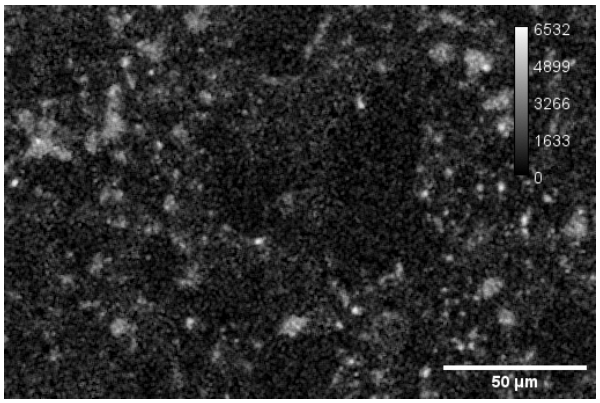

(b) Carbon content in the J0 structure in sample 11. The colour scale indicates the elemental percentage of C atoms. The value is given as 100×percentage. Meaning a value of 10000 is the pure element.

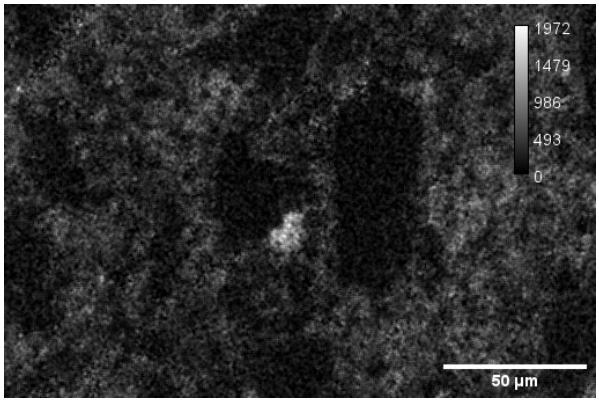

(c) Calcium content in the J0 structure in sample 11. The colour scale indicates the elemental percentage of Ca atoms. The value is given as 100×percentage. Meaning a value of 10000 is the pure element.

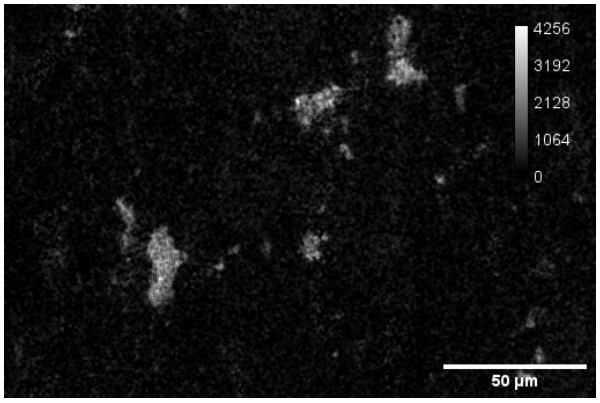

(d) Iron content in the J0 structure in sample 11. The colour scale indicates the elemental percentage of Fe atoms. The value is given as 100×percentage. Meaning a value of 10000 is the pure element.

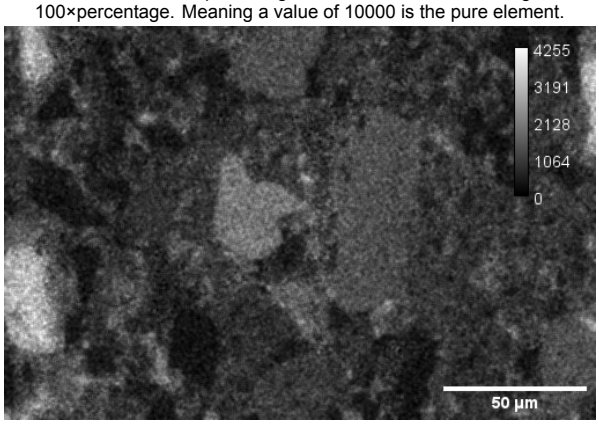

(e) Magnesium content in the J0 structure in sample 11. The colour scale indicates the elemental percentage of Mg atoms. The value is given as 100×percentage. Meaning a value of 10000 is the pure element.

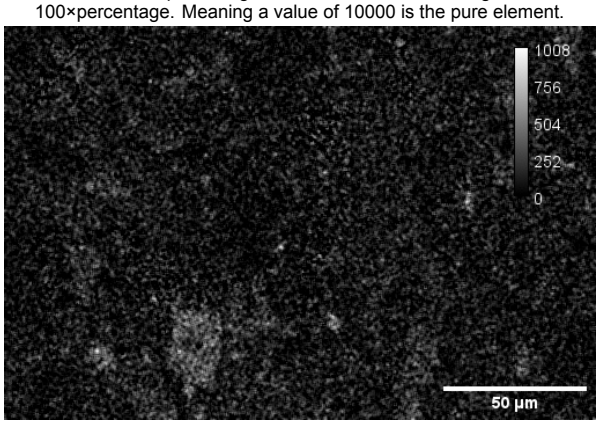

(f) Sodium content in the J0 structure in sample 11. The colour scale indicates the elemental percentage of Na atoms. The value is given as 100×percentage. Meaning a value of 10000 is the pure element.

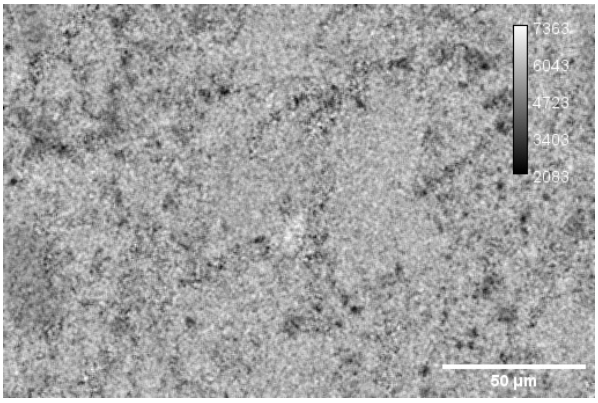

(g) Oxygen content in the J0 structure in sample 11. The colour scale indicates the elemental percentage of O atoms. The value is given as 100×percentage. Meaning a value of 10000 is the pure element.

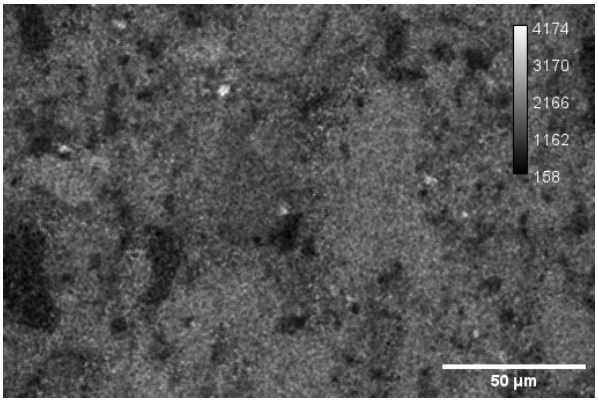

(h) Silica content in the J0 structure in sample 11. The colour scale indicates the elemental percentage of Si atoms. The value is given as 100×percentage. Meaning a value of 10000 is the pure element.

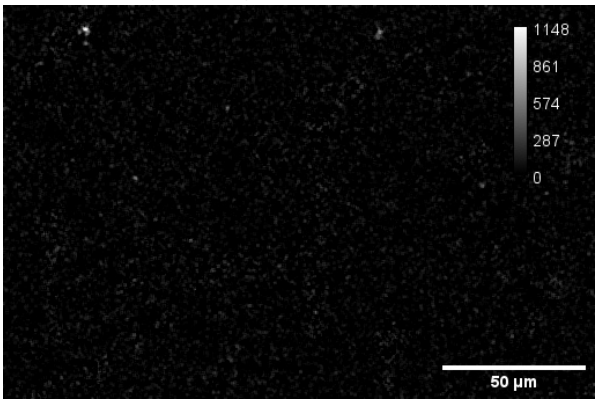

(i) Titanium content in the J0 structure in sample 11. The colour scale indicates the elemental percentage of Ti atoms. The value is given as 100×percentage. Meaning a value of 10000 is the pure element.

Figure E.2: EDS of sample 11 J0 structure.

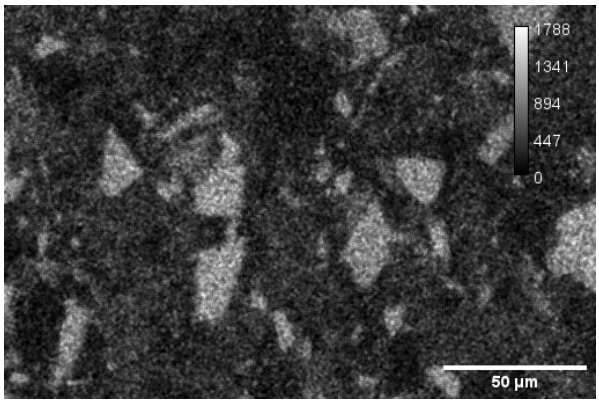

(a) Aluminium content in the J0 structure in sample 11. The colour scale indicates the elemental percentage of Al atoms. The value is given as 100×percentage. Meaning a value of 10000 is the pure element.

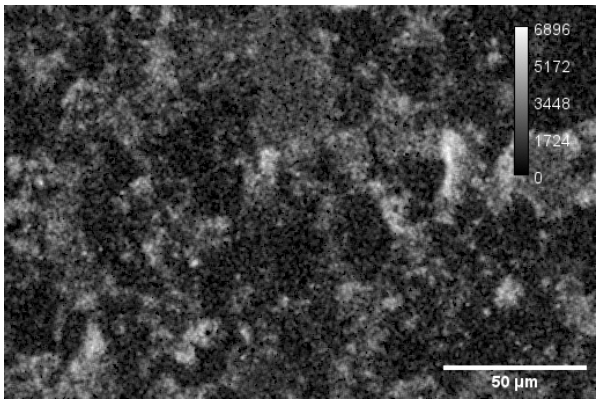

(b) Carbon content in the J0 structure in sample 11. The colour scale indicates the elemental percentage of C atoms. The value is given as 100×percentage. Meaning a value of 10000 is the pure element.

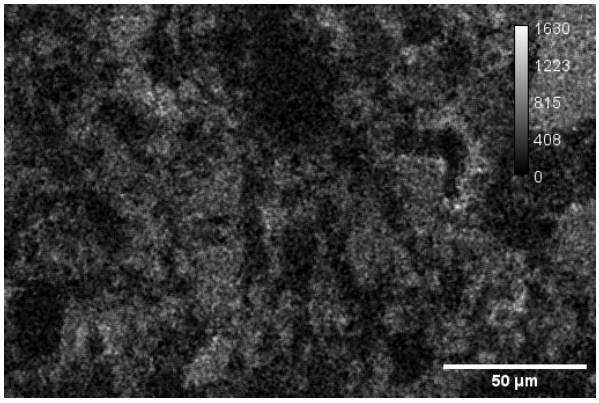

(c) Calcium content in the J0 structure in sample 11. The colour scale indicates the elemental percentage of Ca atoms. The value is given as 100×percentage. Meaning a value of 10000 is the pure element.

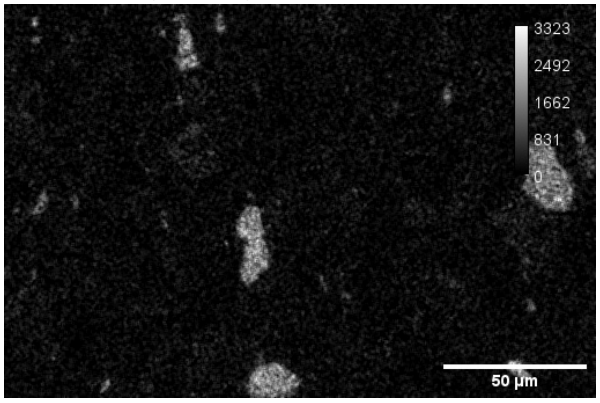

(d) Iron content in the J0 structure in sample 11. The colour scale indicates the elemental percentage of Fe atoms. The value is given as 100×percentage. Meaning a value of 10000 is the pure element.

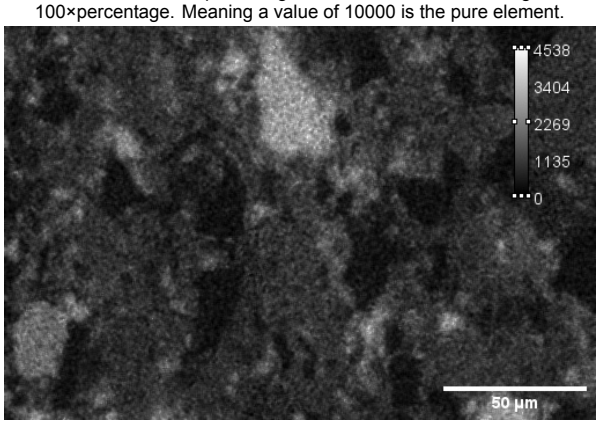

(e) Magnesium content in the J0 structure in sample 11. The colour scale indicates the elemental percentage of Mg atoms. The value is given as 100×percentage. Meaning a value of 10000 is the pure element.

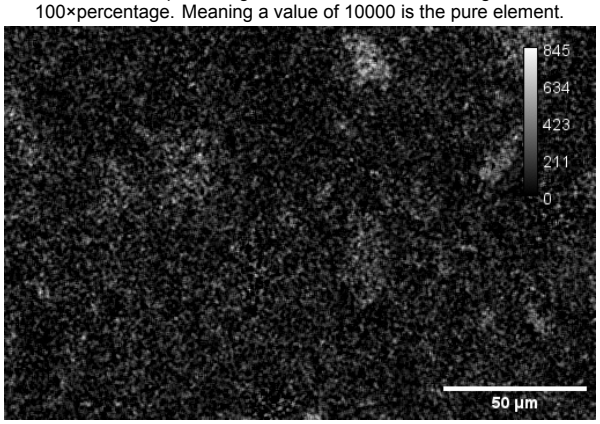

(f) Sodium content in the J0 structure in sample 11. The colour scale indicates the elemental percentage of Na atoms. The value is given as 100×percentage. Meaning a value of 10000 is the pure element.

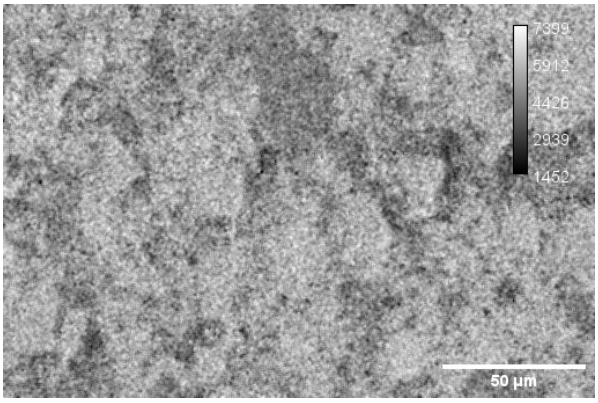

(g) Oxygen content in the J0 structure in sample 11. The colour scale indicates the elemental percentage of O atoms. The value is given as 100×percentage. Meaning a value of 10000 is the pure element.

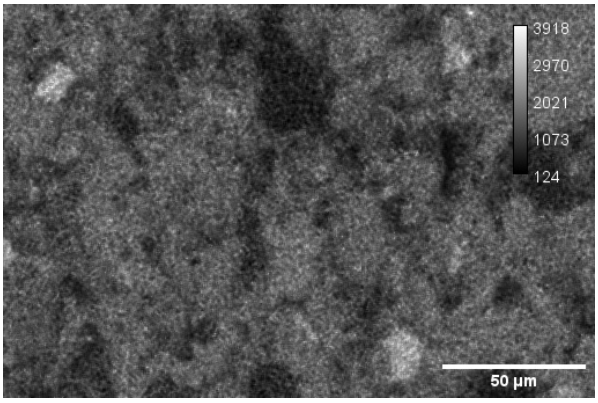

(h) Silica content in the J0 structure in sample 11. The colour scale indicates the elemental percentage of Si atoms. The value is given as 100×percentage. Meaning a value of 10000 is the pure element.

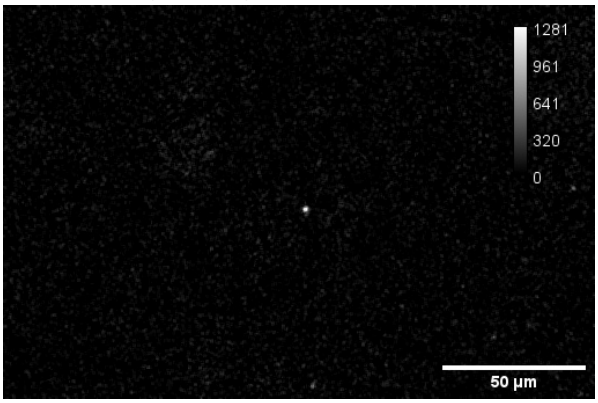

(i) Titanium content in the J0 structure in sample 11. The colour scale indicates the elemental percentage of Ti atoms. The value is given as 100×percentage. Meaning a value of 10000 is the pure element.

Figure E.3: EDS of sample 11 J0 structure.

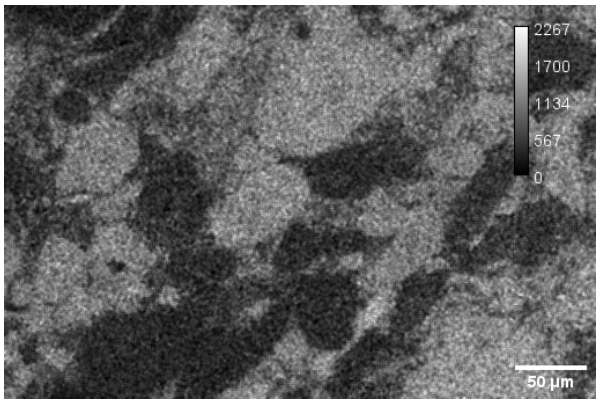

(a) Aluminium content in the M1 structure in sample 13. The colour scale indicates the elemental percentage of Al atoms. The value is given as 100×percentage. Meaning a value of 10000 is the pure element.

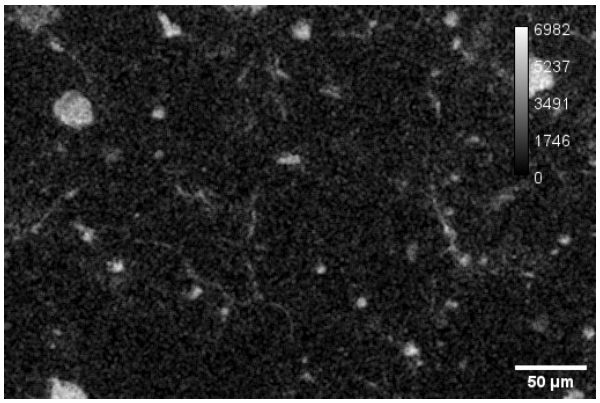

(b) Carbon content in the M1 structure in sample 13. The colour scale indicates the elemental percentage of C atoms. The value is given as 100×percentage. Meaning a value of 10000 is the pure element.

(c) Calcium content in the M1 structure in sample 13. The colour scale indicates the elemental percentage of Ca atoms. The value is given as 100×percentage. Meaning a value of 10000 is the pure element.

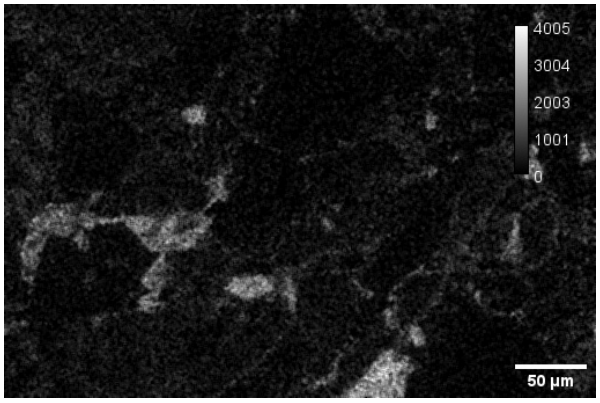

(d) Iron content in the M1 structure in sample 13. The colour scale indicates the elemental percentage of Fe atoms. The value is given as 100×percentage. Meaning a value of 10000 is the pure element.

(e) Magnesium content in the M1 structure in sample 13. The colour scale indicates the elemental percentage of Mg atoms. The value is given as 100×percentage. Meaning a value of 10000 is the pure element.

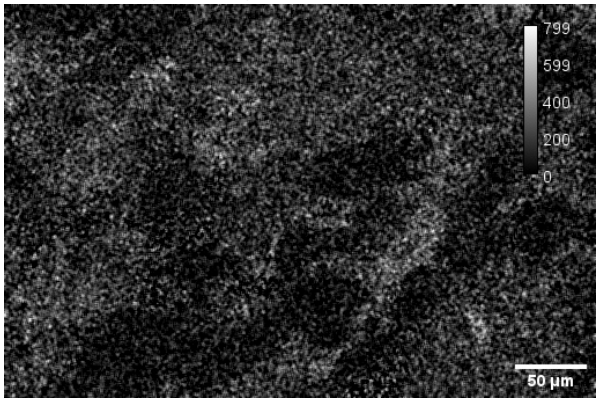

(f) Sodium content in the M1 structure in sample 13. The colour scale indicates the elemental percentage of Na atoms. The value is given as 100×percentage. Meaning a value of 10000 is the pure element.

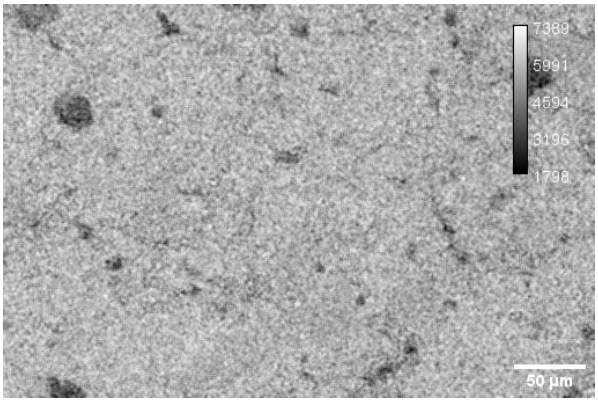

(g) Oxygen content in the M1 structure in sample 13. The colour scale indicates the elemental percentage of O atoms. The value is given as 100×percentage. Meaning a value of 10000 is the pure element.

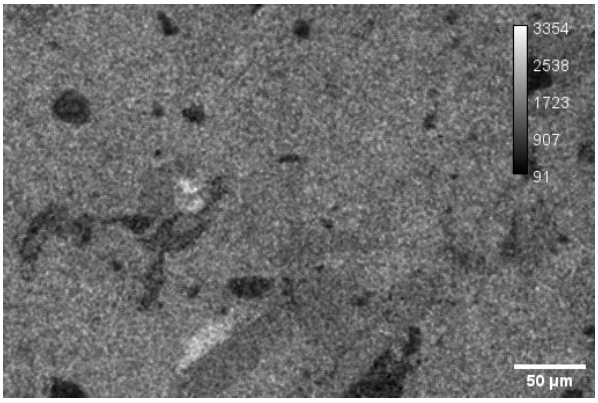

(h) Silica content in the M1 structure in sample 13. The colour scale indicates the elemental percentage of Si atoms. The value is given as 100×percentage. Meaning a value of 10000 is the pure element.

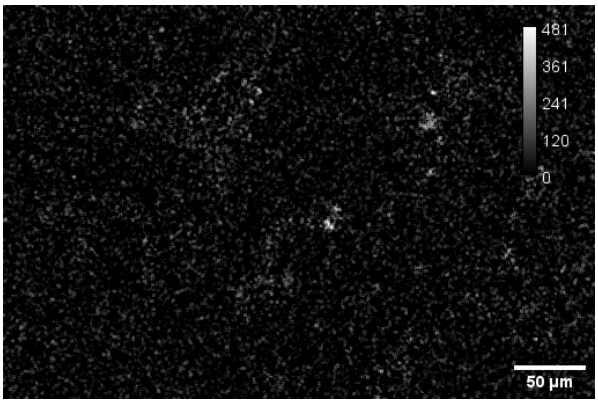

(i) Titanium content in the M1 structure in sample 13. The colour scale indicates the elemental percentage of Ti atoms. The value is given as 100×percentage. Meaning a value of 10000 is the pure element.

Figure E.4: EDS of sample 13 with thermal cracking in the M1 structure.

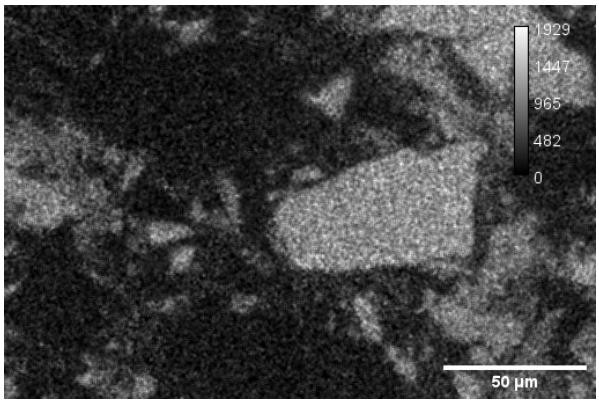

(a) Aluminium content in the M0 structure in sample 15. The colour scale indicates the elemental percentage of Al atoms. The value is given as 100×percentage. Meaning a value of 10000 is the pure element.

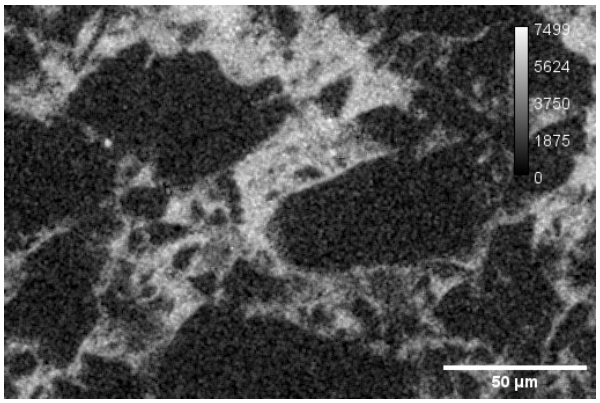

(b) Carbon content in the M0 structure in sample 15. The colour scale indicates the elemental percentage of C atoms. The value is given as 100×percentage. Meaning a value of 10000 is the pure element.

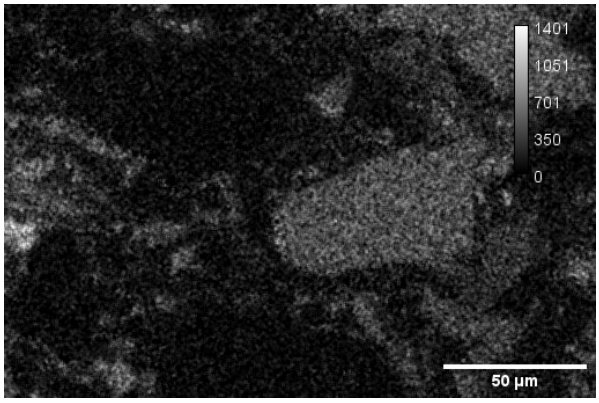

(c) Calcium content in the M0 structure in sample 15. The colour scale indicates the elemental percentage of Ca atoms. The value is given as 100×percentage. Meaning a value of 10000 is the pure element.

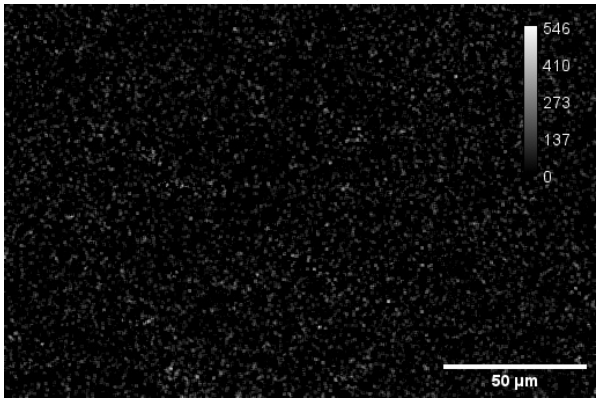

(d) Chrome content in the M0 structure in sample 15. The colour scale indicates the elemental percentage of Cr atoms. The value is given as 100×percentage. Meaning a value of 10000 is the pure element.

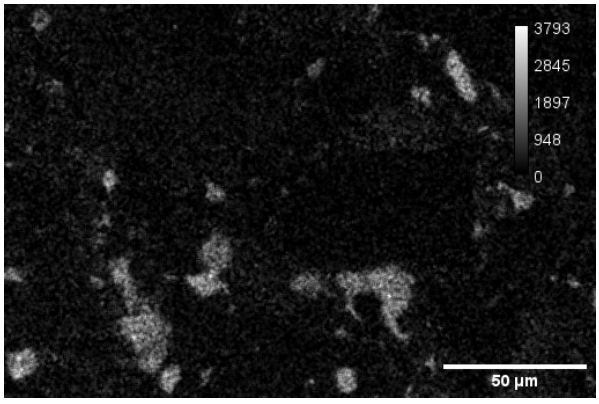

(e) Iron content in the M0 structure in sample 15. The colour scale indicates the elemental percentage of Fe atoms. The value is given as 100×percentage. Meaning a value of 10000 is the pure element.

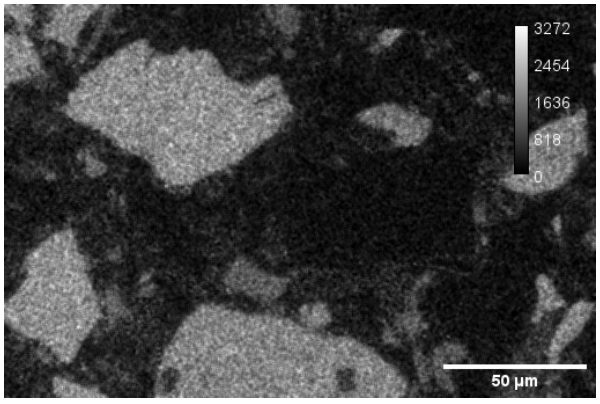

(f) Magnesium content in the M0 structure in sample 15. The colour scale indicates the elemental percentage of Mg atoms. The value is given as 100×percentage. Meaning a value of 10000 is the pure element.

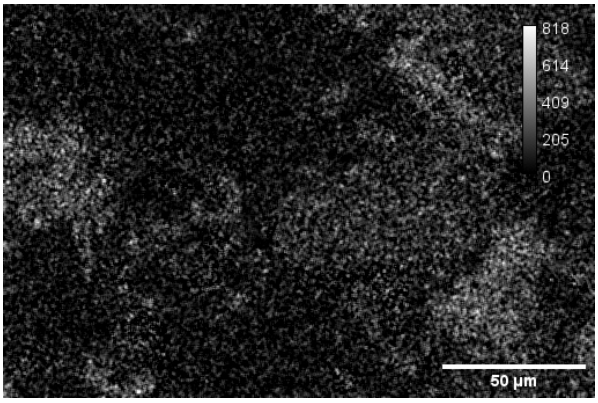

(g) Sodium content in the M0 structure in sample 15. The colour scale indicates the elemental percentage of Na atoms. The value is given as 100×percentage. Meaning a value of 10000 is the pure element.

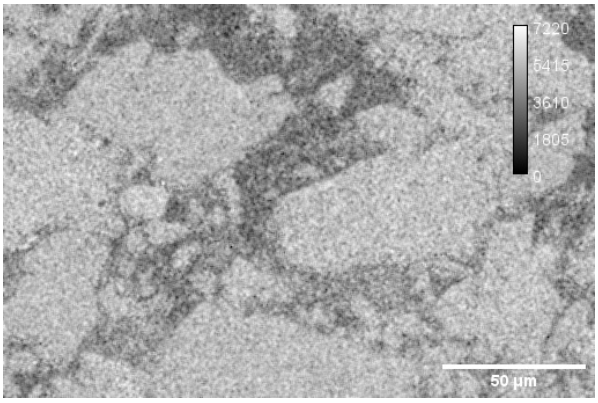

(h) Oxygen content in the M0 structure in sample 15. The colour scale indicates the elemental percentage of O atoms. The value is given as 100×percentage. Meaning a value of 10000 is the pure element.

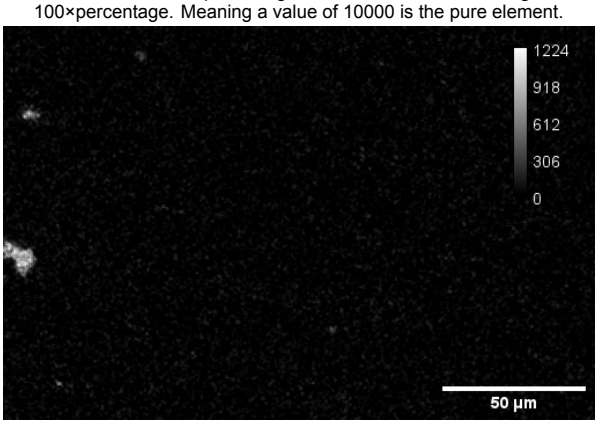

(i) Sulphur content in the M0 structure in sample 15. The colour scale indicates the elemental percentage of S atoms. The value is given as 100×percentage. Meaning a value of 10000 is the pure element.

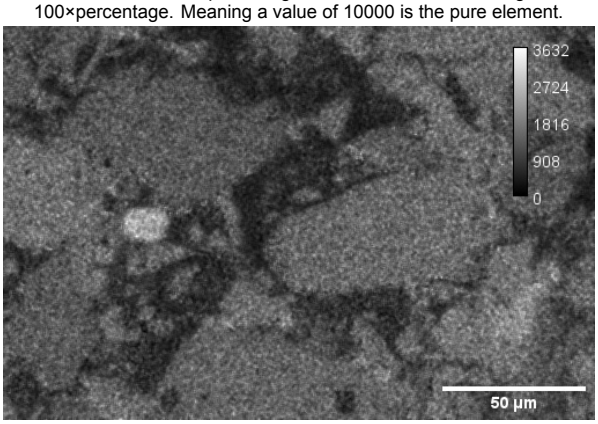

(j) Silica content in the M0 structure in sample 15. The colour scale indicates the elemental percentage of Si atoms. The value is given as 100×percentage. Meaning a value of 10000 is the pure element.

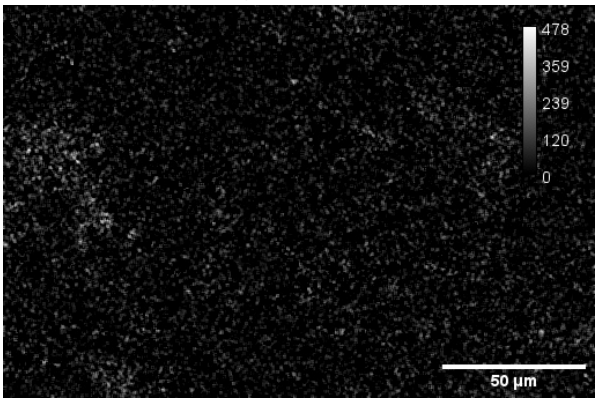

(k) Titanium content in the M0 structure in sample 15. The colour scale indicates the elemental percentage of Ti atoms. The value is given as 100×percentage. Meaning a value of 10000 is the pure element.

Figure E.5: EDS of sample 15 M0 structure.

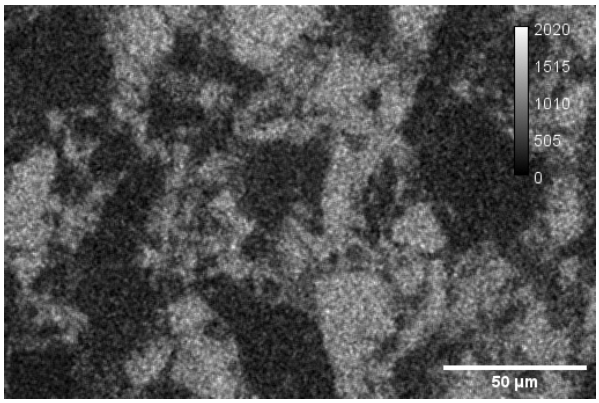

(a) Aluminium content in the M1 structure in sample 16. The colour scale indicates the elemental percentage of Al atoms. The value is given as 100×percentage. Meaning a value of 10000 is the pure element.

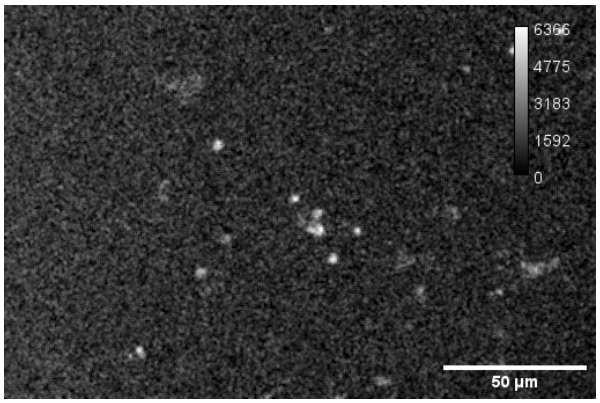

(b) Carbon content in the M1 structure in sample 16. The colour scale indicates the elemental percentage of C atoms. The value is given as 100×percentage. Meaning a value of 10000 is the pure element.

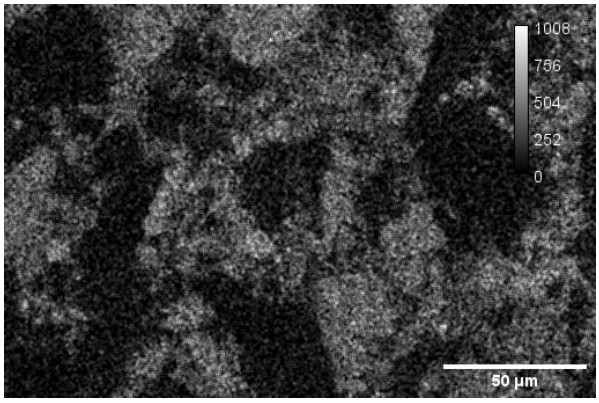

(c) Calcium content in the M1 structure in sample 16. The colour scale indicates the elemental percentage of Ca atoms. The value is given as 100×percentage. Meaning a value of 10000 is the pure element.

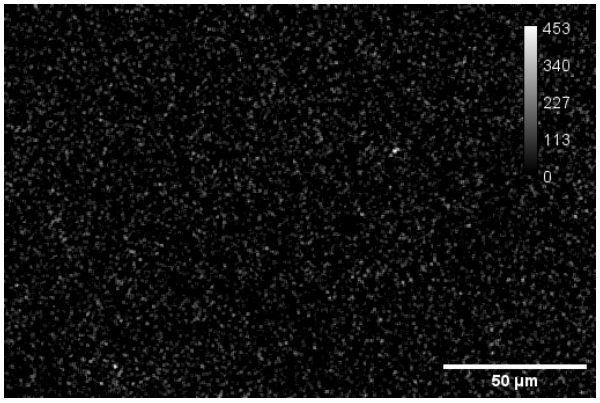

(d) Chrome content in the M1 structure in sample 16. The colour scale indicates the elemental percentage of Cr atoms. The value is given as 100×percentage. Meaning a value of 10000 is the pure element.

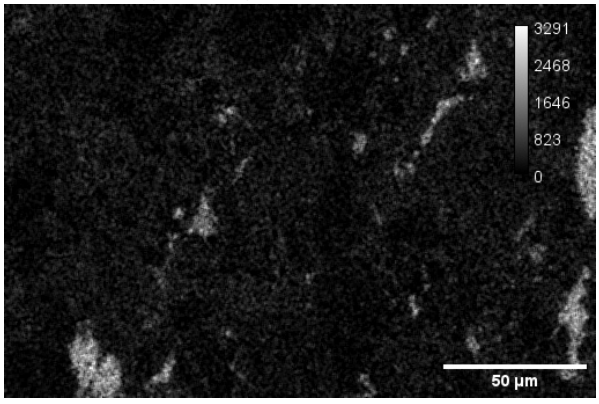

(e) Iron content in the M1 structure in sample 16. The colour scale indicates the elemental percentage of Fe atoms. The value is given as 100×percentage. Meaning a value of 10000 is the pure element.

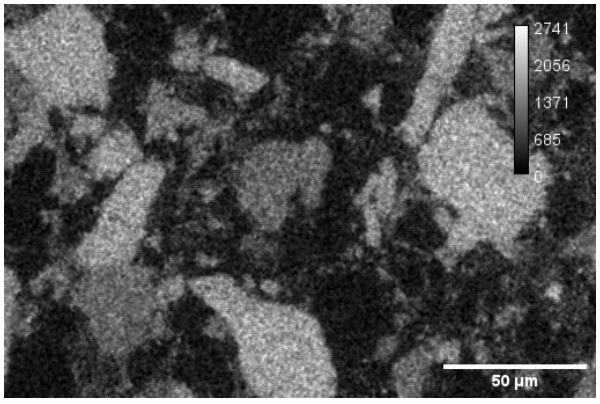

(f) Magnesium content in the M1 structure in sample 16. The colour scale indicates the elemental percentage of Mg atoms. The value is given as 100×percentage. Meaning a value of 10000 is the pure element.

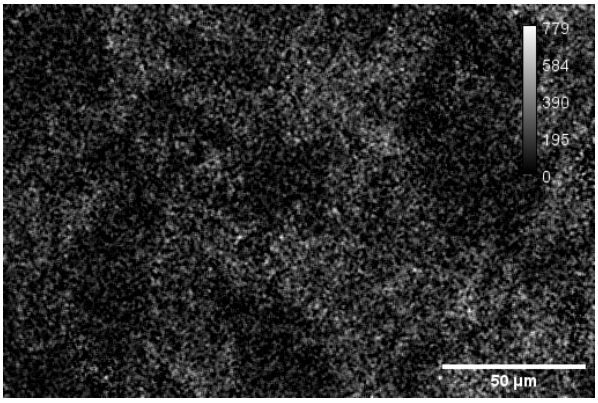

(g) Sodium content in the M1 structure in sample 16. The colour scale indicates the elemental percentage of Na atoms. The value is given as 100×percentage. Meaning a value of 10000 is the pure element.

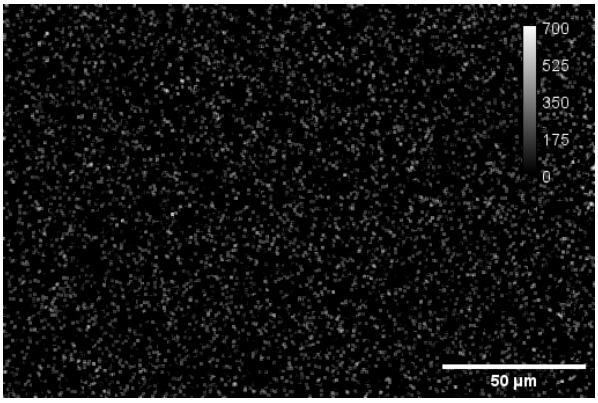

(h) Nickle content in the M1 structure in sample 16. The colour scale indicates the elemental percentage of Ni atoms. The value is given as 100×percentage. Meaning a value of 10000 is the pure element.

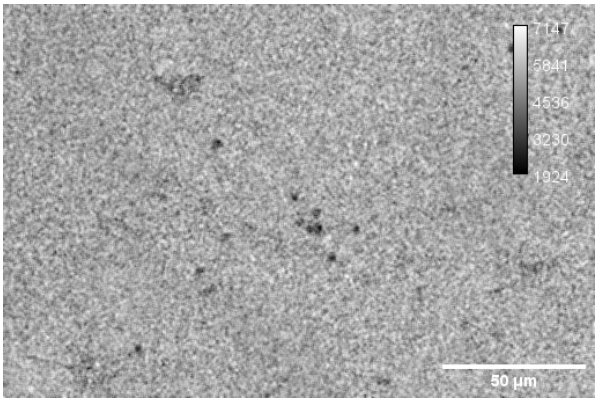

(i) Oxygen content in the M1 structure in sample 16. The colour scale indicates the elemental percentage of O atoms. The value is given as 100×percentage. Meaning a value of 10000 is the pure element.

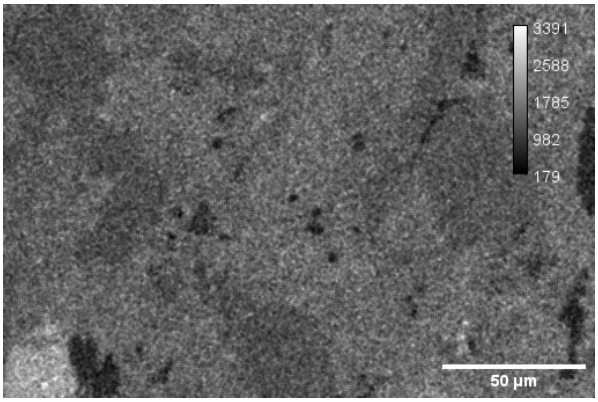

(j) Silica content in the M1 structure in sample 16. The colour scale indicates the elemental percentage of Si atoms. The value is given as 100×percentage. Meaning a value of 10000 is the pure element.

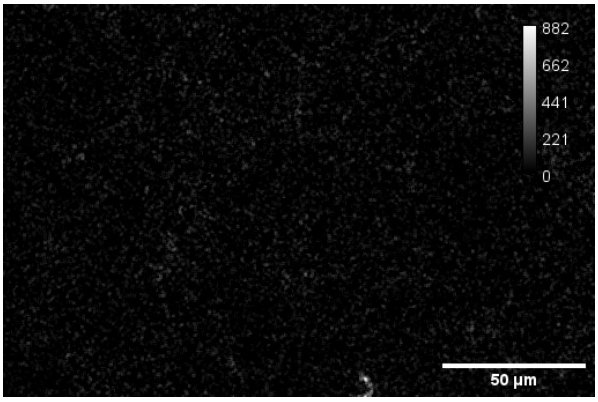

(k) Titanium content in the M1 structure in sample 16. The colour scale indicates the elemental percentage of Ti atoms. The value is given as 100×percentage. Meaning a value of 10000 is the pure element.

Figure E.6: EDS of sample 16 M1 structure.

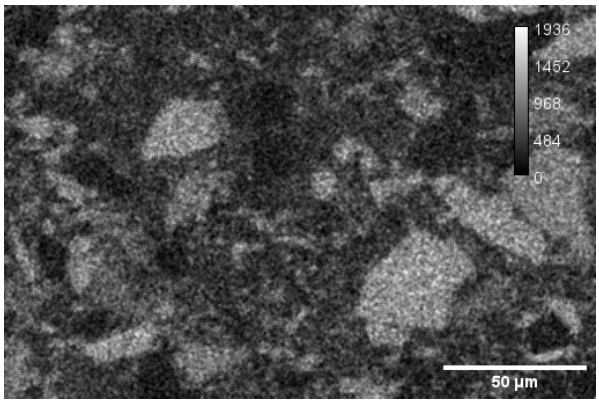

(a) Aluminium content in the J1 structure in sample 17. The colour scale indicates the elemental percentage of Al atoms. The value is given as 100×percentage. Meaning a value of 10000 is the pure element.

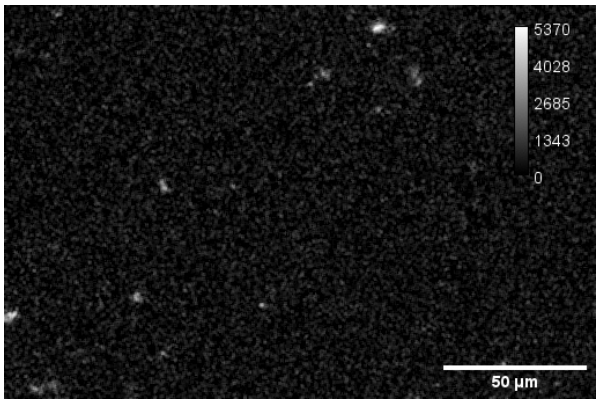

(b) Carbon content in the J1 structure in sample 17. The colour scale indicates the elemental percentage of C atoms. The value is given as 100×percentage. Meaning a value of 10000 is the pure element.

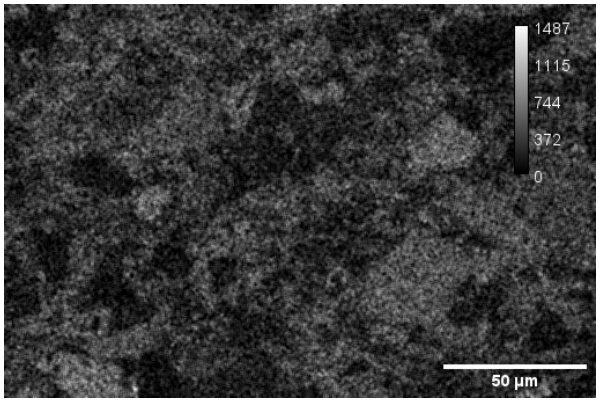

(c) Calcium content in the J1 structure in sample 17. The colour scale indicates the elemental percentage of Ca atoms. The value is given as 100×percentage. Meaning a value of 10000 is the pure element.

(d) Chrome content in the J1 structure in sample 17. The colour scale indicates the elemental percentage of Cr atoms. The value is given as 100×percentage. Meaning a value of 10000 is the pure element.

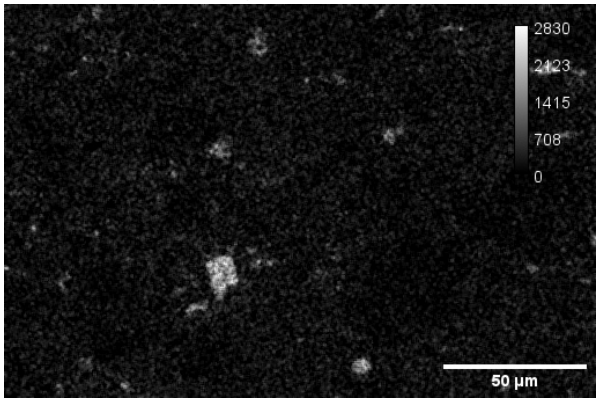

(e) Iron content in the J1 structure in sample 17. The colour scale indicates the elemental percentage of Fe atoms. The value is given as 100×percentage. Meaning a value of 10000 is the pure element.

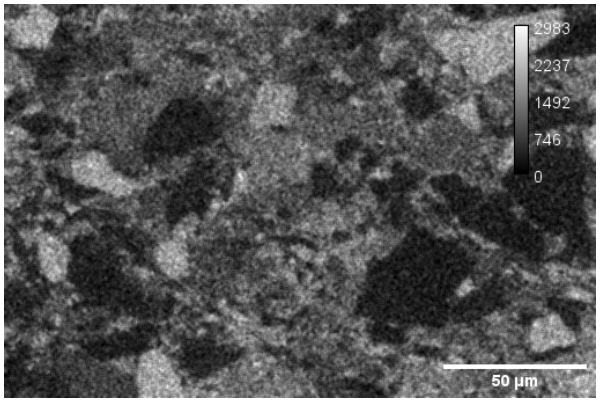

(f) Magnesium content in the J1 structure in sample 17. The colour scale indicates the elemental percentage of Mg atoms. The value is given as 100×percentage. Meaning a value of 10000 is the pure element.

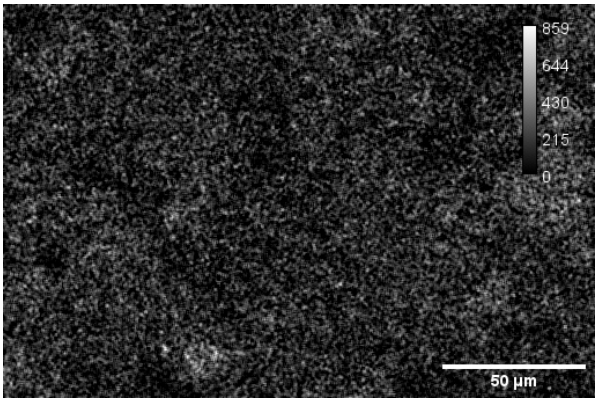

(g) Sodium content in the J1 structure in sample 17. The colour scale indicates the elemental percentage of Na atoms. The value is given as 100×percentage. Meaning a value of 10000 is the pure element.

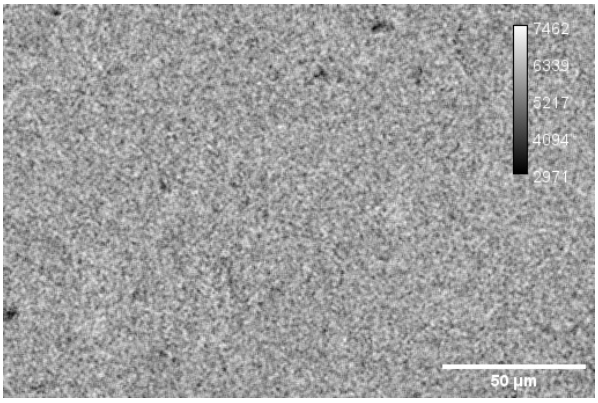

(h) Oxygen content in the J1 structure in sample 17. The colour scale indicates the elemental percentage of O atoms. The value is given as 100×percentage. Meaning a value of 10000 is the pure element.

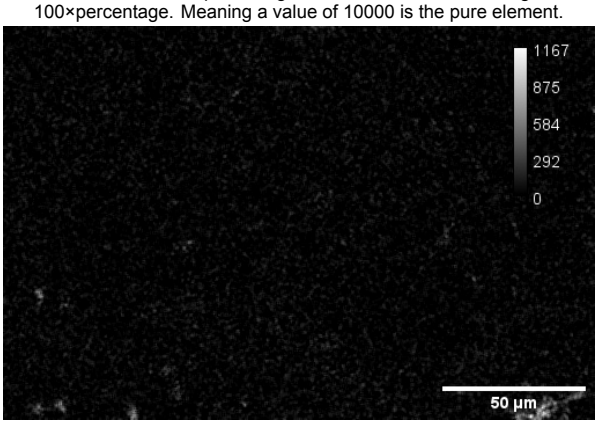

(i) Sulphur content in the J1 structure in sample 17. The colour scale indicates the elemental percentage of S atoms. The value is given as 100×percentage. Meaning a value of 10000 is the pure element.

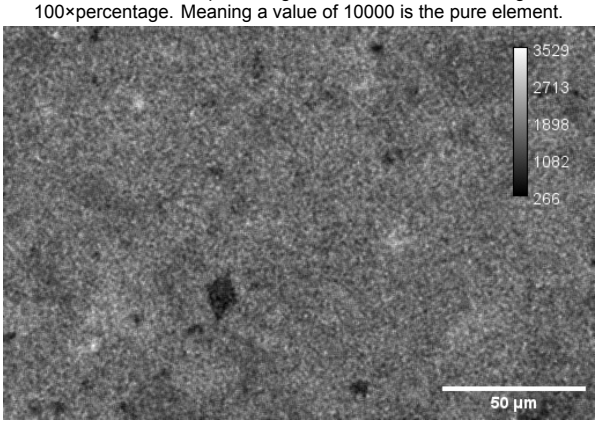

(j) Silica content in the J1 structure in sample 17. The colour scale indicates the elemental percentage of Si atoms. The value is given as 100×percentage. Meaning a value of 10000 is the pure element.

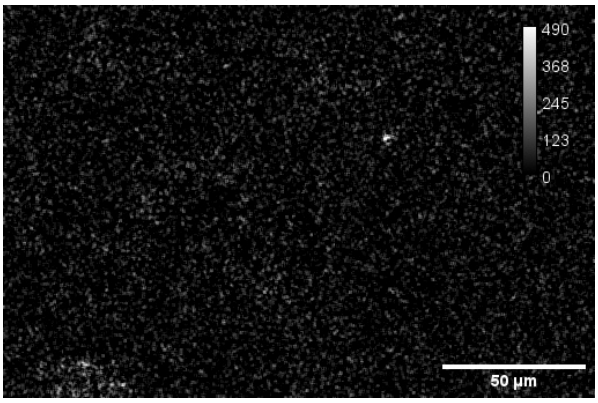

(k) Titanium content in the J1 structure in sample 17. The colour scale indicates the elemental percentage of Ti atoms. The value is given as 100×percentage. Meaning a value of 10000 is the pure element.

Figure E.7: EDS of sample 17 J1 structure.

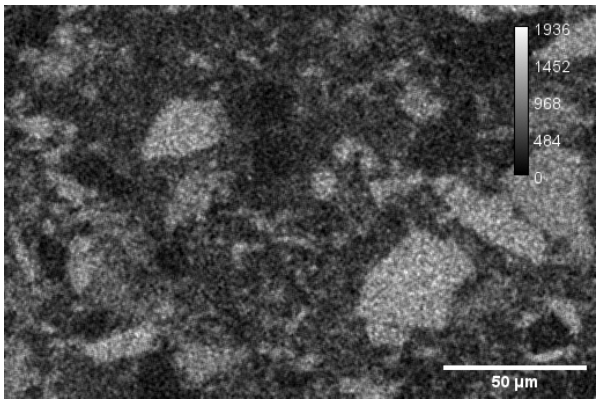

(a) Aluminium content in the J1 structure in sample 17. The colour scale indicates the elemental percentage of Al atoms. The value is given as 100×percentage. Meaning a value of 10000 is the pure element.

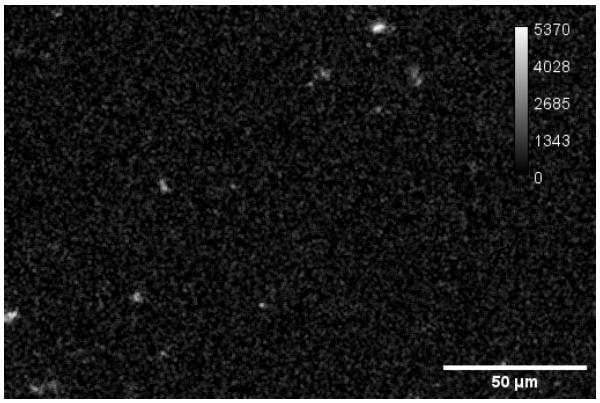

(b) Carbon content in the J1 structure in sample 17. The colour scale indicates the elemental percentage of C atoms. The value is given as 100×percentage. Meaning a value of 10000 is the pure element.

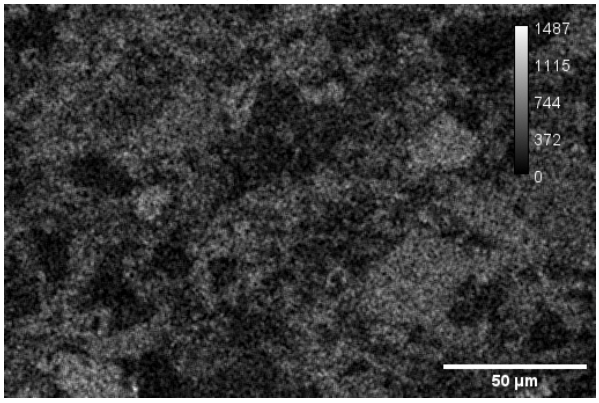

(c) Calcium content in the J1 structure in sample 17. The colour scale indicates the elemental percentage of Ca atoms. The value is given as 100×percentage. Meaning a value of 10000 is the pure element.

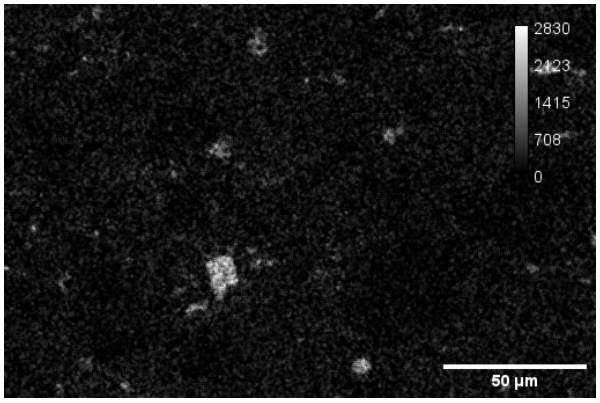

(d) Iron content in the J1 structure in sample 17. The colour scale indicates the elemental percentage of Fe atoms. The value is given as 100×percentage. Meaning a value of 10000 is the pure element.

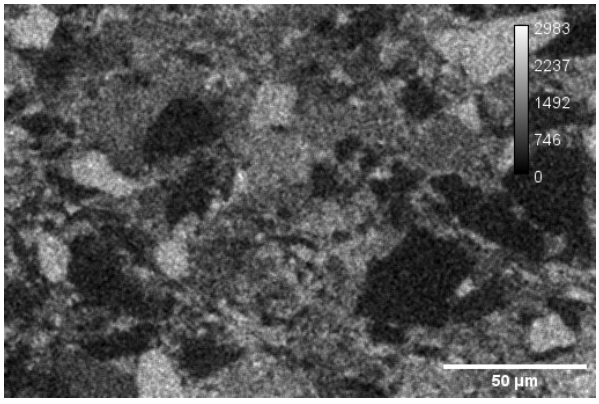

(e) Magnesium content in the J1 structure in sample 17. The colour scale indicates the elemental percentage of Mg atoms. The value is given as 100×percentage. Meaning a value of 10000 is the pure element.

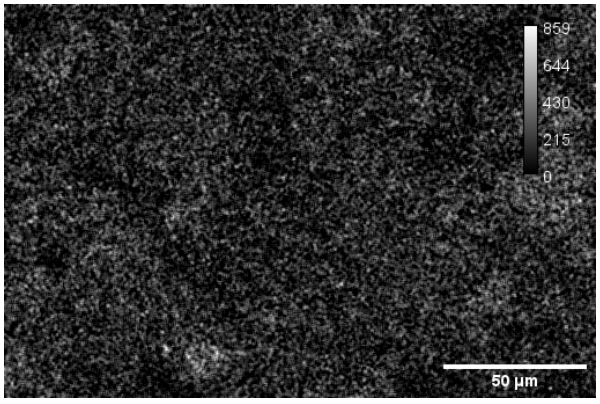

(f) Sodium content in the J1 structure in sample 17. The colour scale indicates the elemental percentage of Na atoms. The value is given as 100×percentage. Meaning a value of 10000 is the pure element.

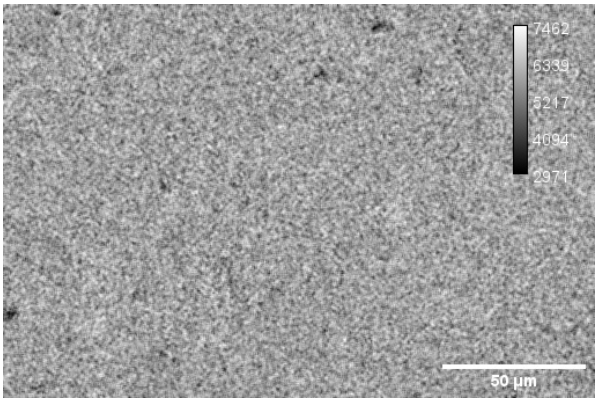

(g) Oxygen content in the J1 structure in sample 17. The colour scale indicates the elemental percentage of O atoms. The value is given as 100×percentage. Meaning a value of 10000 is the pure element.

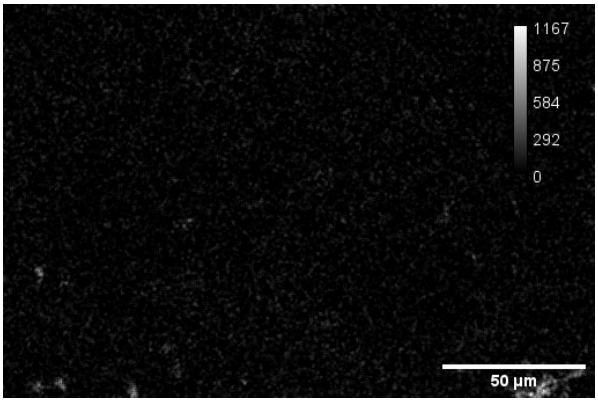

(h) Sulphur content in the J1 structure in sample 17. The colour scale indicates the elemental percentage of S atoms. The value is given as 100×percentage. Meaning a value of 10000 is the pure element.

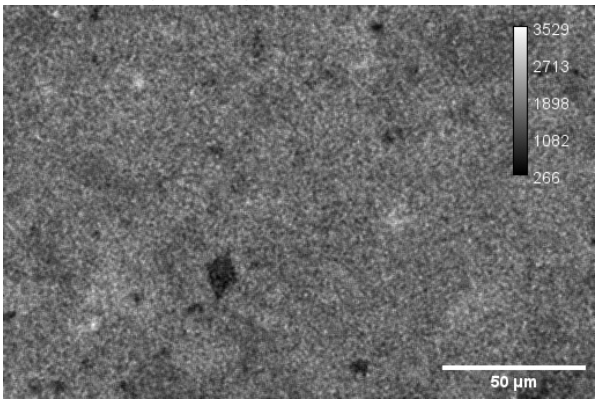

(i) Silica content in the J1 structure in sample 17. The colour scale indicates the elemental percentage of Si atoms. The value is given as 100×percentage. Meaning a value of 10000 is the pure element.

Figure E.8: EDS of sample 17 with a transition from full transition from J0 into J1, from left to right.

F

Supplementary Data of Energy Analysis

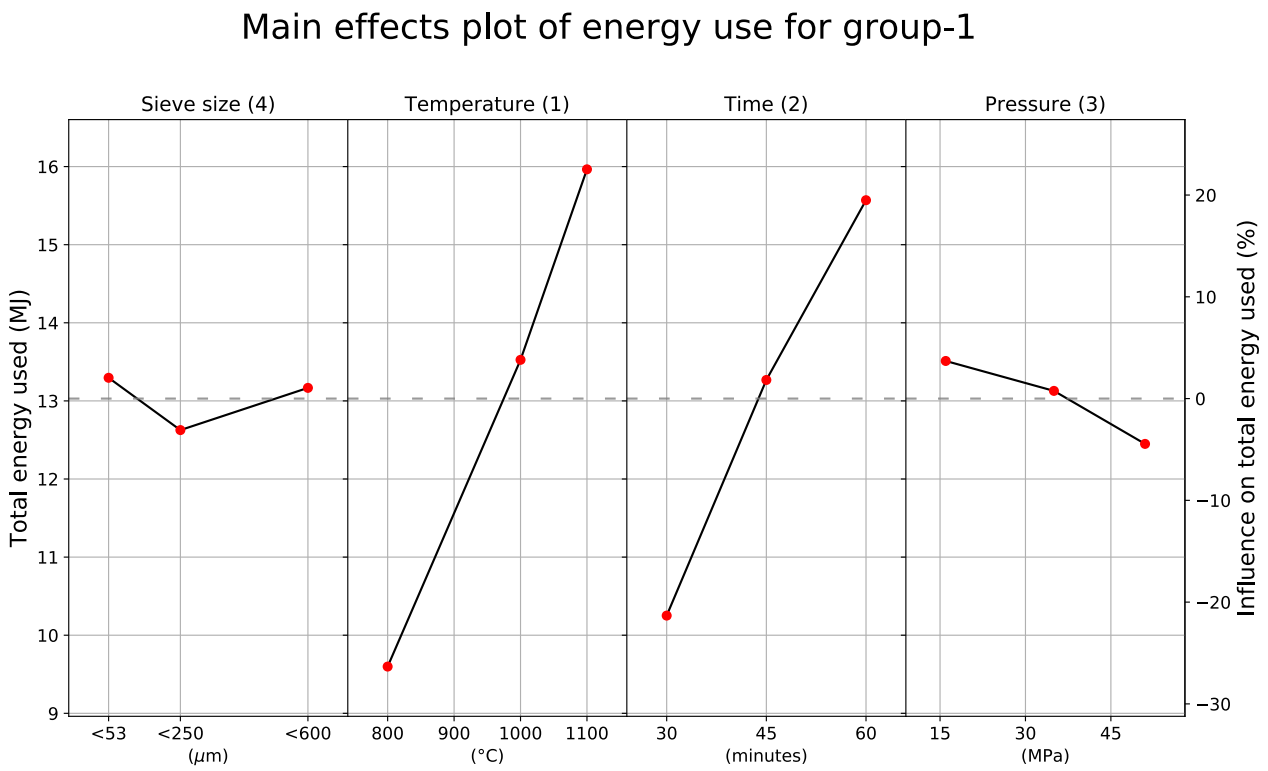

Figure F.1: Energy consumption respective to each variable and variable level. The dotted grey line indicates the mean energy use. Measurement values are in MJ. The mean energy consumption was 13.03 MJ. The numbers in brackets after the variable name indicate the rank of influence, from most influential (1), to least influential (4).
The values are Taguchi deconvoluted values from the real measured values. Each dot does not indicate an individual measurement, but the average of three measurements. The values represent the values to be obtained, if only that variable was changed compared to the mean. The straight connected lines indicate linear interpolation. In reality, the true relation can differ. A lower total energy consumption can be obtained by taking the best-performing level of each variable. This is also visible in Table F.1

Table F.1: Energy consumption values of the analysed Taguchi design, as plotted in F.1. Values are in MJ, except for rank, which has no unit. The delta row indicates the difference between the maximum and minimum value for each column. This value is used to determine the rank. The rank indicates the variable with the most influence on the results, e.g. the largest delta. The level column indicates the set level of each variable from 1 to 3. For sieve size this is <53 µm, <250 µm and <600 µm respectively. For temperature this is 800 °C, 1000 °C and 1100 °C respectively. For time this is 30 minutes, 45 minutes and 60 minutes respectively. For pressure this is 16 MPa, 35 MPa and 51 MPa respectively.

Level	Sieve size	Temperature	Time	Pressure
1	13.296	9.598	10.251	13.511
2	12.626	13.526	13.268	13.128
3	13.167	15.965	15.570	12.449
Delta	0.670	6.366	5.319	1.062
Rank	4	1	2	3

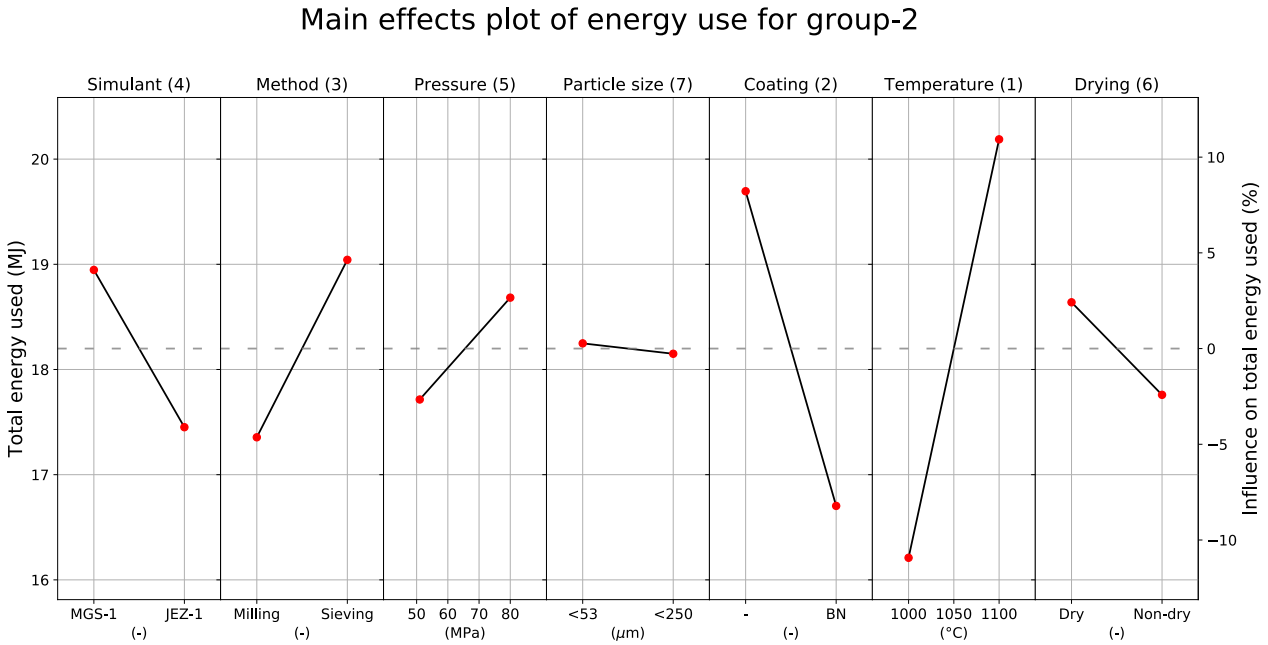

Figure F.2: Energy consumption respective to each variable and variable level. The dotted grey line indicates the mean energy use. Measurement values are in MJ. The mean energy consumption was 18.20 MJ. The numbers in brackets after the variable name indicate the rank of influence, from most influential (1), to least influential (7).
The values are Taguchi deconvoluted values from the real measured values. Each dot does not indicate an individual measurement, but the average of four measurements. The values represent the values to be obtained, if only that variable was changed compared to the mean. The straight connected lines indicate linear interpolation. In reality, the true relation can differ. A lower total energy consumption can be obtained by taking the best-performing level of each variable. This is also visible in Table F.2

Table F.2: Energy consumption values of the analysed Taguchi design, as plotted in F.2. Values are in MJ, except for rank, which has no unit. The delta row indicates the difference between the maximum and minimum value for each column. This value is used to determine the rank. The rank indicates the variable with the most influence on the results, e.g. the largest delta. The level column indicates the set level of each variable from 1 to 2. For simulant this is MGS-1 and JEZ-1 respectively. For method this is ball milling and sieving respectively. For pressure this is 51 MPa and 80 MPa respectively. For particle size this is <53 µm and <250 µm respectively. For coating this is no coating and a BN coating respectively. For temperature this is 1000 °C and 1100 °C respectively. For drying this is dry and non-dry respectively.

Level	Simulant	Method	Pressure	Particle size	Coating	Temperature	Drying
1	18.947	17.355	17.715	18.248	19.695	16.210	18.639
2	17.451	19.042	18.683	18.149	16.703	20.188	17.759
Delta	1.495	1.687	0.968	0.099	2.992	3.978	0.880
Rank	4	3	5	7	2	1	6

Table F.3: Energy consumption per mass values of the analysed Taguchi design, as plotted in F.3. Values are in MJ/kg, except for rank, which has no unit. The delta row indicates the difference between the maximum and minimum value for each column. This value is used to determine the rank. The rank indicates the variable with the most influence on the results, e.g. the largest delta. The level column indicates the set level of each variable from 1 to 3. For sieve size this is <53 µm, <250 µm and <600 µm respectively. For temperature this is 800 °C, 1000 °C and 1100 °C respectively. For time this is 30 minutes, 45 minutes and 60 minutes respectively. For pressure this is 16 MPa, 35 MPa and 51 MPa respectively.

Level	Sieve size	Temperature	Time	Pressure
1	1051.78	644.17	683.58	944.70
2	803.53	945.92	934.74	873.34
3	837.65	1102.88	1074.65	874.93
Delta	248.25	458.72	391.07	71.36
Rank	3	1	2	4

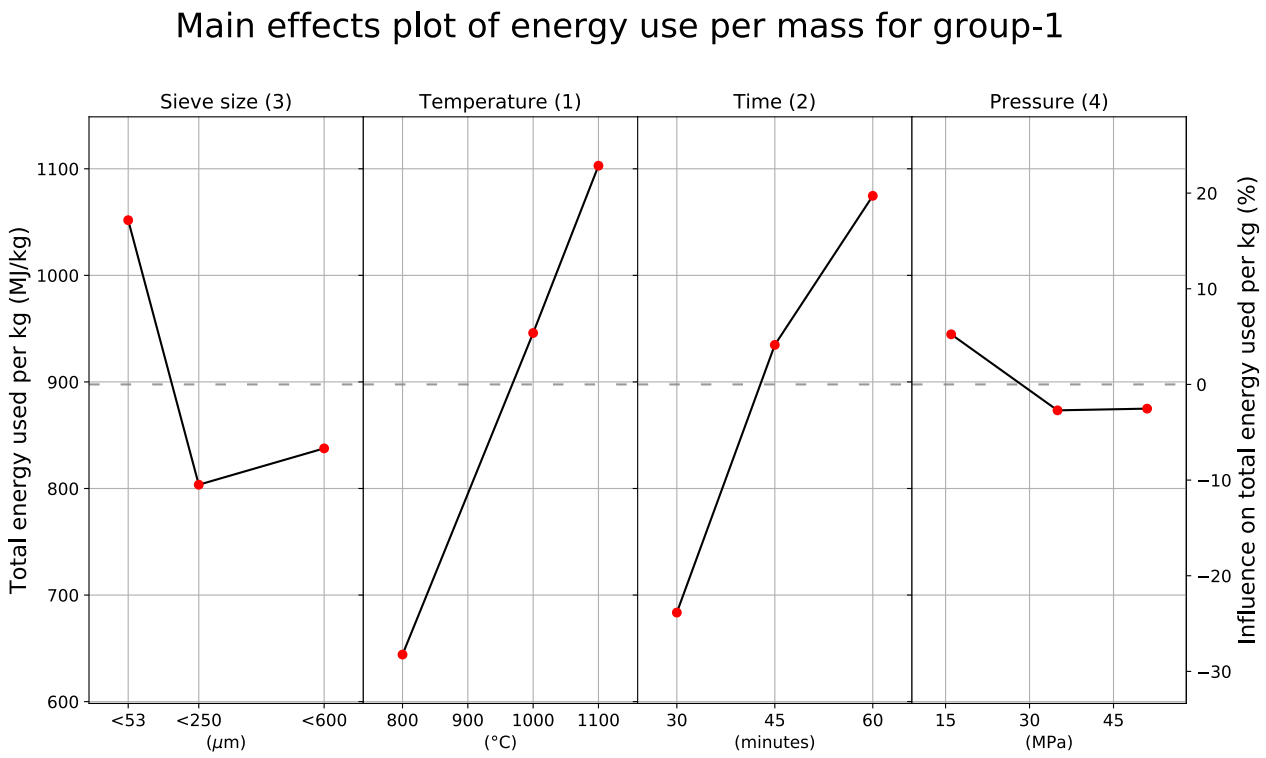

Figure F.3: Energy consumption per mass respective to each variable and variable level. The dotted grey line indicates the mean energy use per mass. Measurement values are in MJ/kg. The mean energy consumption per mass was 897.66 MJ/kg. The numbers in brackets after the variable name indicate the rank of influence, from most influential (1), to least influential (4).
The values are Taguchi deconvoluted values from the real measured values. Each dot does not indicate an individual measurement, but the average of three measurements. The values represent the values to be obtained, if only that variable was changed compared to the mean. The straight connected lines indicate linear interpolation. In reality, the true relation can differ. A lower total energy consumption can be obtained by taking the best-performing level of each variable. This is also visible in Table F.3

Table F.4: Energy consumption per mass values of the analysed Taguchi design, as plotted in F.4. Values are in MJ/kg, except for rank, which has no unit. The delta row indicates the difference between the maximum and minimum value for each column. This value is used to determine the rank. The rank indicates the variable with the most influence on the results, e.g. the largest delta. The level column indicates the set level of each variable from 1 to 2. For simulant this is MGS-1 and JEZ-1 respectively. For method this is ball milling and sieving respectively. For pressure this is 51 MPa and 80 MPa respectively. For particle size this is <53 µm and <250 µm respectively. For coating this is no coating and a BN coating respectively. For temperature this is 1000 °C and 1100 °C respectively. For drying this is dry and non-dry respectively.

Level	Simulant	Method	Pressure	Particle size	Coating	Temperature	Drying
1	1295	1194	1271	1352	1425	1192	1349
2	1297	1398	1321	1240	1167	1400	1243
Delta	2	203	49	111	258	207	107
Rank	7	3	6	4	1	2	5

Table F.5: Energy consumption per volume values of the analysed Taguchi design, as plotted in F.5. Values are in GJ/m^3, except for rank, which has no unit. The delta row indicates the difference between the maximum and minimum value for each column. This value is used to determine the rank. The rank indicates the variable with the most influence on the results, e.g. the largest delta. The level column indicates the set level of each variable from 1 to 3. For sieve size this is <53 µm, <250 µm and <600 µm respectively. For temperature this is 800 °C, 1000 °C and 1100 °C respectively. For time this is 30 minutes, 45 minutes and 60 minutes respectively. For pressure this is 16 MPa, 35 MPa and 51 MPa respectively.

Level	Sieve size	Temperature	Time	Pressure
1	1973	1227	1402	1757
2	1659	1935	1865	1826
3	1786	2257	2152	1835
Delta	313	1030	750	78
Rank	3	1	2	4

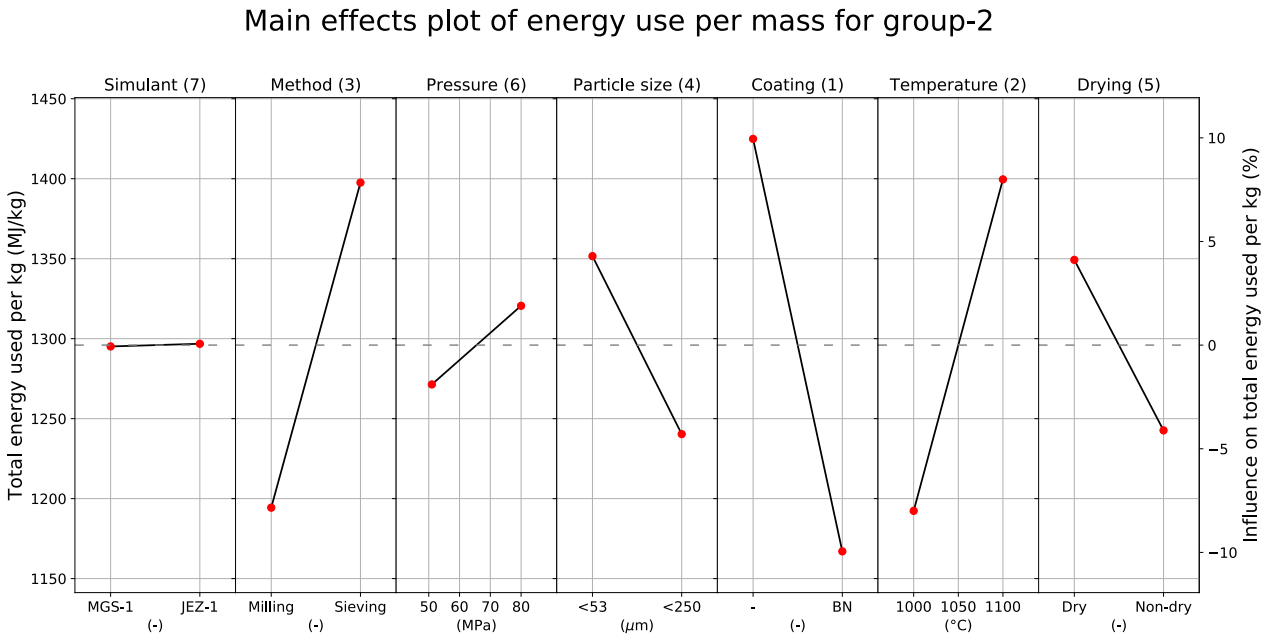

Figure F.4: Energy consumption per mass respective to each variable and variable level. The dotted grey line indicates the mean energy use per mass. Measurement values are in MJ/kg. The mean energy consumption per mass was 18.20 MJ/kg. The numbers in brackets after the variable name indicate the rank of influence, from most influential (1), to least influential (7).
The values are Taguchi deconvoluted values from the real measured values. Each dot does not indicate an individual measurement, but the average of four measurements. The values represent the values to be obtained, if only that variable was changed compared to the mean. The straight connected lines indicate linear interpolation. In reality, the true relation can differ. A lower total energy consumption can be obtained by taking the best-performing level of each variable. This is also visible in Table F.4

Table F.6: Energy consumption per volume values of the analysed Taguchi design, as plotted in F.6. Values are in GJ/m^3, except for rank, which has no unit. The delta row indicates the difference between the maximum and minimum value for each column. This value is used to determine the rank. The rank indicates the variable with the most influence on the results, e.g. the largest delta. The level column indicates the set level of each variable from 1 to 2. For simulant this is MGS-1 and JEZ-1 respectively. For method this is ball milling and sieving respectively. For pressure this is 51 MPa and 80 MPa respectively. For particle size this is <53 µm and <250 µm respectively. For coating this is no coating and a BN coating respectively. For temperature this is 1000 °C and 1100 °C respectively. For drying this is dry and non-dry respectively.

Level	Simulant	Method	Pressure	Particle size	Coating	Temperature	Drying
1	3011	2849	2881	3110	3334	2656	3245
2	3132	3294	3262	3033	2809	3487	2898
Delta	121	445	380	77	524	831	347
Rank	6	3	4	7	2	1	5

Table F.7: Strength obtained per power consumed values of the analysed Taguchi design, as plotted in F.7. Values are in MPa/MJ, except for rank, which has no unit. The delta row indicates the difference between the maximum and minimum value for each column. This value is used to determine the rank. The rank indicates the variable with the most influence on the results, e.g. the largest delta. The level column indicates the set level of each variable from 1 to 3. For sieve size this is <53 µm, <250 µm and <600 µm respectively. For temperature this is 800 °C, 1000 °C and 1100 °C respectively. For time this is 30 minutes, 45 minutes and 60 minutes respectively. For pressure this is 16 MPa, 35 MPa and 51 MPa respectively.

Level	Sieve size	Temperature	Time	Pressure
1	0.8271	0.3835	0.7230	0.2223
2	0.2961	0.5686	0.4468	0.5932
3	0.5648	0.7360	0.5183	0.8726
Delta	0.5309	0.3525	0.2763	0.6503
Rank	2	3	4	1

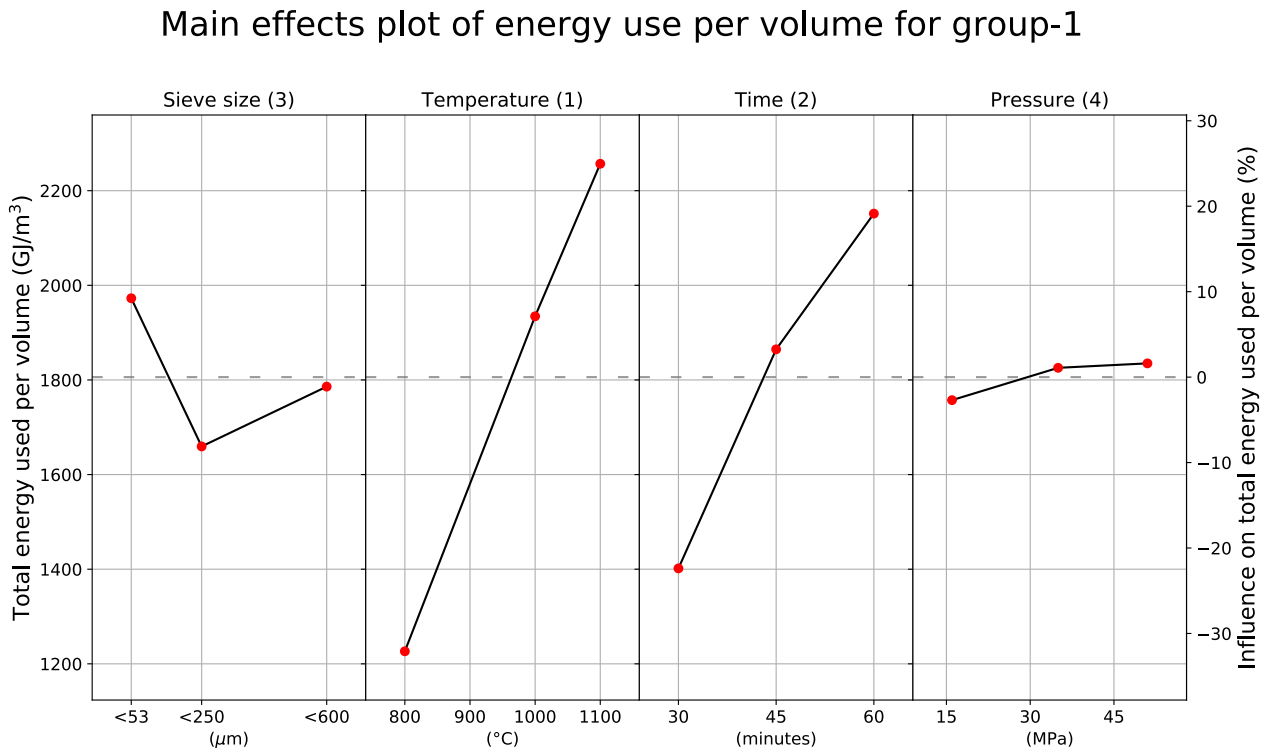

Figure F.5: Energy consumption per volume respective to each variable and variable level. The dotted grey line indicates the mean energy use per volume. Measurement values are in GJ/m^3. The mean energy consumption per volume was 1806 GJ/m^3. The numbers in brackets after the variable name indicate the rank of influence, from most influential (1), to least influential (4).
The values are Taguchi deconvoluted values from the real measured values. Each dot does not indicate an individual measurement, but the average of three measurements. The values represent the values to be obtained, if only that variable was changed compared to the mean. The straight connected lines indicate linear interpolation. In reality, the true relation can differ. A lower total energy consumption can be obtained by taking the best-performing level of each variable. This is also visible in Table F.5

Table F.8: Strength obtained per power consumed values of the analysed Taguchi design, as plotted in F.8. Values are in MPa/MJ, except for rank, which has no unit. The delta row indicates the difference between the maximum and minimum value for each column. This value is used to determine the rank. The rank indicates the variable with the most influence on the results, e.g. the largest delta. The level column indicates the set level of each variable from 1 to 2. For simulant this is MGS-1 and JEZ-1 respectively. For method this is ball milling and sieving respectively. For pressure this is 51 MPa and 80 MPa respectively. For particle size this is <53 µm and <250 µm respectively. For coating this is no coating and a BN coating respectively. For temperature this is 1000 °C and 1100 °C respectively. For drying this is dry and non-dry respectively.

Level	Simulant	Method	Pressure	Particle size	Coating	Temperature	Drying
1	2.825	4.609	3.553	5.124	3.524	3.374	4.421
2	5.684	3.900	4.956	3.385	4.985	5.135	4.088
Delta	2.858	0.709	1.403	1.739	1.462	1.761	0.332
Rank	1	6	5	3	4	2	7

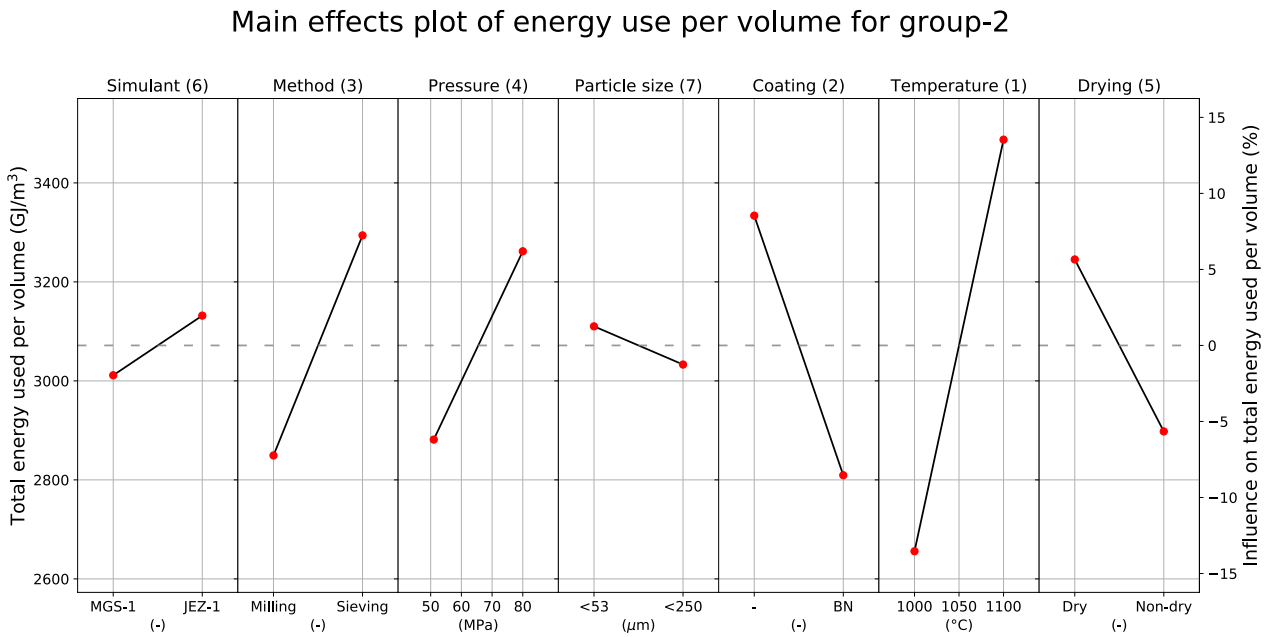

Figure F.6: Energy consumption per volume respective to each variable and variable level. The dotted grey line indicates the mean energy use per volume. Measurement values are in GJ/m^3. The mean energy consumption per volume was 3071 GJ/m^3. The numbers in brackets after the variable name indicate the rank of influence, from most influential (1), to least influential (7).
The values are Taguchi deconvoluted values from the real measured values. Each dot does not indicate an individual measurement, but the average of four measurements. The values represent the values to be obtained, if only that variable was changed compared to the mean. The straight connected lines indicate linear interpolation. In reality, the true relation can differ. A lower total energy consumption can be obtained by taking the best-performing level of each variable. This is also visible in Table F.6

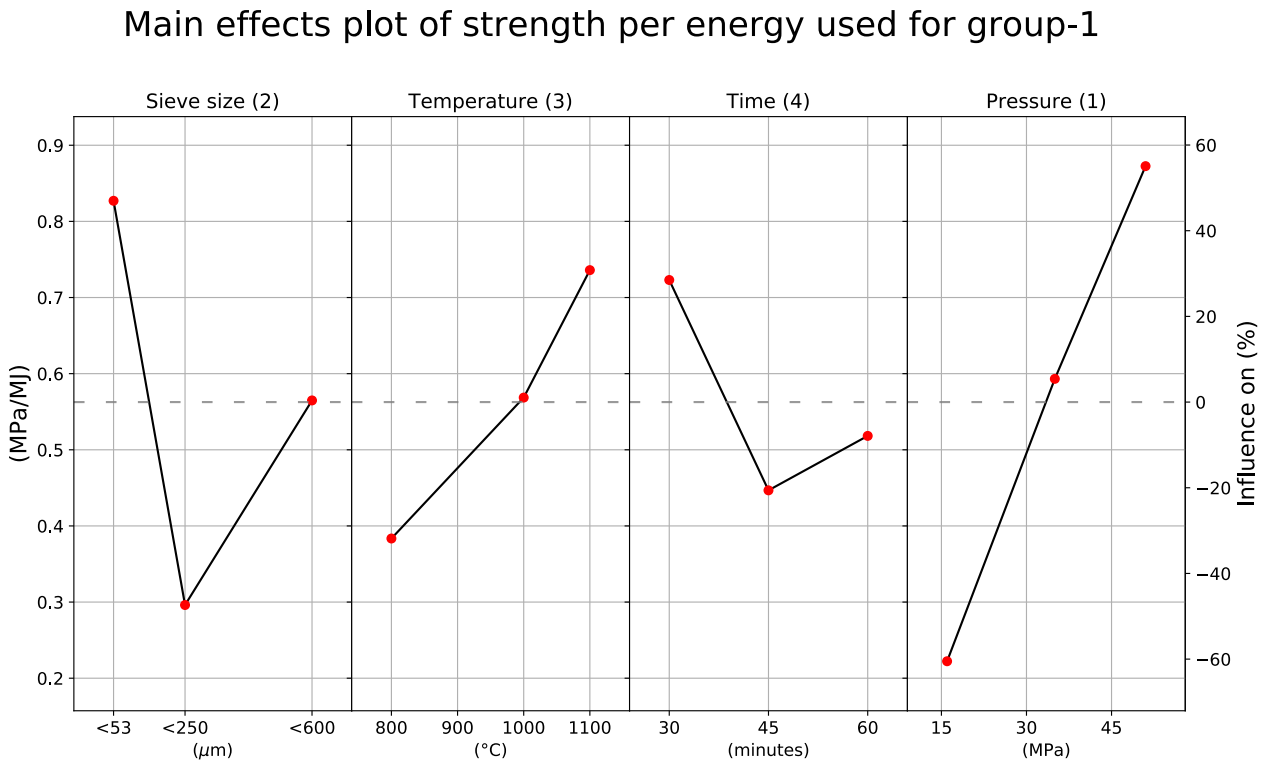

Figure F.7: Strength obtained per power consumed respective to each variable and variable level. The dotted grey line indicates the mean strength obtained per power consumed. Measurement values are in MPa/MJ. The mean strength obtained per power consumed was 0.5627 MPa/MJ. The numbers in brackets after the variable name indicate the rank of influence, from most influential (1), to least influential (4).
The values are Taguchi deconvoluted values from the real measured values. Each dot does not indicate an individual measurement, but the average of three measurements. The values represent the values to be obtained, if only that variable was changed compared to the mean. The straight connected lines indicate linear interpolation. In reality, the true relation can differ. A lower total energy consumption can be obtained by taking the best-performing level of each variable. This is also visible in Table F.7

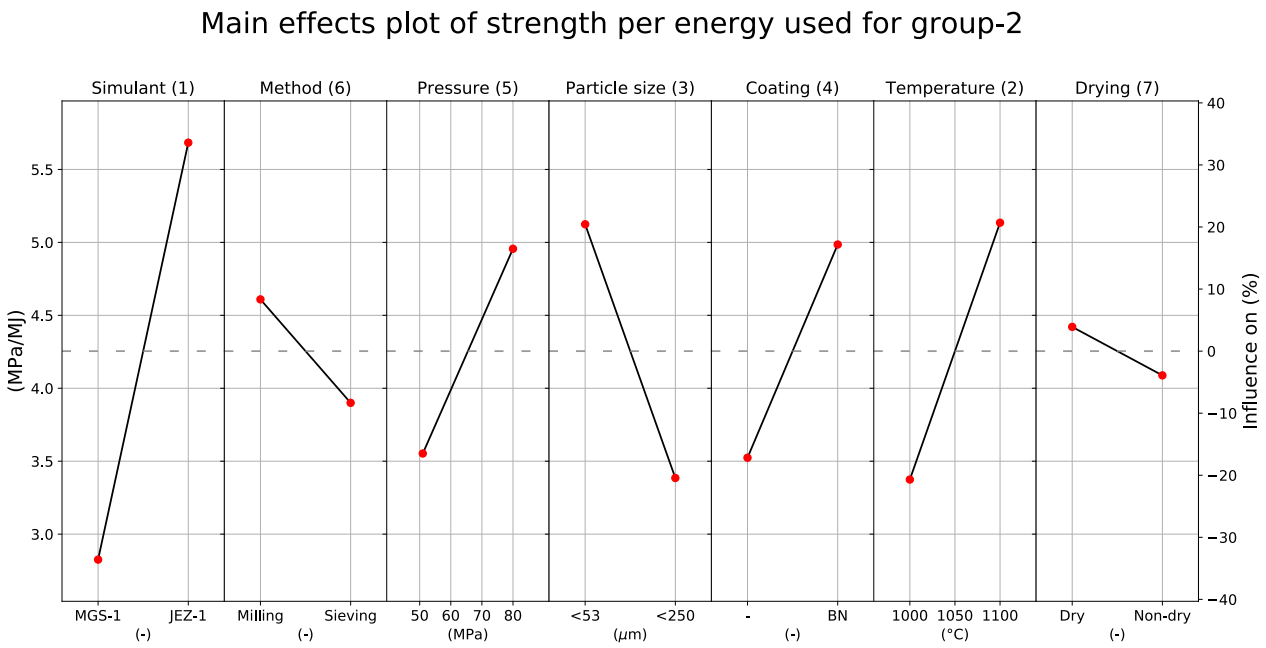

Figure F.8: Strength obtained per power consumed respective to each variable and variable level. The dotted grey line indicates the mean strength obtained per power consumed. Measurement values are in MPa/MJ. The mean strength obtained per power consumed was 4.2545 MPa/MJ. The numbers in brackets after the variable name indicate the rank of influence, from most influential (1), to least influential (7).
The values are Taguchi deconvoluted values from the real measured values. Each dot does not indicate an individual measurement, but the average of four measurements. The values represent the values to be obtained, if only that variable was changed compared to the mean. The straight connected lines indicate linear interpolation. In reality, the true relation can differ. A lower total energy consumption can be obtained by taking the best-performing level of each variable. This is also visible in Table F.8

G

Source Code for Python DSC Analysis

```
# -*- coding: utf-8 -*-
"""
Created on Fri Jan 21 18:05:08 2022

@author: Theo
"""
from IPython.display import display
import pandas as pd
import matplotlib.pyplot as plt
import numpy as np
#import scipy.signal as scp
import matplotlib.ticker as plticker
from scipy.signal import savgol_filter

TitleSize = 18
Y_axisSize = 12
X_axisSize = 10
#padding = 0.1 #%


Blanks = False
Four = False
Argon = True
Air = True
MGS = True
JEZ = True

DTG = True
DDTG = False

DDSC = True
DDDSC = False

TGA = True
DSC = True

Save = True

xmin = 0
xmax = 1450

padding = 0.05

DSCc = 'solid'
TGAc = 'dashed'

GridX = 50
GridY = 0.2
TGAY = 0.5

Ycompr = 3


MGSArMass = 30.1 #mg
JEZArMass = 26.8 #mg
MGSAirMass = 29.2 #mg
JEZAirMass = 27.8 #mg
```

```
#MGSAr1 = pd.read_csv("ExpDat_MGS-1 single;20-01-2022-2.csv", delimiter = ',',header=26, usecols =
    ↪ ['Temp','Time","DSC","Mass"])
#MGSAr2 = pd.read_csv("ExpDat_MGS-1 wder single;20-01-2022-3.csv", delimiter = ',',header=26,
    ↪ usecols = ['Temp","Time","DSC","Mass","DDSC","DDDSC"])


def scaler(ax, data, name):
    range1 = [0]*len(data)
    mins = np.zeros(len(data))
    maxs = np.zeros(len(data))
    for i,j in enumerate(data):
        range1[i] = j.loc[j.loc[:,"Temp"].between(xmin,xmax,inclusive='both')]
        mins[i] = range1[i].loc[:,name].min()
        maxs[i] = range1[i].loc[:,name].max()
    min1 = np.min(mins)
    max1 = np.max(maxs)
    spread1 = max1-min1
    padding1 = spread1*padding
    ax.set_ylim((min1-padding1,max1+padding1))
    loc1 = plticker.MultipleLocator(base=GridX) # this locator puts ticks at regular intervals
    ax.xaxis.set_major_locator(loc1)
    if name == "DSC":
        loc2 = plticker.MultipleLocator(base=GridY) # this locator puts ticks at regular intervals
        ax.yaxis.set_major_locator(loc2)
    if name == "TGA":
        loc2 = plticker.MultipleLocator(base=TGAY) # this locator puts ticks at regular intervals
        ax.yaxis.set_major_locator(loc2)

    ax.set_xlim((xmin,xmax))
    return

def plotter(data):
    n = 1
    if rows > 1:
        fig1, axS = plt.subplots(nrows = rows, ncols = 1, sharex = False, figsize=(16,height),
            ↪ gridspec_kw = {'height_ratios':ratios})
        ax1 = axS[0]
    else:
        fig1, ax1 = plt.subplots(figsize=(16,9))

    ax11 = ax1.twinx()
    scldata = []
    names = []
    atms = []
    for i in data:
        scldata.append(i.get("data"))
        names.append(i.get("name")[:5])
        atms.append(i.get("atm"))

    ax1.grid(True, which='both')
    ax1.set_xlabel('Temperature (°C)', fontsize = X_axisSize)

    if DSC:
        for i in data:
            ax1.plot(i.get("data")['Temp'],i.get("data")['DSC'], label = i.get("name") + ", DSC",
                ↪ color = i.get("color"), linestyle = DSCc)


        scaler(ax1, scldata, "DSC")

        ax1.set_ylabel('Heatflow (mW/mg)', fontsize = Y_axisSize)


    if TGA:
        for i in data:
            ax11.plot(i.get("data")['Temp'],i.get("data")['Mass'], label = i.get("name")+", TGA",
                ↪ color = i.get("color"), linestyle = TGAc)
        ax11.set_ylabel('Mass (%)', fontsize = Y_axisSize)
        scaler(ax11, scldata, "Mass")
```

```
if DTG:
    for i in data:
        axS[n].plot(i.get("data")['Temp'],i.get("data")['DTG'], color = i.get("color"),
            ↪ linestyle = TGAc)#label = i.get("name")+", DTG",

    axS[n].grid(True, which='both')
    axS[n].set_xlabel('Temperature (°C)', fontsize = X_axisSize)
    axS[n].set_ylabel('dMass (%/°C)', fontsize = Y_axisSize)
    scaler(axS[n], scldata, "DTG")
    axS[n].set_title("DTG curve")
    n+=1

if DDTG:
    for i in data:
        axS[n].plot(i.get("data")['Temp'],i.get("data")['DDTG'], color = i.get("color"),
            ↪ linestyle = TGAc)#, label = i.get("name")+", DDTG"

    axS[n].grid(True, which='both')
    axS[n].set_xlabel('Temperature (°C)', fontsize = X_axisSize)
    axS[n].set_ylabel('dMass (%/°C/°C)', fontsize = Y_axisSize)
    scaler(axS[n], scldata, "DDTG")
    axS[n].set_title("DDTG curve")
    n+=1

if DDSC:
    for i in data:
        axS[n].plot(i.get("data")['Temp'],i.get("data")['DDSC'], color = i.get("color"),
            ↪ linestyle = DSCc)#, label = i.get("name")+", DDSC"

    axS[n].grid(True, which='both')
    axS[n].set_xlabel('Temperature (°C)', fontsize = X_axisSize)
    axS[n].set_ylabel('dHeat flow (mW/mg/°C)', fontsize = Y_axisSize)
    scaler(axS[n], scldata, "DDSC")
    axS[n].set_title("DDSC curve")
    n+=1

if DDDSC:
    for i in data:
        axS[n].plot(i.get("data")['Temp'],i.get("data")['DDDSC'], color = i.get("color"),
            ↪ linestyle = DSCc)#, label = i.get("name")+", DDDSC"

    axS[n].grid(True, which='both')
    axS[n].set_xlabel('Temperature (°C)', fontsize = X_axisSize)
    axS[n].set_ylabel('dHeat flow (mW/mg/°C/°C)', fontsize = Y_axisSize)
    scaler(axS[n], scldata, "DDDSC")
    axS[n].set_title("DDDSC curve")
    n+=1


fig1.legend(loc= "upper right", bbox_to_anchor=(1,1), bbox_transform=ax1.transAxes)
fig1.subplots_adjust(hspace=0.3)

names = list(dict.fromkeys(names))
if len(names) == 1:
    naming = names[0]
if len(names) == 2:
    naming = names[0] + " and " + names[1]
atms = list(dict.fromkeys(atms))
if len(atms) == 1:
    atming = atms[0]
if len(atms) == 2:
    atming = "both " + atms[0] + " and " + atms[1]


ax1.set_title("DSC-TGA curve of "+ naming + " in " + atming + " environment", fontsize =
    ↪ TitleSize)

if Save:
    name = 'Plot_' + "DSC-TGA curve of "+ naming + " in " + atming + " environment" + '.svg'
    fig1.savefig(name, format = 'svg', dpi = 1200)
```

```
def specificHeat(data):
    print("For sample "+data.get('name')+" in an " + data.get("atm") + " atmosphere...")
    inputMass = data.get('mass')
    #heatRate = [20,10]
    #print(data["heatRate"])
    data = data.get("data")
    data["heatRate"] = (1/20)
    data["heatRate"].loc[data["Temp"]>400].iloc[0] = (1/10)
    setTemp = [800,1000,1100]
    data["TimeSteps"] = (data["Time"].diff()*60)
    data["Energypermass"] = (data['DSC']*data["TimeSteps"])#mJ/mg

    #data["TempSteps"] = (data["Temp"].diff()*data["heatRate"]*60)
    #data["Energypermass"] = (data['DSC']*data["TempSteps"])#mJ/mg




    data["TotalMass"] = (data["Mass"]/100)*inputMass
    data["EnergyInt"] = (data["Energypermass"]*data["TotalMass"]).cumsum()/1000 #J


    for i in setTemp:
        print("At "+str(i)+" °C :")
        print("The Cp for input mass was:")
        energyReqInit = (data["EnergyInt"].loc[data["Temp"]>i].iloc[0])/inputMass #J/mg
        print(energyReqInit)
        print("\nThe Cp for output mass was: ")
        energyReqAft = (data["EnergyInt"].loc[data["Temp"]>i].iloc[0])/(data["TotalMass"].loc[data[
            ↪ "Temp"]>i].iloc[0]) #J/mg
        print(energyReqAft)


#, delimiter = ','
#names = ['element', 'node', 'layer', 'X', 'Y', 'Z', 'Myy']
#display(MGSAr1)

#MGSAr = pd.concat([MGSAr1,MGSAr2])
"""
Imporing data
"""
CALAr = pd.read_csv("ExpDat_Blank with cover time; 20-1-2022.csv", delimiter = ',',header=26,
    ↪ usecols = ['Temp',"Time","DSC","Mass","DDSC","DDDSC","Segment"])
CALAir = pd.read_csv("ExpDat_Blank air;31-01-2022.csv", delimiter = ',',header=26, usecols = ['Temp
    ↪ ',"Time","DSC","Mass","DDSC","DDDSC","Segment"])
#display(CALAr)

MGSAr = pd.read_csv("ExpDat_MGS-1 all time;20-01-2022.csv", delimiter = ',',header=26, usecols = ['
    ↪ Temp',"Time","DSC","Mass","DDSC","DDDSC","Segment"])
MGSAir = pd.read_csv("ExpDat_MGS-1 Air;31-01-2022.csv", delimiter = ',',header=26, usecols = ['Temp
    ↪ ',"Time","DSC","Mass","DDSC","DDDSC","Segment"])
#display(MGSAr)


JEZAr = pd.read_csv("ExpDat_JEZ-1 single;21-01-2022.csv", delimiter = ',',header=26, usecols = ['
    ↪ Temp',"Time","DSC","Mass","DDSC","DDDSC","Segment"])
JEZAir = pd.read_csv("ExpDat_JEZ-1 Air;31-01-2022.csv", delimiter = ',',header=26, usecols = ['Temp
    ↪ ',"Time","DSC","Mass","DDSC","DDDSC","Segment"])

datass = [MGSAr,MGSAir,JEZAr,JEZAir]
#MGSAr["DTG"] = np.gradient(MGSAr["Temp"],MGSAr["Mass"])
#print(MGSAr['DTG'])
#display(JEZAr)
#display(JEZAr.loc[JEZAr.loc[36.2 <= JEZAr["Temp"],"Temp"] <= 36.23,"DDSC"])
#display(JEZAr.loc[JEZAr["Temp"].between(xmin,xmax,inclusive='both'),"DDSC"].max())

"""
Making plots
"""
dd = [DTG,DDTG,DDSC,DDDSC]
ddn = ["DTG","DDTG","DDSC","DDDSC"]
```

```
rows = 1
ratios = [3]
height = 9
for i,j in enumerate(dd):
    rows += j
    height += j*(9/Ycompr)
    if j:
        ratios.append(3/Ycompr)

        if i < 2:
            indx = 'Mass'
            dercorr = 1
        if i > 1:
            indx = 'DSC'
            dercorr = -1
        for d in datass:
            d[ddn[i]] = savgol_filter(d[indx],289,3,deriv=i+dercorr)



MGSArt = {"data":MGSAr,'name':"MGS-1 Ar",'atm':"Argon",'color':'black','mass':MGSArMass}
JEZArt = {"data":JEZAr,'name':"JEZ-1 Ar",'atm':"Argon",'color':'red','mass':JEZArMass}
MGSAirt = {"data":MGSAir,'name':"MGS-1 Air",'atm':"Air",'color':'dimgrey','mass':MGSAirMass}
JEZAirt = {"data":JEZAir,'name':"JEZ-1 Air",'atm':"Air",'color':'firebrick','mass':JEZAirMass}
#test plot for parameters



if Blanks:
    fig0, ax0 = plt.subplots(figsize=(16,9))
    ax01 = ax0.twinx()
    if DSC:
        ax0.plot(CALAr['Temp'],CALAr['DSC'], label = "Blank Argon, DSC", color = "darkgrey")
        ax0.plot(CALAir['Temp'],CALAir['DSC'], label = "Blank Air, DSC", color = "darkgrey",
            ↪ linestyle='dashed')
        ax0.grid(True, which='both')
        ax0.set_ylabel('Heat flow (mW/mg)')
        ax0.set_xlabel('Temperature (C)')
        scaler(ax0, [CALAr,CALAir], "DSC")



    if TGA:
        ax01.plot(CALAr['Temp'],CALAr['Mass'], label = "Blank Argon, TGA", color = "red")
        ax01.plot(CALAir['Temp'],CALAir['Mass'], label = "Blank Air, TGA", color = "red", linestyle
            ↪ ='dashed')
        ax01.set_ylabel('Mass (%)')
        scaler(ax01, [CALAr,CALAir], "Mass")

    fig0.legend(loc= "upper right", bbox_to_anchor=(1,1), bbox_transform=ax0.transAxes)
    ax0.set_title("Blank DSC-TGA curve in argon environment")

#Real plots

if Argon:
    plotter([MGSArt,JEZArt])


if Air:
    plotter([MGSAirt,JEZAirt])


if MGS:
    plotter([MGSArt,MGSAirt])


if JEZ:
    plotter([JEZArt,JEZAirt])
```

```
if Four:
    plotter([MGSArt,MGSAirt,JEZArt,JEZAirt])

if False:
    fig2, ax2 = plt.subplots(figsize=(16,9))

    #ax21 = ax2.twinx()
    ax2.plot(MGSAr['Temp'],MGSAr['DDSC'], label = "MGS-1 Argon, DDSC", color = MGSc[1], linestyle =
        ↪ DSCc)
    ax2.plot(MGSAir['Temp'],MGSAir['DDSC'], label = "MGS-1 Air, DDSC", color = MGSc[2], linestyle =
        ↪ DSCc)
    ax2.plot(JEZAr['Temp'],JEZAr['DDSC'], label = "JEZ-1 Argon, DDSC", color = JEZc[1], linestyle =
        ↪ DSCc)
    ax2.plot(JEZAir['Temp'],JEZAir['DDSC'], label = "JEZ-1 Air, DDSC", color = JEZc[2], linestyle =
        ↪ DSCc)
    #ax2.plot(CALAr['Temp'],CALAr['DDSC'], label = "Blank Argon, DDSC", color = "darkgrey")
    #ax2.plot(CALAir['Temp'],CALAir['DDSC'], label = "Blank Air, DDSC", color = "darkgrey",
        ↪ linestyle='dashed')

    ax2.set_ylabel('Differential of heat flow (mW/mg/C)')
    ax2.set_xlabel('Temperature (C)')

    ax2.set_title("DDSC curve in argon environment")

    scaler(ax2, [JEZAr, JEZAir, MGSAr, MGSAir], "DDSC")


#print(scp.find_peaks(MGSAr['DSC']))

if False:
    figs = [fig6] #,fig2,fig3,fig4[fig1,fig3,fig4,fig5,fig6]
    for i in range(len(figs)):
        name = 'plot' + str(i) + '.png'
        figs[i].savefig(name, format = 'png', dpi = 1200)


plt.show()
for i in [MGSArt,MGSAirt,JEZArt,JEZAirt]:
    specificHeat(i)
```

H

Source Code for Python Stress-Strain Analysis

```
# -*- coding: utf-8 -*-
"""
Created on Fri May 20 10:37:20 2022

@author: Theo-Jan Min
"""

from IPython.display import display
import pandas as pd
import matplotlib.pyplot as plt
from matplotlib.ticker import FormatStrFormatter
from matplotlib.ticker import ScalarFormatter
import numpy as np
import math
from scipy import stats
from matplotlib.pyplot import cm

def find_neighbours(value, df, colname):
    exactmatch = df[df[colname] == value]
    if not exactmatch.empty:
        return [exactmatch.index]
    else:
        lowerneighbour_ind = df[df[colname] < value][colname].idxmax()
        upperneighbour_ind = df[df[colname] > value][colname].idxmin()
        return [lowerneighbour_ind, upperneighbour_ind]

color = ['#8dd3c7','#ffffb3','#bebada','#fb8072','#80b1d3','#fdb462','#b3de69','#fccde5','#d9d9d9']

color = ['#deebf7','#9ecae1','#3182bd','#fee0d2','#fc9272','#de2d26','#e5f5e0','#a1d99b','#31a354']

color = ['#00441b','#238b45','#74c476','#08306b','#2171b5','#6baed6','#7f2704','#a63603','#d94801']

color = ['#46e830','#22a112','#0f4508','#6baed6','#2171b5','#08306b','#ed5e5e','#cf1717','#a11212']

color = iter(cm.rainbow(np.linspace(0, 1, 20-1+1)))

done = 20

plot1 = True

Instron = [None]*20
InstronFile = [1,2,4,5,6,7,8,9]
InstronFile = InstronFile+[10,11,12,13,14,15,16,17,18,"10b", "11b"]




def cutter(file):
    end = file['Strain'][::-1].diff().gt(0.0001)[1:].idxmin()
    return end

Diameter = [2.035,
2.002,
2.00825,
```

```
2.02775,
2.0165,
2.02775,
2.019,
2.0375,
2.0325
]

Diameter = Diameter+[2.032,
2.0145,
2.01875,
2.0205,
2.00425,
2.011,
2.0295,
2.0285,
2.0145,
2.01075,
2.01575
]


Height = [2.10472,
2.23169,
2.3496,
2.27656,
2.53891,
2.3477,
2.17561,
1.95127,
2.19561
]

Height = Height+[1.552,
1.336284,
1.94389,
2.01778,
2.0391,
2.00201,
1.90292,
1.71569,
1.87138,
1.6372,
1.70985
]

cuts = [1890,1600,2060,1305,1985,1462,1999,2400]
startE = [500,450,600,100,400,500,700,1300]
endE = [1250,1000,1430,650,1400,1000,1450,1900]


startE = startE+[14000,10000,2500,4000,3700,4500,10000,13000,6000,10000,2000]
endE = endE+[32000,30000,7000,11000,11000,13000,30000,35000,19000,30000,9000]


fig2, ax2 = plt.subplots(figsize=(8,6))

types = ['Simulant','Method','Pressure','Grain□size','Coating','Temperature','Drying']
#names = ['Grain size', 'Temperature', 'Time', 'Pressure']
units = [None, None, 'MPa', '$µm$',None, '°C', None]
values = [
        ["<53","<250","<600"],
        [800,1000,1100],
        [30,45,60],
        [16,35,51]
        ]

grains = [[7,8,9],
          [4,5,6],
          [1,2]]
temps = [[6,9],
```

```
          [2,5,8],
          [1,4,7]]

times = [[1,5,9],
          [2,6,7],
          [4,8]]

press = [[5,7],
          [2,4,9],
          [1,6,8]]

fig_types = [None]*4
ax_types = [None]*4

if False:
    for i,n in enumerate(types):
        fig_types[i], ax_types[i] = plt.subplots(nrows = 1, ncols = 3, figsize=(21,6), sharey=True)
        fig_types[i].suptitle("Stress-strain curves sorted by "+n.lower(), fontsize=16)
        fig_types[i].subplots_adjust(wspace=0)



maxStrain = 0

comp = pd.read_csv(r"G:\My Drive\Thesis\3MECompTest\Run2_Comp.csv", delimiter = ',',header=1,
    ↪ skiprows=[2])


test = pd.read_csv(r"G:\My Drive\Thesis\3MECompTest\Run2_17.csv", delimiter = ',',header=1,
    ↪ skiprows=[2])






for i,n in enumerate(InstronFile):
    if i <8:
        Instron[i] = pd.read_csv(r"G:\My Drive\Thesis\Instron\Data\Theo00"+str(n)+".xls.csv",
            ↪ delimiter = ',',header=0, index_col=0, nrows = cuts[i])
        Instron[i]['Stress'] = -Instron[i]['Load(kN)_Filtered']*1000/(np.pi*(5*Diameter[i])**2)
        Instron[i]['Strain'] = -(Instron[i]['Displ(mm)_Filtered']-Instron[i]['Displ(mm)_Filtered'
            ↪ ][0])/(10*Height[i])
    else:
        Instron[i] = pd.read_csv(r"G:\My Drive\Thesis\3MECompTest\Run2_"+str(n)+".csv", delimiter =
            ↪  ',',header=1, skiprows=[2])

        start = find_neighbours(Instron[i]['Standard force'][6], comp, 'Standard force')
        comp['Deformation'] = comp['Deformation']-comp['Deformation'][start[0]]


        comp.set_index('Standard force', inplace=True)
        Instron[i].set_index('Standard force', inplace=True)
        Instron[i] = Instron[i][~Instron[i].index.duplicated()]

        na = pd.Series(np.nan, Instron[i].index)

        combi = comp['Deformation'].combine_first(na)

        Instron[i].reset_index(inplace=True)
        Instron[i].set_index('Deformation', inplace=True)

        combi = combi.interpolate(method = 'values')

        Instron[i].reset_index(inplace=True)
        Instron[i].set_index('Standard force', inplace=True)
        Instron[i]['Deformation'] = (Instron[i]['Deformation'] - combi)[Instron[i].index]
        Instron[i].reset_index(inplace=True)
        comp.reset_index(inplace=True)

        if n == "11b":
```

```
        Instron[i]['Standard force'] = Instron[i]['Standard force']*2.142881497

    Instron[i]['Stress'] = Instron[i]['Standard force']/(np.pi*(5*Diameter[i])**2)
    Instron[i]['Strain'] = Instron[i]['Deformation']/(10*Height[i])

name = ""
for j in range(3):
    if n in grains[j]:
        name = name + "G: " +str(values[0][j])+", "
for j in range(3):
    if n in temps[j]:
        name = name + "T: "+ str(values[1][j])+", "
for j in range(3):
    if n in times[j]:
        name = name + "t: "+ str(values[2][j])+", "
for j in range(3):
    if n in press[j]:
        name = name + "P: "+ str(values[3][j])

currentColor = next(color)

ax2.plot(Instron[i]['Strain'],Instron[i]['Stress'], label = "Sample "+str(n), color =
    ↪ currentColor)

if plot1 == True:

    fig1, ax1 = plt.subplots(figsize=(8,6))
    ax1.plot(Instron[i]['Strain'],Instron[i]['Stress'],color = currentColor)#, color = color[i
        ↪ ])
    ax1.axvline(Instron[i]['Strain'][startE[i]], color = 'lightgrey',linestyle = "--")
    ax1.axvline(Instron[i]['Strain'][endE[i]], color = 'lightgrey',linestyle = "--")
    E = (Instron[i]['Stress'][endE[i]]-Instron[i]['Stress'][startE[i]])/(Instron[i]['Strain'][
        ↪ endE[i]]-Instron[i]['Strain'][startE[i]])

    #Plot for linear E
    #ax1.plot([Instron[i]['Strain'][startE[i]],Instron[i]['Strain'][endE[i]]],[Instron[i]['
        ↪ Stress'][startE[i]],Instron[i]['Stress'][endE[i]]])
    print("Run "+str(n))
    #print(E)

    #Plot for linreg E
    stat = stats.linregress(Instron[i]['Strain'][startE[i]:endE[i]],Instron[i]['Stress'][startE
        ↪ [i]:endE[i]])
    print(stat[0])
    ax1.plot([Instron[i]['Strain'][startE[i]],Instron[i]['Strain'][endE[i]]],[Instron[i]['
        ↪ Strain'][startE[i]]*stat[0]+stat[1],Instron[i]['Strain'][endE[i]]*stat[0]+stat[1]],
            color = 'black')

    #plot E
    ax1.text(Instron[i]['Strain'][startE[i]]*1.1,Instron[i]['Strain'][startE[i]]*stat[0]+stat
        ↪ [1], "E = "+str(int(stat[0])) + " MPa", fontsize=10)
    ax1.set_xlabel("Strain (-)")
    ax1.set_ylabel("Stress (MPa)")
    ax1.set_title("Stress-Strain curve of sample "+str(n)+" with estimated Young's modulus" )
    fig1.savefig("Stress-Strain curve of sample"+str(n)+".svg", format = 'svg', dpi = 1200)

#plot together




ax2.set_title("Stress-Strain curves")
ax2.set_xlabel("Strain (-)")
ax2.set_ylabel("Stress (MPa)")
# define max strain
maxStrain = max(maxStrain , Instron[i]['Strain'].max())
#For different settings
#Grainsize
if False:
    for j in range(3):
        if n in grains[j]:
```

```
                ax_types[0][j].plot(Instron[i]['Strain'],Instron[i]['Stress'], color = color[i],
                    ↪ label = name)
            if n in temps[j]:
                ax_types[1][j].plot(Instron[i]['Strain'],Instron[i]['Stress'], color = color[i],
                    ↪ label = name)
            if n in times[j]:
                ax_types[2][j].plot(Instron[i]['Strain'],Instron[i]['Stress'], color = color[i],
                    ↪ label = name)
            if n in press[j]:
                ax_types[3][j].plot(Instron[i]['Strain'],Instron[i]['Stress'], color = color[i],
                    ↪ label = name)

if False:
    for i,n in enumerate(ax_types):
        fig_types[i].legend(loc= "upper left", bbox_to_anchor=(1,1), bbox_transform=ax_types[i][2].
            ↪ transAxes)#
        n[0].set_ylabel("Stress (MPa)")
        for k,j in enumerate(n):
            j.set_xlabel("Strain (-)")
            j.set_xlim((-0.001,maxStrain*1.05))
            j.set_title(str(values[i][k]) + " " + units[i])
            j.grid(True, which='both')

        fig_types[i].savefig("Stress-strain curves sorted by "+types[i].lower()+".svg", format = '
            ↪ svg', dpi = 1200)


fig2.legend(loc= "upper left", bbox_to_anchor=(0,1), bbox_transform=ax2.transAxes)
fig2.savefig("Stress-Strain curve of all samples.svg", format = 'svg', dpi = 1200)
plt.show()
```

Source Code for Python Strength-Density and Strength-Compaction Curve Analysis

```
# -*- coding: utf-8 -*-
"""
Created on Thu Aug  4 13:55:53 2022

@author: Theo

plottrends
"""

from IPython.display import display
import pandas as pd
import matplotlib.pyplot as plt
from matplotlib.ticker import FormatStrFormatter
from matplotlib.ticker import ScalarFormatter
import numpy as np
import math
from scipy import stats
import numpy.polynomial.polynomial as poly
from scipy.optimize import curve_fit
import re

all_data = pd.read_csv(r"G:\My Drive\Thesis\Plotter\Values.csv", delimiter = ',',header=0)
all_data["Full Corrected Compaction"] = all_data["Full Corrected Compaction"]*100
TitleSize = 18
Y_axisSize = 12
X_axisSize = 12
padding = 0.1 #%


def plotter(X,Y, title, labels, bySize = False, bySim = False, byMethod = False, byTemp = False,
    ↪ byPress = False, secondary = False, fit = True, curve = False, save = True):
    fig1, ax1 = plt.subplots(figsize=(16,9))



    ax1.grid(True, which='both', zorder = 0)
    ax1.set_xlabel(labels[0], fontsize = X_axisSize)
    color = "black"
    marker = '^'
    alpha = 1
    size = {"<600":"green","<250":"red", "<53":"Blue"}
    method = {"Grinded":"s","Sieved":"^"}
    sim = {"MGS-1":1,"JEZ-1":0.4}
    temp = {800:"deepskyblue",1000:"orange", 1100:"red"}
    press = {16:"deepskyblue",35:"gold", 51:"darkorange",80:"red"}

    if False:
        for i in range(len(all_data[Y])):
            if bySize:
                color = size.get(all_data["Grain size (µm)"][i])
            if byMethod:
                marker = method.get(all_data["Method"][i])
            if bySim:
                alpha = sim.get(all_data["Simulant"][i])
            if byTemp:
                color = temp.get(all_data["Temperature (°C)"][i])
```

```
            if byPress:
                color = press.get(all_data["Pressure (MPa)"][i])

            ax1.scatter(all_data[X][i],all_data[Y][i], color = color, marker = marker, alpha =
                ↪ alpha, zorder = 3, s = 100)#label = all_data["Sample"][i],


    ax1.scatter(all_data[X],all_data[Y], color = color, marker = marker, alpha = alpha, zorder = 3,
        ↪  s = 100, label = re.sub("[\(\[].*?[\)\]]", "", labels[1])+"datapoints")



    if fit:
        x_new = np.linspace(all_data[X].min(), all_data[X].max(), 100)

        p0 = [-0.19,1.23]
        coefs, vals = curve_fit(curve,all_data[X], all_data[Y], p0 = p0)
        residuals = all_data[Y]- curve(all_data[X], *coefs)
        SSE = np.sum(residuals**2)
        SST = np.sum((all_data[Y]-np.mean(all_data[Y]))**2)
        R2 = 1 - SSE/SST
        print(coefs)
        print(R2)
        ax1.plot(x_new,curve(x_new,*coefs), color = "black", linestyle = '--', label = "Fit with $R
            ↪ ^{2}$ ="+str(round(R2,4)))

        coefs, vals = poly.polyfit(all_data[X], all_data[Y], 2, full = True)
        print(coefs)
        SSE = vals[0]
        diff = all_data[Y] - all_data[Y].mean()
        square_diff = diff ** 2
        SST = square_diff.sum()
        R2 = 1 - SSE/SST
        print(R2)
        ffit = poly.Polynomial(coefs)

        #ax1.plot(x_new, ffit(x_new))


    if secondary:
        def tomMPa(y):
            return y*9.807/3.721

        def toMPa(y):
            return y*3.721/9.807

        secax_y = ax1.secondary_yaxis(
            'right', functions=(tomMPa, toMPa))
        #secax_y.set_yticks()
        secax_y.set_ylabel("Mars-equivalent compressive strength (MPa)", fontsize = Y_axisSize)

    ax1.set_title(title , fontsize = TitleSize)
    ax1.set_ylabel(labels[1], fontsize = Y_axisSize)
    fig1.legend(loc= "upper right", bbox_to_anchor=(1,1), bbox_transform=ax1.transAxes)

    if save:
        fig1.savefig(title+".svg", format = 'svg', dpi = 1200)

    plt.show()

def curve1(X,a,b):
    return a*(X)+b*((X)**2)#+c

def curve2(X,a,b):
    return a*(X-all_data["Density"].min())+b*((X-all_data["Density"].min())**2)

plotter("Full Corrected Compaction","Corrected Strength", "Compaction vs Corrected Compressive
    ↪ Strength", ["Compaction (%)","Corrected compressive strength (MPa)"], secondary = True, fit
    ↪ = True, curve = curve1)
plotter("Density","Corrected Strength", "Density vs Corrected Compressive Strength", ["Density (kg/
```

```
    ↪ m$^3$)","Corrected compressive strength (MPa)"], secondary = True, fit = True, curve =
    ↪ curve2)
```

J

Source Code for ImageJ and Python CT Analysis of Density Distributions

The CT-data was batch processed in ImageJ to obtain average pixel intensity values over the height of the samples. This is presented here:

```
files = 9;
run("Set Measurements...", "area mean min integrated median area_fraction stack display redirect=
    ↪ None decimal=9");
setBatchMode("hide");



starts = newArray(289,
272,
248,
272,
227,
268,
317,
341,
291
);
ends = newArray(1745,
1828,
1961,
1850,
1981,
1893,
1856,
1699,
1851
);
thresholds = newArray(8000,
8000,
7000,
7500,
6000,
8000,
7500,
7500,
4500
);

thresholdsLow = newArray(7719,
7138,
6441,
6812,
5101,
7565,
6738,
6976,
3989
);
//name_start = "E:/Thesis/CT/Test_";
starts = newArray(900,900)
ends = newArray(1000,1000)
name_start = "E:/Thesis/CT/Sample_";
name_end = "/DicomTop/";
```

```
for (n = 1; n <= files; n++) {

//start = starts[n-1];
//end = ends[n-1];
//count = end-start +1;

//File.openSequence(name_start+toString(n)+name_end, "virtual start="+toString(start)+" count="+
    ↪ toString(count));
File.openSequence(name_start+toString(n)+name_end, "virtual");

run("Clear Results");

setMinAndMax(0, 65535);
setAutoThreshold("Default");
setMinAndMax(0, 65535);
//setThreshold(thresholds[n-1], 65535, "raw");
// set to auto!!
//run("Auto Threshold");


//resetThreshold();
for (i = 1; i <= nSlices; i++) {//2140
//resetThreshold();
//setThreshold(10142, 65535, "raw");
Stack.setSlice(i);
//resetThreshold();
resetThreshold;
setAutoThreshold();
getThreshold(lower, upper);
if (lower > thresholdsLow[n-1]){
        run("Analyze Particles...", "size=144-Infinity display exclude include summarize");
}
showProgress(i, nSlices);
}
//resetThreshold();
Table.save("E:/Thesis/CT/Results_Porosity_Summary_"+toString(n)+".csv","Summary of DicomTop");
Table.create("Summary of DicomTop");
Table.save("E:/Thesis/CT/Results_Porosity_"+toString(n)+".csv","Results");
//saveAs("Results", "E:/Thesis/CT/Results_Porosity_"+toString(n)+".csv");
close();

}
```

The measurements from the batch-processing are then used to plot the density distribution in Python. Calibrations are made by using the average pixel intensity of the air and the maximum pixel value possible.

```
# -*- coding: utf-8 -*-
"""
Created on Fri Apr 29 19:25:34 2022

@author: Theo

%matplotlib qt for outside
%matplotlib inline for inline
"""
from IPython.display import display
import pandas as pd
import matplotlib.pyplot as plt
from matplotlib.ticker import FormatStrFormatter
from matplotlib.ticker import ScalarFormatter
import numpy as np
import math
from scipy import stats

color = ['#8dd3c7','#ffffb3','#bebada','#fb8072','#80b1d3','#fdb462','#b3de69','#fccde5'
    ↪ ,'#d9d9d9']
```

```
color = ['#deebf7','#9ecae1','#3182bd','#fee0d2','#fc9272','#de2d26','#e5f5e0','#a1d99b'
    ↪ ,'#31a354']

color = ['#893FFF','#3182bd','#2B61FF','#F4D03F','#fc9272','#de2d26','#1FC56C','#47CB31'
    ↪ ,'#196F3D']
done = 9

files = [""]*9
contours = [""]*9
Airs = [""]*9
porositys = [""]*9

startsAbs = [289,
272,
248,
272,
227,
268,
317,
341,
291]

endsAbs =  [1745,
1828,
1961,
1850,
1981,
1893,
1856,
1699,
1851]

AirMids = [5871,
5309,
4907,
5319,
3883,
5772,
5209,
5212,
3058
]

maxS = [24721,
21951,
21363,
21664,
16979,
22650,
19675,
19292,
11606
]

for i in range(9):
    files[i] = pd.read_csv(r"G:\My Drive\Thesis\CT\Results_"+str(i+1)+".csv", delimiter
        ↪ = ',',header=0, index_col=0)
    Airs[i] = pd.read_csv(r"G:\My Drive\Thesis\CT\Results_Air_"+str(i+1)+".csv",
        ↪ delimiter = ',',header=0, index_col=0)
    contours[i] = pd.read_csv(r"G:\My Drive\Thesis\CT\Values_"+str(i+1)+".csv",
```

```
        ↪ delimiter = ',',header=0)
    porositys[i] = pd.read_csv(r"G:\My Drive\Thesis\CT\Results_Porosity_"+str(i+1)+".csv
        ↪ ", delimiter = ',',header=0, index_col = -1)

    #print(Airs[i][(np.abs(stats.zscore(Airs[i]['Mean'])) < 3).all(axis=0)])
    #print(Airs[i]['Mean'][(np.abs(stats.zscore(Airs[i]['Mean'])) <3)].mean())
    #print(Airs[i]['Mean'].mean())
    #plt.plot(Airs[i]['Mean'][(np.abs(stats.zscore(Airs[i]['Mean'])) <1)].diff())
    files[i]["Height"] = files[i]["Slice"]*15

#Sample_1 = pd.read_csv(r"G:\My Drive\Thesis\CT\Results_1.csv", delimiter = ',',header
    ↪ =0, index_col=0)

#print(porositys[0])
#print(contours[0].iloc[:,300:1400].T)

def contourPlotter(data, cal):
    fig1, ax1 = plt.subplots(figsize=(9,16))

    #ax1.grid(True, which='both')
    start = 2
    end = 2140

    start_name = 'slice_'+str(start)
    end_name = 'slice_'+str(end)
    y = np.arange(0,(end-start+1)*15/1000 ,15/1000) #len(data.columns)
    X, Y = np.meshgrid(data['Radius_[mm]'],y)
    #xlist = np.linspace(-3.0, 3.0, 100)
    #ylist = np.linspace(-3.0, 3.0, 100)
    #X, Y = np.meshgrid(xlist, ylist)
    levels = np.concatenate((np.linspace(0.8,2,34), np.linspace(2+((3.5-2)/160),3.5,160)
        ↪ ))
    cmaps = "gist_ncar"#"gist_rainbow" nope#"gist_ncar" #Yes! #"nipy_spectral" Good#"brg
        ↪ " only highlights#"inferno" meh #"plasma" Meh #"rainbow" Pretty good
    cp = ax1.contourf(X, Y, data.loc[:,start_name:end_name].T/equal(cal), levels, cmap =
        ↪ cmaps)#np.sqrt(X**2 + Y**2)
    fig1.colorbar(cp)

    #scaler(ax1, scldata, "DSC")
    ax1.set_xlabel('Radius (mm)')
    ax1.set_ylabel('Height (mm)')
    plt.show()
    #fig1.legend(loc= "upper right", bbox_to_anchor=(1,1), bbox_transform=ax1.transAxes)

def aggregateLineRadial(data, files, cal):
    fig1, ax1 = plt.subplots(figsize=(16,9))

    ax1.grid(True, which='both')
    ax1.set_xlabel('Radius from centre (mm)')

    for i, n in enumerate(files):
        h,start,end = contourCutter(n)
        A = calibrate2(data[i].iloc[:,start:end].T,i)
        #print(data[i].iloc[:,0])
        #x = np.arange(0,(end-0+1)*15/1000 ,15/1000)

        #Y = n['IntDen']-equal(cal[i])
        ax1.plot(data[i].iloc[:,0], A.mean(), label = "Run-1 s"+str(i+1), color = color[
            ↪ i])
        #print(A.mean())
```

```
    ax1.set_xlim((0,10.5))
    ax1.set_ylim((0.225,0.375))
    ax1.set_ylabel('Density (Arbitrary)')
    ax1.set_title('Radial profile of average density as measured by CT')
    fig1.legend(loc="lower left", bbox_to_anchor=(0,0), bbox_transform=ax1.transAxes)
    plt.show()
    fig1.savefig("RadialProfile.svg", format='svg', dpi=1200)
    return

def contourCutter(file):
    fact = 0.98
    #print("here")
    #print(file.loc[file['IntDen'] > fact*file['IntDen'].median()]['IntDen'].diff().gt
        ↪ (0).argmax())
    #display(file.loc[file['IntDen'] > fact*file['IntDen'].median()]['IntDen'][::-1].
        ↪ diff().gt(0)[1:].iloc[0:50])
    start = file.loc[file['IntDen'] > fact*file['IntDen'].median()]['IntDen'].diff().gt
        ↪ (0)[1:].idxmin()
    end = file.loc[file['IntDen'] > fact*file['IntDen'].median()]['IntDen'][::-1].diff()
        ↪ .gt(0)[1:].idxmin()
    #print(start)
    #print(end)
    #print(np.searchsorted(file.loc[file['IntDen'] > fact*file['IntDen'].median()]['
        ↪ IntDen'].diff(),0))
    #print(file.loc[file.loc[file['IntDen'] > fact*file['IntDen'].median()]['IntDen'].
        ↪ diff() > 0])
    #start = file.loc[file.loc[file['IntDen'] > fact*file['IntDen'].median()].diff() >
        ↪ 0][0]
    #print(start)
    #plt.plot(file.loc[file['IntDen'] > fact*file['IntDen'].median()]['IntDen'].diff())
    #plt.axvline(start,color = 'red')
    #plt.axvline(end,color = 'red')
    #plt.show()
    file['Height'] = file['Height']-file.loc[start,'Height']
    return file['Height'].loc[start:end], start, end

def cutter(file):
    fact = 0.98
    #print("here")
    #print(file.loc[file['IntDen'] > fact*file['IntDen'].median()]['IntDen'].diff().gt
        ↪ (0).argmax())
    #display(file.loc[file['IntDen'] > fact*file['IntDen'].median()]['IntDen'][::-1].
        ↪ diff().gt(0)[1:].iloc[0:50])
    start = file.loc[file['IntDen'] > fact*file['IntDen'].median()]['IntDen'].diff().gt
        ↪ (0)[1:].idxmin()
    end = file.loc[file['IntDen'] > fact*file['IntDen'].median()]['IntDen'][::-1].diff()
        ↪ .gt(0)[1:].idxmin()
    #print(start)
    #print(end)
    #print(np.searchsorted(file.loc[file['IntDen'] > fact*file['IntDen'].median()]['
        ↪ IntDen'].diff(),0))
    #print(file.loc[file.loc[file['IntDen'] > fact*file['IntDen'].median()]['IntDen'].
        ↪ diff() > 0])
    #start = file.loc[file.loc[file['IntDen'] > fact*file['IntDen'].median()].diff() >
        ↪ 0][0]
    #print(start)
    #plt.plot(file.loc[file['IntDen'] > fact*file['IntDen'].median()]['IntDen'].diff())
    #plt.axvline(start,color = 'red')
    #plt.axvline(end,color = 'red')
    #plt.show()
```

```
    file['Height'] = file['Height']-file.loc[start,'Height']
    return [file.loc[start:end], start, end]

def equal(file):
    return file['Mean'].mean()

def calibrate2(Data,i):
    return (Data-AirMids[i])/maxS[i] #

def calibrate(Data,i, start, end):
    startA = start+startsAbs[i]
    endA = end+startsAbs[i]
    return (Data-Airs[i]["Mean"].loc[startA:endA].to_numpy())/maxS[i] #AirMids[i]

def plotter(data, cal):
    fig1, ax1 = plt.subplots(figsize=(16,9))

    ax1.grid(True, which='both')
    ax1.set_xlabel('Density (Arbitrary)')

    for i, n in enumerate(data):
        d, start, end = cutter(n)
        #Y = calibrate(d['Mean'],i, start, end)
        Y = calibrate2(d['Mean'],i)
        ax1.plot(Y,d['Height']/1000, label = "Run-1 s"+str(i+1), color = color[i])
        print(Y.mean())

    ax1.set_xlim((0.3,0.4))
    ax1.set_ylim((0,20))
    ax1.set_title("Average density across sample height as measured by CT")
    ax1.set_ylabel('Height (mm)')
    fig1.legend(loc= "lower right", bbox_to_anchor=(1,0), bbox_transform=ax1.transAxes)
    fig1.savefig("DensityDistribution.svg", format = 'svg', dpi = 1200)
    plt.show()

def porosity(datas, starts, ends):
    porosity = np.zeros(len(datas))

    fig1, ax1 = plt.subplots(figsize=(16,9))

    #ax1.grid(True, which='both')

    for i, n in enumerate(datas):
        #print(starts[i],ends[i])
        #print(n.loc[starts[i]:ends[i],"%Area"])
        porosity[i] = 100-n.loc[starts[i]:ends[i],"%Area"].mean()#["%Area"]

    ax1.bar(np.linspace(1,len(datas),len(datas)),porosity)
    ax1.set_xticks(np.linspace(1,len(datas),len(datas)))
    ax1.set_xticklabels(np.linspace(1,len(datas),len(datas)).astype(int).astype(str).
        ↪ tolist())
    ax1.set_xlabel("Sample")
    ax1.set_ylabel("Porosity (%)")
    ax1.set_title("(Macro) Porosity as measured by CT")
    print(porosity)
    fig1.savefig("Porosity.svg", format = 'svg', dpi = 1200)
    return

#porosity(porositys, startsAbs, endsAbs)
plotter(files, Airs)
aggregateLineRadial(contours,files, Airs)
```

```
for i in range(done):
    #contourPlotter(contours[i], Airs[i])
    a=1
```

K

Source Code for Python Taguchi Deconvolution

```
# -*- coding: utf-8 -*-
"""
Created on Tue Jun 14 11:15:37 2022

@author: Theo

MiniTab Grapher
"""

from IPython.display import display
import pandas as pd
import matplotlib.pyplot as plt
from matplotlib.ticker import FormatStrFormatter
from matplotlib.ticker import ScalarFormatter
import numpy as np
import math
from scipy import stats

import re

#plt.rcParams.update({'axes.labelsize': 'Large'})
pd.options.display.float_format = '{:.2f}'.format
pd.set_option('display.max_columns', 10)

TitleSize = 18
Y_axisSize = 12
X_axisSize = 10
padding = 0.1 #%



all_data = pd.read_csv(r"G:\My Drive\Thesis\Plotter\Values.csv", delimiter = ',',header=0)
#print(all_data)


names1 = ['Sieve size', 'Temperature', 'Time', 'Pressure']
units1 = ['$µ$m', '°C', 'minutes', 'MPa']
values1 = [
        ["<53","<250","<600"],
        [800,1000,1100],
        [30,45,60],
        [16,35,51]]


names2 = ['Simulant','Method','Pressure','Particle size','Coating','Temperature','Drying']
#units2 = [None, None, 'MPa', '$µm$',None, '°C', None]
units2 = ['-', '-', 'MPa', '$µ$m','-', '°C', '-']
values2 = [
        ["MGS-1","JEZ-1"],
        ["Milling", "Sieving"],
        [51,80],
        ["<53","<250"],
        ["-","BN"],
        [1000,1100],
        ["Dry","Non-dry"]]
```

```
def reOrder4(rawData):
    # converts from test sequence to design sequence and vise versa
    return [rawData[2],rawData[1],rawData[0], rawData[5],rawData[4],rawData[3], rawData[8],
        ↪ rawData[7],rawData[6]]

def reOrder7(rawData):
    # converts from test sequence to design sequence. Not the other way around!!!
    return [rawData[2],rawData[3], rawData[6],rawData[5], rawData[10],rawData[9], rawData[7],
        ↪ rawData[4]]

def calc(rawData, title,ylabels ):
    plot(calc4(rawData[0:9].to_numpy(), convert = False), title,ylabels)

    if not(("Porosity" in title) or ("surface" in title)):
        plot(calc7(rawData[9:17].to_numpy(), convert = False), title,ylabels)

def calc4(rawData, convert = True):
    if not(convert):
        rawData = reOrder4(rawData)

    grains = [[7,8,9],
              [4,5,6],
              [1,2,3]]
    temps = [[3,6,9],
             [2,5,8],
             [1,4,7]]

    times = [[1,5,9],
             [2,6,7],
             [3,4,8]]

    press = [[3,5,7],
             [2,4,9],
             [1,6,8]]

    results = np.zeros((4,5))
    std = np.zeros((4,3))
    delta = np.zeros(4)

    for a, d in enumerate([grains,temps,times,press]):
        for i,n in enumerate(d):
            total = np.zeros(3)
            for p, j in enumerate(n):
                total[p] = rawData[j-1]
            results[a,i] = np.average(total)
            std[a,i] = np.std(total, ddof =1)

        delta[a] = results[a,:3].max()-results[a,:3].min()
        results[a,3] = delta[a]



    dataF = {"Level":[1,2,3,"Delta","Rank"]}
    n = 4
    for a, d in enumerate(delta.argsort()):
        results[d,4] = n
        n-=1
        dataF[names1[a]] = results[a]

    print(delta)
    return [pd.DataFrame(dataF),std]

def calc7(rawData, convert = False):
    if convert:
        rawData = reOrder7(rawData)

    simulant = [[1,2,3,4],
                [5,6,7,8]]

    method = [[3,4,7,8],
```

```
            [1,2,5,6]]

    press = [[1,2,7,8],
             [3,4,5,6]]

    size = [[1,3,5,7],
            [2,4,6,8]]

    coating = [[1,3,6,8],
            [2,4,5,7]]

    temps = [[1,4,5,8],
             [2,3,6,7]]

    dry = [[1,4,6,7],
             [2,3,5,8]]

    results = np.zeros((7,4))
    std = np.zeros((7,2))
    delta = np.zeros(7)

    for a, d in enumerate([simulant,method,press,size,coating,temps,dry]):
        for i,n in enumerate(d):
            total = np.zeros(4)
            for p, j in enumerate(n):
                total[p] = rawData[j-1]
            results[a,i] = np.average(total)
            std[a,i] = np.std(total)#, ddof =1

        delta[a] = results[a,:2].max()-results[a,:2].min()
        results[a,2] = delta[a]


    dataF = {"Level":[1,2,"Delta","Rank"]}
    n = 7
    for a, d in enumerate(delta.argsort()):
        results[d,3] = n
        n-=1
        dataF[names2[a]] = results[a]

    print(delta)
    #plot(pd.DataFrame(dataF),'Main effects plot v3', ["Compressive strength (MPa)", 'Mars
        ↪ equivalent compressive strength (m-MPa)'], secondary = True)
    return [pd.DataFrame(dataF), std]

def plot(data, title, ylabels, secondary = False, save = True, printer = True ):

    data = data[0]

    if len(ylabels) == 2:
        secondary = True



    T_Design = len(data.columns)

    if T_Design == 5:
        names = names1
        units =  units1
        values = values1
        num = 3
        run = 1
    elif T_Design == 8:
        names = names2
        units =  units2
        values = values2
        num = 2
        run = 2
    else:
        print("ERROR, WRONG DATA")
```

```
fig1, axS1 = plt.subplots(nrows = 1, ncols = T_Design-1, figsize=((9+T_Design),8), sharey =
    ↪ True)

padsY = data.iloc[num,1:T_Design].max()*padding
axS1[0].set_ylabel(ylabels[0], fontsize = Y_axisSize)
axS1[0].set_ylim((data.iloc[0:num,1:T_Design].min().min()-padsY,data.iloc[0:num,1:T_Design].max
    ↪ ().max()+padsY))

fig1.suptitle("Main effects plot of "+title.lower()+" for group-"+str(run), fontsize=TitleSize)

fig1.subplots_adjust(wspace=0)
mean = data.iloc[0:num,1:T_Design].mean().mean()
print(mean)
data.to_csv(title + str(run) + " Taguchi values.csv")
(100*((data.iloc[0:num,1:T_Design]-mean)/mean)).to_csv(title+ str(run) +" Taguchi percentages.
    ↪ csv")
if printer:
    print(data)
    print((100*((data.iloc[0:num,1:T_Design]-mean)/mean)))

if not("%" in ylabels[0]):
    def toPerc(y):
        return ((y-mean)/mean)*100

    def toOriginal(y):
        return ((y*mean)+mean)/100

    secax_y = axS1[T_Design-2].secondary_yaxis(
        'right', functions=(toPerc, toOriginal))
    #secax_y.set_yticks()

    secax_y.set_ylabel("Influence on "+re.sub("[\(\[].*?[\)\]]", "", ylabels[0]).lower()+ "(%)"
        ↪ , fontsize = Y_axisSize)

if secondary:
    def tomMPa(y):
        return y*9.807/3.721

    def toMPa(y):
        return y*3.721/9.807

    secax_y = axS1[T_Design-2].secondary_yaxis(
        1.45, functions=(tomMPa, toMPa))
    #secax_y.set_yticks()
    secax_y.set_ylabel(ylabels[1], fontsize = Y_axisSize)

for i in range(T_Design-1):
    if names[i] == "Particle size":
        X = [int(s.strip('<')) for s in values[i]]
        axS1[i].set_xticks(X)
        axS1[i].set_xticklabels(values[i])
    elif names[i] == "Time":
        X = values[i]
        axS1[i].set_xticks(values[i])
    elif names[i] == "Pressure":
        X = values[i]
        if run ==1:
            axS1[i].set_xticks(np.array([15,30,45]))
        else:
            axS1[i].set_xticks(np.array([50,60,70,80]))#[45,60,75,90]
    else:
        X = values[i]

    axS1[i].plot(X,data.iloc[0:num,i+1], color = 'black', marker = 'o', mfc = 'red', mec = 'red
        ↪ ') #errorbar yerr = error
    axS1[i].grid(True, which='both')
    axS1[i].axhline(y=mean, color = 'gray', alpha = 0.8, ls = '--', lw = 1.5, dashes=(5, 10))
    #
    axS1[i].set_xmargin(0.4/(num-1))
    axS1[i].autoscale_view()
    axS1[i].set_xlabel('('+units[i]+')', fontsize = X_axisSize)
```

```
        axS1[i].set_title(names[i]+" ("+str(int(data.iloc[num+1,i+1]))+")")

    if save:
        fig1.savefig(title+" run-"+str(run)+".svg", format = 'svg', dpi = 1200)
    plt.show()
    return



calc(all_data["Corrected Strength"], "Corrected Compressive Strength", ["Compressive strength (MPa)
    ↪ ","Mars-equivalent compressive strength (MPa)"])
calc(all_data["Full Corrected Compaction"]*100, "Compaction",["Compaction (%)"])
calc(all_data["Mass Loss"]*100, "Mass loss",["Mass loss (%)"])
calc(all_data["Density"], "Density",["Density (kg/m$^3$)"])
calc(all_data["Porosity Vol"]*100, "Macro Porosity",["Porosity (%)"])
calc(all_data["Porosity Encl vol"]*100, "Macro Enclosed Porosity",["Porosity (%)"])
calc(all_data["SA"], "Macro pores surface area",["Surface area (mm$^2$)"])
##SA??
```

L

Source Code for Python Porosity analysis

```
# -*- coding: utf-8 -*-
"""
Created on Sun Jul 31 22:29:03 2022

@author: Theo
"""
import pandas as pd
import matplotlib.pyplot as plt
from matplotlib.ticker import FormatStrFormatter
from matplotlib.ticker import ScalarFormatter
import numpy as np

Drive_letter = "E"

porositys = [""]*9



slices = [1333,
1322,
1451,
1449,
1619,
1482,
1358,
1249,
1421]


Diameter = [2.035,
2.002,
2.00825,
2.02775,
2.0165,
2.02775,
2.019,
2.0375,
2.0325
]

color = ['#893FFF','#3182bd','#2B61FF','#F4D03F','#fc9272','#de2d26','#1FC56C','#47CB31','#196F3D']

sampleData = pd.DataFrame({"Sample":np.arange(1,10,1),"Slices":slices,"Diameter":Diameter})
sampleData["Height"] = sampleData["Slices"]*15/1000 #mm
sampleData["Diameter"] = sampleData["Diameter"]*10 #mm
sampleData["Volume"] = sampleData["Height"]*((sampleData["Diameter"]*0.5)**2)*np.pi

#bins = np.logspace(np.log10(0.0001),np.log10(0.0011), num = 20)
bins = np.linspace(0.0001,0.7, num = 20)
bins = np.logspace(np.log10(0.0001),np.log10(0.7), num = 50)
maxbin = 0.7
numbin = 50

def Hist(Data,n, values = True, cumsum = False, logy = False, logx = False):
    fig1, ax1 = plt.subplots(figsize=(8,4))
    #ax11 = ax1.twinx()
    if logx:
        bins = np.logspace(np.log10(0.0001),np.log10(maxbin), num = numbin)
```

```
    else:
        bins = np.linspace(0.0001,maxbin, num = numbin)

    value = np.zeros(len(bins)-1)
    for i in range(len(bins)-1):
        interest = Data.between(bins[i],bins[i+1],inclusive = "left")
        if values:
            interest = Data[interest]
        value[i] = interest.sum()

    if cumsum:
        value = value.cumsum()

    widths = bins[1:] - bins[:-1]
    ax1.bar(bins[:-1],value, width = widths, align = "edge", log = logy, color = "grey", edgecolor
        ↪ = 'black')
    if logx:
        ax1.set_xscale('log')

    ax1.set_title("Porosity distribution of run-1s"+str(n+1))
    ax1.set_ylabel("Total pore volume per bin (mm$^3$)")
    ax1.set_xlabel("Pore size (mm$^3$)")

    ax1.set_xlim((0.0001,1))
    if n <3:
        ax1.set_ylim((0,2.3))
    elif n <6:
        print("No")
        #ax1.set_ylim((0,1.6))
    else:
        print("No")
        #ax1.set_ylim((0,0.001))
    #ax11.set_y
    #ax11.set_ylim((0,1))
    #ax11.set_ylabel("Normalised pore volume per bin")
    if True:
        fig1.savefig("Porosity run-"+str(n+1)+".svg", format = 'svg', dpi = 1200)
    plt.show()

for i in range(9):
    porositys[i] = pd.read_csv(Drive_letter+r":\Thesis\CT\Sample_"+str(i+1)+"\Mask\Results_v2.csv",
        ↪  delimiter = ',',header=0, index_col = 0, encoding = 'unicode_escape')
    sampleData.loc[i, "Total Volume"] = porositys[i]["Vol. (mm³)"].sum()
    sampleData.loc[i, "Total Encl. Volume"] = porositys[i]["Encl. Vol. (mm³)"].sum()
    sampleData.loc[i, "Total SA"] = porositys[i]["SA (mm²)"].sum()

    sampleData.loc[i, "Volume Low"] = porositys[i]["Vol. (mm³)"][porositys[i]["Vol. (mm³)"].between
        ↪ (0.0001,0.0011,inclusive = "left")].sum()
    sampleData.loc[i, "Volume High"] = porositys[i]["Vol. (mm³)"][porositys[i]["Vol. (mm³)"
        ↪ ]>=0.0011].sum()
    sampleData.loc[i, "Count"] = [porositys[i]["Vol. (mm³)"]>0].sum()
    sampleData.loc[i, "Max pore size"] = porositys[i]["Vol. (mm³)"].max()
    print("\nSample: " + str((i+1)))
    #print("Volume Porosity")
    #Hist(porositys[i]["Vol. (mm³)"])
    print("Volume Porosity, x-log scale")
    Hist(porositys[i]["Vol. (mm³)"],i, logx = True)
    #print("Volume Porosity, x-log scale, counts")
    #Hist(porositys[i]["Vol. (mm³)"], values = False, logx = True)
    #plt.hist(porositys[i]["Encl. Vol. (mm³)"], bins = bins, log = False)
    #plt.xscale('log')
    #plt.bar(porositys[i]["Vol. (mm³)"], bins = bins,)
    #plt.show()

sampleData["Porosity"] = sampleData["Total Volume"]/sampleData["Volume"] #mm
sampleData["Porosity Encl"] = sampleData["Total Encl. Volume"]/sampleData["Volume"]

sampleData["Porosity Low"] = sampleData["Volume Low"]/sampleData["Volume"] #mm
print(sampleData)
sampleData.to_csv("Sample Data.csv")
```

```
plt.plot(sampleData["Porosity"]*100)
plt.plot(sampleData["Porosity Encl"]*100)
plt.plot(sampleData["Porosity Low"]*100)
```